A position sensitive time of flight setup for heavy ion elastic recoil detection analysis

Master of Science (MSc) Stephan Eschbaumer

Vollständiger Abdruck der von der Fakultät für Luft– und Raumfahrttechnik der Universität der Bundeswehr München zur Erlangung des akademischen Grades eines

Doktors der Ingenieurwissenschaften (Dr.–Ing.)

genehmigten Dissertation.

Vorsitzender: Univ.–Prof. Dr.–Ing. habil. Ferdinand Svaricek
1. Gutachter: Univ.–Prof. Dr. rer. nat. habil. Günther Dollinger
2. Gutachter: Prof. Timo Sajavaara

Die Dissertation wurde am 20. Juni 2017 bei der Universität der Bundeswehr München eingereicht und durch die Fakultät für Luft– und Raumfahrttechnik am 15. November 2017 angenommen. Die mündliche Prüfung fand am 16. November 2017 statt.

Abstract

The measurement of elemental concentrations as a function of depth is vital for the understanding of the physical properties and thereby quality of thin, functional layers produced and utilized in e.g. microelectronics and in the semiconductor technology.

In this work, a position sensitive time of flight setup (TOF-E) for the quantitative analysis by high energetic ($E_P \approx 0.2$ MeV·A) heavy ion elastic recoil detection (ERD) was developed and installed at the scattering chamber of the Q3D magnetic spectrograph located at the Munich Tandem Accelerator. The spectrometer is utilized for the quantification of the high resolution, single element depth profiles obtained with the Q3D magnetic spectrograph and as stand alone ERD detection system for the simultaneous analysis of all elements from $1 \leq M \leq 178$ with high depth resolution. A high energy- and thereby depth resolution can only be achieved by the correction of kinematic effects of the scattering process. Thus, the first timing detector, as well as the ionization chamber based energy detector were designed to additionally offer a position sensitivity. Using an electrostatic lens which images the secondary electrons created by the recoil ions on penetration of a thin carbon foil in forward emission direction, a position resolution of 0.6 mm (FWHM) was achieved by the first time detector. In combination with a position resolution of the energy detector of 2.4 mm (FWHM), which is acquired by a drift time measurement of the ionization electrons within the gas volume, the true scattering angle of each recoil ion can be determined with an angular resolution of 2.5 mrad (FWHM). This allows to reduce the contributions of the kinematic effects on the energy resolution from 3.3 % to 0.4 %.

By the detection of secondary electrons in backward emission direction within the first timing detector and within a second timing detector, an overall time resolution of 280 ps (FWHM) was achieved. In standard ERD measurements this allows, utilizing a 40 MeV [197]Au projectile beam at an incident angle of 4° to achieve a surface energy resolution from the time of flight information of 0.76 % and thereby a depth resolution of 2.3 nm (FWHM). Furthermore, the setup allows elemental separation up to a mass of 40 with a mass resolution of $\Delta M < 1$.

At high projectile energies ($E_P \approx 1.3$ MeV·A), the setup also offers the ability to per-

form ERD analysis utilizing a TOF-ΔE-E$_{\text{Res}}$ technique. The benefit of this technique is given by combining the inherent mass sensitivity of the TOF-E method with the sensitivity of the ΔE-E$_{\text{Res}}$ method to the nuclear charge. Both together allow to create unique filter conditions for background suppression and an overall sensitivity enhancement. This was demonstrated for the difficult case of the detection of low nitrogen amounts within diamond. A sensitivity of $10\,\text{ppm}$ was achieved with this technique, which is better by two orders of magnitude compared to conventional ΔE-E$_{\text{Res}}$ analysis. In addition to that, the method also allows for isotope separation in a medium heavy mass range of $12 \leq \text{M} \leq 40$, which is not possible with the ΔE-E$_{\text{Res}}$ method.

Zusammenfassung

Die tiefenaufgelöste Bestimmung der Elementzusammensetzung von Dünnschicht-systemen, wie sie in der Mikroelektronik und Halbleitertechnik zum Einsatz kommen, bildet die Grundlage zum Verständnis ihrer physikalischen Eigenschaften und damit deren Qualität sowie Funktionalität.

Im Rahmen dieser Arbeit wurde ein ortsauflösendes Flugzeitspektrometer (TOF-E) für die quantitative Elementanalytik mittels der elastischen Vorwärtsstreuung hoch-energetischer, schwerer Ionen ($E_P \approx 0.2\,\mathrm{MeV}$·A) entwickelt und an der Streukam-mer des Q3D Magnetspektrographen am Münchner Tandem Beschleuniger installiert. Das Spektrometer dient dabei sowohl zur Quantifizierung der hochaufgelösten Einzelelement-Tiefenprofilen des Q3D Magnetspektrographen sowie zur eigenständigen ERD Analyse einer Vielzahl an Probenelementen im Massenbereich von $1 \leq M \leq 178$ in einer einzelnen Messung mit hoher Tiefenauflösung.

Eine hohe Energie- und damit Tiefenauflösung wird nur erreicht, wenn Beiträge kinematischer Effekte des Streuprozesses korrigiert werden. Dazu wurde sowohl der erste Zeitdetekor als auch der auf Basis einer Ionisationskammer arbeitende Energiede-tektor ortsauflösend ausgelegt. Mit Hilfe einer elektrostatischen Linsenabbildung in-nerhalb des ersten Zeitdetektors von Sekundärelektronen in Vorwärtsrichtung, erzeugt durch die Ionen bei Durchtreten einer dünnen Kohlenstofffolie, wird erstmals eine Ortauflösung von $0.6\,\mathrm{mm}$ (FHWM) erreicht. In Kombination mit einer über eine Driftzeitmessung der Ionisationselektronen innerhalb des Energiedetektors erreichten Ortsauflösung von $2.4\,\mathrm{mm}$ (FWHM) kann so der tatsächliche Streuwinkel für jedes Ion mit einer Winkelauflösung von $2.5\,\mathrm{mrad}$ (FWHM) erfolgen. Dies erlaubt die kinema-tischen Beiträge zur Energieauflösung von $3.3\,\%$ auf $0.4\,\%$ zu reduzieren.

Anhand der Detektion von in Rückwärtsrichtung emittierten Sekundärelektronen innerhalb des ersten sowie eines zweiten Zeitdetektors konnte eine Gesamtzeitauflösung von $280\,\mathrm{ps}$ (FWHM) erreicht werden. Damit kann unter Standardmessbedingungen mit einem $40\,\mathrm{MeV}$ ^{197}Au Projektilstrahl bei einem Einfallswinkel von $4°$ eine aus der Flugzeitmessung gewonnene Energieauflösung an der Probenoberfläche von 0.76% er-reicht werden, was einer Tiefenauflösung von $2.3\,\mathrm{nm}$ (FWHM) entspricht. Weiterhin

ermöglicht das System die Massentrennung aller Probenelemente bis hin zur Masse 40 mit einer Auflösung von $\Delta M < 1$.

Bei Verwendung hochenergetischer Projektile ($E_P \approx 1.3$ MeV·A) erglaubt das Spektrometer zudem eine ERD Analyse mittels einer TOF-ΔE-E_{Rest}-Technik durchzuführen. Hierbei wird die inhärente Massensensitivität der TOF-E-Methode mit der Kernladungssensitivität der ΔE-E_{Rest}-Methode kombiniert, wodurch sich einzigartige Filtermöglichkeiten zur Untergrundreduzierung und damit Sensitivitätssteigerung ergeben. Für den schwierigen Nachweis kleiner Stickstoffkonzentrationen in Diamant konnte damit eine Sensitivität von 10 ppm erreicht werden, was einer Verbesserung um mehr als zwei Größenordnungen entspricht im Vergleich zu konventioneller ΔE-E_{Rest}-Methode. Weiterhin können damit für einen mittleren Massenbereich von $12 \leq M \leq 40$ die Isotopenverhältnisse bestimmt werden, was die alleinige Anwendung der ΔE-E_{Rest}-Methode nicht erlaubt.

Contents

Chapter 1

Introduction

The successive miniaturization in microelectronics recently lead to the 14 nanometer (14 nm) semiconductor device fabrication node of which first devices were shipped to customers in the year 2014. At such scale levels, gate lengths and thicknesses of functional layers only consist of a few atomic layers. The physical properties and thereby the quality of the produced device strongly depends on the stoichiometric composition of the thin, functional films. Elemental concentrations of doping elements, but also unwanted impurities in the ppm (parts per million) range as well as diffusion effects occurring at the interfaces of the thin layers are of vital importance. Only a quantitative and depth resolved elemental analysis allows to understand and to optimize the functionality as well as the manufacturing quality of such semiconductor devices.

Several, well established methods for analysis are available. These methods include the secondary ion mass spectroscopy (SIMS [1]), the Auger electron spectroscopy (AES [2]), the X-ray photoelectron spectroscopy (XPS [3]), the nuclear reaction analysis (NRA [4]) and methods utilizing the elastic scattering of swift ions.

The main advantages of the elastic scattering methods are the great range of analyzable elements, the inherent quantification accuracy due to the well known scattering cross sections as well as the ability to achieve elemental depth profiles utilizing the known stopping forces of ions in matter.

The two most common elastic ion scattering methods are the Rutherford backscattering spectrometry (RBS [4]) and the elastic recoil detection (ERD), first introduced by L'Ecuyer et al. in 1976 [5]. In RBS, the energy of back scattered incident ions, usually protons or helium ions within an energy range of $100 \, \text{keV} - 3 \, \text{MeV}$, is analyzed. The energy of the back scattered ions is determined by the scattering angle, the masses of the sample atoms as well as the energy loss within the sample matrix towards the target atom and back to the surface. Thus, elemental depth profiles can be obtained with this method. However, with the energy being the only measured quantity, the

drawback of this method lies in the ambiguity between the elemental/mass identifica-
tion and the depth determination. Therefore, with RBS only elements being heavier
than the sample atoms are detectable without significant background. Another disad-
vantage lies in the fact that the detection of hydrogen is not possible with this method
due to the scattering kinematics.

1.1   Elastic Recoil Detection (ERD)

The mentioned ambiguity occurring with the RBS method can be circumvented by
the use of the elastic recoil detection (ERD) technique: The sample atoms scattered
out of the solid body are detected in forward direction [6, 7]. The ERD principle is
illustrated in Fig. 1.1: Swift heavy ions (e.g. $50 - 200\,\mathrm{MeV}$ ^{127}I) directed at low incident
angles α (e.g. $4° - 20°$) onto the sample surface offer sufficient momentum transfer in
the elastic collision to scatter the target atoms (recoil ions) into the detector up to
a sample thickness of $\approx 1\,\mu$m. Besides the measurement of the particle energy, this
technique allows the immediate determination of the mass and/or the nucleus charge,
which in contrast to RBS, facilitates a background free analysis of light elements. In
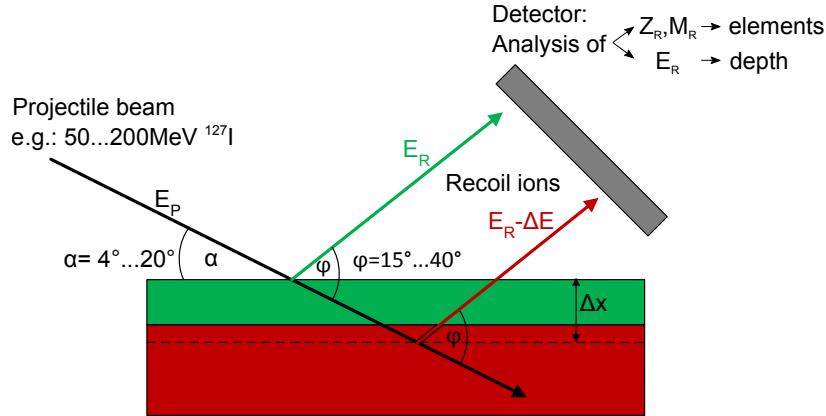
Figure 1.1: *Schematic illustration of an elastic recoil detection (ERD) experiment.*

contrast to the SIMS technique, no sputtering process of the surface is used in ERD.
Every detected recoil ion originates from a single binary collision. The kinetic energy
of the recoil ions is determined by the scattering angle φ, the combination of the
scattering masses as well as of the energy loss of the projectile- and recoil ion within
the sample matrix. Similar to RBS, the well known stopping force within the sample
matrix allows to obtain quantitative depth profiles of multiple elements simultaneously.
Since the sample atoms exclusively represent the testing probe, the above mentioned

ambiguity occurring in RBS is eliminated by an independent measurement of the recoil ion energy as well as of its mass and/or nuclear charge.

1.2   High resolution ERD with heavy ions at the Munich Tandem Accelerator

Most laboratories, at which ERD analysis is performed, host accelerators offering terminal voltages limited to $1-2$ megavolts (MV) primarily optimized for RBS measurements with light projectiles. The received low projectile energies with these accelerators and thereby the resulting low momentum transfer to the target atoms restrict ERD analysis mainly to light masses and the method is often exclusively used for the detection of hydrogen in addition to the RBS measurements (e.g. with He projectile beams). With the Munich Tandem Accelerator, however, terminal voltages up to 14 MV are available and heavy projectiles such as ^{58}Ni, ^{127}I or ^{197}Au with energies in the range of $0.2-2$ MeV·A (A: mass number) can be created. This increases the field of application greatly with respect to the analyzable mass- and depth range [5, 7, 8].

The achievable depth resolution in ERD experiments primarily depends on the energy resolution of the detectors. High resolution elastic recoil detection is performed at the Munich Tandem Accelerator routinely utilizing a Q3D magnetic spectrograph offering a unique energy resolution of $\Delta E/E = 5 \times 10^{-4}$ at a solid angle of detection of $\Delta \Omega = 6$ msr [9, 10]. This resolution offers the ability to resolve single adjacent atomic layers as demonstrated for the first five atomic layers in highly orientated pyrolytic graphite [11]. One drawback with the use of the Q3D magnetic spectrograph, however, is the fact that only a certain range of magnetic rigidity and thereby momentum to charge ratio of the recoiling ions is accepted. As a result, high resolution depth profiles are only obtained for one isotope of a selected charge state and for a limited depth range within one single measurement. Therefore, for quantification of the high resolution depth profiles, as well as for monitoring multiple elements of the sample, an additional detection system based on the ΔE-E method has been installed in the Q3D scattering chamber. It runs simultaneously to the Q3D measurements or as stand alone system offering a sensitivity in the ppm range and a depth resolution of about 10 nm [12]. With this setup (Q3D and ΔE-E detector) numerous questions in the field of materials research, solid state physics and surface physics have been answered very successfully within the past years. Studies were focused on diamond layers [13–16], cubic boron nitride layers [17–19], Group-III nitrides [20–22] and several other material systems [23–26]. Both methods, the ΔE-E method and the ERD analysis utilizing the Q3D magnetic spectrograph, are introduced in detail in chapter 2.2 of this work.

1.3   Demand for a position sensitive time of flight – energy (TOF-E) setup

Limitations in high resolution elastic recoil detection in view of sensitivity and accuracy are not only given by the performance of the detection system. A most severe limit is given by irradiation damage, which represents a general limit for any ion beam analysis method. The original depth profiles can be altered during measurement by ion beam stimulated processes before the required statistics are recorded with the detection system [10].

A way to minimize this problem is to lower the deposited energy into the sample by a reduction of the projectile energy and by a simultaneous increase of the scattering cross section by the choice of heavier projectile masses [27]. This is demonstrated by ERD analysis of oxygen in a 6 nm SiO_2 layer deposited on Si: The ratio of sputtered ions per detected oxygen recoil ion is determined for every ion beam type at a count rate of 4 kHz in the focal plane detector of the Q3D magnetic spectrograph ($\varphi = 15°$). As illustrated in Tab. 1.1, in contrast to the most commonly used 170 MeV ^{127}I projectile beam for ERD measurements at the Munich Tandem Accelerator, the irradiation damage is reduced by three orders of magnitude utilizing a 40 MeV ^{197}Au projectile beam.

Beam type	sputtered ions/detected ion	dE/dx $\left(\frac{keV}{\mu m}\right)$	dσ/dΩ (mb/msr)
170 MeV ^{127}I	4×10^{13}	1.4×10^4	2.86
25 MeV ^{35}Cl	2×10^{12}	4.5×10^3	1.73
80 MeV ^{197}Au	4×10^{11}	1.2×10^4	63.62
40 MeV ^{197}Au	6×10^{10}	7.3×10^3	254.48

Table 1.1: *Measurements on a 6 nm SiO_2 layer demonstrate a reduction of irradiation damage by three orders of magnitude utilizing a 40 MeV ^{197}Au projectile beam in contrast to a 170 MeV ^{127}I beam, which is used for most standard ERD measurements performed at the Munich Tandem Accelerator.*

However, the low recoil ion energies obtained by the 40 MeV ^{197}Au projectile beam are within an inaccessible regime for the ΔE-E, detector running simultaneously to the Q3D measurements. Thus, an alternative detection system for quantification of the high resolution depth profiles in this energy regime is required.

The time of flight – energy (TOF-E) method represents a well established technique for ERD depth profiling at low recoil ion energies and can be utilized to

replace the ΔE-E method [4]. For mass discrimination this method uses a combined measurement of both the particle's energy (e.g. with an ionization chamber) and of its velocity. The velocity is determined by the measurement of the time of flight (TOF) of the recoil ion to traverse a certain distance between two timing detectors. One advantage of the TOF-E method is that once the mass has been identified, the energy information can be obtained from the TOF spectra exclusively. In most cases, the time information transformed into the energy information is superior to the energy resolution of the energy dispersive detector at low recoil ion energies [28].

In order to achieve a sensitivity similar to the ΔE-E detector, a large solid angle of detection is essential which is accompanied by a degradation of the energy resolution up to several percent due to kinematic effects. In addition to that, for high resolution ERD measurements performed with the Q3D magnetic spectrograph, projectile incident angles below 5° are used in order to maximize stopping within the sample for an increased depth resolution close to the sample surface [10]. These low incident angles lead to an effective beam spot size of $> 6\,$mm on the sample surface causing an additional kinematic effect, which degrades the energy resolution. For an efficient correction of the kinematic effects, a determination of the true scattering angle for each recoil event is necessary. This requires the TOF-E setup to feature a position sensitivity.

1.4   Objectives of the work

The aim of the present work is to develop, install and characterize a position sensitive time of flight – energy (TOF-E) setup at the scattering chamber of the Munich Q3D magnetic spectrograph. The TOF-E setup has to detect the low energetic recoil ions obtained by a 40 MeV ^{197}Au projectile beam which is impossible for the existing ΔE-E detector. The setup has to work in the low recoil energy regime as stand alone detection system or as a dedicated tool for the quantification of the high resolution ERD depth profiles obtained by the Q3D magnetic spectrograph. Design focus lies on the additional capability to spatially resolve the scattering angle of the recoil ions within the scattering plane, in order to correct for kinematic effects. This involves the development of a position sensitive time of flight detector as well as a position sensitive ionization chamber.

The following chapter 2 describes the basic fundamentals of quantitative elastic recoil detection and introduces the common methods used for detection of the recoil ions such as the Q3D magnetic spectrograph, the ΔE-E method and the TOF-E method, which is highlighted in this work. Chapter 3 is dedicated to the unavoidable influence of kinematic effects on the energy-/depth resolution and discusses the possibilities of correcting these effects by means of multiple recoil ion position determinations in the framework of a TOF-E detection system. The fourth chapter defines the requirements on the TOF-E system and describes in detail the development and intrinsic performance of a position sensitive timing detector (T_1), which features an electrostatic lens for secondary electron focusing, necessary to achieve an appropriate spatial resolution. Section 4.4 of chapter 4 describes the design of a position sensitive ionization chamber serving as energy dispersive detector. The characterization and performance of the entire system is demonstrated in chapter 5 by TOF-E measurements on a variety of samples.

Chapter 2

Elastic Recoil Detection for elemental depth profiling

In this chapter, the physical principles of the ERD technique as well as the technical realization with respect to the most commonly used detection methods are summarized.

Heavy ion elastic recoil detection is based on the elastic collision of a swift heavy projectile with the atoms of a sample. After collision, the sample atoms (recoil ions) are detected in forward scattering direction (see Fig. 1.1). By use of the energy loss information of the projectile and the recoil ion within the sample matrix, elemental depth profiles are obtainable. Thus, for accurate quantitative elemental analysis, knowledge of the scattering cross sections and the involved stopping forces are of great concern, as discussed in section 2.1 of this chapter. Equal importance, however, has to be accredited to the detection methods and detectors used for analysis. In quantitative ERD, the task of the detectors is to identify the recoiling ion species and its energy independently of each other. Their performance usually is the dominating factor with respect to depth- and mass resolution. Section 2.2 of this chapter introduces the detection methods used at the Munich Tandem Accelerator for quantitative ERD and discusses their limits of application with respect to the measurement conditions, such as projectile beam type, recoil ion energy, accuracy and sensitivity. The time of flight – energy (TOF-E) method, which has to be utilized for ERD measurements at low recoil ion energies, is introduced in section 2.2.3 of this chapter.

2.1   Fundamentals of heavy ion ERD analysis

2.1.1   Physics of elastic recoil detection

The energy E_R transferred in a binary collision from the projectile with the energy E_P to the recoil ion (zero velocity before scattering event) is given in the laboratory frame in dependence of the scattering angle φ of the recoil ion (see Fig. 1.1) by

$$E_R = k_R \cdot E_P = 4 \cdot \frac{M_P M_R}{(M_P + M_R)^2} \cdot \cos^2 \varphi \cdot E_P \; . \tag{2.1}$$

For kinematics $\varphi \leq 90°$ the parameter k_R represents the kinematic factor of ERD. M_P and M_R are the masses of the projectiles and recoil ions, respectively. The scattering cross section $(d\sigma/d\Omega)$ is well described by a Rutherford scattering cross section in the laboratory frame:

$$\left(\frac{d\sigma}{d\Omega} \right)_{Ruth} = \left(\frac{e^2}{8\pi\epsilon_0} \frac{Z_P Z_R}{E_P} \frac{(M_P + M_R)}{M_R} \right)^2 \frac{1}{\cos^3 \varphi} \; . \tag{2.2}$$

Here, Z_P, Z_R represent the atomic numbers and M_P, M_R the masses of the projectile and recoil ion, respectively. However, due to screening effects by the electrons of the projectiles and recoil ions the ERD cross section is reduced. Thus, in comparison to the Rutherford cross section $(d\sigma/d\Omega)_{Ruth}$, the ERD cross section $(d\sigma/d\Omega)_{ERD}$ is given by [29]:

$$\left(\frac{d\sigma}{d\Omega} \right)_{ERD} = \frac{\left(1 + \frac{V_1}{2E_P} \right)}{\left(1 + \frac{V_1}{E_P} + \left(\frac{V_1}{2E_P \cos \varphi} \right)^2 \right)^2} \cdot \left(\frac{d\sigma}{d\Omega} \right)_{Ruth} \tag{2.3}$$

with

$$V_1 = \frac{M_P + M_R}{M_R} \cdot 48.73 \cdot Z_P \cdot Z_R \cdot \sqrt{Z_P^{2/3} + Z_R^{2/3}} \quad \text{in eV.} \tag{2.4}$$

As an additional advantage of heavy ion ERD analysis, the maximum projectile scattering angle $\varphi_{P,max}$ has to be mentioned, which is given by Eq. 2.5 to be

$$\varphi_{P,max} = \arcsin \left(\frac{M_R}{M_P} \right) \; . \tag{2.5}$$

As long as the projectile mass is heavier than the majority of the sample elements $\varphi_{P,max}$ stays small. Therefore, an appropriate choice of the projectile mass allows to avoid that incident particles are scattered in forward direction into the detection system.

2.1.2 Quantitative depth analysis with ERD

The number Y_i of particles of the species i registered by the detection system is defined by the concentration n_i, the detection efficiency f_i, the projectile dose N_P, the differential cross section $(d\sigma/d\Omega)_i$, the solid angle of detection $\Delta\Omega$ and the effective thickness $\Delta x/\sin\alpha$ of the layer to be considered with α representing the incident angle of the projectile beam with respect to the sample surface (see Fig. 1.1):

$$Y_i = n_i \cdot f_i \cdot \left(\frac{d\sigma}{d\Omega}\right)_i \cdot \Delta\Omega \cdot N_P \cdot \frac{\Delta x}{\sin\alpha} \ . \tag{2.6}$$

With detection systems such as ionization chambers or solid state detectors offering a detection efficiency for the high energetic recoil ions of virtually $100\,\%$ ($f_i = 1$), one obtains the integral concentration ratios according to Eq. 2.6 by evaluation of the particular events and weighting them with the corresponding cross sections.

In order to obtain elemental depth profiles of a certain layer, the beam current measurement is not required. An iterative algorithm taking the different stopping force of each element in dependence of the sample composition and the energy dependence of the scattering cross section into account, is used [30]. For the determination of the relative concentration n_i of a certain element i within a depth interval Δx, two independent correlations are considered. The first is described by Eq. 2.6 to obtain the number of detected particles. The second uses the dependence of the stopping force in relation to the sample composition and the relation of a measured energy interval ΔE_i to a depth interval Δx of the analyzed layer:

$$\Delta E_i = \Delta x \cdot S_i(x) \tag{2.7}$$

with

$$S_i(x) = \sum_{j=1}^{m} n_j \left[k_i \cdot \frac{(dE_P/dx)_j}{\sin\alpha} + \frac{(dE_i/dx)_j}{\sin\beta} \right] \ , \tag{2.8}$$

in which k_i represents the kinematic factor of Eq. 2.1. $S_i(x)$ is defined as the energy loss factor for the element i. It contains the stopping force contributions of each the projectile and the recoil ion within all m elements of the sample composition within the depth interval Δx. The combination of Eq. 2.6 and Eq. 2.7 leads to a system of m linear equations for the concentrations n_j for the m elements within the depth x. This system of equations is solved with the application of an iterative algorithm implemented in the program KONZERD, which is described in detail in [30].

Equations 2.7 and 2.8 demonstrate the importance of exact knowledge of the stopping forces with respect to quantification accuracy. These energy loss values can be found in literature, however, for heavy ions as used in ERD deviations of

up to 20 % can be observed leading to uncertainties of the calculated depth profiles in the same order of magnitude. One solution to obtain more accurate energy loss values is the use of the program SRIM/TRIM by Ziegler et al. [31, 32]. The program does not only calculate energy loss values analytically, but also interpolates between the latest, in the program incorporated, energy loss data measured by several groups around the world, which utilize ion beam analysis methods. This leads to a constant improvement of the program and the results obtainable by it. However, most accurate values can only be received by direct measurement of the stopping force for the corresponding combination of traversing ion and sample composition and by taking charge dependent effects into account, as demonstrated in [33–35].

The achievable depth resolution in ERD measurement Δx primarily depends on the energy resolution $\Delta E/E_R$ of the used detection system:

$$\Delta x = \frac{\Delta E/E_R}{\frac{S_P}{E_P \cdot \sin \alpha} + \frac{S_R}{E_R \cdot \sin \beta}} \quad . \tag{2.9}$$

Here, $E_{P,R}$ are the energies and $S_{P,R}$ the stopping forces of the projectile P and recoil ion R. α represents the incident and β the exiting angle with respect to the sample surface (see Fig. 1.1).

Principle limits with respect to the achievable depth resolution Δx are also, besides the detector energy resolution, given by two physical contributions, the energy loss straggling and small angle scattering, both increasing with depth.

The energy loss straggling of the ions is dominated by statistics of energy transfer to the target electrons and can be described according to Bohr [36]: A mono energetic projectile beam shows an energy distribution after traversing the thickness Δl of a sample matrix incorporating the nuclear charge Z_T and the atomic density N. The full width at half maximum (FWHM) of the energy distribution can be described by

$$\Delta E_{strag} = \sqrt{\frac{2\ln 2}{\pi}} \cdot \frac{Z_P e^2}{\epsilon_0} \cdot \sqrt{(Z_T N \Delta l)} \,, \tag{2.10}$$

with Z_P representing the nuclear charge of the projectile. However, Eq. 2.10 is only valid for projectiles devoid of electrons and with velocities greater than the effective velocities of the electrons attached to the target atoms. A proposed correction for lower projectile velocities by Lindhard and Scharff [37], however, does not affect the proportionality

$$\Delta E_{strag} \propto Z_P \sqrt{\Delta l} \,, \tag{2.11}$$

but a better description of the energy straggling at low projectile velocities can be given by the theories of Chu [38] or Yang [39].

Small angle scattering (also referred to as multiple scattering) describes the resulting angular distribution of an ion projectile beam with the nuclear charge Z_P and the energy E_P after traversing a particular distance x within a sample matrix of the nuclear charge Z_T and the atomic density N. The half FWHM of this distribution can be described according to Sigmund and Winterbon [40] by

$$\Delta\alpha_{1/2} = C \cdot \frac{2 Z_P Z_T e^2}{4\pi\epsilon_0 \, E_P \, a} \cdot (\pi a^2 N x)^D \, , \qquad (2.12)$$

with the screening radius a, which can be calculated using the Bohr radius a_0

$$a = \frac{0.885 \cdot a_0}{\sqrt{Z_P^{2/3} + Z_T^{2/3}}} \quad \text{and} \qquad (2.13)$$

the parameters C, D, valid for ERD measurements with $C = 0.5$ and $D = 0.62$ according to [41]. Utilizing Eq. 2.12, the proportionality of the angular distribution is therefore given by

$$\Delta\alpha_{1/2} \propto \frac{Z_P Z_T}{E_P} \cdot \left(\frac{x}{\sin\alpha}\right)^{0.62} \, , \qquad (2.14)$$

with $x/\sin\alpha$ representing the effective path length of the particle at an incident angle α with respect to the sample surface. Two negative contributions to the achievable depth resolution by small angle scattering can be observed: On the one hand, the projectile's original incident angle α spreads by $\Delta\alpha$ with sample depth until the projectile reaches its partner for binary collision. Thus, the scattering angle φ and therefore the kinematics of the scattering process according to Eq. 2.1 are also altered leading to an unavoidable broadening in energy transferred to the recoil ion. On the other hand, small angle scattering leads to an increase of the effective path length for both, the projectile and recoil ion, thus the additional caused energy loss straggling represents the dominating limit for depth resolution at greater sample depths.

The following figures 2.1 and 2.2 exemplarily illustrate the contributions of energy loss straggling and small angle scattering (multiple scattering) to the achievable energy-/depth resolution in ERD measurements on a silicon oxide layer. The corresponding values are calculated with the program code DEPTH, developed by Szilágyi et al. [42]. The code uses the same stopping forces as SRIM [31]. Energy loss straggling is calculated according to Yang et al. [39] and the multiple scattering effects are incorporated [43]. Results obtained by using the 40 MeV [197]Au projectile beam at an incident angle $\alpha = 4°$ are put in contrast to results obtained by use of the 170 MeV [127]I projectile beam at an incident angle $\alpha = 7°$. The particular incident angles are chosen in way, that for high resolution Q3D measurements the path length effects are utilized to maintain the kinematic correction with increasing sample depth [11]. Oxygen represents the considered recoil ion in the calculations.

The contributions of energy loss straggling and multiple scattering to the achievable energy-/depth resolution for a sample depth range of 300 nm in case of the 170 MeV [127]I projectile beam are illustrated in Fig. 2.1(a). Multiple scattering of the projectile within the sample represents the dominating contribution, nevertheless, a very consistent depth resolution is achieved for the entire displayed range of sample depth. However, as seen from Fig. 2.1(b), showing the first 25 nm of the sample at an assumed energy resolution of the detection system of $\approx 1\%$ no surface depth resolution of better than ≈ 12 nm can be achieved with this projectile beam.

The situation changes significantly for the 40 MeV [197]Au projectile beam in terms of the contribution by multiple scattering as well as in terms of the achievable surface energy-/depth resolution as illustrated in Fig. 2.2(a). The achievable resolution is extensively dominated by multiple scattering of the heavy [197]Au projectile already within the first 100 nm of the sample. The plateau is caused by a compensation of kinematic- and path length effects (see chapter 3 and [11]). However, as seen in Fig. 2.2(b), close to the surface of the sample an energy-/depth resolution better by a factor of ≈ 4 can be achieved by the use of the 40 MeV [197]Au projectile beam.

(a)   (b)
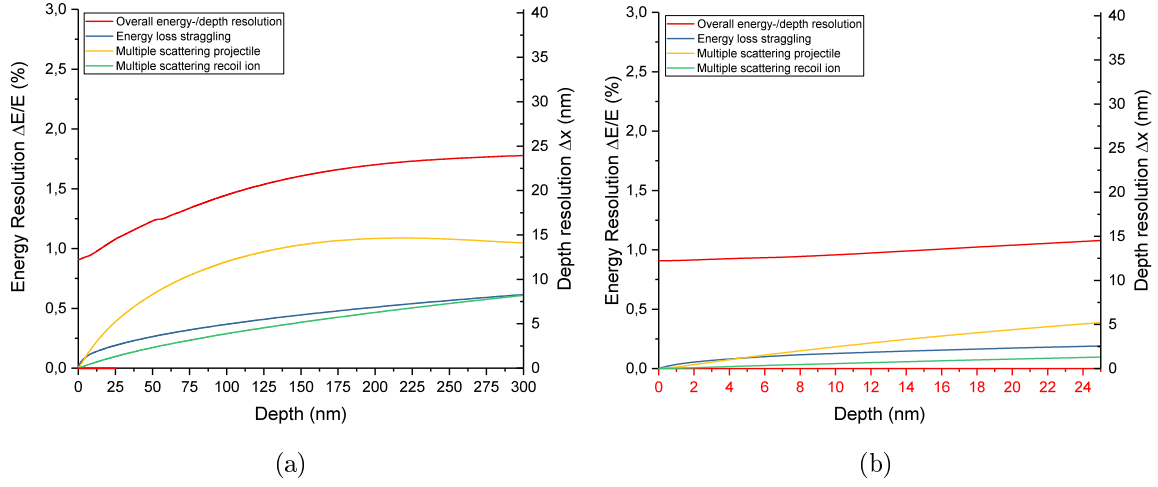
Figure 2.1: *(a)*: *Contributions of energy loss straggling and multiple scattering to the overall energy-/depth resolution in ERD measurements on a silicon oxide layer utilizing a 170 MeV ^{127}I projectile beam at an incident angle of $\alpha = 7°$ calculated with DEPTH. The achievable energy resolution is dominated by multiple scattering of the iodine projectile, but a relatively consistent depth resolution is achieved up to a sample depth of 300 nm. (b): Closer view of the first 25 nm of sample depth: At an assumed energy resolution of the detection system of $\approx 1\%$, the achievable surface energy resolution is limited to ≈ 12 nm.*

(a)   (b)
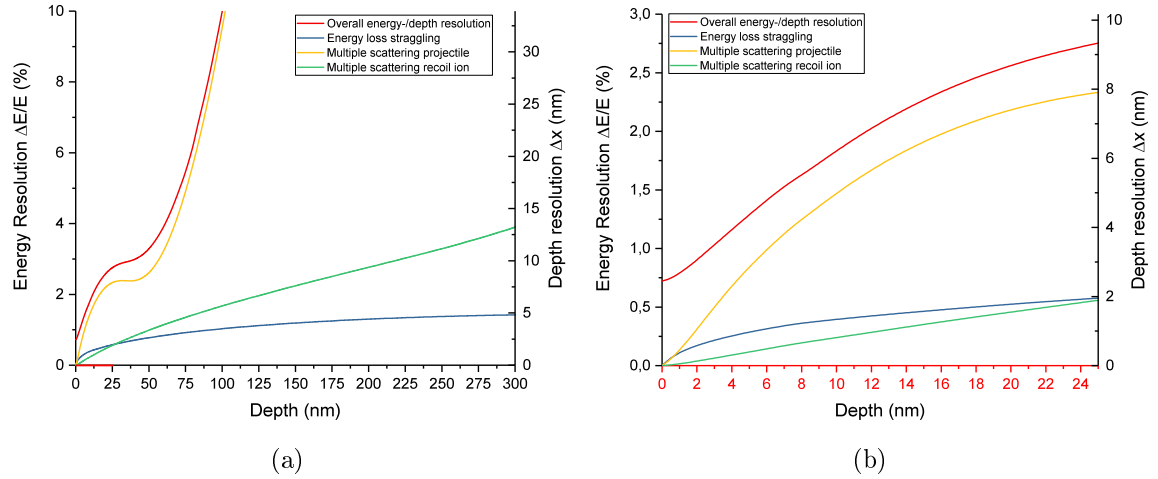
Figure 2.2: *(a)*: *DEPTH results for the same sample as shown in Fig. 2.1, however, a 40 MeV ^{197}Au projectile beam at an incident angle of $\alpha = 4°$ is utilized for the analysis. Within the first 300 nm of the sample, the resolution is extensively dominated by multiple scattering of the heavy ^{197}Au projectile. The plateau is caused by a compensation of kinematic- and path length effects. (b): Closer view of the first 25 nm of sample depth: The achievable surface depth resolution at a given energy resolution is increased in contrast to the 170 MeV ^{127}I projectile beam.*

2.2   Methodology in ERD

The detection systems used for heavy ion ERD have to fulfill two main tasks. First, the forward scattered recoil ions have to be identified in terms of their nuclear charge or mass, and second, their total energy has to be measured in order to obtain elemental depth profiles of the sample. However, depending on the recoil ion energy range, only certain approaches for detection are applicable.

The following section gives an overview over the detection methods used for ERD at the Munich Tandem Accelerator with respect to their field of application. These common methods include the magnetic analysis utilizing a Q3D magnetic spectrograph, the ΔE-E method and the time of flight – energy (TOF-E) method. The latter is dedicated to the use with a 40 MeV ^{197}Au projectile beam at which the ΔE-E method fails to discriminate elements due to the low recoil ion energies, as explained in the following.

2.2.1   Magnetic Spectrograph (Q3D)

As already mentioned in section 1.2, the use of a Q3D magnetic spectrograph at the Munich Tandem Accelerator allows to achieve single atomic layer depth resolution close to the surface, due to its high energy resolution $\Delta E_R/E_R$ of 5×10^{-4}. The spectrograph consists of one magnetic quadrupole and three dipoles (Q3D). An additional multipole element, which is located between the first and second dipole, allows to adjust the ion optical properties of the spectrograph. A schematic illustration of the Q3D magnetic spectrograph is shown in Fig. 2.3. Within the magnetic field provided by the spectrograph, the forward scattered recoil ions are separated spatially with high dispersion ($\Delta p_R/p_R = 5\,\%$) according to their ratio of momentum p_R to charge. After traversing the magnetic field, the recoil ions are ion optically imaged into the focal plane of the spectrograph [44]. A detector placed in the focal plane identifies the nuclear charge, measures the energy and simultaneously determines the position. A particle originating from a certain depth within the sample is, due to its lower magnetic rigidity, more deflected than one being scattered from the surface. The momentum p_R therefore is determined by means of a position measurement in the focal plane. From the momentum and the total energy the mass of the particle is derived. As in terms of a microscope, a depth range of $\approx 40\,\mathrm{nm}$ is ion optically imaged into the $1\,\mathrm{m}$ long focal plane. Thus, the resulting magnification factor of $\approx 3{\cdot}10^7$ allows to resolve single adjacent atomic layers [11]. With the large solid angle of detection (6 msr) and by multiple redundant particle identification processes within the focal plain detector a sensitivity of less than
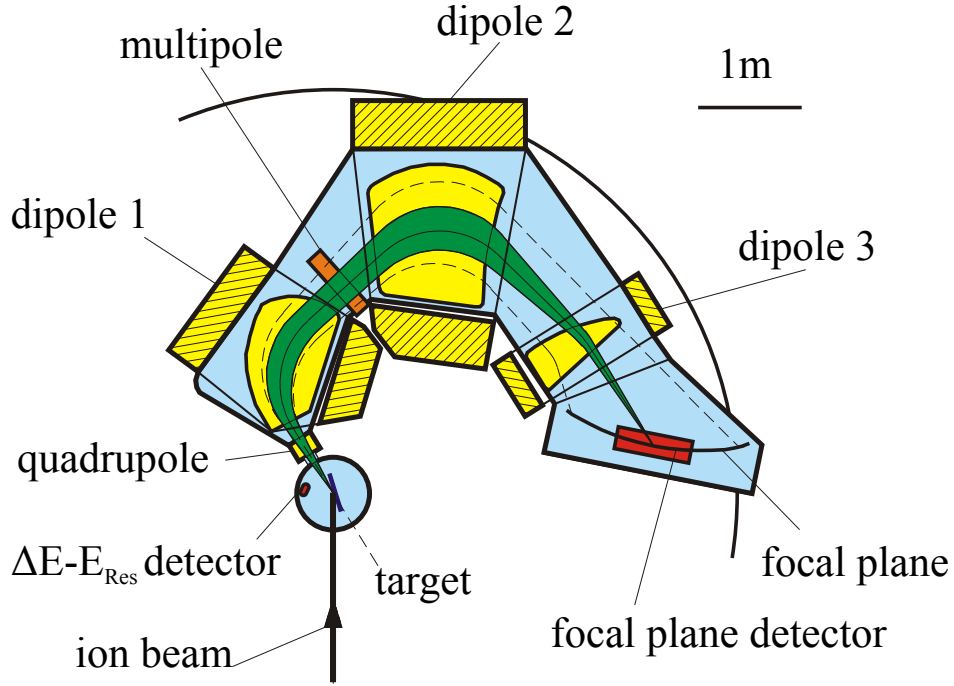
Figure 2.3: *Schematic illustration of the Q3D magnetic spectrograph with its focal plane detector utilized for high resolution ERD at the Munich Tandem Accelerator (illustration taken from [28]).*

1 ppm is achieved with the Q3D in ERD experiments [13].

One drawback, however, accompanied by the high precision of the Q3D magnetic spectrograph, is that only an energy range $\Delta E_R/E_R$ of $\approx 10\,\%$ is accepted for one particular magnetic field setting. Thus, only one isotope of a selected charge state originating from a limited depth range can be analyzed within one single measurement.

In order to monitor multiple elements of the sample as well as to quantify the high resolution depth profiles, a ΔE-E detector is installed directly within the Q3D scattering chamber (see Fig. 2.3), which runs simultaneously to the high resolution Q3D measurements. The working principle of this monitoring detector and its limitations are discussed in the following section.

2.2.2   The ΔE-E method

The principle of elemental identification with ΔE-E method is based on the specific energy loss values for ions in matter. As long as the velocities of the recoiling ions with the nuclear charge Z_R, are within $v_B \cdot Z_R^{2/3}$ (v_B: Bohr velocity, $v_B = e^2/\hbar \approx 2.188 \cdot 10^6$ m/s) or greater, the specific energy loss values differ and a measurement of both the energy loss value and the total energy allows to identify the element. At the Munich Tandem Accelerator the measurement of both quantities is carried out by a combined gas/solid-state hybrid detector, designed and installed by Bergmaier et al. within the Q3D scattering chamber (see Fig. 2.3) [12]. As illustrated in Fig. 2.4, the ΔE-E detector consists of a gas filled parallel plate capacitor for energy loss (ΔE) measurement and a silicon PIN diode for determination of the residual energy E_{Res}. If the ΔE signal
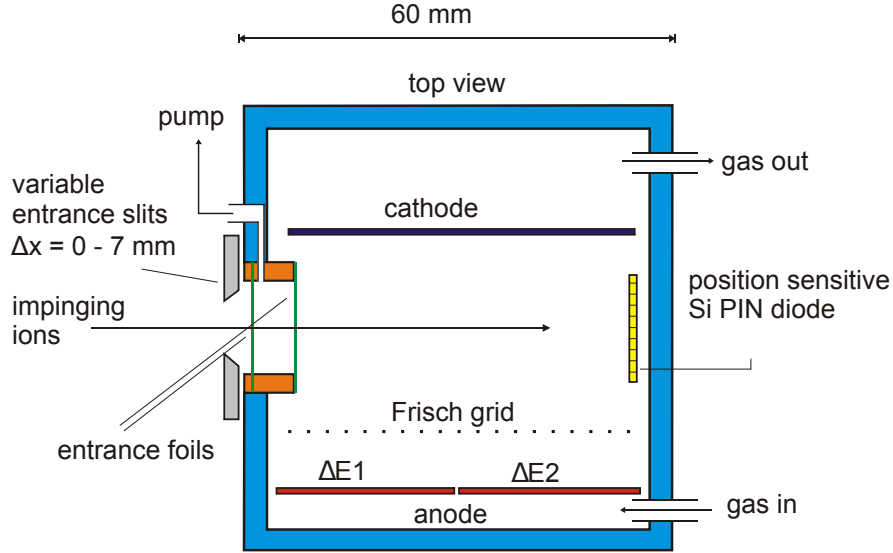

Figure 2.4: *Schematic illustration of the ΔE-E detector installed within the Q3D scattering chamber (illustration from [28]).*

is plotted versus the residual energy E_{Res} or the total energy ($E_{Tot} = \Delta E + E_{Res}$), the different elements of the sample are separated from each other due to their different energy loss signals at a given total energy. Fig. 2.5 exemplarily illustrates a ΔE-E_{Tot} histogram of a sample consisting of two particular layers: The top layer is made of $10.6\,\mu g/cm^2$ MgF_2 deposited on the second layer, composed of $23\,\mu g/cm^2$ Al. Both layers are deposited on a borosilicate glass substrate. All light and medium-heavy elements, including hydrogen, are well-separated and identified. Since the elements do not only originate from the surface (maximum E_{Tot}), but also from deeper within the sample (less total energy), each element shows a characteristic "elemental band".

Furthermore, each particular elemental band shows a maximum ΔE value (Bragg-maximum) at the velocity $v_R = v_B \cdot Z_R^{2/3}$. For ion velocities beyond this maximum (higher E_{Tot} values), the elemental bands are separated efficiently since here ΔE scales according to

$$\Delta E \propto \frac{MZ^2}{E} \cdot \ln E \; . \tag{2.15}$$

The ΔE-E detector installed at the Q3D scattering chamber allows to perform ERD
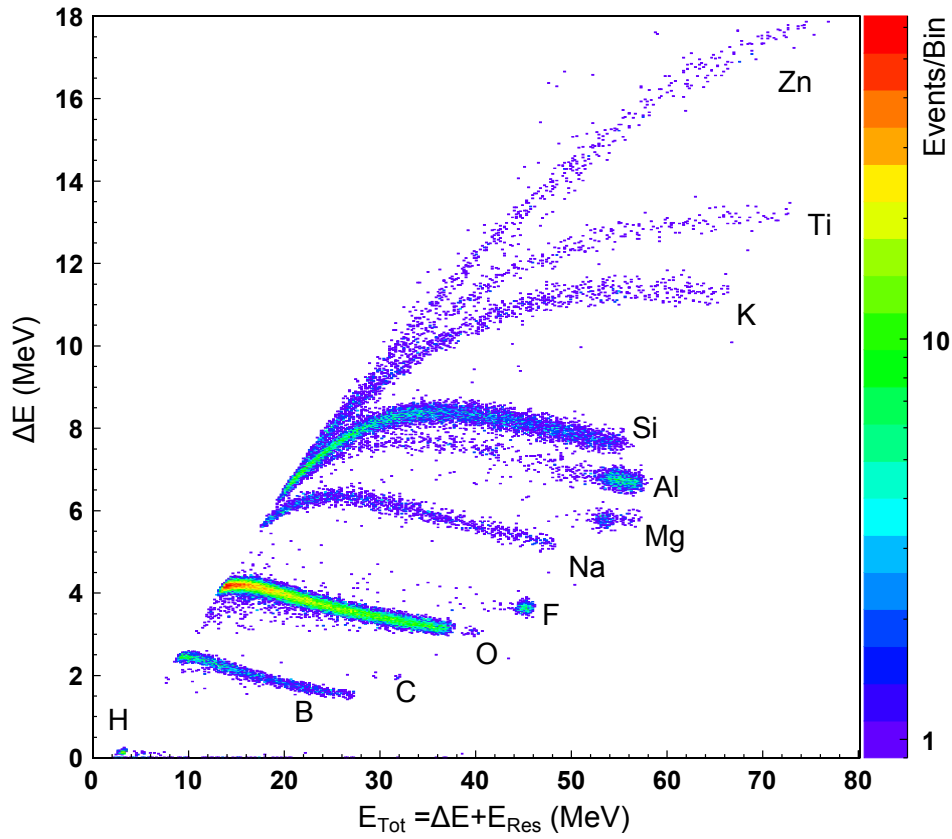
Figure 2.5: *ΔE-E histogram of a sample consisting of a 10.6 $\mu g/cm^2$ thick MgF_2 layer on top of a 23 $\mu g/cm^2$ thick Al layer. The substrate is borosilicate glass. A 170 MeV ^{127}I projectile beam at a detection angle of $\varphi = 40°$ is utilized for the ERD analysis (histogram acquired with the energy detector of the TOF-E setup developed in this work).*

measurements for elements ranging from $Z_R = 1$ up to $Z_R = 40$, with a sensitivity in the ppm range and a depth resolution of ≈ 10 nm, thus representing an excellent tool for quantification of the high resolution depth profiles or as stand alone device [12].

• Limitations of the ΔE-E technique

The histogram illustrated in Fig. 2.5 also shows the limits of the ΔE-E technique. With increasing sample depth, the total energy E_{Tot} of the recoil ions decreases due to the energy loss within the sample matrix of both, the projectile and recoil ion. For recoil ions with velocities $v_R \ll v_B \cdot Z_R^{2/3}$ (total energies appearing before the energy loss maximum), the energy loss value ΔE does not scale according to Eq. 2.15 anymore. It becomes proportional to the ion velocity and therefore almost equal for all elements. The "elemental bands" start to overlap and separation becomes impossible with this technique.

For the analysis of irradiation damage sensitive samples a 40 MeV ^{197}Au projectile beam is used at the Munich Tandem Accelerator. Utilizing this beam, the momentum transferred in the binary collision in general leads to recoil energies at which the ΔE-E technique does not allow for elemental separation. However, in order to sustain the required quantification capabilities for the high resolution depth profiles obtained with the Q3D magnetic spectrograph, an alternative detection system to the ΔE-E detector is inevitable.

The time of flight – energy (TOF-E) method, introduced in the following section, offers the potential to replace the ΔE-E detector as quantification tool or as stand alone system for the use of heavy, low energetic projectile beams, such as the 40 MeV ^{197}Au projectile beam.

2.2.3   The TOF-E method

The time of flight – energy (TOF-E) method makes use of the fact that recoil ions of different mass M_R, but equal energy E_R, differ in their velocity v_R and thereby in time T_R to traverse a particular distance L in vacuum. If, besides the time of flight determination, an additional energy measurement is carried out, elemental separation becomes possible as illustrated by a TOF versus energy ERD histogram in Fig. 2.6. The histogram illustrates the TOF-E data obtained for the exact same sample, as previously analyzed utilizing the ΔE-E method at high recoil ion energies (see Fig. 2.5). Analogue to the ΔE-E histogram, each element shows a characteristic "elemental band" and the mass of the recoil can be derived from definition of the kinetic energy at non relativistic velocities by

$$M_R = \frac{2E_R}{v_R^2} = 2E_R \cdot \left(\frac{T_R}{L}\right)^2 \ . \tag{2.16}$$

In contrast to the ΔE-E technique, which is primarily sensitive to the particle's nuclear charge (Eq. 2.15), the TOF-E method is only sensitive to the mass of the particle. The
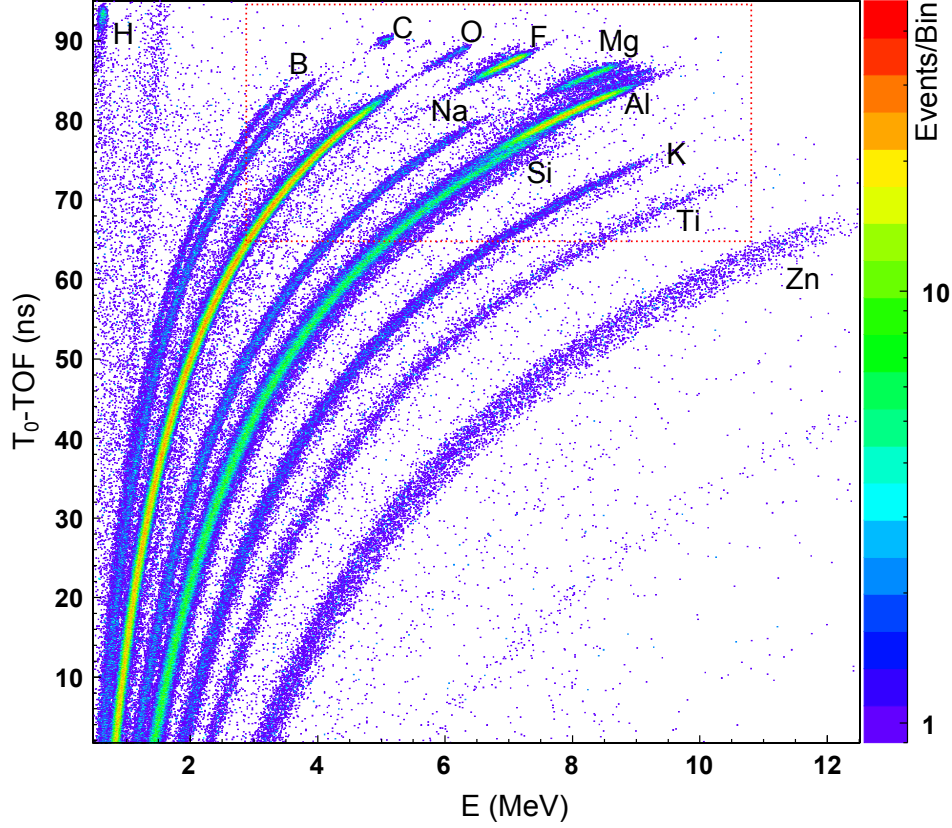
Figure 2.6: *TOF-E histogram of a sample consisting of a $10.6\,\mu g/cm^2$ thick MgF_2 layer on top of a $23\,\mu g/cm^2$ thick Al layer. The substrate is borosilicate glass. A $40\,MeV$ ^{197}Au projectile beam at a detection angle of $\varphi = 40°$ is utilized for the ERD analysis. The highlighted area (red dotted line) is illustrated in Fig. 2.7 (histogram acquired with the TOF-E setup developed in this work).*

mass sensitivity is demonstrated in Fig. 2.7, which illustrates a magnified area of the TOF-E histogram obtained for the MgF-Al-sample shown in Fig. 2.6. In contrast to the ΔE-E histogram illustrated in Fig. 2.5, the stable isotopes of various elements are resolved (e.g. ^{10}B, ^{11}B or ^{24}Mg, ^{25}Mg and ^{26}Mg). The mass resolution $\Delta M_R/M_R$ depends on both the energy resolution $\Delta E_R/E_R$ and the time resolution $\Delta T_R/T_R$ according to

$$\frac{\Delta M_R}{M_R} = \sqrt{\left(\frac{\Delta E_R}{E_R}\right)^2 + \left(2 \cdot \frac{\Delta T_R}{T_R}\right)^2}. \tag{2.17}$$

The main advantage of the TOF-E method becomes evident at low energy recoil ions: Energy dispersive detectors, such as silicon detectors and ionization chambers, rely on the amount of charge created within their active volume. For low energy particles, the charge statistics decrease and the signal to noise ratio worsens. In addition to that, for
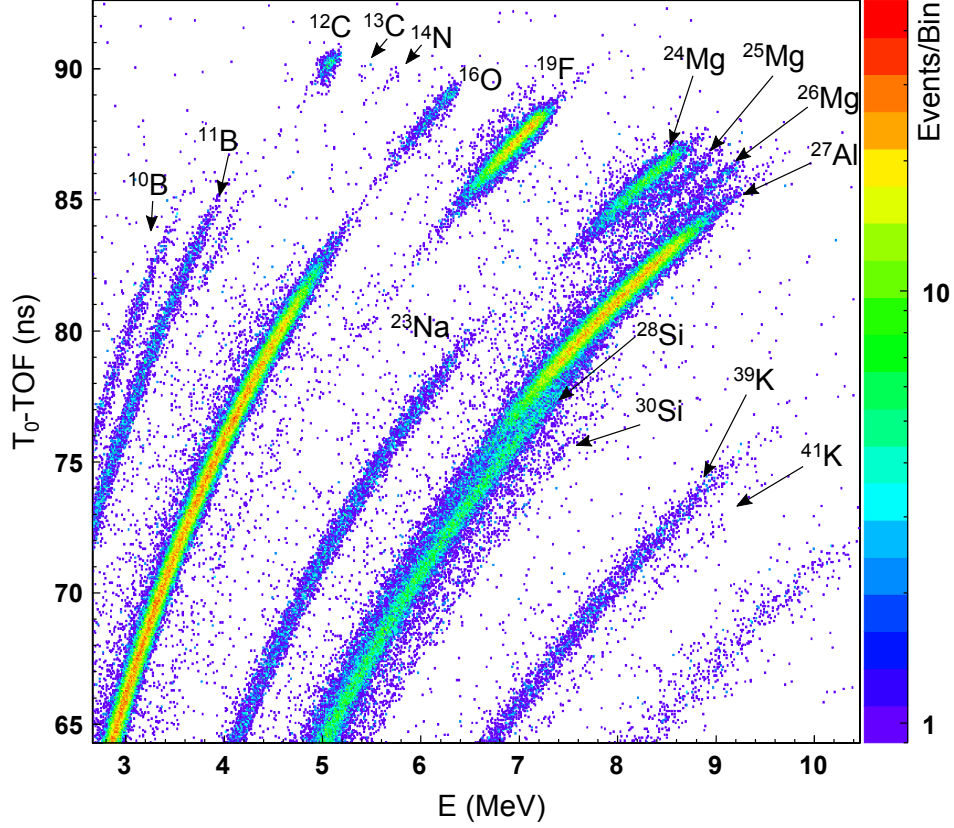
Figure 2.7: *Highlighted area of the TOF-E histogram illustrated in Fig. 2.6: In contrast to the ΔE-E method, the mass sensitivity of the method allows to resolve the stable isotopes of a variety of elements.*

heavy, low energy recoil ions, the energy loss straggling within the surface passivation layer of a silicon detector or within the entrance window of an ionization chamber is also increased. With the TOF-E method, however, the time of flight measurement shows an improved relative resolution $\Delta T_R/T_R$ at a given time resolution ΔT_R for lower recoil ion velocities v_R and thereby longer time of flights T_R. Once the recoil ion mass has been identified, the time of flight information can be used to calculate the ion energy. The timing resolution then transforms into an energy resolution by

$$\frac{\Delta E_R}{E_R} = 2 \cdot \frac{\Delta T_R}{T_R} \ . \tag{2.18}$$

A widely used TOF-E detection setup design consists of two separate timing detectors, a start detector (T_1) and a stop detector (T_2), both placed apart by the distance L, followed by a third detector for determination of the recoil ion energy (E), as illustrated in Fig. 2.8: The time detectors use thin carbon foils $(0.5 - 10\,\mu g/cm^2)$, which release secondary electrons on transmission by the recoil ion. The secondary electrons are accelerated by grids close to the foil onto a micro channel plate (MCP)

detector for amplification and detection (see section 4.2.2). Such setups are also used
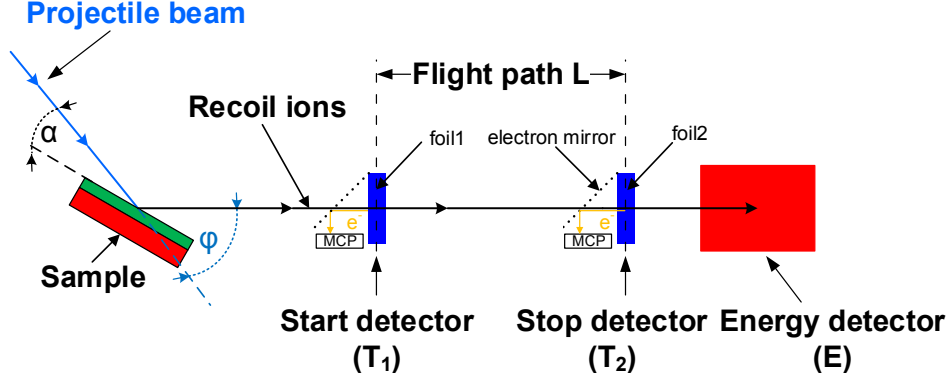
Figure 2.8: *Schematic illustration of a typical time of flight – energy (TOF-E) setup (see text for explanation).*

for high energy heavy ion ERD (e.g. with 250 MeV ^{129}Xe or 120 MeV ^{86}Kr projectile beams) with a silicon based energy detector that offers an excellent energy resolution and thereby good mass discrimination at high recoil ion energies ($v_R \gg v_B \cdot Z_R^{2/3}$) [45]. However, the common field of application of the TOF-E method is for the use with heavy ion projectile beams created by small accelerators (< 2 MV terminal voltage) with projectile energies in the range of ≤ 0.5 MeV·A (A: mass number) [46–48]. Here, the silicon detector resolution degrades and in order to still be able to obtain a good mass discrimination an alternative way to carry out an efficient energy measurement has to be utilized. One way is to use a compact ionization chamber as the energy detector, which uses a $50 - 200$ nm thick silicon nitride entrance window in order to minimize energy loss straggling of the recoil ions during entrance [49]. Compared to standard silicon type detectors, an improvement by more than a factor of 2.5 in energy resolution has been achieved [50]. An additional advantage accompanied by the use of a gas ionization chambers serving as energy detectors is that they do not suffer from irradiation damage, thus, maintaining their performance independently of measurement time, projectile energy and recoil ion species.

Chapter 3

Correction of kinematic effects in the framework of a TOF-E setup

The achievable sensitivity for the detection of trace elements in ERD measurements is limited by two main contributions [10]: One is given by the performance of the detection system, the other being a fundamental limitation, is represented by irradiation damage induced into the sample during analysis.

In order to minimize sample alteration throughout the measurement, large solid angles of detection are desired, which allow collecting the necessary statistics at low beam doses. The consequence, however, is a deterioration of the energy resolution by the kinematic effect due to the angular acceptance $\Delta\varphi$ within the scattering plane, as discussed in section 3.1.1 of this chapter.

An additional kinematic effect correlates to a large effective beam spot size on the sample surface at low incident angles, which are typically used in ERD measurements with the Q3D magnetic spectrograph aiming for optimal depth resolution. The TOF-E setup working simultaneously as quantification tool for the high resolution depth profiles therefore is also affected by this kinematic contribution, which adds to the one caused by the solid angle of detection, as described in section 3.1.2.

Correction possibilities of both kinematic effects by means of multiple recoil ion position determinations in the framework of a TOF-E are discussed in section 3.2 of this chapter.

3.1   Kinematic effects in ERD

3.1.1   Kinematic effect due to the solid angle of detection

According to Eq. 2.1, the energy transferred from the projectile to the sample atom in the binary collision is proportional to $\cos^2 \varphi$ with φ representing the scattering angle as given by the geometry of the experimental setup (see Fig. 1.1). Depending on the solid angle of detection Ω and thereby on the actual detector opening, a specific angular range $\Delta\varphi$ around the scattering angle φ within the scattering plane is accepted, as exemplary illustrated for a TOF-E detection system in Fig. 3.1. The expression of Eq. 2.1 developed by a Taylor series around φ shows the resulting angular dependence of the energy transfer and thereby the kinematic effect due to $\Delta\varphi$:

$$\left(\frac{\Delta E_R}{E_R}\right)_{kin} = -2 \cdot \tan\varphi \cdot \Delta\varphi + (\tan^2 \varphi - 1) \cdot \Delta\varphi^2 + \frac{4}{3} \cdot \tan\varphi \cdot \Delta\varphi^3 + \dots . \qquad (3.1)$$

In addition to the angular acceptance $\Delta\varphi$ within the scattering plane, an angular range perpendicular to it, $\Delta\varphi_{perp}$ is accepted as well. This causes a second order kinematic effect by the detector opening perpendicular to the scattering plane [51], which can be described by

$$\left(\frac{\Delta E_R}{E_R}\right)_{kin,perp} \approx \frac{dz^2}{I_0^2} \approx \left(\frac{\Delta\varphi_{perp}}{2}\right)^2 , \qquad (3.2)$$

with $(2 \cdot dz)$ representing the height of the detector entrance window and I_0 the distance to the target. This second order kinematic effect is mainly relevant for high resolution ERD measurements performed with the Q3D magnetic spectrograph due to its unique energy resolution, however, it is mentioned for the sake of completeness.

For thin samples such as foil targets, which allow to be analyzed in transmission geometry, the first order kinematic effect in principle vanishes if the recoil ions are detected at $\varphi = 0°$ (e.g. by a magnetic spectrograph). However, for massive samples φ has to be $> 0°$, thus, the kinematic effect becomes inherent and a correction by a measurement of the scattering angle for each detected recoil ion is inevitable: In order to achieve a depth resolution in the range of 10 nm in ERD measurements, a relative energy resolution $\Delta E_R / E_R$ of $\approx 1\%$ is required[1]. For a detection system installed at e.g. a scattering angle of $\varphi = 40°$ this means that an angular measurement with an accuracy of at least 6 mrad or 0.3° is necessary.

At typical projectile beam widths in the range of 1 mm and incident angles $\alpha > 10°$, the kinematic contribution to the energy resolution is dominated by the effect due to

---

[1] e.g.: Detection of oxygen in SiO_2 utilizing a 170 MeV ^{127}I projectile beam with α=10° and φ=40°
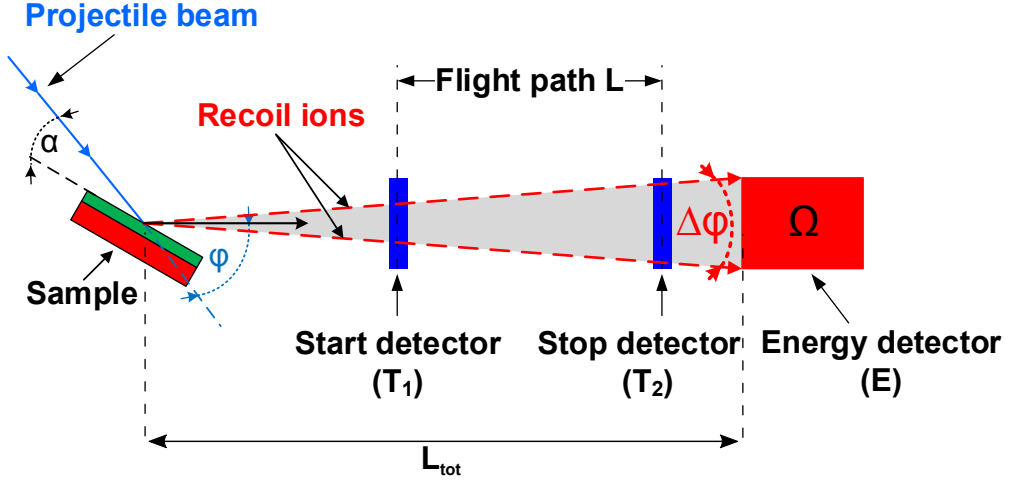
Figure 3.1: *First order kinematic effect due to the angular acceptance $\Delta\varphi$ within the scattering plane, illustrated exemplarily for a TOF-E detection system.*

the solid angle of detection Ω. Therefore, a position measurement carried out by the energy detector in case of a TOF-E setup allows to determine the scattering angle φ and thereby to apply first order kinematic corrections. However, the situation changes if high resolution depth profiles with the Q3D magnetic spectrograph are acquired simultaneously as described in the following.

3.1.2   Kinematic effect due to beam spot size

The scattering geometry is modified when high resolution depth profiles with the Q3D magnetic spectrograph are measured simultaneously. An incident angle of $\alpha = 4°$ is then used in order to achieve maximum depth resolution close to the sample surface [27]. An increase of the effective beam spot size $b_{eff}(\alpha, \varphi)$ according to

$$b_{eff} = b_0 \cdot \frac{\sin(\varphi - \alpha)}{\sin \alpha} \tag{3.3}$$

is observed, which is caused by the projection of the initial beam width b_0 towards the detector placed at the scattering angle φ, as schematically illustrated in Fig. 3.2. Now, the uncertainty in scattering angle incorporates, besides the contribution due to the angular acceptance of the detector a contribution due to the effective beam spot width.

Contrary to the kinematic effect caused by the angular acceptance of the detector
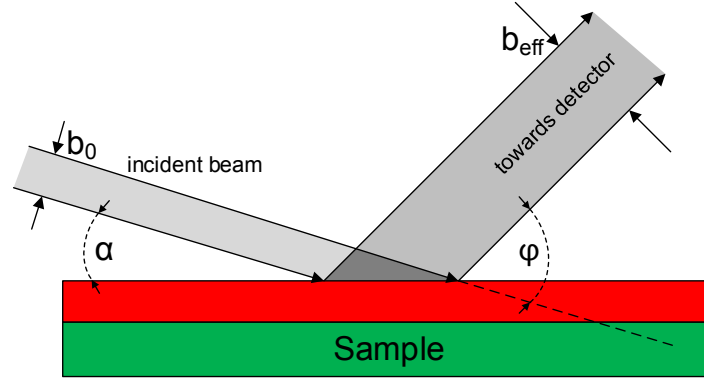

Figure 3.2: *Incident angles α of $< 4°$ lead to a large effective beam spot width $b_{eff}(\alpha, \varphi)$, which is projected towards the detector.*

at small beam spot sizes, this effect can not be corrected by a single position determination, as demonstrated exemplarily for two recoil ions (green trajectories) in Fig. 3.3 in case of a TOF-E detection setup[2]: Although the same position is determined by the energy detector, the scattering angle of both recoil ions differs by $\Delta\Theta$. Thus, only a true angular measurement of the recoil ion trajectory by two independent position determinations allows to correct for this kinematic effect caused by the beam spot size.

---

[2] This applies for all ERD detection setups. The TOF-E setup is chosen for illustration purposes only.
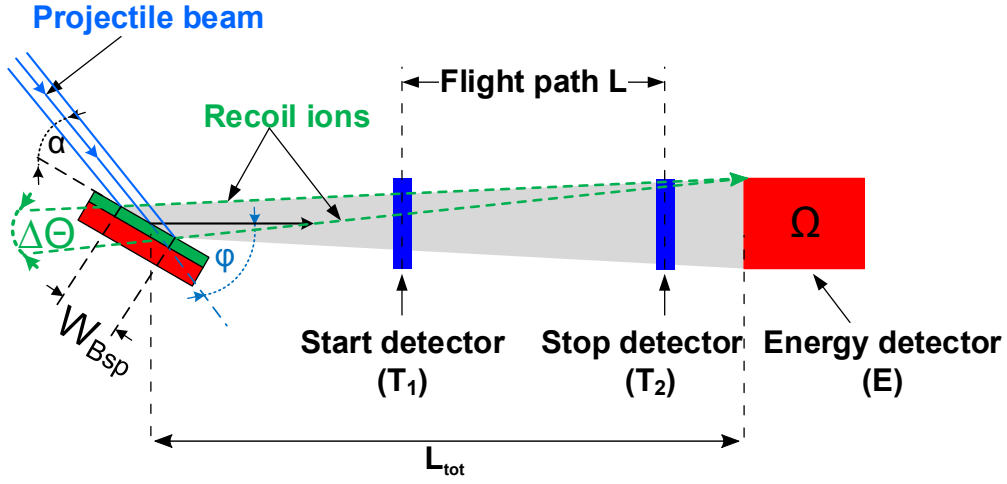
Figure 3.3: *First order kinematic effect due to the angular uncertainty $\Delta\Theta$ caused by the beam spot size W_{Bsp} on the sample surface in case of a TOF-E detection setup. Here, a singular position determination carried out by the energy detector does not account for the potential angular difference $\Delta\Theta$ (green recoil ion trajectories). Only a true angular measurement by means of two independent position determinations (e.g. T_1 and energy detector) allows to fully correct for both kinematic contributions (beam spot and angular acceptance).*

3.2   Angular sensitivity versus singular position determination for kinematic corrections

The ERD measurement conditions with respect to incident angle and therefore beam spot size on the sample surface define the optimal method of kinematic correction to be utilized: At effective beam spot sizes of $\leq 1\,\text{mm}$ a single position determination of the recoil ion within the scattering plane typically allows to obtain the scattering angle φ with sufficient accuracy. However, at incident angles $\alpha < 8°$ the kinematic contribution by the beam spot size increases significantly. In this case, for obtaining an optimal depth resolution, a true angular measurement of every single recoil ion trajectory becomes mandatory.

In the framework of a TOF-E setup, as illustrated in Fig. 3.4, consisting of two timing detectors ($T_1 \,\&\, T_2$) and a position sensitive energy detector E (see Fig. 2.8), this means that either one or both timing detectors have to carry out an additional position measurement. As mentioned in section 2.2.3, the time of flight detectors use thin
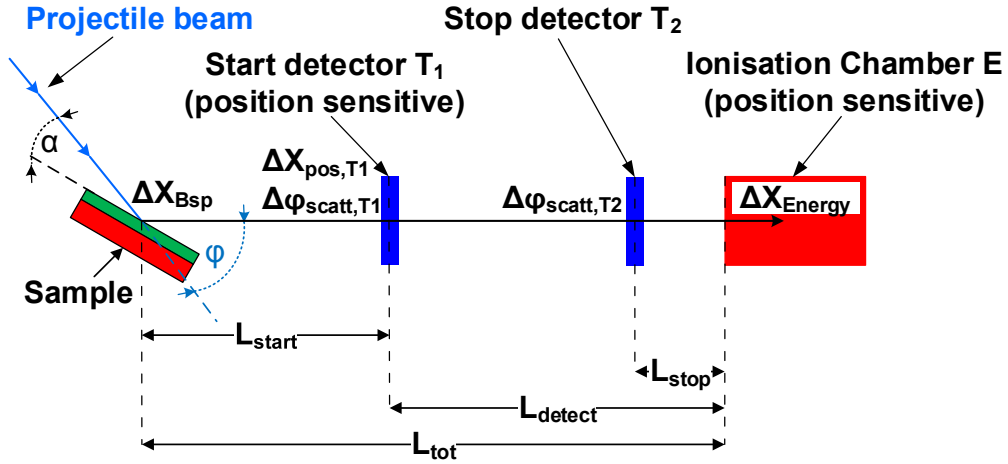
Figure 3.4: *In the framework of a multi-position sensitive TOF-E setup, the scattering angle $\Delta\varphi$ can be determined by a position sensitive start detector (T_1) and a position sensitive energy detector E. The accuracy is affected by the position resolutions ΔX of the corresponding detectors, the beam spot influence ΔX_{Bsp} (in case of a singular position measurement being carried out) and angular straggling effects within the carbon foils of the timing detectors $\Delta\varphi_{scatt}$. Depending on the method of kinematic correction, the contributions have to be put into ratio to the distances L involved.*

carbon foils which emit secondary electrons on recoil ion penetration used for detection. Thus, the accuracy of position- and angular determination is not only limited by the corresponding position resolution of each detector, but also by angular straggling

induced in the carbon foils. This leads to an additional angular uncertainty $\Delta\varphi_{scatt}$.

Thus, in case of a TOF-E setup featuring a position sensitive start detector (T_1) and a position sensitive energy detector E, **three** possible options to perform kinematic corrections can be used with respect to the residual angular uncertainty $\Delta\varphi$ in dependence of the beam spot size on the sample (ΔX_{Bsp}), the position resolutions of the detectors (ΔX) and the angular straggling effects ($\Delta\varphi_{scatt}$) within the timing detectors:

(1) Singular position measurement carried out by the energy detector E.

(2) Singular position measurement carried out by the first timing detector T_1.

(3) True angular measurement carried out by the first timing detector T_1 and the energy detector E.

(1): Singular position measurement carried out by the energy detector E

In case of a singular position measurement performed by the energy detector of the TOF-E setup, the contributions to the residual angular uncertainty $\Delta\varphi$ are given by the beam spot size on the sample ΔX_{Bsp}, by the angular straggling induced by the carbon foils of both timing detectors $\Delta\varphi_{scatt,T_{(1,2)}}$, and by the position resolution ΔX_{Energy} of the energy detector itself. The three contributions do not depend on each other. Thus, the residual uncertainty $\Delta\varphi_{(1)}$ is given by

$$\Delta\varphi_{(1)} = \left(\left(\frac{\Delta X_{Bsp}}{L_{tot}}\right)^2 + \left(\frac{L_{detect}}{L_{tot}}\right)^2 \cdot (\Delta\varphi_{scatt,T_1})^2 + \right.$$
$$\left. \left(\frac{L_{stop}}{L_{tot}}\right)^2 \cdot (\Delta\varphi_{scatt,T_2})^2 + \left(\frac{\Delta X_{Energy}}{L_{tot}}\right)^2 \right)^{\frac{1}{2}} . \tag{3.4}$$

(2): Singular position measurement carried out by the first timing detector T_1

If the position resolution of the first timing detector T_1 is sufficient enough, it can be used to determine the scattering angle with the advantage to eliminate the contributions given by angular straggling effects within the carbon foils of both timing detectors. In this case, the angular uncertainty $\Delta\varphi_{(2)}$ is reduced to the contributions given by the beam spot size ΔX_{Bsp} and the achievable position resolution of the start detector $\Delta X_{pos,T_1}$:

$$\Delta\varphi_{(2)} = \left(\left(\frac{\Delta X_{Bsp}}{L_{start}}\right)^2 + \left(\frac{\Delta X_{pos,T_1}}{L_{start}}\right)^2 \right)^{\frac{1}{2}} . \tag{3.5}$$

(3): True angular measurement carried out by the first timing detector T_1 and the energy detector E

A true angular measurement of the recoil ion trajectory eliminates the contribution by the beam spot size ΔX_{Bsp} to the residual angular uncertainty $\Delta\varphi_{(3)}$. The remaining contributions are angular straggling within the first and second carbon foil $\Delta\varphi_{scatt,T_{(1,2)}}$, as well as the position resolution of the energy detector ΔX_{Energy} and the first timing detector $\Delta X_{pos,T_1}$, respectively:

$$\Delta\varphi_{(3)} = \left(\left(\frac{\Delta X_{pos,T_1}}{L_{detect}} \right)^2 + (\Delta\varphi_{scatt,T_1})^2 + \left(\frac{L_{stop}}{L_{detect}} \right)^2 \cdot (\Delta\varphi_{scatt,T_2})^2 + \left(\frac{\Delta X_{Energy}}{L_{detect}} \right)^2 \right)^{\frac{1}{2}} . \tag{3.6}$$

Expression 3.6 can be rewritten to

$$\Delta\varphi_{(3)} = \frac{1}{L_{detect}} \cdot \left((\Delta X_{pos,T_1})^2 + (L_{detect})^2 \cdot (\Delta\varphi_{scatt,T_1})^2 + (L_{stop})^2 \cdot (\Delta\varphi_{scatt,T_2})^2 + (\Delta X_{Energy})^2 \right)^{\frac{1}{2}} , \tag{3.7}$$

showing that $\Delta\varphi_{(3)}$ scales by $1/L_{detect}$ with L_{detect} representing the distance from the first timing detector T_1 to the energy detector E.

   All three possibilities to perform kinematic corrections in the framework of the TOF-E setup developed in this work are discussed in detail in section 4.1 of the following chapter 4.

Chapter 4

Development of a position sensitive TOF-E setup

The present chapter of this work is dedicated to the development of the position sensitive TOF-E spectrometer. In Section 4.1 of this chapter, first, the general TOF-E system requirements are presented. Section 4.2 then describes the development of the position sensitive start timing detector T_1, featuring an electrostatic lens for secondary electron focusing, necessary to achieve the required position resolution. The stop timing detector T_2, originally built by A. Kern [52] according to the design of Busch et al. [53], is revised in this work and presented in section 4.3. The development of a position sensitive ionization chamber serving as energy detector of the setup is described in section 4.4. Finally, the used readout electronics are presented in the last section 4.5 of this chapter.

4.1 System requirements

The distinct system requirements on the TOF-E setup are introduced separately in this section: First, the requirements on the position sensitivity with respect to the necessary position resolution of each detector involved in the angular measurement are discussed. The first part also includes an additional discussion of the optimal correction method in dependence on the projectile incident angle. Then, general requirements with respect to mass separation capability and time-/energy resolution are given for the use of the setup with the 40 MeV ^{197}Au projectile beam. The requirements to carry out a combined TOF-ΔE-E measurement with the setup in order to achieve unique mass separation capabilities and filter conditions for measurements at high projectile energies (170 MeV ^{127}I projectile beam) are presented at the end of this section.

• Position-/angular resolution

As a designated tool for the quantification of the high resolution ERD depth profiles obtained with the Q3D magnetic spectrograph, the TOF-E setup is installed at the Q3D scattering chamber at the smallest possible scattering angle of $\varphi = 40°$ (see Fig. 4.1). Space constraints given by the close presence of the spectrograph, however, do not only determine the scattering angle, but also partly restrict the distances between the detectors and thereby affect the achievable solid angle of detection. The minimal distance from the target to T_1 is given to be 77.6 cm due to the close presence of the quadrupole magnet, located directly at the entrance of the spectrograph, as illustrated in Fig. 4.1. The flight path length has to be added to this distance.

An envisaged depth resolution of $< 10\,\mathrm{nm}$ requires an energy resolution of $< 1\,\%$, which in case of the energy information being retrieved from the time spectra leads to a required relative time resolution of $\approx 0.5\,\%$ (see Eq. 2.18). Since recoil ions with
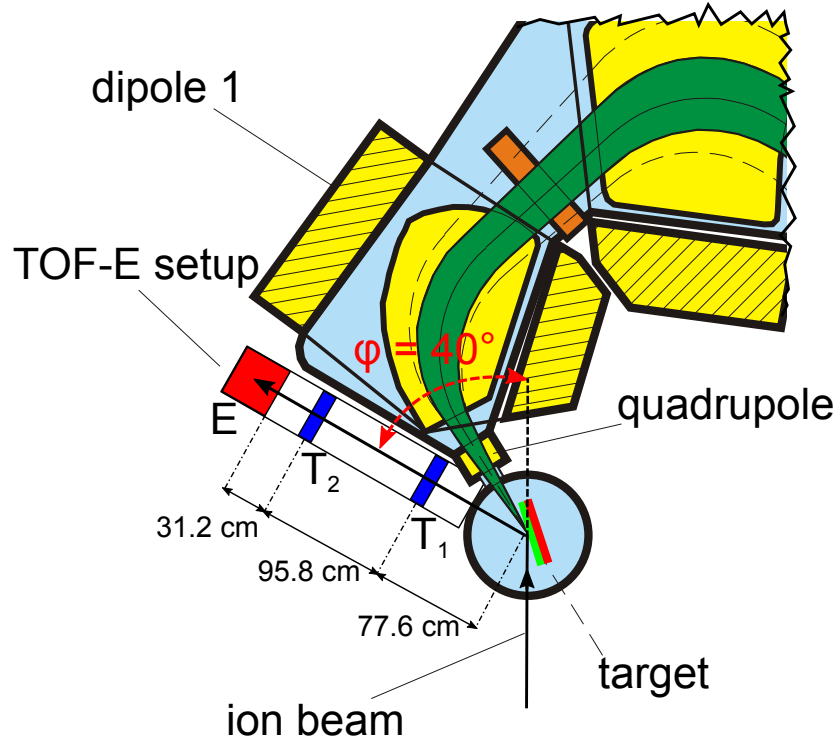
Figure 4.1: *Schematic illustration of the TOF-E setup installed at the scattering chamber of the Q3D magnetic spectrograph at a scattering angle $\varphi = 40°$.*

energies of $1\,\mathrm{MeV/nucleon}$ travel at velocities of $\approx 1\,\mathrm{cm/ns}$ and typical time resolutions achieved by secondary electron detectors are within a range of $250 - 500\,\mathrm{ps}$ [48, 49], a

flight path length of $\approx 1\,\mathrm{m}$ (95.8 cm) is chosen.

With a vacuum valve between the TOF line and the energy dispersive detector, the distance from T_2 to the energy detector entrance window is set to 31.2 cm, resulting in a total distance to the target of 204.6 cm. This represents approximately twice the distance than compared to typical stand alone TOF-E setups [48, 49, 54]. As a result, the large total distance limits the solid angle of detection and therefore the achievable sensitivity in ERD measurements with the TOF-E setup. Thus, in order to reach a solid angle Ω of $\approx 0.3\,\mathrm{msr}$, an entrance window[3] of the energy detector of the dimensions $40 \times 40\,\mathrm{mm}^2$ is used.

The resulting detector opening within the scattering plane, however, leads to an angular acceptance of $\Delta\varphi = 20\,\mathrm{mrad}$ limiting the achievable energy resolution by the kinematic effect to $(\Delta E_R/E_R)_{kin} = 3.3\,\%$.

As described in section 3.1.2, for high resolution ERD measurements carried out with the Q3D magnetic spectrograph an incident angle of $\alpha = 4°$ is used routinely. This causes an effective beam spot width b_{eff} of $\geq 6.7\,\mathrm{mm}$ ($b_0 = 0.8\,\mathrm{mm}$, see Eq. 3.3) on the sample surface leading to an additional kinematic contribution of $\geq 0.6\,\%$, which adds to the one by the detector opening. Only a true measurement of the particular scattering angle of each recoil ion by means of two position measurements, one by the energy detector and one by the start timing detector (T_1), offers the ability to correct for both effects. Thus, in order to achieve an energy resolution of $\Delta E/E < 1\,\%$, an accuracy of the angular measurement carried out by both detectors of $\leq 3\,\mathrm{mrad}$ is required. This can be achieved by a position resolution of 0.8 mm (FWHM) at T_1 and 2.5 mm at the energy detector.

Figure 4.2 puts the three discussed options of kinematic correction (see section 3.2) in contrast to each other with respect to the residual angular uncertainty $\Delta\varphi$ and thereby to the residual kinematic contribution in dependence on the beam spot size/incident angle. An average angular straggling of the recoil ion within each carbon foil ($4\,\mu\mathrm{g/cm}^2$) is assumed and calculated to be $\Delta\varphi_{scatt,T_{(1,2)}} \approx 1.6\,\mathrm{mrad}$ (FWHM) with the program code ENELOSS (considered recoil ion mass range $9 \leq M \leq 73$)[55].

With the given values of position resolutions and straggling effects, the advantage of a true angular measurement becomes obvious for effective beam spot sizes $b_{eff} > 4.2\,\mathrm{mm}$ (incident angles $< 5°$): In this case, the constant angular resolution of 2.5 mrad allows to reduce the residual kinematic contribution to $(\Delta E_R/E_R)_{kin} = 0.42\,\%$. However,

---

[3] As described in section 4.4, a silicon nitride membrane with a thickness of 100 nm is used as entrance window of the gas ionization chamber. At the time of the detector design, the largest multi- segmented SiN-windows being commercially available were $40 \times 40\,\mathrm{mm}^2$ in overall dimension consisting of $5 \times 5\,\mathrm{mm}$ free standing membranes.
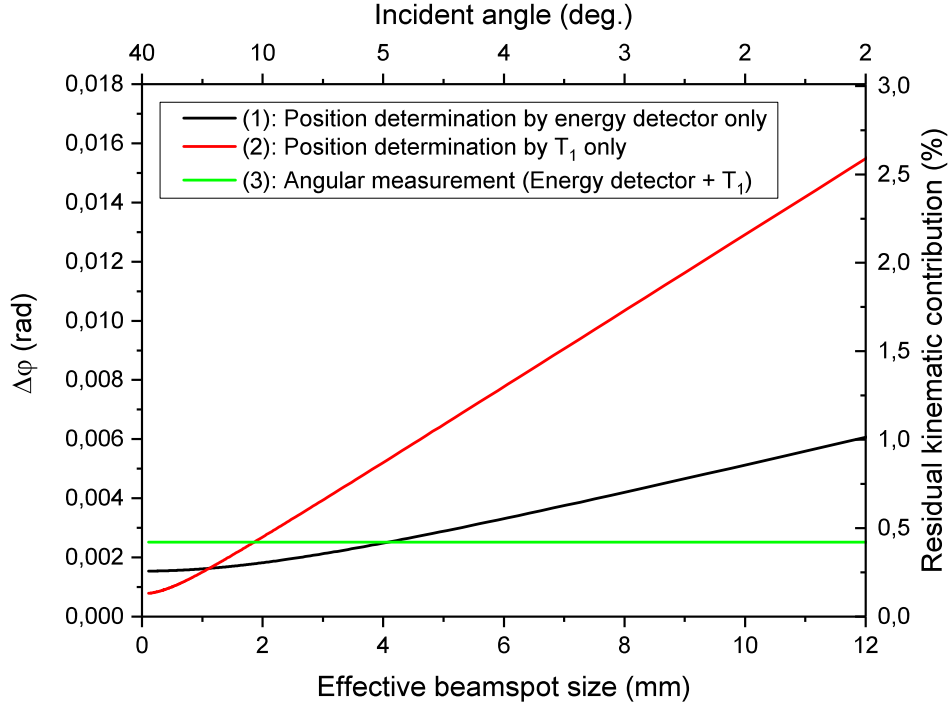
Figure 4.2: *Residual kinematic effect and angular uncertainty $\Delta\varphi$ in dependence on the beam spot size for the three applicable options of kinematic correction in the framework of a TOF-E setup consisting of a position sensitive start detector (T_1) and a position sensitive energy detector. A position resolution of 0.8 mm (FWHM) by T_1 and 2.5 mm (FWHM) by the energy detector allows to reduce the kinematic contribution to the energy resolution to $\leq 0.5\,\%$. Average angular straggling within the carbon foils is $\approx 1.6\,mrad$ (FWHM).*

for smaller effective beam spot sizes ranging from $1.3\,\mathrm{mm} \leq b_{eff} \leq 4.2\,\mathrm{mm}$, a single position determination carried out by the energy detector provides a better correction performance than by the angular measurement and allows to reduce the kinematic contribution down to $\approx 0.26\,\%$ at a beam spot size of 1.3 mm. Yet, with the position resolution of the first timing detector $\Delta X_{pos,T_1}$ being assumed to be approximately three times better than the one by the energy detector, only at effective beam spot sizes $b_{eff} < 1.3\,\mathrm{mm}$ a single position measurement carried out by the T_1 provides for the best correction option.

● **Time-/energy resolution**

The mass resolution of the TOF-E setup is given by Eq. 2.17 with $\Delta T/T$ being the overall time resolution and $\Delta E/E$ the resolution of the energy detector. For a mass identification up to $A = 100$, a time resolution of $0.5\,\%$ and an energy resolution of $1\,\%$ is necessary. This translates for $A = 100$ into a required energy resolution of the

energy detector of 210 keV and a time resolution of 780 ps (40 MeV ^{197}Au projectile beam, $\varphi = 40°$).

However, after mass discrimination, the actual depth profiles are obtained by separate analysis of the TOF data. In order to obtain a depth resolution of ≤ 3 nm in, e.g. a pure carbon matrix ($E_{R,^{12}C} = 5.08$ MeV), a time resolution of 533 ps is required according to the surface approximation given by Eq. 2.9 (40 MeV ^{197}Au projectile beam, $\alpha = 10°$, $\varphi = 40°$).

• Combined TOF-ΔE-E capability

With its terminal voltage up to $14\,\mathrm{MV}$, the Munich Tandem Accelerator allows to create high energetic, heavy ion projectile beams such as the $170\,\mathrm{MeV}$ ^{127}I beam, which is used routinely for ERD analysis with a ΔE-E type detection system [12]. The ΔE-E method uses the dependence of the recoil ion energy loss on the nuclear charge Z_R for elemental identification according to the relation $\Delta\mathrm{E} = \propto (M Z_R^2 \cdot \ln E_R)/E_R$ (see secction 2.2.2). Thus, it favors the nuclear charge of the recoil ion in contrast to the TOF-E method with its exclusive mass sensitivity. However, with the total energy being $\mathrm{E}_{ToT} = \Delta\mathrm{E} + \mathrm{E}_{Res}$ and with an additional time of flight determination, the TOF-E method is also applicable to ERD analysis utilizing the $170\,\mathrm{MeV}$ ^{127}I projectile beam. It has to be considered that in this energy range the actual advantage of the TOF-E method to extract the energy information from the TOF spectra for a better energy resolution is not given, since the relative time resolution decreases for the obtained high recoil ion velocities. The energy measurement being carried out usually provides superior resolution at the high recoil ion energies. Table 4.1 shows the obtained recoil ion surface energies and time of flights (distance between timing detectors $L = 95.8\,\mathrm{cm}$) for a variety of elements for the $40\,\mathrm{MeV}$ ^{197}Au projectile beam as well as for the $170\,\mathrm{MeV}$ ^{127}I for comparison. However, the advantage of a TOF-ΔE-E measurement is not only given by the better mass sensitivity for e.g. isotope separation but also lies in the fact that unique filter conditions can be applied for background suppression to either the ΔE-E histogram or the TOF-E histogram, since both are acquired simultaneously [56].

In order to apply this technique, the energy dispersive detector incorporated into the the TOF-E setup is required to feature an additional ΔE-E capability.

	40 MeV ^{197}Au projectile beam		170 MeV ^{127}I projectile beam	
Recoil ion	Energy (MeV)	TOF (ns)	Energy (MeV)	TOF (ns)
^{1}H	0.47	104.0	3.09	40.6
^{7}Li	3.11	107.1	19.76	42.5
^{12}C	5.08	109.7	31.48	44.1
^{16}O	6.52	111.8	39.65	45.4
^{28}Si	10.23	118.1	59.60	59.1
^{48}Ti	14.41	127.6	77.89	54.9
^{74}Ge	18.64	142.3	92.82	63.8

Table 4.1: *Recoil ion surface energies (scattering angle $\varphi = 40°$) and time of flight values of various recoil ion species obtained for the $40\,\mathrm{MeV}$ ^{197}Au projectile beam and for the $170\,\mathrm{MeV}$ ^{127}I projectile beam, which is utilized for the combined TOF-ΔE-E measurements.*

4.2   Position sensitive timing detector (T_1)

In this section, first, general aspects with respect to the detector design layout are presented, justifying the use of an electrostatic lens necessary to achieve the envisaged position resolution. In the following section, 4.2.2, the development of a micro channel plate (MCP) stack, used for secondary electron amplification, is described. The MCP stack provides the option to carry out a time- as well as a position readout. First, its performance with respect to the achievable time resolution is determined by an experimental setup as presented in section 4.2.3. For the position readout a 2-dimensional Backgammon anode is developed as described in section 4.2.4. In order to guarantee that the position resolution achieved utilizing the Backgammon anode readout is not the limiting factor with respect to the overall position resolution of the detector, its performance is also tested by an appropriate experimental setup. This setup is presented in section 4.2.4 as well. The following section, 4.2.5, describes the development of an electrostatic lens, which focuses the electrons onto the micro channel plate stack, thus maintaining the position information despite their momentum distribution. Ray tracing simulations leading to the final design of the lens as well as the mechanical realization of it are also presented in this section. The performance of the lens and thereby the overall achievable position resolution with the detector is finally determined in section 4.2.6.

4.2.1   Detector Design

The most commonly used timing detector is based on a design introduced in the year 1980 by Busch et al. [53], which is schematically illustrated in Fig. 4.3. The design incorporates a thin carbon foil that is orientated perpendicular to the recoil ion flight path emitting secondary electrons (SE) on penetration. The secondary electrons are accelerated by grids placed close to the carbon foil and are injected into a field free region, continuing their way towards a second arrangement of grids. These grids represent an electrostatic mirror positioned at 45° towards the carbon foil, which deflects the electrons by 90° onto a micro channel plate (MCP) electron amplifier (see section 4.2.2), necessary to create an appropriate pulse height for readout. The geometry of the detector setup is chosen in a way that the secondary electron tracks, in principle, equal in length independent of their start location on the carbon foil. As a result, the SE flight times within the detector are isochronous and intrinsic time resolutions in the range of $100 - 150 \, \text{ps}$ have been reported [46, 53].

The addition of a position sensitive anode for the MCP readout allows to determine
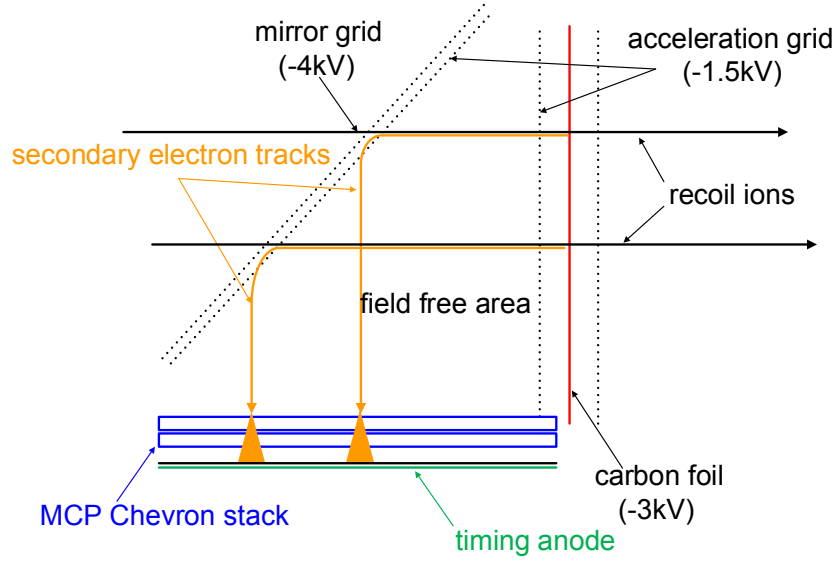
Figure 4.3: *Schematic layout of the most commonly used timing detector design according to Busch et al. (potentials are given exemplarily): Secondary electrons created by the recoil ion passing through a thin carbon foil are deflected by 90° onto a micro channel plate stack (MCP Chevron stack) for amplification and detection.*

the recoil ion position with this detector design. However, in general, the achievable accuracy is limited to $1.3 - 2.3\,$mm (FWHM) [53, 57] due to multiple reasons, which are discussed with the help of Fig. 4.4: Illustrated is the detector layout as previously shown in Fig. 4.3, however, overlaid are the simulation results of the corresponding field configuration (green equipotential lines) as well as numerous calculated secondary electron drift lines (orange lines) originating from the same location on the carbon foil. One can observe that residual potential differences occur in the "field-free" region, which potentially deflect the electrons once they enter. Furthermore, the grid wires cause deflections of the secondary electrons in their close vicinity (see section 4.2.5). The most dominating contribution to the position inaccuracy, however, results from the fact that the secondary electrons show a certain momentum distribution on emission [58]. Velocity components parallel to the carbon foil are maintained during initial acceleration, which affect the injection angle into the field volume of the electrostatic mirror and thereby cause deviations from the envisaged 90° projection.

As a result, position deviations from the ideal projection on the MCP surface up into the centimeter range can be observed for single electrons (red marks Fig. 4.4). This is an important fact to consider, since only a very limited number of secondary electrons is emitted from the thin carbon foil. Especially for light recoiling elements, the secondary electron yield reaches values of zero to only a few electrons per incident
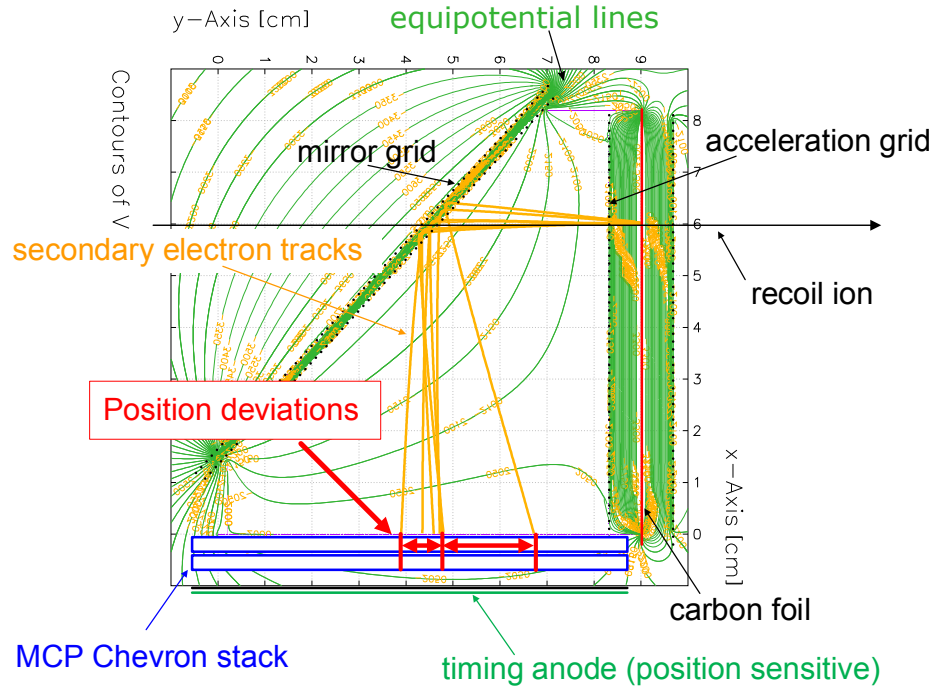
Figure 4.4: *The field configuration as well as secondary electron trajectories are simulated for the potential values illustrated in Fig. 4.3: Multiple deviations in the position on the MCP surface of the secondary electron tracks are observed for one single location of origin on the carbon foil. The deviations are caused by residual field inhomogeneities, gird wire deflections and in particular by the secondary electron momentum distribution.*

ion [59]. Therefore, it is required that even for a single emitted electron the position information is preserved accurately, since no statistical mean value is present.

• The new detector design:

An accurate determination of the recoil ion position, even in case of only one single electron being emitted with a certain velocity parallel to the carbon foil, can be accomplished by utilizing an electrostatic lens which images its location of origin from the carbon foil onto the surface of the micro channel plate stack. The electric field configuration, being exclusively given by the electron lens, counteracts the spreading of the secondary electron tracks caused by their momentum distribution (for details see section 4.2.5). This approach leads to the detector layout illustrated in Fig. 4.5 and described in the following:

In order to obtain a timing measurement, which is not influenced by any lens properties, the detector layout is divided into two separate units. One dedicated timing unit and one unit for position measurement only. The timing unit uses secondary

electrons emitted in backward direction from the carbon foil, which is tilted by 40°. These electrons are accelerated via a grid on a straight way directly into a MCP stack for exclusive timing measurement. Secondary electrons created simultaneously by the same recoil ion, but in forward direction, are also accelerated by a grid and then injected into the electrostatic lens volume. The electrostatic lens, following a modified Einzel lens design, subsequently focuses the electron tracks onto a second MCP stack, dedicated to the position determination.

In accordance to Fig. 4.4 of the Busch design, Fig. 4.6 illustrates simulation results of the new detector design highlighting the position unit: The electrostatic field is exclusively determined by the electrostatic lens (green equipotential lines). Secondary electron tracks (orange lines) starting from multiple emission centers on the carbon foil are focused and directly imaged on the MCP stack. The position readout of the
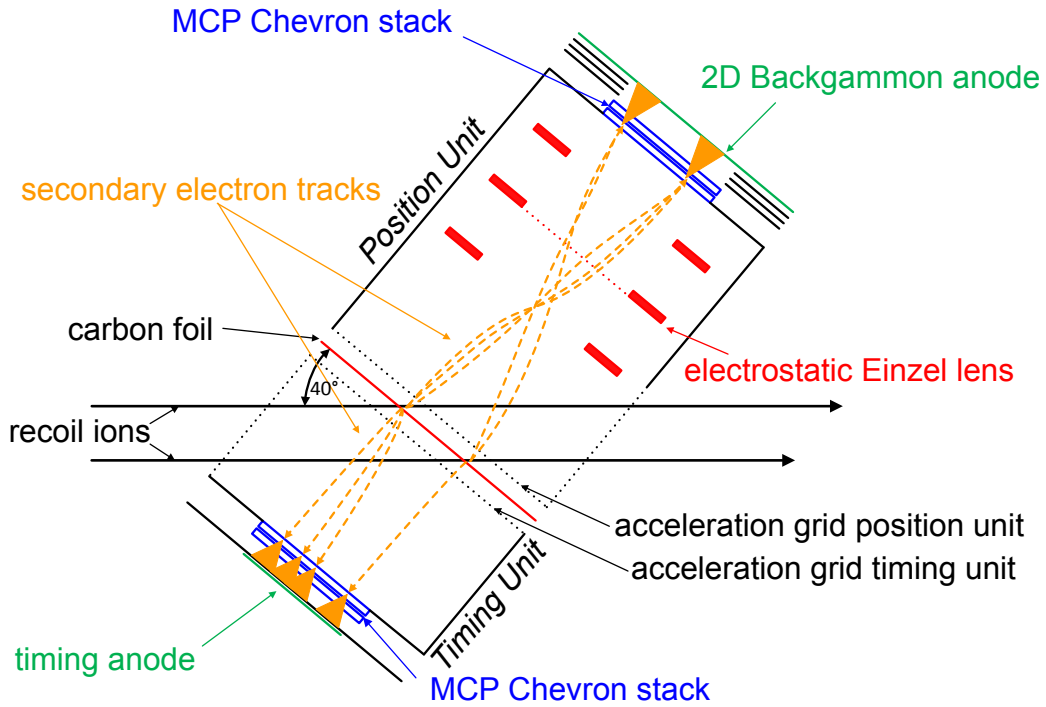
Figure 4.5: *Schematic layout of the new position sensitive timing detector: The carbon foil is tilted by 40°. Secondary electrons emitted in forward direction are focused by an electrostatic lens on the MCP surface, thus maintaining the position information despite their momentum distribution (position unit). Backward emitted electrons are straightly accelerated towards a second MCP stack for timing measurement only (timing unit).*

MCP stack is executed by a 2-dimensional Backgammon anode as described in detail in section 4.2.4. The development of the electrostatic lens including 2- and 3-dimensional
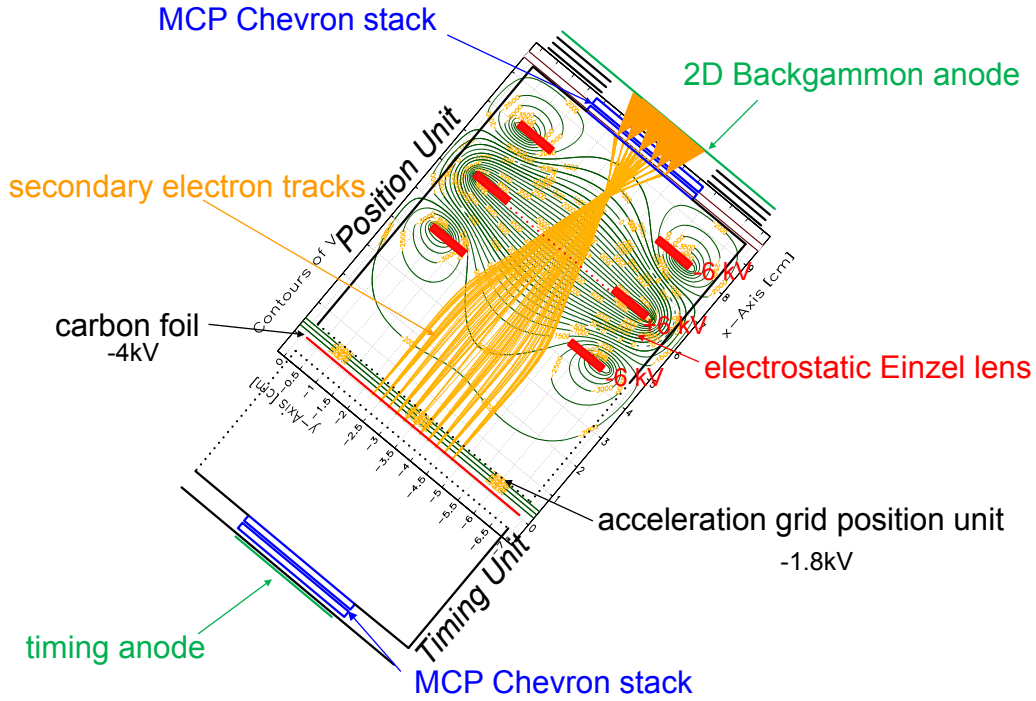
Figure 4.6: *Working principle of the position unit (schematic): The field configuration (green equipotential lines) within the position unit is exclusively determined by the electrostatic Einzel lens (potential values given exemplarily). Secondary electron tracks (orange lines) originating from multiple locations on the carbon foil are focused onto the MCP stack for accurate position measurement despite their momentum distribution. The actual position readout is performed utilizing a 2-dimensional Backgammon anode.*

simulations is described in section 4.2.5 of this chapter.

• Drawback accompanied by the new detector design:

One drawback of this design is given by the fact that the effective thickness of the carbon foil is increased due to the tilt angle. This causes greater energy straggling and angular straggling. However, in case of a single position measurement carried out by the first timing detector with sufficient accuracy for kinematic corrections (small effective projectile beam spot on the sample), the effect of an increased angular straggling becomes irrelevant (see section 3.2). Energy loss and energy straggling, however, can only be reduced by a decrease of the effective foil thickness.

A second disadvantage of this design is given by the separation of the position and the timing measurement: Especially for light elements at a given foil thickness the secondary electron creation probability and thereby the detection efficiency is reduced [59]. Thus, for light recoil masses (less energy loss in the carbon foils) the probability

to obtain a coincident time- and position information is reduced.

4.2.2   Chevron micro channel plate stack for secondary electron amplification, position- and timing measurement

The time measurement is carried out by the detection of secondary electrons generated by the recoil ions on penetration of a thin carbon foil within the timing detector as described before. Typical values of foil thicknesses used for time of flight detectors are below $5\,\mu g/cm^2$ ($\approx\,\le 20\,nm$) in order to minimize energy straggling of the recoil ion [48, 49, 54]. At such foil thicknesses, the mean secondary electron yield reaches values of zero[4] to only multiple electrons per incident ion [58, 59]. This requires the ability to obtain an appropriate signal for detection created by at least one single electron. Therefore, in order to obtain a signal amplitude in the range of several tenths of millivolts for discrimination a fast amplification process (picoseconds regime) of the secondary electrons has to be carried out. Furthermore, spatial information of the amplification process has to be provided for position determination.

For this task, micro channel plate (MCP) stacks in the "Chevron" configuration are most suitable. The Chevron stack consists of two MCPs, which are stacked on top of each other in order to achieve a total gain of $> 10^6$, as schematically illustrated in Fig. 4.7. The stacks provide time resolutions of $< 100\,ps$ and set the basis to achieve
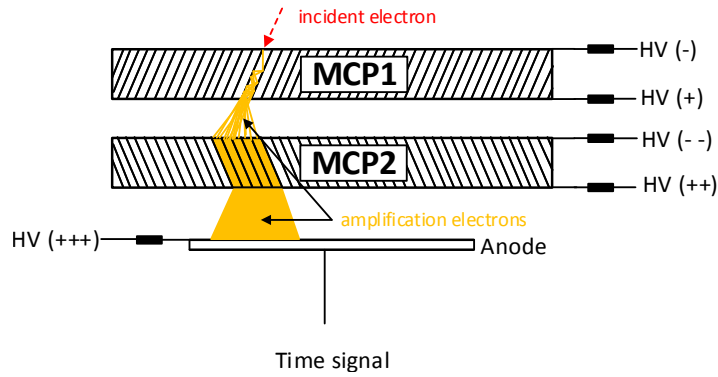
Figure 4.7: *In the "Chevron" configuration two micro channel plates (MCP) are stacked on top of each other. An incident particle (e.g. a electron) creates secondary electrons within the first MCP which are amplified within the micro channels. The created charge cloud exits the first MCP, expands within the gap between them and is amplified again by the second MCP. A total gain of $> 10^6$ can be achieved, which allows for the detection of a single incident electron.*
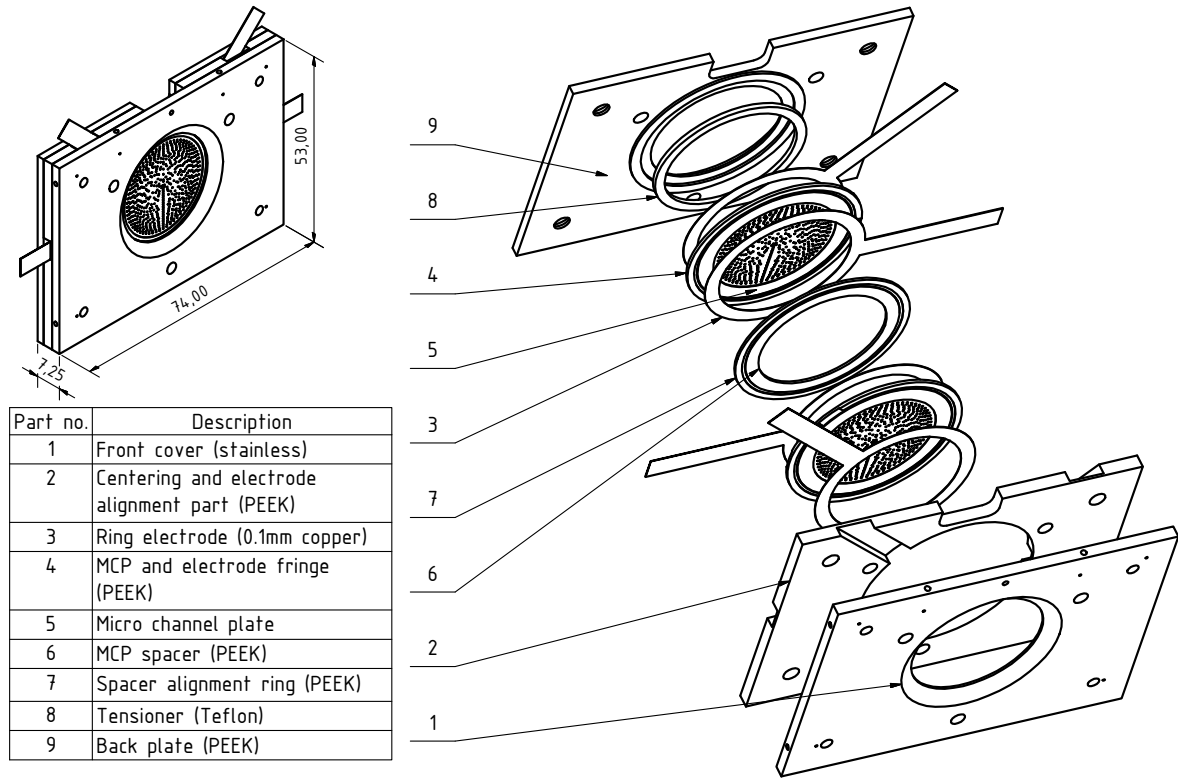
---

[4] In case of zero electrons, no detection is possible. This represents e.g. the difficulty for the detection of hydrogen in TOF-E measurements as discussed in section 5.4 of this work

spacial resolutions in the micrometer range [60] (see section 4.2.4 for further discussion of the position readout).

MCP Chevron stacks are commercially available by a number of suppliers (e.g. Hamamatsu, Tectra, Photonis), however, for the application within the new developed position sensitive timing detector multiple constraints regarding the general dimensions, the ease of integration into the detector as well as parameters of the stack itself (MCP diameter, gap between MCPs, electrical connections) can not all be overcome by those "off the shelve" MCP stacks. Therefore, an appropriate MCP stack for the use within the new timing detector is designed:

An exploded assembly drawing as well as a parts list of the newly designed MCP stack is illustrated in Fig. 4.8. As central element of the stack detection grade micro channel plates (part no.5) with an outer diameter of 32.7 mm, a channel diameter of 10 μm and a channel pitch of 12 μm are chosen. At a 40:1 ratio, the plate thickness is stated to be 0.48 mm at a channel bias angle of 12° by the supplier Tectra. A gain of ≥ 1500 at an applied potential difference of 800 V for a single plate is stated. The active area of the channel plate has a diameter of 25 mm. Four ring electrodes (part no.3) used to apply the high voltage to each MCP side are laser cut from 0.1 mm copper foil, featuring an outer diameter of 34 mm, an inner diameter of 28 mm as well as an extended contact pad. The distance between both channel plates is adjusted by a PEEK (polyether-ether-keton) spacer ring (part no.6) to be 0.6 mm. This results in a larger gap than compared to commercially available stacks, which typically use distances of < 0.2 mm [60]. The enlarged gap between the plates supports the position readout as discussed in detail in section 4.2.4. The PEEK spacer ring is supported by an outer alignment ring also made of PEEK (part no.7). For accurate centering of the four electrodes and both channel plates within the stack, two PEEK fringes surrounding the MCPs are introduced (part no.4), featuring milled-in notches (0.14 mm in depth), which align the two ring electrodes per channel plate by 45° to each other. The electrode guidance is continued by channels within the main centering- and alignment part (part no.2). The front cover, being in direct contact with the first MCP, is made of stainless steel.
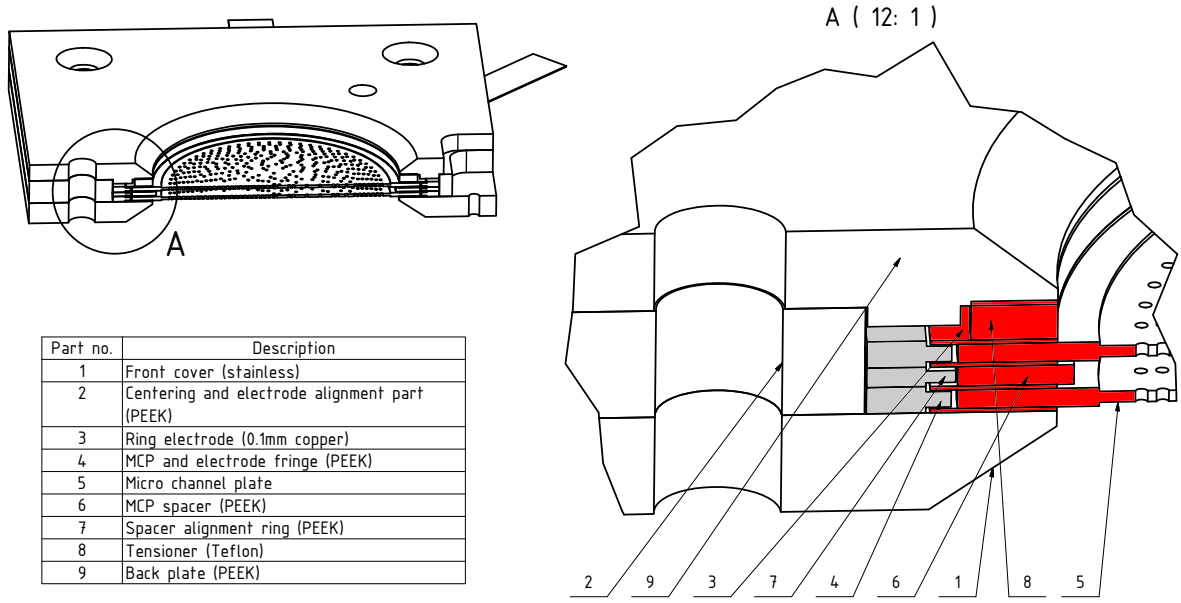
With respect to the assembly of the stack, the main advantage of this design is that the pressure (necessary for electrical contacting) by the Teflon tensioner piece (part no.8) is applied only in a straight way on components, which are in direct contact to each other. Thereby, twist on the MCPs and electrodes is avoided, which could result in breakage of the brittle MCP glass substrate and affect the amplification characteristics. A detail display (A 12:1) of a sectional view of the MCP stack is

Part no.	Description
1	Front cover (stainless)
2	Centering and electrode alignment part (PEEK)
3	Ring electrode (0.1mm copper)
4	MCP and electrode fringe (PEEK)
5	Micro channel plate
6	MCP spacer (PEEK)
7	Spacer alignment ring (PEEK)
8	Tensioner (Teflon)
9	Back plate (PEEK)

Figure 4.8: *Exploded assembly drawing, overall dimensions and parts list of the newly designed micro channel plate Chevron stack for secondary electron amplification as basis for time- and position readout within the new position sensitive time of flight detector.*

illustrated in Fig. 4.9. The components accentuated in gray (part no.7 + 2 × part no.4) as well as the back plate (part no.9) are exclusively designed for accurate centering of the inner parts on which pressure is applied. The inner parts are highlighted in red (part no.8, 6, 3, 5). Tolerances regarding e.g. the distance between the channel plates are kept to a minimum with this design. Another advantage of this design is that only by change of the dimensions of the centering components as well as of the thickness of the tensioner piece, the stack can be adopted to accept a variety of channel plates. This can be of great help if e.g. the channel plates can only be replaced by ones of slightly different dimensions. Even with these design features included, a small overall package size can be realized resulting in a total thickness of 7.25 mm as illustrated in Fig. 4.8. The stack has a width of 74 mm and a height of 54 mm.

Part no.	Description
1	Front cover (stainless)
2	Centering and electrode alignment part (PEEK)
3	Ring electrode (0.1mm copper)
4	MCP and electrode fringe (PEEK)
5	Micro channel plate
6	MCP spacer (PEEK)
7	Spacer alignment ring (PEEK)
8	Tensioner (Teflon)
9	Back plate (PEEK)

Figure 4.9: *Sectional view of the newly designed micro channel plate Chevron stack: Red accentuated in view A (12:1) are the components at which pressure is applied for electrical contacting. The gray highlighted parts are for centering/alignment purpose only.*

• Time readout

The amplitude of the output pulse created by the MCP stack contains no valuable information with respect to the time measurement, but it has to be of sufficient magnitude for discrimination. Its height varies according to the number of incident secondary electrons primarily involved in the amplification process. Thus, constant fraction discriminators (CFD) are used to eliminate any dependence of the time measurement on the pulse height [61]. However, if the raising slope of pulse shape is not steady, time jitter affecting the time resolution can be generated. Furthermore, negative post-pulse oscillations ("ringing") can cause discrimination problems, which potentially lead to false, but discrete time measurements. An appropriate pulse shape can only result from an "unobstructed" current flow within the system. Typical pulse rise times created by MCP stacks are in the range of one nanosecond or less, leading to the necessity of proper current flow in the GHz frequency domain. Here, effects like the skin effect as well as appropriate impedance matching of cables and feedthroughs have to be taken into account. Therefore, a proper electronic circuit for the time readout of the MCP stack is developed to minimize these problems as presented in the following:

The charge cloud exiting the second MCP of the Chevron stack is acceler-

ated towards a metal anode for detection (see Fig. 4.10(a)). The time readout anode consists of a printed circuit board (FR4, 80 mm x 50 mm) with a thickness of 0.4 mm, metalized on both sides by $35\,\mu$m thick copper. Positive voltage of 160 V applied to the anode side facing towards the second MCP at a distance of 6 mm attracts the charge cloud. As a result, a signal pulse is induced by capacitive coupling into the backside of the anode, which is kept on ground potential via a $50\,\Omega$ resistor. Potential of each single channel plate side is supplied by separate high voltage channels for flexibility regarding gain adjustment and the total voltage configuration of the stack. The input of the CFD is directly connected to the anode by a $50\,\Omega$ coax cable, which has a shielding of silver coated wires. This shielding is used for high frequency current conductance:

The front side of the anode as well as the electrodes of each single channel plate are connected to the wires of the shielding via high voltage SMD capacitors (1812, 3 kV) with a capacity of 470 pF and e.g. C0G/NP0 as dielectric medium. The capacitors act as conductors at high frequencies, thus allowing the generated current to flow appropriately resulting in a clean voltage pulse shape. The electrical circuit is illustrated in Fig. 4.10(a). In contrast to the concept of a floating time anode, in which the current has to be totally sourced or sunk by the CFD input (potentially damaging the CFD), higher signal amplitudes as well as smoother signal shapes with a minimum of post oscillations are achieved. A typical time signal shape from secondary electrons created by alpha particles penetrating a $4\,\mu$g/cm^2 thick carbon foil obtained with the new developed MCP stack and the described time readout configuration is shown in Fig. 4.10(b).

(a)

(b)
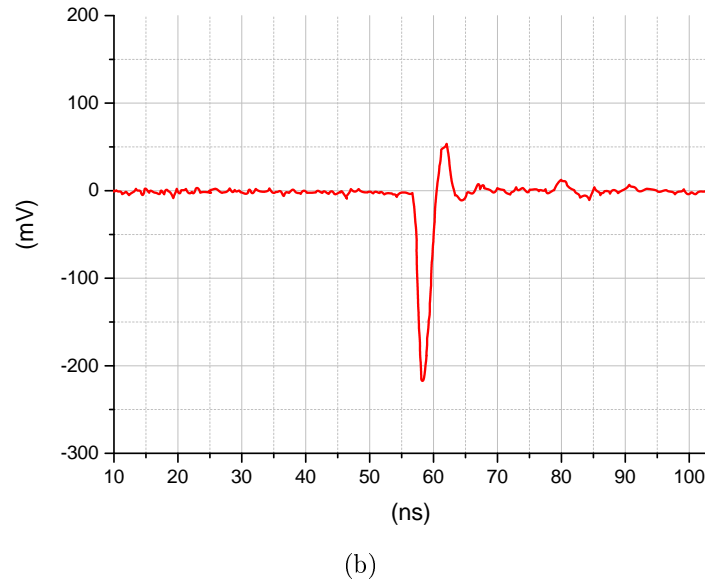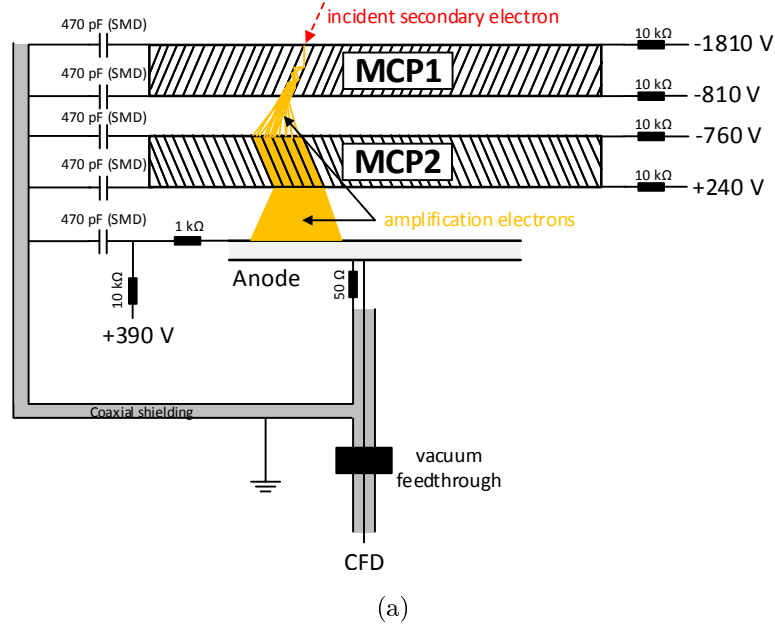
Figure 4.10: *(a): Time readout configuration: SMD capacitors connect each MCP side as well as the front side of the anode to the silver coated coax shielding of the time signal cable for optimal high frequency current conduction. A $50\,\Omega$ resistor also connects the backside of the anode to the shielding for impedance matching. (b): A smooth voltage pulse shape ($\approx 1\,\mathrm{ns}$ rise time, digitized with a $500\,\mathrm{MHz}$, $4\,\mathrm{GSa/s}$ oscilloscope) is obtained without significant negative post-pulse oscillations ideal for constant fraction discrimination.*

4.2.3   Intrinsic time resolution

In order to determine the achievable time resolution of the detector, a coincidence setup consisting of two time units is developed in accordance to [62]:

The components of a single timing unit are the new developed MCP Chevron stack with the time readout anode (see Fig. 4.10(a)) as well as a Faraday cage. The Faraday cage consists of the secondary electron acceleration grid, a particle entrance grid as well as side-, bottom- and top shielding covers, of which all are kept at the same potential (-1810 V). Thus, a field free region is created within in the cage volume, in which, after acceleration, the secondary electrons drift over a distance of 56.1 mm towards the MCP stack for amplification. The grids are made of gold coated tungsten wires of a diameter of 35 μm, spaced apart by 1 mm.

The coincidence setup consists of two timing units, equally distanced by 5 mm to a carbon foil, which is set at a potential of -4010 V (4μg/cm^2) as illustrated in Fig. 4.11(a). Alpha particles emitted by a 40 kBq americium source (tilted by 40°) are used for secondary electron creation simultaneously in forward and backward direction as schematically illustrated in Fig. 4.11(b). The time signal created in backward direction is fed into a constant fraction discriminator (CFD), used as start trigger of a time to amplitude converter (TAC). The TAC is stopped by the signal obtained in forward direction, which is delayed by ≈ 16 ns.
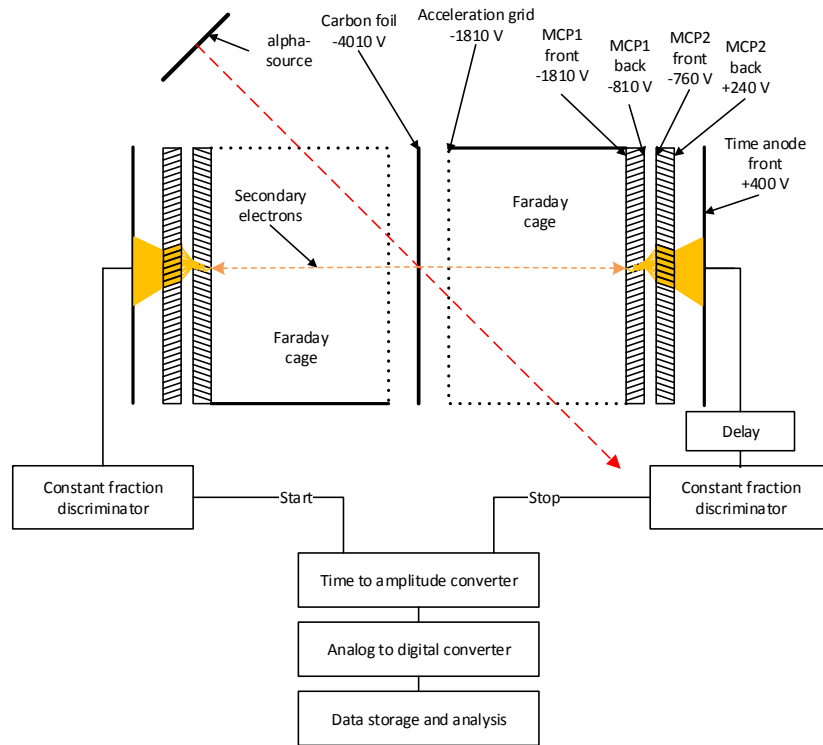
Considering both identical timing units to be operating equally, the contributions of both units to the recorded time spectrum illustrated in Fig. 4.12 are also equal. Therefore, with an obtained value of the full width at half maximum ΔT_{coin} of 136 ps $\pm$ 1.2 ps the time resolution ΔT_{intr} of a single unit is given by

$$\Delta T_{intr} = \frac{\Delta T_{coin}}{\sqrt{n=2}} \qquad (4.1)$$

to be 96 ps $\pm$ 0.8 ps (FWHM).
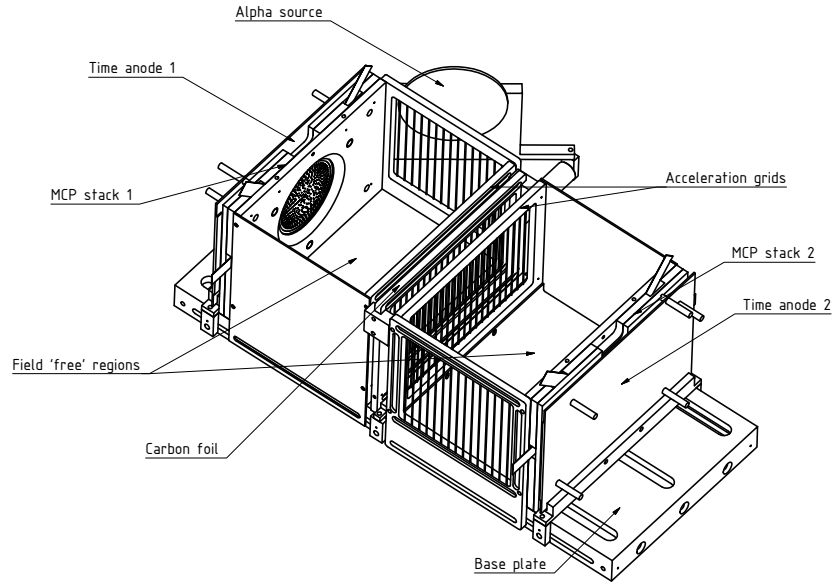
(a)

(b)

Figure 4.11: *(a)*: *Coincidence setup consisting of two timing units for the determination of the intrinsic time resolution (top covers of both Faraday cages are not displayed).* *(b)*: *Secondary electrons are created by alpha particles simultaneously in forward and backward direction. The signal obtained in forward direction is delayed and used as stop signal, secondary electrons detected in backward direction start the timing measurement (displayed grids are not of true scale and wire orientation).*
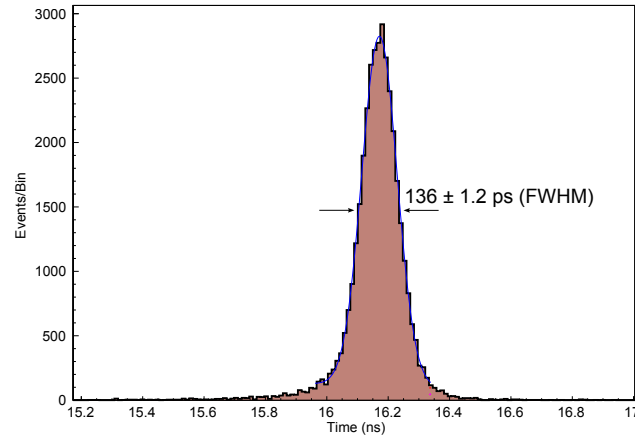
Figure 4.12: *Time spectrum obtained utilizing the coincidence setup, illustrated in Fig. 4.11. A full width at half maximum (FWHM) of 136 ps ± 1.2 ps is measured. Assuming equal contributions of both MCP timing units, the time resolution obtained with a single unit is determined to be 96 ps ± 0.8 ps (FWHM).*

4.2.4   Position readout utilizing a 2D-Backgammon anode

As illustrated in Fig. 4.7, the location of the first amplifying channel corresponds to
the center of mass of the charge cloud exiting the second micro channel plate. Thus,
a determination of this center utilizing a position sensitive anode allows for a position
readout of the MCP stack with an accuracy in principle only limited by the pore size
of the MCPs.

For the position readout of the MCP stack located in the position unit of the
TOF detector (see Fig. 4.5), a 2-dimensional Backgammon anode is developed. Its
performance with respect to the achievable position readout resolution is determined
by an appropriate experimental setup as described in the following.

• The 2D-Backgammon anode

Miscellaneous approaches for the position readout of MCP stacks have evolved over the
last decades offering different performances with respect to spatial resolution, count
rate capability, timing- or multiple hit capabilities. The methods are based on differ-
ent techniques, for instance resistive readouts, such as the resistive sheet anode [63],
signal transit time readouts such as the delay line anode [64] and readouts based on
the charge division technique such as the wedge-and-strip anode [65] or the Vernier
anode [66, 67].

The charge division type based anodes can be manufactured by standard circuit
board printing technologies, which are cheap and immediately available. Another ad-
vantage is the ease in scalability of these printed anode types, allowing for quick adap-
tion to a certain detector type without great effort. A clear disadvantage of the charge
division type readout, however, lies in the preservation of the center of mass of the
charge cloud on its travel towards the read out anode. Small inhomogeneities of the
electric field influence the charge centroid causing image distortions. Incorrect field
strengths between the anode and the last channel plate potentially limit the expansion
of the charge cloud, which causes distortions occurring with the periodicity of the read
out structure [68].

For the new position sensitive time of flight detector, a charge division type 2D-
Backgammon anode was developed. Its functional principle is based on the "modified
backgammon method with weighted coupling capacitors (MBWC)", which is discussed
in detail by Mizogawa et al. in [68–71]. However, the basic functional principle, details
of the development and the achieved spatial readout resolution are presented in the
following:

Figure 4.13 schematically illustrates the front as well as the backside of the 2D-

(a)

(b)
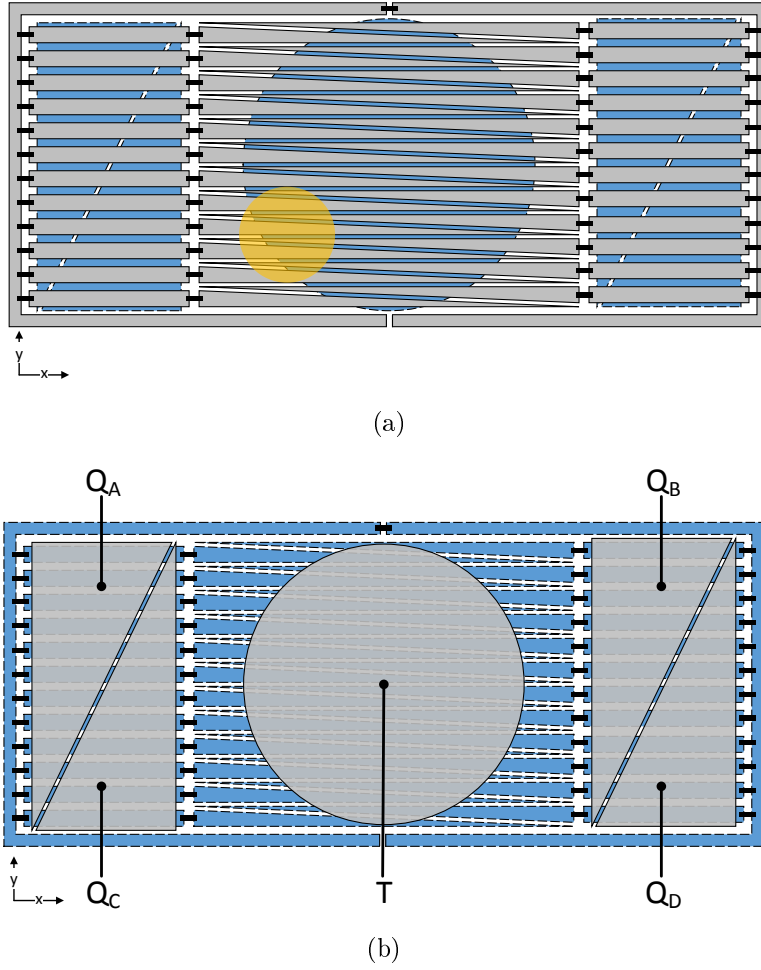
Figure 4.13: *(a): 2D-Backgammon anode front side: The charge cloud (finite size, yellow circle) created by the MCP Chevron stack is geometrically separated by the horizontal triangles (grey) of the Backgammon pattern, defining the x-position of the center of mass of the charge cloud. The corresponding amounts of charge are then carried to the rectangles on both sides. (b): 2D-Backgammon anode back side: The charge on the rectangles induces a signal into the vertical triangles of the Backgammon pattern (grey) on the backside of the anode by capacitive coupling. This allows to determine the y-position of the charge cloud center. The signals Q_{A-D} are used for positioning. The signal T allows for timing measurement.*

Backgammon anode. The anode consists of a 0.4 mm thick circuit board (FR4) with the backgammon charge division structures (35 μm copper) printed on both sides. The height of the 27 horizontal triangles on the front side, which are spaced apart by 190 μm, is 1.25 mm, the width 42 mm. A charge cloud, represented by the yellow circle in Fig. 4.13(a), is geometrically divided by the horizontal triangles of the backgammon pattern on the front side of the anode according to the proportions given by the triangle areas covered by the charge cloud area. Thus, the x-position of the

centroid is determined. Subsequently, the corresponding amounts of charge are carried through $20\,\Omega$ resistors (SMD 0402, used for oscillation damping) to the rectangle shaped charge collectors ($1.25\,$mm x $17\,$mm) located on both sides of the anode. With the $100\,$kΩ resistors a RC discharge time is defined, long enough for the charge to induce a signal on the vertical backgammon triangles located on the backside of the anode (Fig. 4.13(b)) by capacitive coupling. Hence, the y-position of the centroid is determined. Four charge sensitive preamplifier (Cremat CR-111, $150\,$mV/pC) pick up the induced signals on the triangles of the backside for subsequent main amplification by a multichannel spectroscopy amplifier (Mesytec MDS-8). The x- and y-positions are calculated depending on the corresponding charge amounts Q_{A-D} and the total charge $Q_{tot} = Q_A + Q_B + Q_C + Q_D$ according to equation 4.2 and 4.3:

$$X_{pos} = \frac{Q_A + Q_C}{Q_{tot}} \tag{4.2}$$

$$Y_{pos} = \frac{Q_A + Q_B}{Q_{tot}} \tag{4.3}$$

An additional circle shaped electrode on the backside of the 2D-Backgammon anode also allows to obtain a timing signal T.

● Position resolution

For determination of the achievable position resolution with the 2D-Backgammon anode, a dedicated test setup was developed. It incorporated the position readout module, as integrated into the final detector setup as well as an alpha particle source for signal creation. The position readout module consists of the new developed MCP Chevron stack (section 4.2.2), three field electrodes and the newly designed 2D-Backgammon anode. The three ring shaped electrodes (inner diameter $31\,$mm) serve for preservation of the charge centroid by smoothing the field between the last MCP and the Backgammon anode. They are spaced apart by $1.5\,$mm. At a total distance of $8.5\,$mm between the 2D-Backgammon front side and the MCP surface, a potential difference of $85\,$V is applied, resulting in a field strength of $10\,$V/mm serving for expansion of the charge cloud.

   An image to be read out is defined by a laser cut stainless steel mask with a thickness of $0.1\,$mm, which is placed directly on the surface of the first channel plate. Squares with a length of $0.2\,$mm and a pitch of $0.6\,$mm as well as a slit structure are cut into the mask with a precision of $\pm\,5\,\mu$m. The mask covers the entire active surface area of the first channel plate. Thus, only particles passing through the mask create a position signal. The data acquisition is triggered with the timing signal obtained from the

2D-Backgammon anode. The alpha source was placed at a distance of 56 mm towards the image mask and on axis with the channel plate center. A schematic illustration of the setup as well as the applied potentials are given by Fig. 4.14.
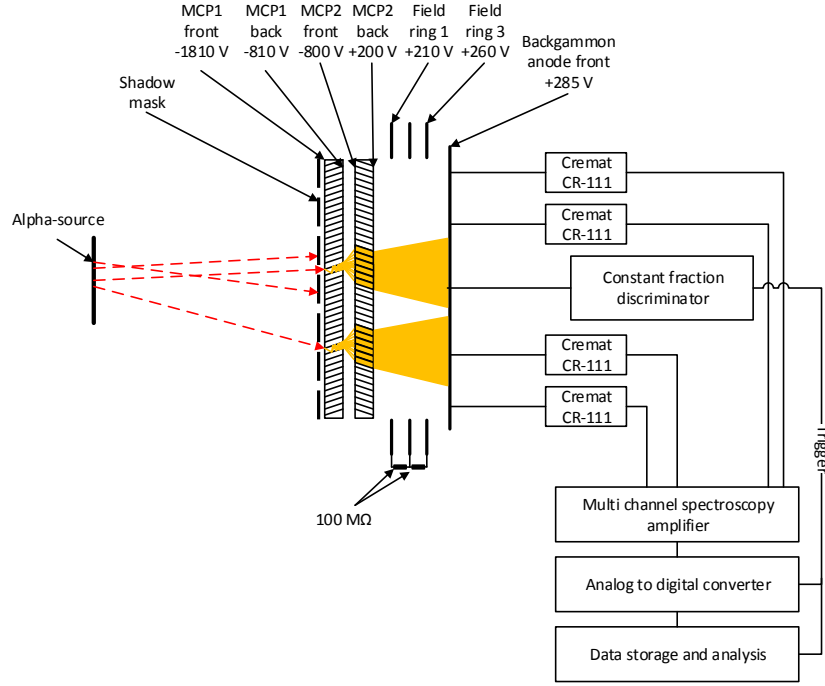
Figure 4.14: *Experimental setup for determination of the position readout resolution: Alpha particles passing through a mask create an image, which is read out utilizing the 2D-Backgammon anode (see text for further explanation).*

The obtained position raw data of the image is illustrated in Fig. 4.15(a). The shape of the mask with its square holes, as well as its slits are clearly resolved. Distortions of the image at the boundaries of the channel plates are caused by the transition of the active area to the non active area of the second MCP. Here, the secondary electron amplification process is limited by the available number of the remaining channels of the active area of the second MCP. Thereby the center of mass of the created charge cloud is unavoidably shifted towards the center of the MCP, where it overlaps with the fully resolved outer squares. The overall linearity is affected by distortions due to residual field inhomogeneities between the surface of the second MCP and the 2D-Backgammon anode. These field inhomogeneities are either not fully corrected by the three field electrode rings or caused by an insufficient flatness of the anode surface (e.g. backgammon structure or solder spots of the resistors).

In order to determine the achieved position resolution, a software distortion cor-

rection is applied, which is described in section 4.2.6. Figure 4.15(b) illustrates the calibrated image of the mask with the correction being applied. An overall linearity of $< 150\,\mu$m over the entire area of the channel plate is achieved.

Figure 4.16(a) shows the inner area of the obtained image of the mask. Highlighted in red are five selected squares, of which the position data is projected onto the x-axis as illustrated in Fig. 4.16(b). By fitting error functions (blue lines) to the data, the mean position resolution of the readout module is determined to be $60\,\mu\mathrm{m} \pm 7\,\mu\mathrm{m}$ (FWHM).

It has to be pointed out that the obtained position resolution consists of a convolution of the image mask function and the readout function of the 2D-Backgammon anode. Therefore, a deconvolution process would be necessary to obtain the true position resolution. However, the already obtained value of $60\,\mu\mathrm{m} \pm 7\,\mu\mathrm{m}$ (FWHM) is not limiting the envisaged overall position resolution of 0.8 mm (FWHM) (see section 4.1). The achievable overall position resolution of the TOF detector, however, is restricted by other factors, as discussed in the following section.
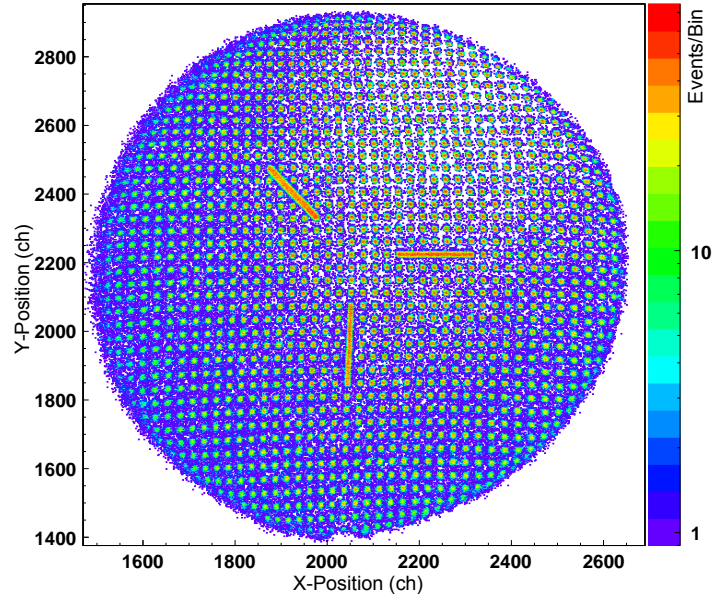
(a)
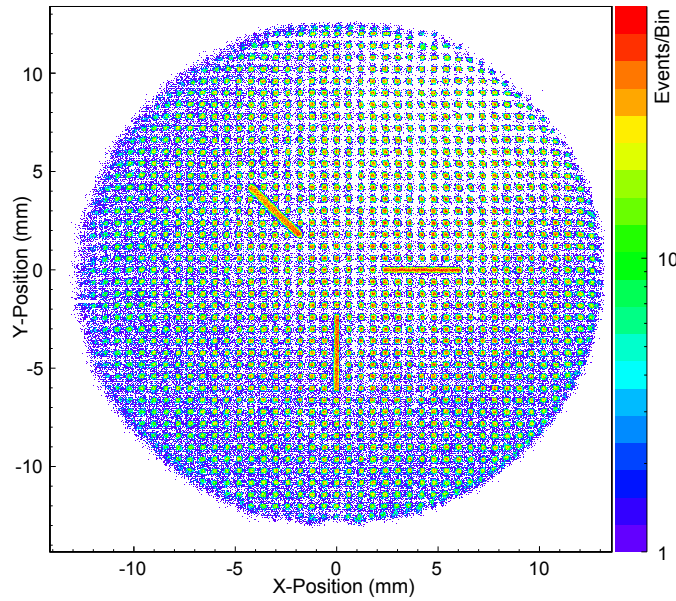
(b)

Figure 4.15: *(a): Position readout raw data obtained with alpha particles: The X- and Y-axis present the acquired position data defined by a mask (0.2 mm × 0.2 mm squares, 0.6 mm pitch) placed directly onto the surface of the first MCP. Image distortions at the outer boundaries are caused by the transition from the active to the non active area of the MCPs. Overall distortions occur due to residual field inhomogeneities between the 2D-Backgammon anode and the second MCP. (b): Calibrated image of the mask: Using a software distortion correction (see section 4.2.6, the overall linearity is improved to $< 150\,\mu m$.*
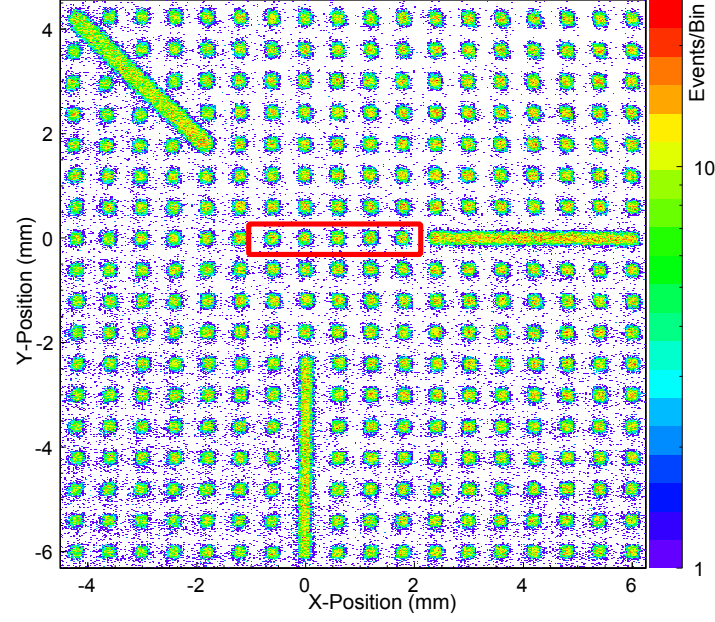
(a)
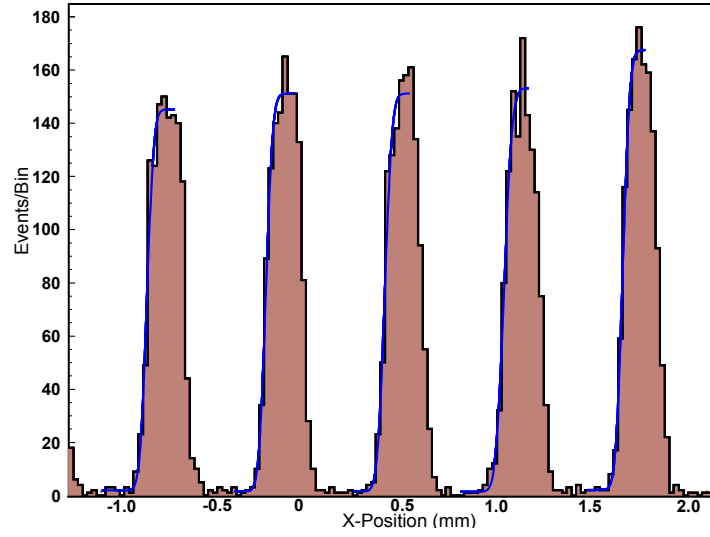
(b)

Figure 4.16: *(a)*: *Inner area of the mask image obtained with the 2D-Backgammon anode (see Fig. 4.15(b)): The position data (red highlight) of five selected squares (0.2 mm × 0.2 mm, pitch 0.6 mm) is projected onto the X-axis.* *(b)*: *By fitting error functions (blue lines) to the position data a mean intrinsic position resolution of 60 μm ± 7 μm (FWHM) is determined.*

4.2.5   Design and simulation of an electrostatic lens for secondary electron focusing

The secondary electrons created by the recoil ions on penetration of the carbon foil show a certain momentum distribution on emission [58, 72]. Thus, velocity components perpendicular as well as parallel to the carbon foil surface do occur. In case of a perpendicular acceleration towards the micro channel plate stack, the velocity components parallel to the foil plane are maintained. This results in a deviation in position on the channel plate surface in contrast to a straight projection of the point of origin. To overcome this problem, an electrostatic lens is developed, which is installed between the carbon foil and the MCP stack (see Fig. 4.6) as previously suggested by T.Schaefer [73]. The electrostatic lens focuses the secondary electrons thereby projecting an image of the points of origin from the carbon foil onto the channel plate surface, thus maintaining the position information despite their momentum distribution.

This chapter is dedicated to the development of the electrostatic lens incorporated into the position unit of the start timing detector (T_1), necessary to achieve the required position resolution of 0.8 mm (FWHM).

In order to find an appropriate lens design, ray tracing simulations are performed, which go hand in hand with the mechanical design. Therefore, it is required to initially discuss individual design aspects in closer detail such as:
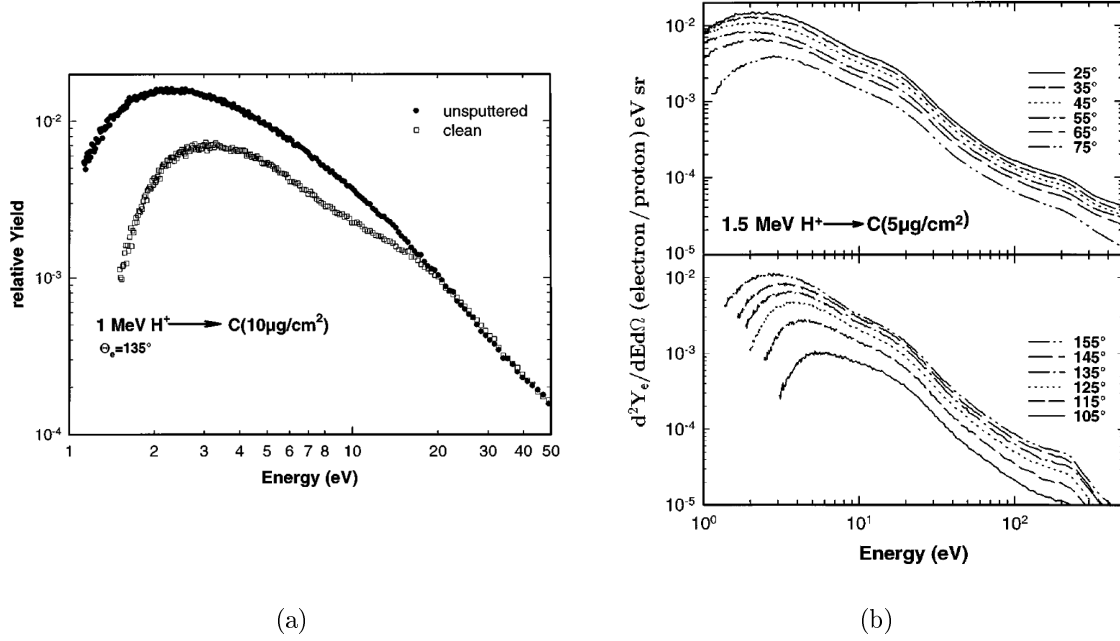
- Secondary electron momentum distribution

- Lens type

- Influence of grids on the optical properties of the lens

- Potentials applied to the lens

- Mechanical implementation of the lens

The design phase, including the treatment of each listed aspect as well as the final design of the electrostatic lens is presented in the following:

• Secondary electron momentum distribution

The energy distribution of the secondary electrons is dominated by electrons within a low energy range of $\approx 1-10$ eV, however, also a minority of electrons is emitted within an energy range of > 20 eV. This is exemplary demonstrated by Drexler et al. [58] for 1 MeV protons penetrating a carbon foil with a thickness of $10\,\mu\mathrm{g/cm^2}$ as illustrated in Fig. 4.17(a). Surface properties e.g. adsorbents like atmospheric hydrocarbons or the surface roughness of the carbon foil do affect the secondary electron distribution in the

low energy range of 1-10 eV, which is demonstrated by the comparison between a non treated and a sputter cleaned carbon foil surface according to Fig. 4.17(a).

(a)   (b)

Figure 4.17: *(a): Measured energy distribution of secondary electrons created by 1 MeV protons penetrating a 10 µg/cm² carbon foil for a unsputtered (black dots) and a clean carbon foil surface (white squares) [58]. (b): Measured differential secondary electron yield at different emission angles for 1 MeV protons penetrating a 5 µg/cm² thick carbon foil: The low energy peak dominates the distribution in both, forward- (angles from 25° to 75°) and backward direction (angles from 105° to 155°), however, in forward direction greater yields for higher energies are observed at all emission angles and the peak is broadened. Data taken from Drexler et al. [58].*

As illustrated in Fig. 4.17(b), the energy distribution of secondary electrons emitted in both, forward- (emission angles from 25° to 75°, with respect to the carbon foil surface) and backward direction (emission angles from 105° to 155°) is dominated by the low energy peak. However, the secondary electrons emitted in forward direction show a higher yield at higher energies for all emission angles as well as a wider energy distribution overall. Drexler suggests a cosine distribution for electrons of an energy higher than 10 eV, but states that the emission angles of electrons below 10 eV are also strongly governed by the surface properties of the foil [58].

The narrower energy distribution in backward emission direction would preferably be used for position measurement carried out by the position sensitive TOF detector,

since large velocity components perpendicular to the carbon foil occur less frequently. However, space constrains due to the close presence of the Q3D magnetic spectrograph force the use of forward emitted secondary electrons for position measurement (see section 4.2.1).

Since the true momentum distribution and its variations are unknown, a secondary electron momentum distribution is derived from the data given in [58], which will be used as basis for the lens design and simulations. The experimentally determined energy distribution (unsputtered), illustrated in Fig. 4.17(a), is parametrized according to the function

$$y = y_0 + A \cdot \left(1 - e^{-\frac{x-x_0}{t_1}}\right)^P \cdot e^{-\frac{x-x_0}{t_2}} \tag{4.4}$$

with parameters chosen to resemble the empiric data. The fit function, as well as its parameters are illustrated in Fig. 4.18. Corresponding to this function random energy
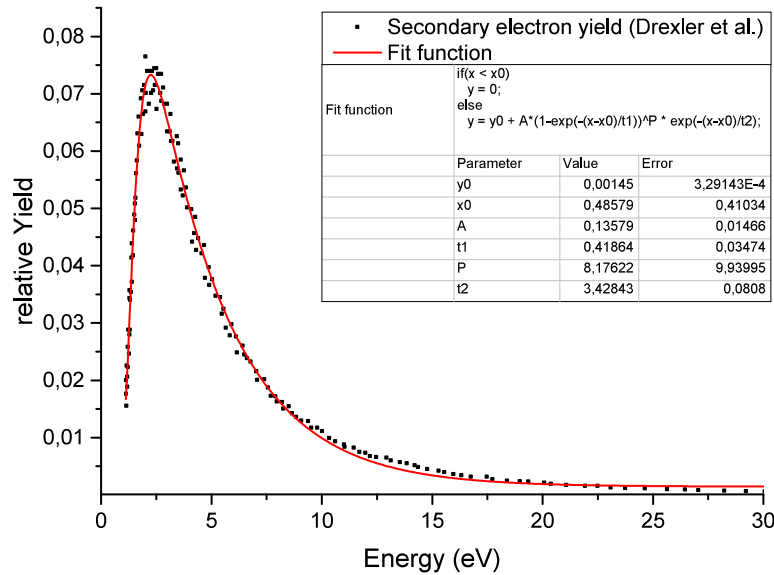
Figure 4.18: *Secondary electron energy yield: A function (red line) fitted to the empiric secondary electron emission data (black dots) obtained by Drexler et al. [58] is utilized in combination with a cosine distribution for the emitting angles as basis for the secondary electron momentum distribution used within the lens design simulations. The fit parameters are listed in the table next to the graph.*

values are created for every secondary electron event within the simulations.

Regarding the emitting angles, a cosine distribution is assumed for all energy values, even though, as demonstrated by Drexler et al. and as illustrated in Fig. 4.17(b), only higher energies tend to occur at angles more close to 90° with respect to the carbon foil plane. However, with this assumption all energy values can occur at smaller

angles with respect to the carbon foil surface. This considerably enhances the requirements on the correction ability of the lens. Within the design simulations, for every secondary electron event, values of the parametrized energy distribution and of the cosine distribution are randomly chosen and assigned to the corresponding event in order to calculate the velocity components of each spatial axis.
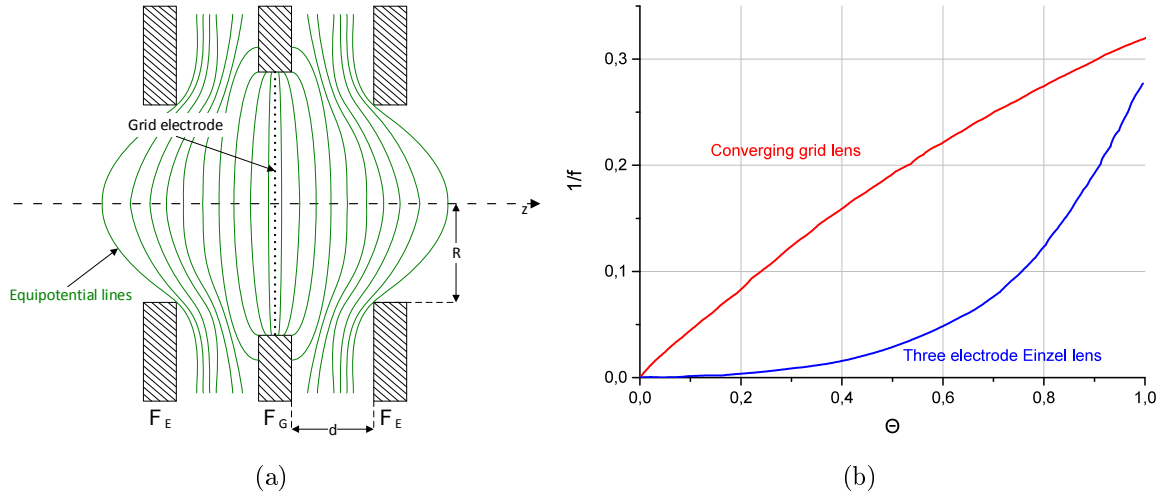
• Lens type

For electron focusing either magnetic or electrostatic lenses can be used [74]. In case of the position sensitive time of flight detector, the use of a magnetic lens is avoided for two main reasons: First, besides the optical properties, the option to carry out an additional timing measurement with the lens is envisaged. Therefore, the path lengths of the electrons within the lens should be kept as short as possible in order to maintain low time variations. Gyrating trajectories, as found in magnetic lenses lead to long paths, thereby possibly counteract good timing properties. Secondly, as described in section 4.2.4, the accuracy of the position readout strongly relies on the sustainment of the charge cloud centroid. Any parasitical magnetic field overlapping with the electrostatic field between the 2D-Backgammmon anode and the MCP stack would potentially cause deformations of the centroid, worsening the achievable position resolution.

Hence, for the position sensitive time of flight detector an electrostatic lens is developed following an "Einzel" lens design, which is discussed in detail in [74, 75]. The basic design consists of three circular shaped electrodes with a radius R, which are equally spaced apart by a distance d and centered along the optical axis z. The two outer electrodes are kept at the same potential Φ_E, the inner electrode at the potential Φ_G. Thus, an electrostatic field is formed in between them, with the ability to focus electrons. A parameter Θ can be defined for a fixed geometry of the lens to be:

$$\Theta = \frac{\Phi_G - \Phi_E}{\Phi_E} \tag{4.5}$$

The required high optical refraction power of the lens, however, leads to an altered "Einzel" lens design, in which the inner circular electrode is replaced by a grid of thin wires, which is also held at the potential Φ_G. A schematic sectional view of this altered grid lens design with qualitatively drawn equipotential lines is illustrated in Fig. 4.19(a).

With respect to the mechanical feasibility, the advantage of this lens design is given by the higher refractive power at lower applied potentials. The compact detector design forces close distances between parts at high potentials and therefore the possibility

<div align="center">(a)   (b)</div>

Figure 4.19: *(a): Schematic illustration of the grid lens type used for secondary electron imaging within the new developed position sensitive TOF detector. In contrast to the typical "Einzel" lens design, the inner circular electrode is replaced by a fine meshed grid. (b): For a given geometry, the grid lens shows a higher refractive power $1/f$ (red line) than the Einzel lens (blue line) at lower applied potential ratios Θ (data taken from Grivet et al. [74]).*

of accidental discharges is reduced. A comparison of the refractive power ($1/f$, with f being the focal length) between the classical Einzel lens and the grid lens in dependence of the parameter Θ is illustrated in Fig. 4.19(b).

The cardinal elements of the grid lens can be calculated for an ideal geometry analytically [74], however, since the grid lens within the TOF detector does not comply with any idealized conditions, the electrostatic field of the lens is calculated with the help of the simulation program Garfield [76] in case of 2-dimensional simulations (taking wires into account) and by a finite element approach with the program COMSOL Multiphysics® [77] for 3-dimensional simulations. Final dimensioning follows the results obtained by electron drift calculations within the obtained 2- and 3D field maps as presented in the following.

• Influence of grids on the optical properties of the lens

For the acceleration and injection of the secondary electrons into the lens volume, grids made of gold coated tungsten wires are used. These grids are intended to represent a virtual plane of attracting potential, however, besides the loss of optical transparency, the secondary electrons also suffer a deflection between the single grid wires according to the shape of the electric field in the close vicinity of the wires. Also, the grid of the electrostatic lens causes additional aberrations to the ones created by the acceleration

grid, both affecting the position resolution achievable by the electrostatic lens.

Analytical approaches to calculate the "grid aberration" for a single grid can be found in [74, 78, 79], however, since the total position resolution obtained with the lens is affected by a combination of several grids, 2-dimensional ray tracing simulations are carried out. Here, the entire secondary electron trajectory from point of origin through both grids and onto the final plane defined by the channel plate surface, is calculated.

It has to be pointed out that the 2D simulations are only intended for the study of the influence of grid spacings of both the acceleration grid and the lens grid, but they do not lead to the final design of the electrostatic lens, especially regarding the final potential values to be applied. These values will be obtained by 3D finite element method (FEM) simulations, in which the grids are replaced by virtual potential planes. This course of action is taken due to the problem, that finite element simulations are limited by the meshing process (creation of polygonal elements) regarding the geometric dimensions, known as the "multiscale problem" [80]. With respect to computational power and accuracy, even with "intelligent" meshing methods, at which finer meshes are created at smaller structures and more corsair meshes at larger structures, it is not possible to cover the micrometer dimensions occurring at the grids and the overall dimension of the lens of approximately 10 cm within one 3D mesh.

The program code Garfield introduced by Rob Veenhof (CERN) is primarily designed for the simulation of drift chambers consisting of thin wires and infinite equipotential planes [76]. It calculates and visualizes the electrostatic fields according to the Maxwell's equations and drift lines of electrons and ions within the field. Different drift calculation algorithms such as the Runge-Kutta or a Monte-Carlo approach can be utilized. In addition to that, a "thin-wire" approximation [81] is used to calculate the 2-dimensional electrostatic field between the wires, responsible for electron deflection. Results obtained by these 2-dimensional simulations with respect to the wire spacings will be incorporated into the final mechanical design of the lens.

The 2-dimensional layout of the electrostatic grid lens including the acceleration grids, the lens mounting pads as well as the MCP surface created with Garfield is illustrated in Fig. 4.20(a). The three rings of the lens are approximated by a row of wires of a diameter of 1 mm with no distance between them. The optical axis of the lens is highlighted as red dotted line at y = -3.5 cm. Figure 4.20(b) illustrates the electrostatic field created by the lens (green equipotential lines). The acceleration grid, the side grids as well as the MCP are set to a potential of -1810 V, thus allowing
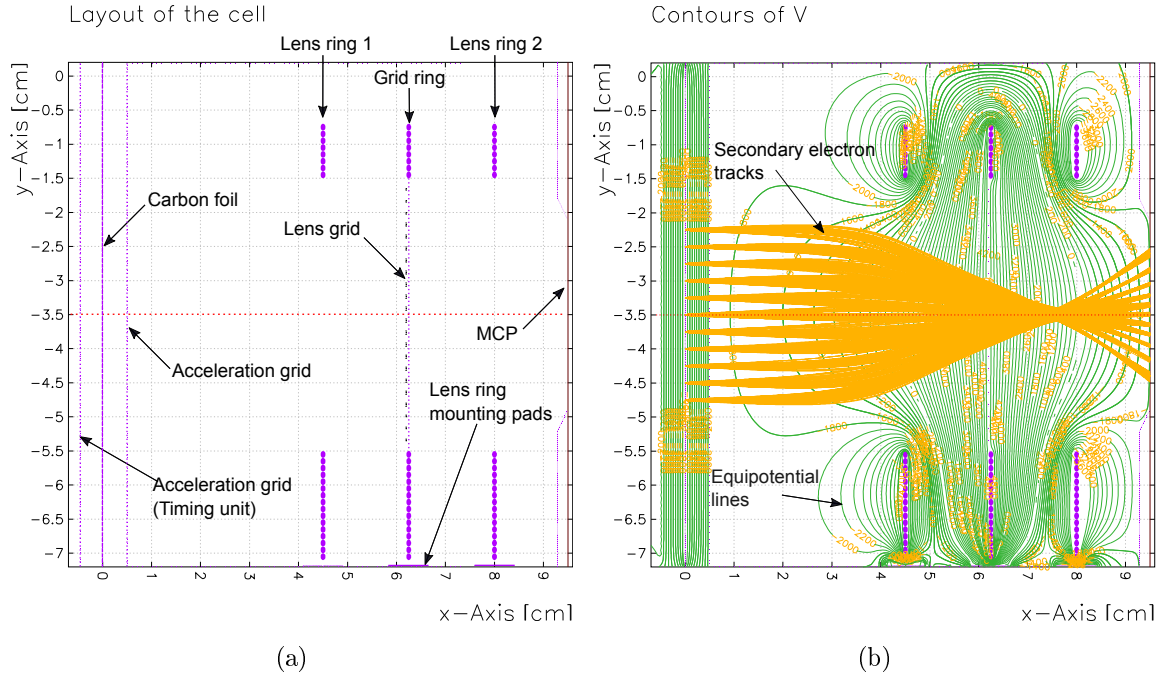
Figure 4.20: *(a): Layout of the drift area created with the program Garfield: The 2-dimensional simulation of the electrostatic lens is used to estimate the optical aberrations caused by the acceleration- and the lens grid. (b): Electric field- and drift simulation: The equipotential lines (green) visualize the electrostatic field created by the lens as well as by the acceleration grids (see text for potential values). Secondary electron tracks (orange lines) are simulated starting at several points of origin on the carbon foil, which are consecutively spaced apart by 2.5 mm. The furthest starting points are located at a distance of 12.5 mm from the optical axis (red dotted line).*

the inner field to be formed by the grid lens exclusively, with a potential of $+5000\,\mathrm{V}$ set to the lens grid and -4250 V to both lens rings. Also illustrated in Fig. 4.20(b) are secondary electron trajectories (orange lines) starting at different points of origin on the carbon foil. They are equally spaced apart by 2.5 mm. The most outer starting points are located at a distance of 12.5 mm from the optical axis. The secondary electron trajectories expand due to their momentum distribution, but they are focused by the grid lens onto the channel plate surface. In case of an image scale of 1:1, the entire active area of the channel plate would be illuminated, however, in order to clear space for the recoil ions to pass through the detector and thereby through the optical tube, the grid lens is not centered within the optical tube. Thus, an image scale of $\approx 1{:}0.75$ is obtained. The simulated position resolutions are presented in dependence of the voltage configuration for several secondary electron emission distances on the carbon foil in Fig. 4.21. The mechanical dimensions of the entire grid lens used for
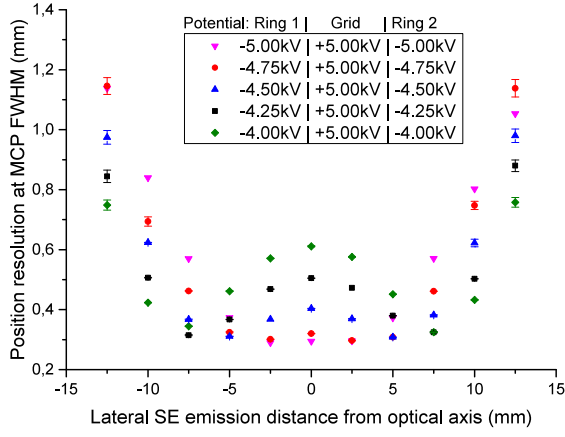
Figure 4.21: *Position resolution obtained by the 2-dimensional simulation: The voltage configuration at which the lens rings 1 & 2 are set at -4250 V offers the best overall position resolution for all simulated SE emission centers on the carbon foil.*

Dimension	(mm)
Lens ring OD	56
Lens ring ID	40
Lens ring thickness	1
Distance between rings	17.5
Distance carbon foil to accel. grids	5
Distance accel. grid to first lens ring	40
Wire ⌀ acceleration grid	0.035
Wire ⌀ lens grid	0.022

Table 4.2: *Critical dimensions and potential values used for the 2-dimensional simulation of the electrostatic grid lens.*

the simulation are found in Table 4.2. With the lens grid set at $+5000\,\mathrm{V}$, an increase of the negative potential of the lens rings $1\,\&\,2$ causes the lens to focus close to the optical axis. An achievable position resolution of $< 0.4\,\mathrm{mm}$ (FWHM) is indicated for SE emission centers distanced by $\pm 5\,\mathrm{mm}$ from the optical axis. SE emission centers located further away from the optical axis show a strong decrease in position resolution due to lens aberrations. However, a decrease of the negative potential applied to the lens rings $1\,\&\,2$ allows to shift the parable towards the surface plane of the micro channel plate. This gives the possibility to adjust for a best overall position resolution of $< 0.6\,\mathrm{mm}$ for SE emission centers located within $\pm 10\,\mathrm{mm}$ from the optical axis, which is achieved by a voltage configuration, at which the grid potential is set at $+5000\,\mathrm{V}$ and the lens rings $1\,\&\,2$ to -4250 V. For this particular voltage

(a)　　　　　　　　　　　　　　(b)
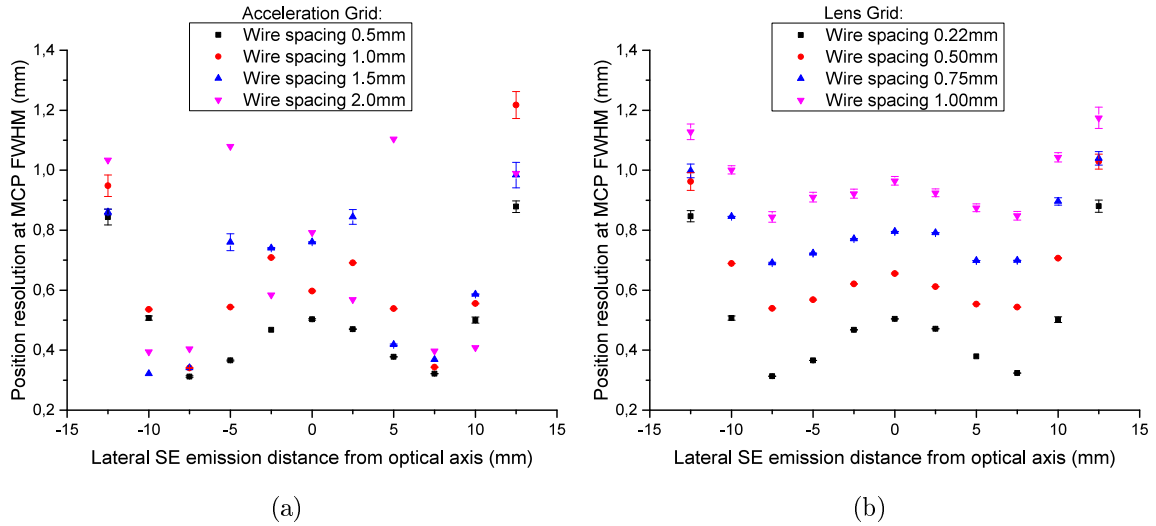
Figure 4.22: *(a): Acceleration grid wire spacings $> 0.5\,\mathrm{mm}$ strongly decrease the achievable position resolution (lens grid set to $0.22\,\mathrm{mm}$). Spacings $< 0.5\,\mathrm{mm}$ are avoided due to the loss of electron transparency of the grid. (b): With the spacing of the acceleration grid set to $0.5\,\mathrm{mm}$, values of the lens grid $> 0.22\,\mathrm{mm}$ decrease the achievable position resolution considerably. A total SE transmission from the carbon foil to the MCP surface of $88\,\%$ is obtained at a wire spacing of $0.5\,\mathrm{mm}$ for the acceleration grid and $0.22\,\mathrm{mm}$ for the lens grid.*

configuration further simulations are carried out in order to determine the influence of the grid wire spacings at a wire diameter of $22\,\mu\mathrm{m}$. The results are illustrated in Fig. 4.22(a): Different wire spacings of the secondary electron acceleration grid show a huge impact on the injection conditions into the lens volume and thereby on the obtainable position resolution. At a fixed wire spacing of the lens grid of $0.22\,\mathrm{mm}$, spacings of the acceleration grid larger than $0.5\,\mathrm{mm}$ cause to worsen the position resolution considerably. This originates from an increasing but weak "lens effect"

between the wires, occurring at an increasing wire distance [74]. Wire distances below 0.5 mm are in general avoided due to the loss of optical transparency ($< 95\,\%$) for secondary electrons emitted from the carbon foil. The influence of the wire spacing of the lens grid on the position resolution is illustrated in Fig. 4.22(b). Here, larger wire spacings also considerably worsen the position resolution. The lens grid ideally represents a constant plane of localized charge within the altered Einzel lens design, but larger wire spacings cause more irregularity and "weakness" of this virtual plane, which results in a more blurred image as well as a loss of refractive power.

The best simulated overall position resolution of < 0.6 mm, at an electron transmission of 88 %, is achieved at a wire spacing of 0.5 mm for the acceleration grid and 0.22 mm for the lens grid.

• Potentials applied to the lens

The 2-dimensional simulations presented previously were used to study the grid effects within the lens design, however, in order to determine the final potential values to be applied for optimal SE focusing 3-dimensional simulations are carried out:

The simulation program COMSOL Multiphysics® [77] is used to calculate a 3-dimensional electrostatic finite element field map for a given geometry at specified potentials. This field map is then imported into the Garfield code to carry out drift calculations taking the secondary electron momentum distribution into account (see Fig. 4.18). A similar approach using a finite element field map, which is then imported into the Garfield code for drift calculation can be found in [82]. However, the secondary electron momentum distribution used for the 2-dimensional simulations has to be modified by the addition of a rotational angle within the y-z-plane (carbon foil plane, see Fig. 4.23). This angle is randomly chosen for each event from a uniform distribution within a range of 0°-360° resulting, in combination with the cosine distribution within the x-z-plane, in a 3-dimensional SE emission cone.

For the creation of the 3-dimensional field map, a simplified CAD model of the lens is created and imported into COMSOL for a subsequent meshing process. The thin grid wires of the acceleration- and the lens grid, however, are replaced by virtual potential planes. Figure 4.23 illustrates the CAD model imported into COMSOL with its two lens rings, the grid ring and the appropriate virtual potential planes (carbon foil, acceleration grid and MCP surface plane). Highlighted are also two planes with their line of intersection being the optical axis of the grid lens. Within these planes an extraction of the finite element mesh is shown exemplarily. The potential values, in this case are set to +6000 V for the lens grid, -5450 V for the lens rings 1 & 2,

-4010 V for the carbon foil and -1810 V for surrounding faces. These faces include the acceleration grid and the MCP surface. The potential values are highlighted within the mesh according to the displayed color scale. The geometric properties of the model are listed in Table 4.2. In order to simulate an image created by the lens, a
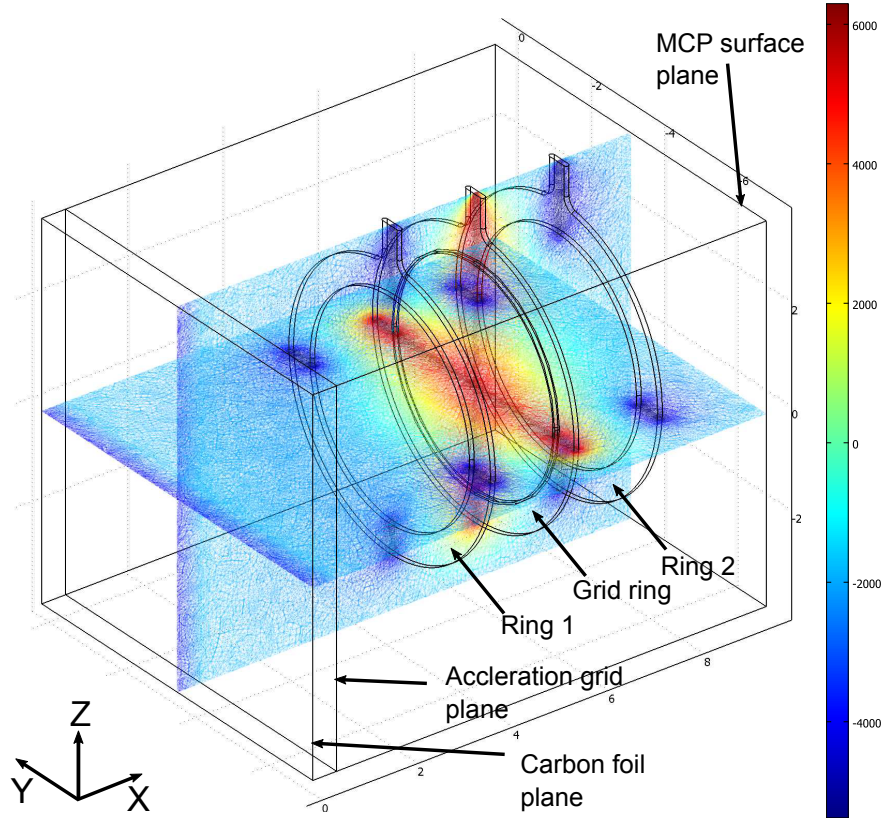
Figure 4.23: *3-dimensional field calculation using the finite element method (FEM): A simplified CAD model of the grid lens including the carbon foil, the acceleration grid and the MCP surface is imported into COMOSOL for the creation of a finite element field map. This map is subsequently imported into the program code Garfield to perform electron drift calculations. Two planes are illustrated, which exemplary show an extraction of the electrostatic finite element field map. Their line of intersection corresponds to the optical axis of the lens. Potential values are highlighted according to the color scale.*

secondary electron emission pattern is established on the carbon foil (see Fig. 4.24(a)). The pattern consists of emission centers along the y-axis spaced apart by 2.5 mm, as well as of an array within the fourth quadrant of the coordinate system, in which the optical axis (x-axis) is located at z = 0 mm and y = -35 mm. Starting from every

emission center 500 secondary electron trajectories within the 3-dimensional field map are calculated and their spatial end-coordinates on the MCP plane as well as their drift time are recorded. The data is then imported into ROOT for subsequent analysis [83].

Figure 4.24(a) illustrates the end-coordinate data obtained at the MCP surface plane. The array is imaged from the fourth quadrant into the second as to be expected by the grid lens design. The evaluated position resolutions for the 13 SE emission centers located on the y-axis ($z = 0$ mm) are shown in Fig. 4.24(b): In comparison to the 2D simulations, an equal behavior regarding the distribution of the focal points (parabolic function) for the emission centers is observed. With an increasing distance of the emission centers from the optical axis the position resolution decreases. By increasing the negative voltage of the outer lens rings 1 & 2, one can optimize the achieved position resolution for secondary electron emission centers on the carbon foil located close to the optical axis. This allows to adapt in case of a smaller required solid angle of detection of the detector.

The simulations indicate an achievable position resolution of ≤ 0.6 mm (FWHM) over a range of 25 mm on the carbon foil with the lens grid set to +6.00 kV and the lens rings 1 & 2 set to -5.45 kV. An increase of negative potential of the lens rings to -6.00 kV allows to reach a position resolution of < 0.4 mm (FWHM) over a range of 10 mm on the carbon foil.

The obtained image of the emission center array also gives an impression of the occurring lens aberrations: A radial "pincushion distortion" is observed due to an increasing magnification factor with distance from the optical axis. This aberration is typical for Einzel lens design types [74, 84]. However, such distortions can be software corrected, as demonstrated in section 4.2.6.

(a)

(b)
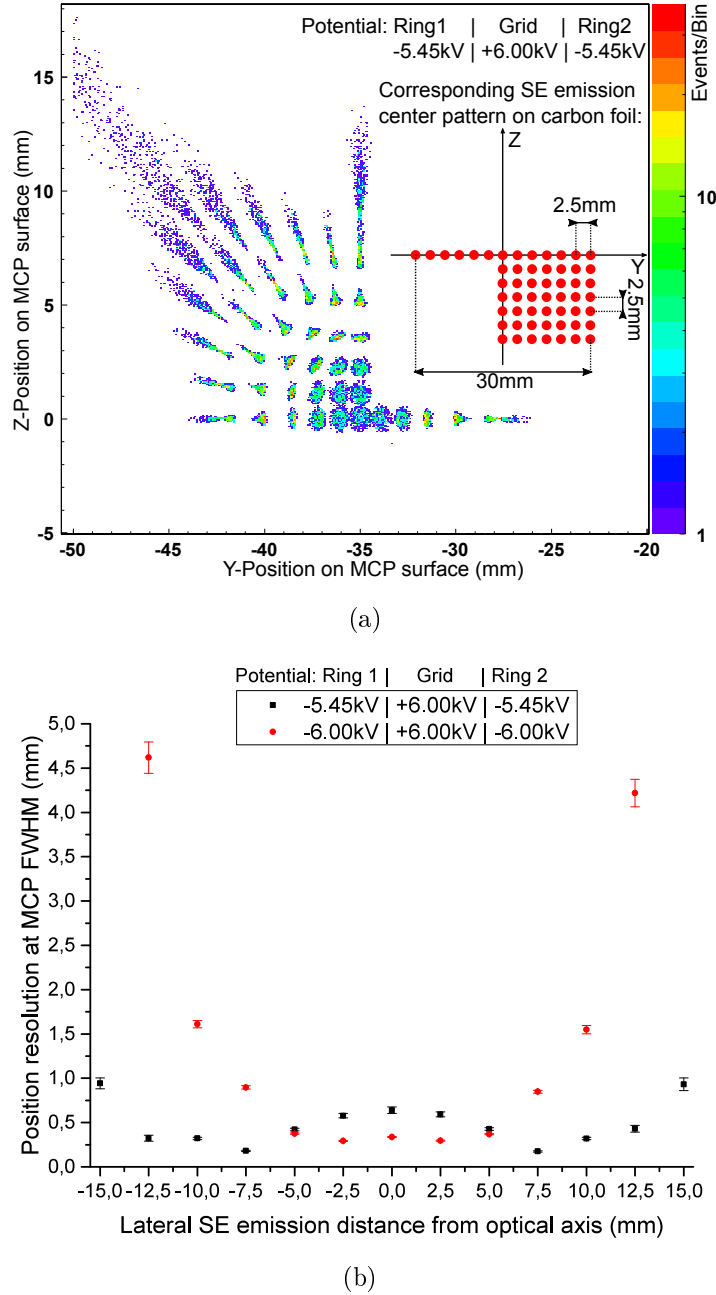
Figure 4.24: *3-dimensional simulation of the grid lens.* **(a)***: The histogram shows the position data obtained at the MCP surface for a pattern of SE emission centers located on the carbon foil. The pattern (red dots) consists of emission centers along the y-axis at $z = 0\,mm$ and of an array within the fourth quadrant. The array is projected into the second quadrant of the coordinate systems by the grid lens (optical axis at $z = 0\,mm$ and $y = -35\,mm$). Lens aberrations cause a "pincushion distortion".* **(b)***: The obtained position resolution for the 13 SE emission centers located along the y-axis: An achievable position resolution of $< 0.6\,mm$ (FWHM) over a range of 25 mm on the carbon foil is indicated by the simulations. An increase of the negative potential applied to the lens rings 1 & 2 allows to obtain a position resolution $< 0.5\,mm$ (FWHM) over a range of 10 mm on the carbon foil according to the simulations.*

● **Time characteristics of the lens**

Within the detector design, the electrostatic lens is mainly intended for the position determination of recoil ions but a time measurement could be carried out by it as well. However, the grid lens affects the time resolution due to different electron path
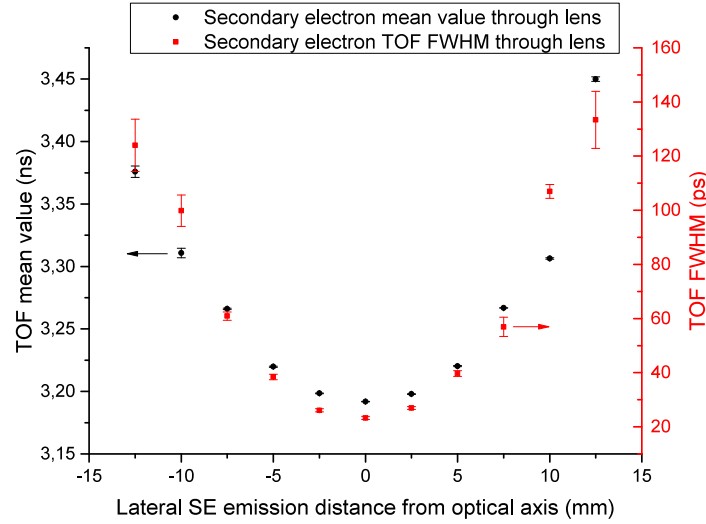
Figure 4.25: *Simulated time characteristics of the lens: The difference in secondary electron TOF mean values through the lens could be corrected using the position information. The contribution to the time resolution depends on the SE emitting position on the carbon foil with a maximum of $\approx$ 144 ps. Potentials applied to the lens are -5450 V to lens ring 1 & 2 and +6000 V to the grid ring.*

lengths and their variations within the lens volume in dependence on the location of SE emission on the carbon foil. Figure 4.25 presents the time characteristics of the lens obtained by the 3-dimensional simulation of 11 secondary electron emission centers along the y-axis at $z = 0$ mm, according to the potential values and coordinate system illustrated in Fig. 4.24(a). The simulated TOF mean values are within a range of $3.19 - 3.38$ ns for secondary electron emission centers distanced from the optical axis by a range of $0 - 12.5$ mm. These differences in TOF mean values are caused by the different flight path lengths through the lens, which could be software corrected using the determined position of each corresponding event. However, the time spread (TOF FWHM) caused by the path length variations per emission location due to the secondary electron momentum distribution also increases with the distance from the optical axis. A simulated maximum value of 144 ps (FWHM) is calculated for secondary electrons emitted by a distance of 12.5 mm from the optical axis. This time spread can not be corrected.

• Mechanical implementation of the lens

The electrostatic grid lens is entirely integrated into the top cover of the position unit. This allows for an exact positioning between the acceleration grid and the surface of the first micro channel plate. The lens rings, fabricated from 1.0 mm thick stainless steel (1.4435), are held by PEEK insulators within the top cover as illustrated in Fig. 4.26. Each lens ring is fixated vertically by a PEEK alignment pin within the insulator part. Horizontal alignment and the distance between the rings (17.5 mm) are given by precision milled slots within the top cover, which accept the PEEK insulator parts, each holding one lens ring. The grid lens ring is covered by gold coated tungsten wires (25 μm in diameter) in horizontal direction (scattering plane) with a wire pitch of 0.25 mm[5]. The surface, as well as the edges of all lens rings are polished in order to avoid any possible field emission effects or accidental discharges caused by the potential differences of 12 kV (at maximum) between the rings. Mechanical deviations with respect to a repeated assembly and disassembly of the lens, are determined to be $< 160\,\mu$m utilizing a CNC controlled 3D coordinate measuring machine (Wenzel LH 108). Figure 4.27 schematically illustrates the electrostatic lens being integrated into
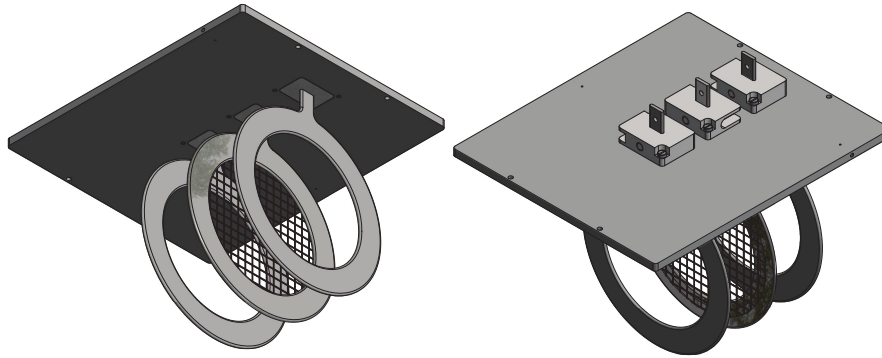
Figure 4.26: *Mechanical design of the electrostatic grid lens: The lens is part of the top cover of the position unit. Each lens ring is mechanically aligned by an insulation part made of PEEK (illustrated grids are not of true shape and scale).*

the position unit of the detector. The recoil ions exit the detector through a large grid (wires orientated within scattering plane, wire diameter 35 μm, 1 mm pitch), which is part of the optical tube. The carbon foil (4 μg/cm^2) is supported by a laser cut grid (96 % transparency) and hosted by a separate frame, which is centered between the acceleration grid of both units. A photograph of the fully assembled detector is shown in Fig. 4.28(a): The three lens rings, as well as the surface of the first micro channel

---

[5] The manufacturing process of the grid limits the distance between wires to be 0.25 mm. Simulations regarding the wire deflections, however, consider a wire pitch of 0.22 mm.
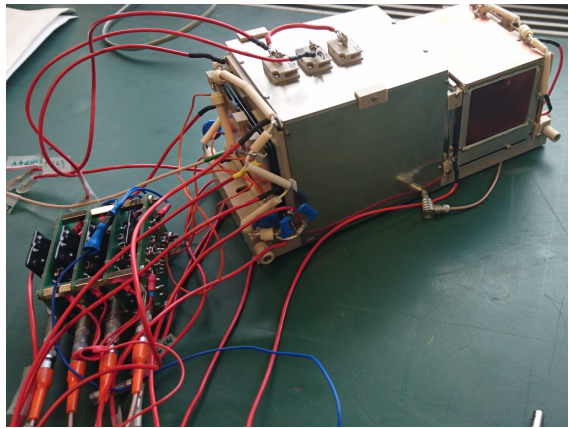
plate, are visible through the large exit grid. Figure 4.28(b) shows the opposite side of the detector, at which the recoil ions enter through the grid of the timing unit. The four preamplifiers (Cremat CR-111), used to readout the 2-dimensional Backgammon anode, are mounted on custom made power supply boards and are also contained within the vacuum.
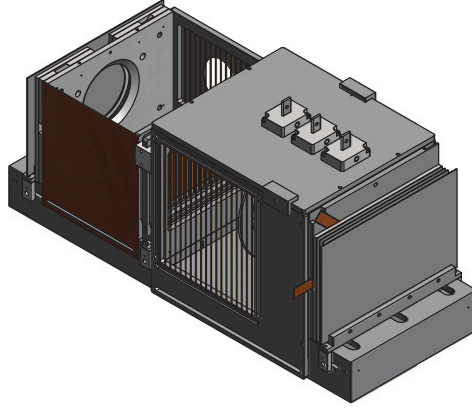
Figure 4.27: *Schematical illustration of the TOF detector: The electrostatic grid lens is part of the top cover of the position unit. Recoil ions exit the detector through a grid, which is part of the optical tube (illustrated grids are not of true scale and orientation, top cover of the timing unit is not shown).*
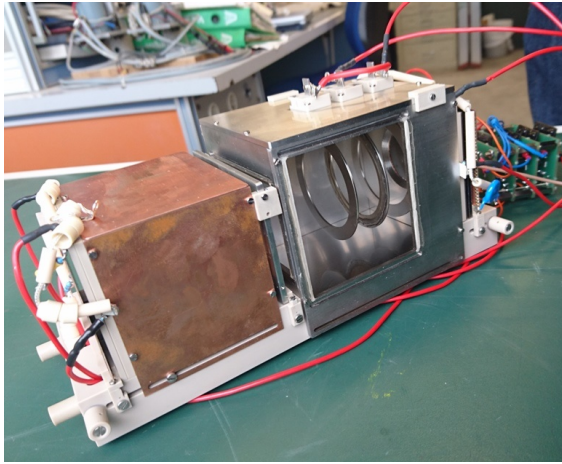
(a)   (b)

Figure 4.28: *(a): Fully assembled TOF detector: The rings of the electrostatic grid lens as well as the surface of the first micro channel plate are visible through the exit grid of the detector. (b): The recoil ions enter through the grid of the timing unit. The preamplifier of the 2-dimensional Backgammon anode (lower left side), mounted on custom made power supply boards are also contained within the vacuum.*

4.2.6 Intrinsic position resolution with the use of the electro-static lens

For the determination of the achievable position resolution using the electrostatic lens, an altered version of the final detector setup, as schematically illustrated in Fig. 4.29 is utilized: Here, the readout anode of the timing unit is replaced by a second 2-dimensional Backgammon anode. This allows for a comparison of an image created with- and without the use of the grid lens. In order to define a secondary electron starting point pattern, a laser cut stainless steel mask with 11×11 holes (2.5 mm pitch) with a diameter of 0.5 mm is covered by a $4\,\mu g/cm^2$ carbon foil. Alpha
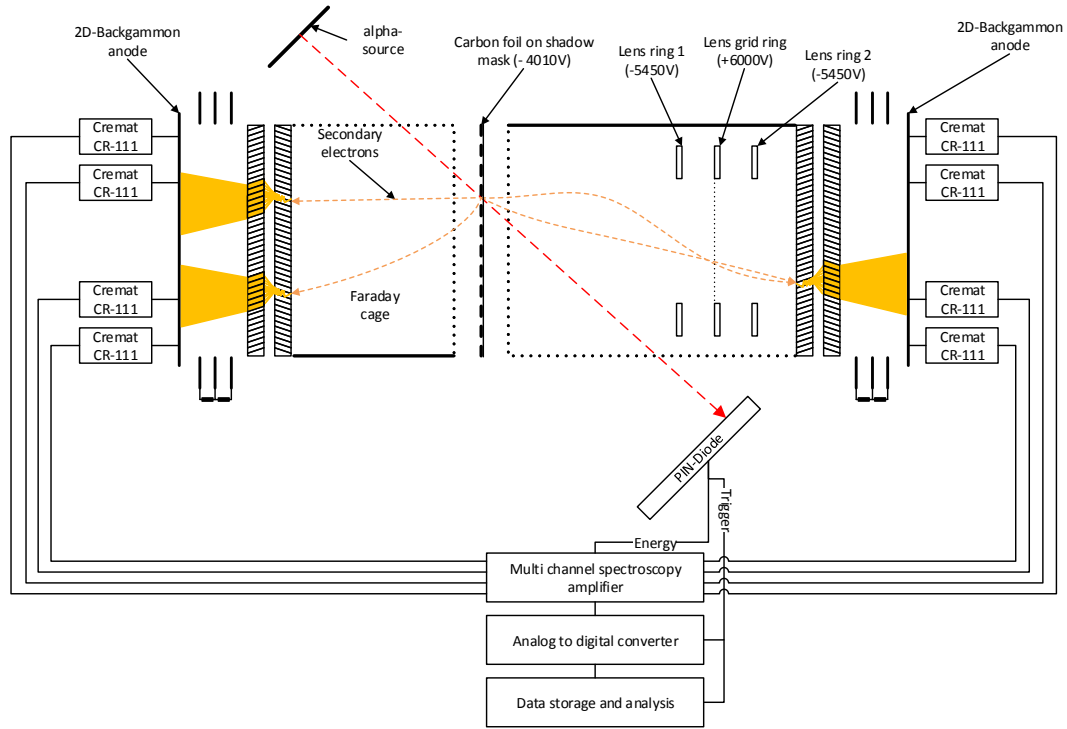
Figure 4.29: *Determination of the position resolution utilizing the electrostatic grid lens: In this detector setup, the readout anode of the timing unit is replaced by a second 2-dimensional Backgammon anode (see text for explanation). Alpha particles create secondary electron images in forward- and backward direction on penetration of a $4\,\mu g/cm^2$ carbon foil, which covers a shadow mask. A silicon PIN diode detects the alpha particles passing the mask and creates a trigger for data acquisition.*

particles create secondary electrons in forward- and backward direction on penetration of the carbon foil covered holes that are subsequently detected by a silicon PIN diode behind the detector. Thus, an detection efficiency independent trigger is created. Figure 4.30(a) illustrates the obtained secondary electron image (forward emission

direction) of the mask utilizing the electrostatic lens. Potentials are applied according to the values given by Fig. 4.29. An increase in statistics from left to right is caused by the solid angle of detection not being optimized for the alpha test setup geometry. Lens aberrations can clearly be observed, which result in a "pincushion" distortion as previously predicted by the 3-dimensional simulations (see Fig. 4.24(a)).   A software

(a)   (b)
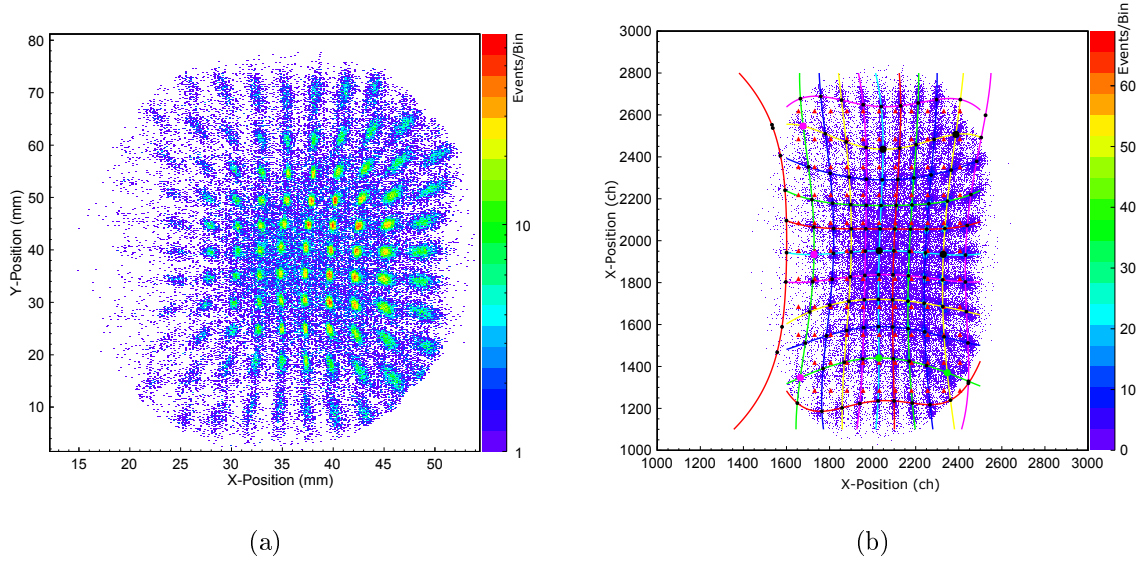
Figure 4.30: *(a)*: *Secondary electron image of a mask with 11×11 holes of a diameter of 0.5 mm (2.5 mm pitch), which are covered by a $4\,\mu g/cm^2$ carbon foil using the electrostatic lens. Lens aberrations lead to a "pincushion" distortion. The increase in statistics from left to right is caused by the solid angle of the detector not being adapted to the alpha test geometry (see Fig. 4.29).* **(b)**: *Software distortion correction: 6 th order polynomials are fitted to the measured raw data for creation of the distorted grid. A comparison between the true grid positions (red triangles) and the distorted (black dots) allows to obtain the required correction coefficients. The distortion corrected image is illustrated in Fig. 4.31(a).*

correction method is utilized to correct this distortion: The procedure uses 6th order polynomials (11 functions for x- and y-direction, respectively) in order to create the distorted grid according to the measured position of the holes, as illustrated in Fig. 4.30(b) (black dots). A comparison between the true grid positions (red triangles in Fig. 4.30(b)) and the distorted ones allows to create a look-up table containing the appropriate correction coefficients for the entire image area.   These can then be applied to any measured image for numerical rectification.   The corrected and calibrated secondary electron image of the mask is shown in Fig. 4.31(a) (optical axis
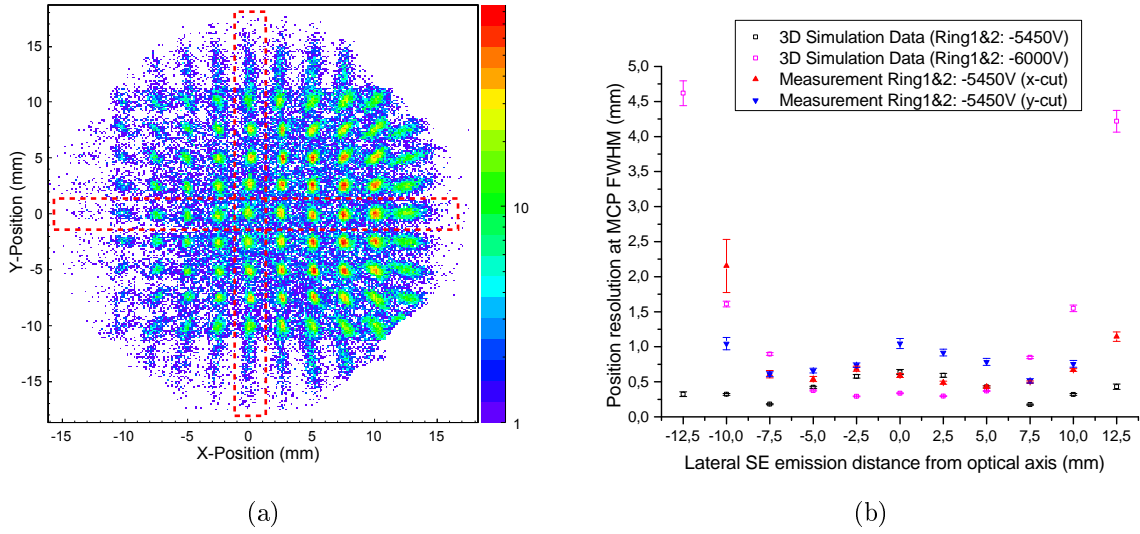
Figure 4.31: *(a): Distortion corrected secondary electron image of the mask: Voltages applied to the lens rings 1 & 2 are -5450 V. The grid ring is set at +6000 V. The lens aberrations lead to a radial decrease of the position resolution. (b): Position data of the two cuts (red dotted lines in Fig. 4.31(a)): A position resolution within the scattering plane (x-cut) of < 0.6 mm (FWHM) is achieved over a width of > 15 mm on the carbon foil (for discussion see text).*

and center of the image at $x = 0$ mm and $y = 0$ mm). The position data of two cuts, one in x-direction and one in y-direction (red dotted lines) as well as the simulation results for two lens potential configurations are given in Fig. 4.31(b).

An average position resolution (data x-cut) of < 0.6 mm (FWHM) is achieved over a width of > 15 mm on the carbon foil within the scattering plane. An obtained position resolution of < 0.75 mm (FWHM) over a range of 20 mm on the carbon foil within the scattering plane satisfies the requirement of 0.8 mm for the entire required solid angle of detection (see section 4.1).

The impact on the achievable position resolution with the electrostatic lens is confirmed by a comparison between an image obtained for secondary electrons emitted in backward direction without the lens and in forward emission direction utilizing the lens (shadow mask dimensions given in Fig 4.32(a)). The images obtained simultaneously for both emission directions are illustrated in Fig. 4.32.

In general, the 3-dimensional simulations are in good agreement with the measured position resolution values and do reproduce the general grid lens behavior. However, the 3-dimensional simulations do not consider the impact of the grid wire deflections

on the position resolution, which leads to the discrepancy compared to the measured values. The difference in position resolution between the x- and y-direction can also be explained by the grid wire influence: The grid wires of the secondary electron acceleration grid as well as of the lens grid are orientated parallel to the scattering plane in order to minimize the deflection effects on the position measurement in x-direction. Thus, the position resolution obtained in y-direction is slightly worse.

Further discrepancies between the measured and simulated values can also be accredited to the secondary electron distribution: As described in section 4.2.5 and illustrated in Fig. 4.17(a), the SE momentum distribution strongly relies on the surface

(a)   (b)
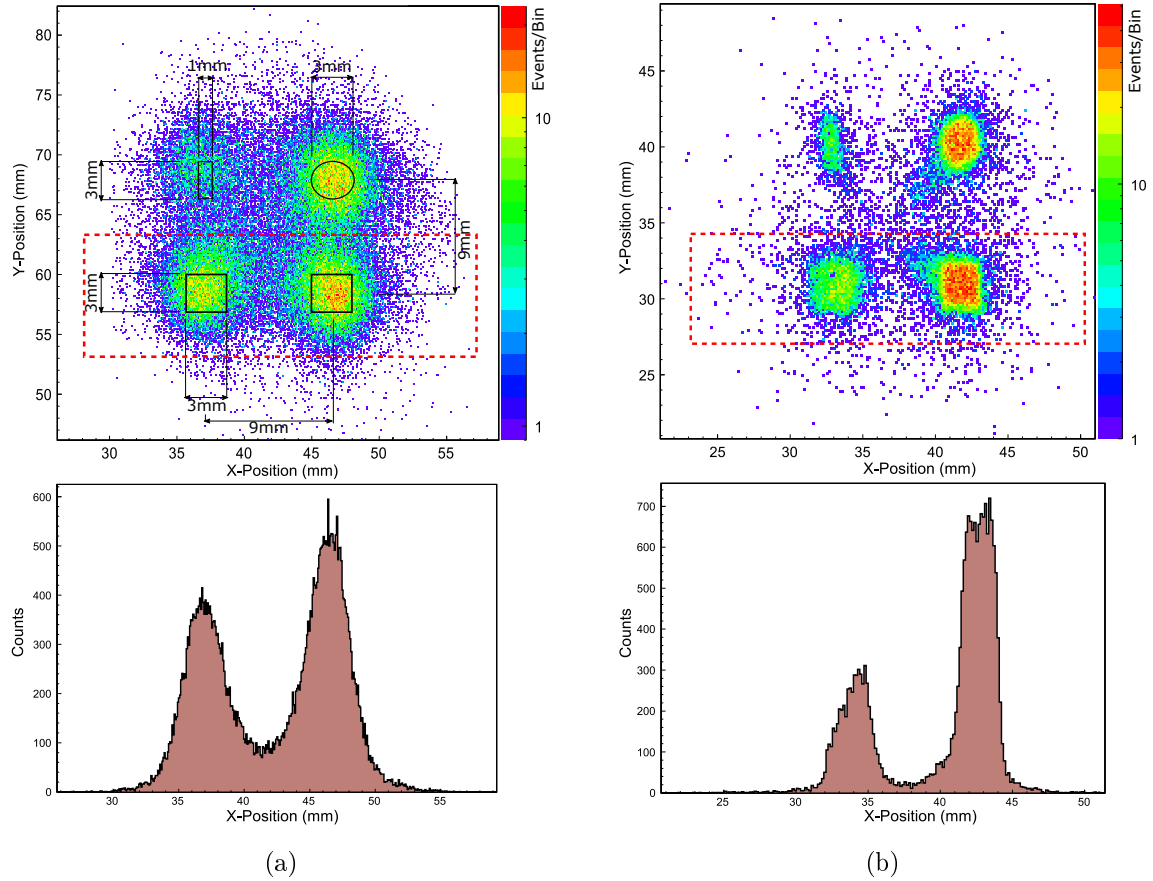
Figure 4.32: *(a): Secondary electron image (backward direction) of a carbon foil covered mask (solid black lines) without the use of the electrostatic lens (see Fig. 4.29 for experimental setup). The projection of the lower two squares (red dashed lines) shows a position resolution of 5.4 mm (FWHM) (b): Image obtained simultaneously for forward emitted secondary electrons with the electrostatic lens being active. The position resolution is improved by one order of magnitude. The increase in statistics from left to right is caused by the solid angle of the detector not being adapted to the alpha test geometry.*

properties of the carbon foil. Since the exact surface properties of the used carbon foil are unknown, the used SE momentum distribution might deviate from the true one. In addition to that, the secondary electrons emitted in forward direction show higher kinetic energies than the ones in backward emission direction (see Fig. 4.17(b). Thus, even a better position resolution can be expected utilizing the electrostatic grid lens with backward emitted electrons. However, in case of the TOF-E setup installed at the Q3D magnetic spectrograph, space constraints do only allow to use the grid lens for secondary electrons emitted in forward direction.

4.3   Stop Timing Detector (T$_2$)

The stop timing detector of the TOF-E setup follows the design introduced by Busch et al. [53] (see Fig. 4.3) and was originally built by A. Kern [52]. However, it was completely revised in this work in order to accommodate for the total angle of detection of the TOF-E setup of $\approx 0.3\,\mathrm{msr}$ (see section 4.1) and for an optimal time signal output. A schematic drawing of the revised stop detector including the potential values as well as the time readout configuration is given in Fig. 4.33.

For secondary electron amplification, micro channel plates with an outer diameter of 88 mm, a channel diameter of 21 μm (bias angle = 6°) and an active area of 80 mm are utilized. All grids are made of gold coated tungsten wires (35 μm in diameter) using a wire to wire distance of 1 mm. The distance between the acceleration grids and the carbon foil is 5 mm, which equals the distance between the inner- and outer mirror grid. The $4\,\mu\mathrm{g/cm^2}$ thick DLC carbon foil with a size of 40 mm × 40 mm is supported by a laser cut grid, offering a geometrical transmission of 96 %.
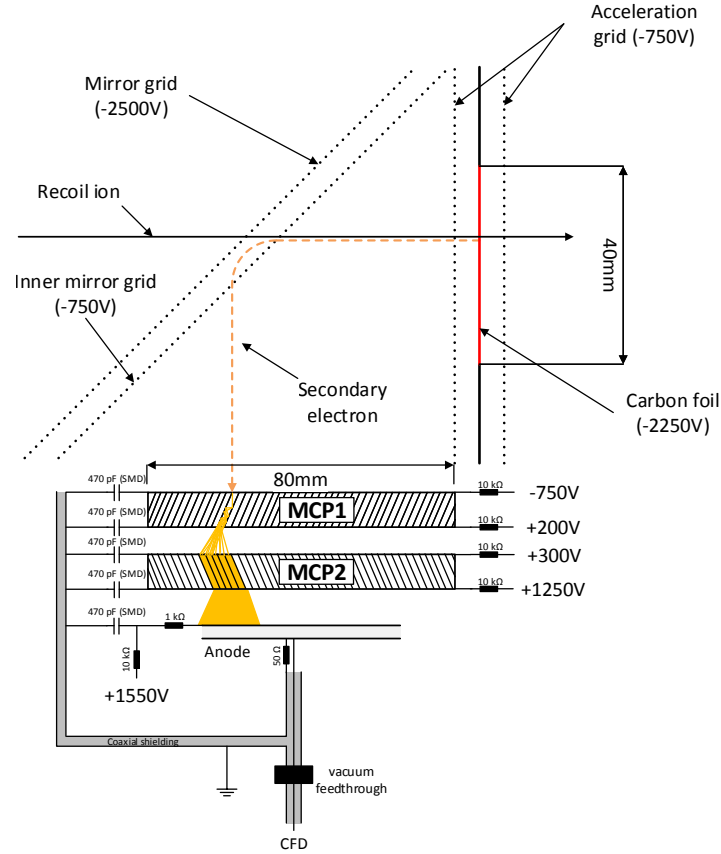
Figure 4.33: *Schematic layout, voltage configuration and time readout configuration of the stop timing detector T$_2$.*

4.4   Position sensitive energy detector

This section is dedicated to the development of an energy detector for the time of flight setup. The energy detector is required, since mass separation with the TOF-E method only becomes attainable by the simultaneous determination of the recoil ion's flight time as well as of its energy (see section 2.2.3). Both the time resolution and the energy resolution limit the obtainable mass resolution (see Eq. 2.17). One method to measure the energy of the recoil ion is to use a solid state silicon detector (PIN diode). However, at the low recoil ion energies obtained utilizing the 40 MeV ^{197}Au projectile beam (see Tab. 4.3), the energy resolution of standard silicon based detectors degrades considerably [50]. In addition to that, the silicon based detectors severely suffer from irradiation damage over time. Therefore, a gas ionization chamber (GIC) is developed as energy dispersive detector for the time of flight setup.

As explained in section 4.1, a combined TOF-ΔE-E measurement at the high recoil ion energies obtained with the 170 MeV ^{127}I projectile beam facilitates the ability to enhance the mass separation capabilities of the standard ΔE-E measurement. It also allows to apply unique filter conditions for effective background suppression to either the TOF-E or the ΔE-E spectra. Therefore, the energy detector features an added ΔE-E capability as described in section 4.4.2.

In order to apply kinematic corrections (see section 3.1), the energy detector is required to determine the position of the recoil ion. Thus, the available options of position sensitivity in the framework of the used detector design and their performance are discussed in the last section 4.4.3 of this chapter.

4.4.1   Detector Design

### • Gas ionization chamber with Frisch grid

The energy detector design is based on a transversal ionization chamber layout with a Frisch grid located between the anode and cathode. This fundamental design layout is well discussed and has been used for several decades for nuclear physics experiments, but also for elastic recoil detection setups [12, 50, 85–88]. The design is schematically illustrated in Fig. 4.34 and discussed in closer detail in the following:

Recoil ions enter the detector through an entrance window and ionize the molecules of the detection gas. The ionization chamber is used in ionization mode, thus the potentials applied to anode, cathode and Frisch grid separate the created ionization electrons from the positive charged ions without creating secondary ionization events. Therefore, the number of created secondary electrons is proportional to the energy deposited into the gas by ionization. Currents are induced on the electrodes of the

chamber by the created charge. The corresponding change in voltage V^- due to the current flow $I^-(t)$ created by the electrons, however, depends on the position x within the ionization volume [89]:

$$V^- = \frac{1}{C_0} \int_0^{t^-} I^-(t)dt = \frac{en^-}{C_0} \frac{x}{\omega^-} \; , \tag{4.6}$$

with C_0 representing the capacity of the GIC including all parasitical capacities, n^- the number of electrons and ω^- their drift velocity. The time t^- for the electrons to travel to the corresponding electrode from their point of origin ($t=0$) is given by $t^- = \frac{x}{\omega^-}$ (the induced signal ends by arrival of the charge on the readout electrode). This ambiguity between the deposited energy and the position of the ionization track is eliminated by the Frisch grid [90]. The grid is made of gold coated tungsten wires, $50\,\mu$m in wire diameter at a pitch of $1.2\,$mm. It screens the anode until the created electrons pass through it. Thus, the position x of every ionization track is "equalized" to the distance between the anode and the Frisch grid for a precise energy measurement [91].
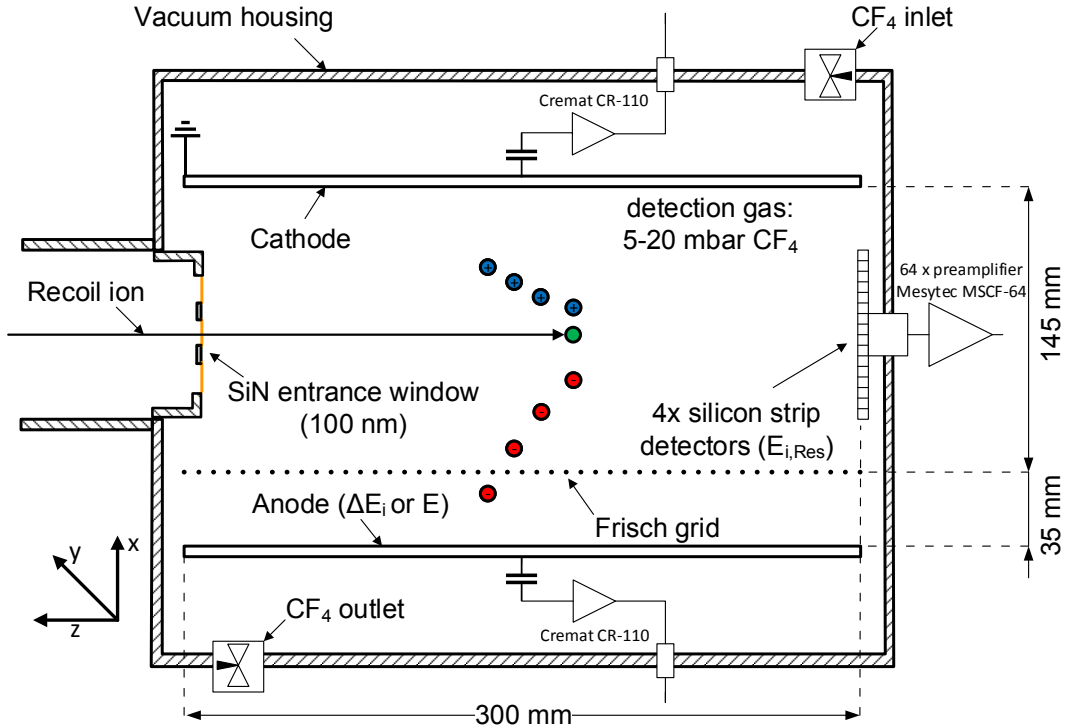
Figure 4.34: *Schematic layout of the gas ionization chamber utilized as energy detector of the TOF-E setup (see text for explanation). The scattering plane corresponds with the x-direction. Electrodes utilized for field smoothing are not illustrated.*

• Detection gas and pressure regulation

One commonly used detection gas for gas ionization chambers is isobutane (C_4H_{10}) [49, 50, 88]. However, for the energy detector of the TOF-E setup tetrafluoromethane (CF_4, 99.995 % purity) is utilized: Although, the average energy to create an electron-ion pair in isobutane is only 23 eV in contrast to CF_4 with 36 eV [92], the advantage of greater amounts of created charge (potentially higher signal amplitudes) is neglected due to an increased electron drift velocity by a factor of ≈ 2.5 and a reduced diffusion by a factor of ≈ 2 in CF_4 (see section A for discrete values).

The increased drift velocity helps to achieve greater count rate stability, reducing possible pile up effects. This is of special importance for ΔE-E measurements, in which low energetic recoil ions originating from greater sample depths, are stopped completely within the ionization volume before they reach the E_{Res} measurement (e.g. a silicon detector or the E_{Res} region in case of a divided anode). Hence, a count rate increased by a factor of ≈ 10 can be observed for the ΔE measurement other than for actual events triggering the data acquisition [56].

The decreased electron diffusion in contrast to isobutane plays a substantial role with respect to position sensitivity via a drift time measurement as discussed in closer detail section 4.4.3 of this chapter.

The gas pressure is regulated in flow-through mode by a back pressure controller (EL-PRESS, Bronkhorst$^{\circledR}$), offering an accuracy of ± 0.5 % over a range of $5 - 100$ mbar.

• Entrance window and general dimensioning

One major contribution to the achievable energy resolution is given by the entrance window, which fulfills the task to separate the gas volume from the vacuum of the beam line: The recoil ions suffer energy loss and energy straggling within the window. In order to reduce both contributions, a segmented silicon nitride entrance window with a thickness of 100 nm is utilized as suggested in [49, 50]. In contrast to e.g. a standard Mylar entrance foil, the silicon nitride windows are manufactured utilizing standard semiconductor technology. This manufacturing process leads to a very homogenous density of the SiN layer as well as to a variation in thickness over the entire window area in the range of a only few atomic layers.

The entire window has a size of 40×40 mm. Each window segment has a size of $5\,\text{mm} \times 5\,\text{mm}$. The lands between the segments are 1 mm and the center bar 5 mm in width. The window restricts the solid angle of detection of the TOF-E setup to $\Omega = 0.25$ msr at a distance of 2046 mm to the target. A photograph of the entrance

window installed in the detector housing is illustrated in Fig. 4.35.

Table 4.3 lists the surface scattering energies (maximum scattering energy) of a variety of recoil ion species obtained with the 40 MeV ^{197}Au projectile beam and with the 170 MeV ^{127}I projectile beam (further discussion in section 4.4.2) at a scattering angle of $\varphi = 40°$. In order to determine the recoil ion energy with the GIC, the particles are required to be stopped completely within the gas volume, thus depositing their entire energy into ionization events. In principle, the particle range can easily be adjusted by the detection gas pressure, however, the thin silicon nitride membranes have a limited burst pressure of ≈ 25 mbar. Therefore, a maximum gas pressure of 20 mbar to guarantee safe operation is not to be exceeded. From the corresponding particle ranges in 20 mbar CF_4, listed in Tab. 4.3 (values calculated with SRIM), an effective length of the anode, cathode and Frisch grid of 300 mm is derived for the 40 MeV ^{197}Au projectile beam. This length allows to center the average Bragg peak positions of the recoil ions approximately in the middle of the ionization volume, minimizing possible influences by the detector boundaries (e.g. field inhomogeneities in the close vicinity of the entrance window). The distance between the Frisch grid and the cathode is set to 145 mm in order to avoid any particle hit of the detector structure. The distance between the Frisch grid and anode is set to 35 mm. The anode and cathode are made of single sided, copper printed circuit boards (1.5 mm in thickness).

Recoil ion	40 MeV ^{197}Au projectile beam		170 MeV ^{127}I projectile beam	
	Energy (MeV)	Range (mm)	Energy (MeV)	Range (mm)
^{1}H	0.47	167	3.09	2840
^{12}C	5.08	165	31.48	978
^{28}Si	10.23	164	59.60	594
^{74}Ge	18.64	229	92.82	509

Table 4.3: *Recoil ion surface energies (scattering angle $\varphi = 40°$) and ranges (SRIM) in 20 mbar CF_4 of various elements utilizing the 40 MeV ^{197}Au projectile beam (TOF-E measurement), as well as the 170 MeV ^{127}I projectile beam (ΔE-E measurement).*

For field homogenization within the ionization volume, solid copper strips held by a PEEK supporting structure surround the ionization volume. The strips are connected by 100 MΩ resistors, representing an appropriate voltage divider for field smoothing between the Frisch grid and the electrodes. Figure 4.36(a) shows a photograph of the

GIC installed in its detector housing. The field smoothing structure surrounding the ionization volume is illustrated in Fig. 4.36(b).

Pre-amplification of the charge pulse is carried out by Cremat CR-110 pream-
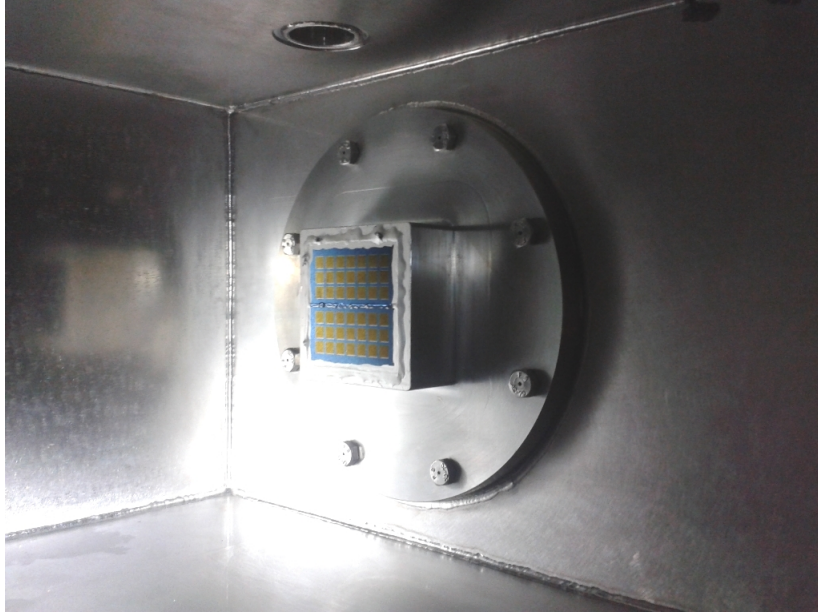

Figure 4.35: *Photograph of the segmented, 100 nm thick silicon nitride membrane (Silson Ltd) used as entrance window for the GIC. Each segment has a size of 5 mm × 5 mm. The lands between the segments are 1 mm and the center bar 5 mm in width.*

plifiers. Their power is supplied by custom made power supply boards. In order to reduce electronic noise and external pick-up, the preamplifiers are mounted directly on the backside of the electrodes (anode and cathode), thus they are located within the detector housing as illustrated in Fig. 4.36(a).

Potential applied to the anode is +660 V and +480 V to the Frisch grid. The cathode is always at ground potential.
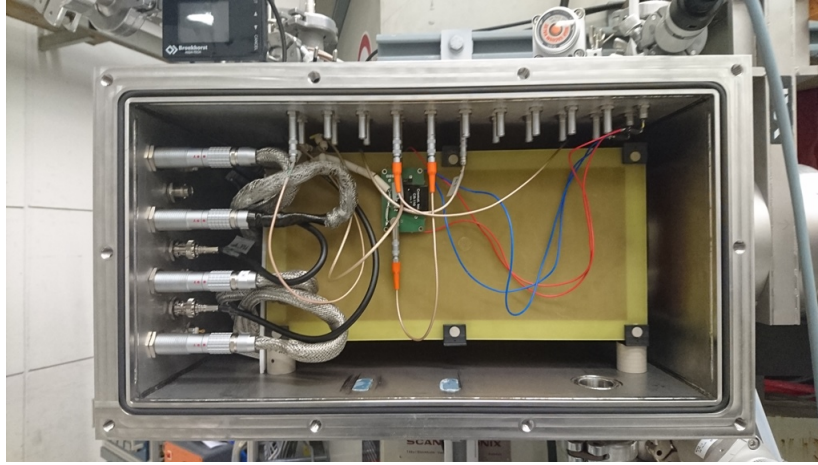
(a)
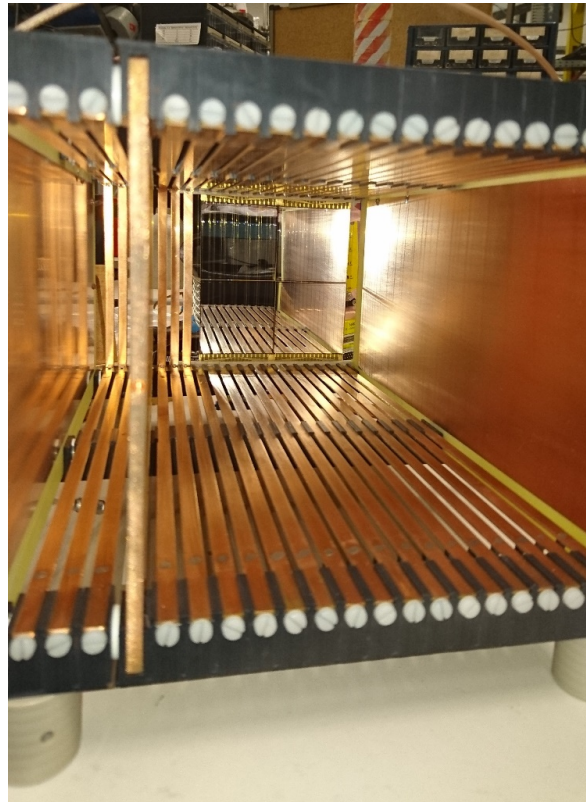
(b)

Figure 4.36: *(a)*: *GIC installed in its detector housing: The preamplifiers of the anode (green electronics board) and cathode (not visible) are directly mounted on each electrode.* *(b)*: *The ionization volume of the GIC is surrounded by a field smoothing structure, consisting of free standing copper strips (6 mm in width). For an additional ΔE-E capability, an array of four silicon strip detectors (16 strips each) is located at the end of the ionization volume.*

4.4.2 ΔE-E capability

One simple way to achieve separate energy loss (ΔE) and residual energy (E_{Res}) measurement in the framework of an ionization chamber is to divide the anode into at least two independent sections for each readout [86]. This method demands to stop the particle within the length of the gas volume, however, as mentioned previously the detection gas pressure of the energy detector is limited to 20 mbar due to the silicon nitride entrance window. As seen from table 4.3, which also outlines the calculated ranges in 20 mbar CF_4 for a variety of recoil ion energies obtained utilizing the 170 MeV ^{127}I projectile beam, the particles cannot be stopped within the detector length of 300 mm. Thus, silicon strip detectors are used for the measurement of the residual particle energy, located at the end of the ionization volume.

The silicon strip detectors (Micron Semiconductor Ltd) are single sided with 16 strips of a width of 3.1 mm (49 mm in height) in a minimum material transmission package (Design W1 2M/2M). In order to reduce energy loss- and straggling of the heavy recoil ions within the passivisation layer of the detectors, the layer is custom fabricated to a thickness of $< 0.1\,\mu$m (standard thickness $= 0.3\,\mu$m). Four silicon strip detectors are arranged to a 2×2-array at the end of the ionization volume as illustrated in Fig. 4.36(b). In order to avoid any distortions of the field within the ionization volume, the field smoothing structure is continued by wires (50 μm in diameter, two wires per field smoothing strip) located at a distance of 4 mm to the surface of the strip detectors (see Fig. 4.36(b)). Preamplification for each strip is carried out by a 64-channel preamplifier (Mesytec MSCF-64), which is located outside the detector housing.

In the ΔE-E mode, the gas pressure is reduced to 5 mbar. Potentials applied to the anode are $+410$ V and $+325$ V to the Frisch grid, respectively.

4.4.3 Position sensitivity

Multiple options for the determination of the recoil ion position within the scattering plane by the energy detector are available. These include the position determination by the anode-cathode signal height ratio, a measurement of the ionization electron drift time within the detector, as well as by the silicon strip detectors utilized for high recoil ion energy measurements. Each option is described in the following:

• **Anode-cathode signal height ratio**

The Frisch grid is used to eliminate the position dependency of the energy signal on the anode. However, the ionization electrons also induce a current on the cathode while drifting towards the Frisch grid (see Eq. 4.6). Thus, the signal acquired by the cathode still incorporates the position dependency. A comparison of both signal heights obtained for each recoil ion allows to determine the position of the ionization track within the ionization volume of the GIC. With this method a position resolution of $< 0.3\,$mm is demonstrated utilizing the compact ΔE-E detector introduced by Bergmaier et al. [12] for the recoil ion energies listed in Tab. 4.3.

However, the situation changes significantly at the low recoil ion energies obtained utilizing the 40 MeV ^{197}Au projectile beam and the large detector dimensions: Due to the low amplitudes observed at low energies, the relative difference in signal height between the anode and cathode decreases in relation to the observed signal noise. Thus, this position measurement method depends on the particle energy. In addition to that, with increasing distance to the cathode (close vicinity to the Frisch grid), the signal induced into the cathode decreases due to the smaller drift distance x within the ionization volume. This leads to a decrease in position resolution for ionization tracks close to the Frisch grid, affecting the linearity of the position measurement. A position spectrum obtained by alpha particles utilizing this method is illustrated in Fig. 4.37(a). The alpha particles are not stopped within the detection gas CF_4 at 20 mbar, however, $\approx 1\,$MeV is deposited within the gas volume. The position peaks are caused by the structure of the segmented silicon nitride window (see Fig. 4.35). Statistics shift towards position values close to the Frisch grid (lower channels) and the window segment width of 5 mm becomes unresolvable in this region. Figure 4.37(b) shows a position spectrum obtained by carbon recoil ions with an energy of 5.08 MeV, which are completely stopped within the gas volume. Utilizing a software linearity correction, a position resolution of $4.7\,$mm $\pm\,0.2\,$mm (FWHM) is observed.

(a)

(b)
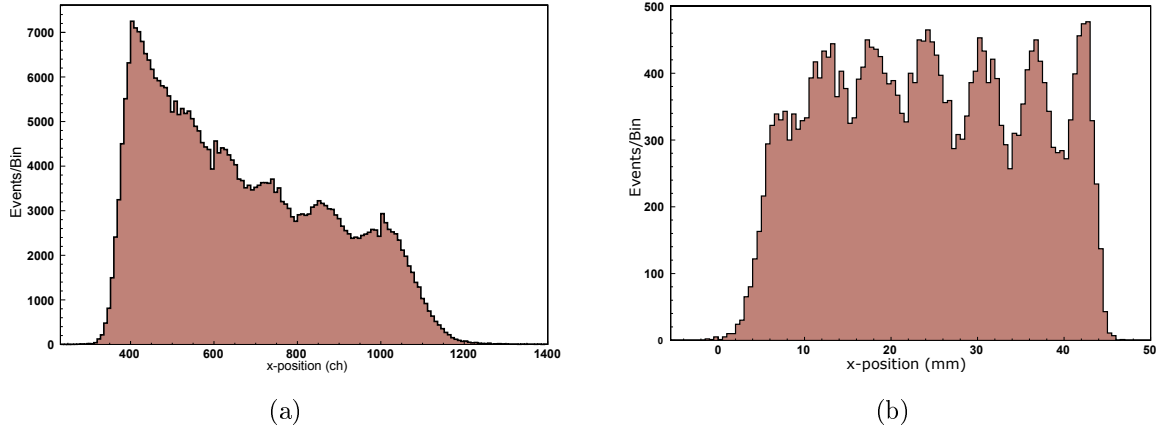
Figure 4.37: *(a): Position spectrum obtained by alpha particles (1 MeV deposited into detection gas) utilizing the anode-cathode signal height ratio: The position resolution decreases in the close vicinity of the Frisch grid (lower channel numbers), thus a strong non-linearity is observed (see text for explanation). (b): Position spectrum obtained by 5.08 MeV carbon recoil ions (completely stopped within detection gas). The spectrum is software corrected for linearity. A position resolution of 4.7 mm ± 0.2 mm (FWHM) is observed.*

(a)

(b)
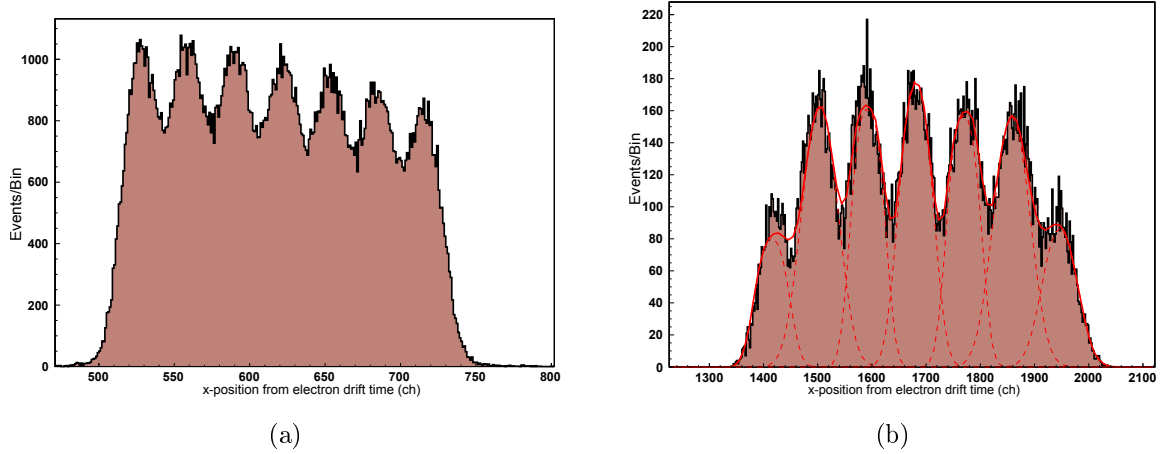
Figure 4.38: *(a): Position spectrum obtained by alpha particles (1 MeV deposited in gas) utilizing the electron drift time measurement: In contrast to the anode-cathode measurement (see Fig. 4.37(a)) the position resolution is improved and linearity is restored. The dependency of the position determination on the particle energy is vastly reduced. (b): Position spectrum obtained by 5.08 MeV carbon recoil ions utilizing the drift time measurement. An average position resolution of 2.4 mm ± 0.1 mm (FWHM) is observed.*

• Electron drift time measurement

The time for the ionization electrons to drift within the electrostatic field from their point of origin on the ionization track to the anode correlates to the position of the recoil ion within the GIC. Thus, by means of a drift time measurement a position determination can be carried out [88]. The advantage of this method lies within the fact that in contrast to the anode-cathode signal height ratio method, the dependency of the position determination on the recoil ion energy is significantly reduced (see Fig. 4.38).

This method is easy to realize in the framework of the TOF-E setup, since two timing detectors (T_1 or T_2) are available for the creation of a fast start signal to start the drift time measurement. The measurement is stopped by the preamplifier signal of the anode. At the used potentials and gas pressures (see section 4.4.1), the drift time is within $\approx 1\,\mu s$, thus, the time of flight variance of the recoil ions contributes by $\approx 2\,\%$ to the position determination if the stop detector (T_2) is utilized for start signal creation (shortest possible TOF distance to GIC entrance window).

A major contribution to the achievable accuracy is given by diffusion processes of the electrons within the gas during drift [85]. With respect to this contribution, the detection gas CF_4 resembles an optimal choice, since in contrast to e.g. isobutane the diffusion coefficients show a minimum for the used field strengths. In addition to that, the drift velocity is higher resulting in less influence per obtained diffusion length. A closer discussion of this topic is found in section A of this work.

A position spectrum acquired by drift time measurement for alpha particles, utilizing the stop timing detector for start signal creation, is shown in Fig. 4.38(a). A comparison with the spectrum obtained by the anode-cathode signal height ratio, which is illustrated in Fig. 4.37(a), demonstrates the improvement in position resolution and linearity. The energy dependency of the position measurement is vastly reduced and the peaks of the spectrum clearly correspond to the 7 segments of the silicon nitride window (see Fig. 4.35).

Figure 4.38(b) illustrates a position spectrum acquired by 5.08 MeV carbon recoil ions similar to the one recorded utilizing the anode-cathode signal height ratio method (see Fig. 4.37(b)). In order to determine the achieved position resolution, a function consisting of a convolution of a Gaussian- and a square function is fitted to the peak position data. A position resolution of $2.4\,mm \pm 0.1\,mm$ (FWHM) is achieved (inner five peaks). The decreased statistics of the first and the last peak in Fig. 4.37(b) is caused by the decreased illumination of the detector.

● Silicon strip detectors

In case of the gas ionization chamber being used for ΔE-E measurements, the recoil ions are stopped within the strips of the silicon detectors for residual energy measurement. Each strip works as a single PIN diode, offering an active width of 3.1 mm within in the scattering plane. Thus, by an individual strip readout, an inherent position resolution of 3.1 mm is given for the ionization chamber.

Although, the position determination utilizing the electron drift time method provides for a better position resolution, the strip readout offers a position determination independent of the detection efficiency of one of the timing detectors. This is an important option to consider, especially for light recoiling elements (see section 5.4).

4.5 Readout electronics

Figure 4.39 schematically illustrates the individual time detectors ($T_{1,2}$), the energy detector (E), as well as the readout electronics of the TOF-E setup. For all TOF-E and TOF-ΔE-E measurements, the main trigger for data acquisition is created by the energy detector of the setup. All channels are read out for each triggered recoil ion.

In case of pure TOF-E measurements 9 signal channels are digitized in total by a single ADC (Mesytec MADC-32). The 9 channels involve the four position signals of the 2-dimensional Backgammon anode, three individual time readouts (TOF 1 – 3), as well as the energy signal from the cathode and anode, respectively.

The actual time of flight of the recoil ion is given by TOF 3. This value is determined utilizing a start-stop inversion technique in order to reduce dead time within the detection system [93]. This dead time is mainly caused by higher count rates in T_1 than in T_2 (difference in absolute solid angle of detection). Thus, the stop timing detector is used for start signal creation of the timing measurement, and the signal created by the start detector is delayed by a fixed value T_0. Hence, the time axis of the TOF-E spectra shows the value T_0-TOF, and shorter time of flight values appear at higher channel numbers (see Fig. 2.6).

The second TOF value, TOF 2, is either used to perform an internal time readout of the position sensitive start detector (timing unit against position unit) in order to obtain certain filter conditions (see chapter 5) or to simultaneously perform a second TOF-E measurement utilizing the time signal of the position unit against T_2.

The third TOF value, TOF 1, is the drift time utilized for the position determination within the gas ionization chamber (see section 4.4.3). Here, the time signal of T_2 starts the drift time measurement while the energy signal from the anode is used to stop it. For this purpose, the preamplifier output is split and fed into two separate spectroscopy amplifiers, an Ortec Mod. 572 for energy measurement and a Silena Mod. 7614 for the timing circuit. The main trigger of the data acquisition is received from the anode signal, which is first analyzed by a single channel analyzer (SCA, Mod. ED 1100, in-house made) for discrimination. The SCA output signal is passed onto a gate generator (Phillips Scientific Mod. 794) to create an appropriate gate for the ADC readout.

The individual timing signals are processed utilizing fast constant fraction discriminators (Mod. 2228, in-house made). The CFD outputs are fed into time to amplitude converters (TAC, Ortec 566), either as start- or as stop trigger of the corresponding time measurement.

The four position signals of the 2-dimensional Backgammon anode are pre-amplified

by Cremat CR-111 preamplifiers. Main amplification is carried out by a multichannel spectroscopy amplifier (Mesytec MDS-8). Due to the fast signal creation by the micro channel plate stack, the resulting fast position signals of the Backgammon anode are delayed by $4.75\,\mu$s, utilizing four delay amplifiers (Ortec Mod. 427A) in order to shift them into the gate time length.

For TOF-ΔE-E measurements, further 64 channels are added to the readout due to the addition of the four silicon strip detectors (4×16). The individual signals of the strips are preamplified utilizing a multichannel preamplifier (Mesytec MPR-64) and passed on to four 16-channel shaping/timing filter units for main amplification (Mesytec MSCF-16). A fast coincidence module (Mod. K1200, in-house made) allows to switch the main data acquisition trigger from the anode signal (now serving for ΔE signal creation) to the silicon strip detectors. For each single-strip hit event a common trigger is created by the MSCF-16. The four common triggers are "OR-gated" by the logic of the coincidence module and a main trigger is created for each detected particle. Two additional 32-channel ADCs digitize the silicon strip signals.

The actual data acquisition is VME-bus based and involves a trigger module (GSI TRIVA) as well as a Power-PC for data readout (RIO3).
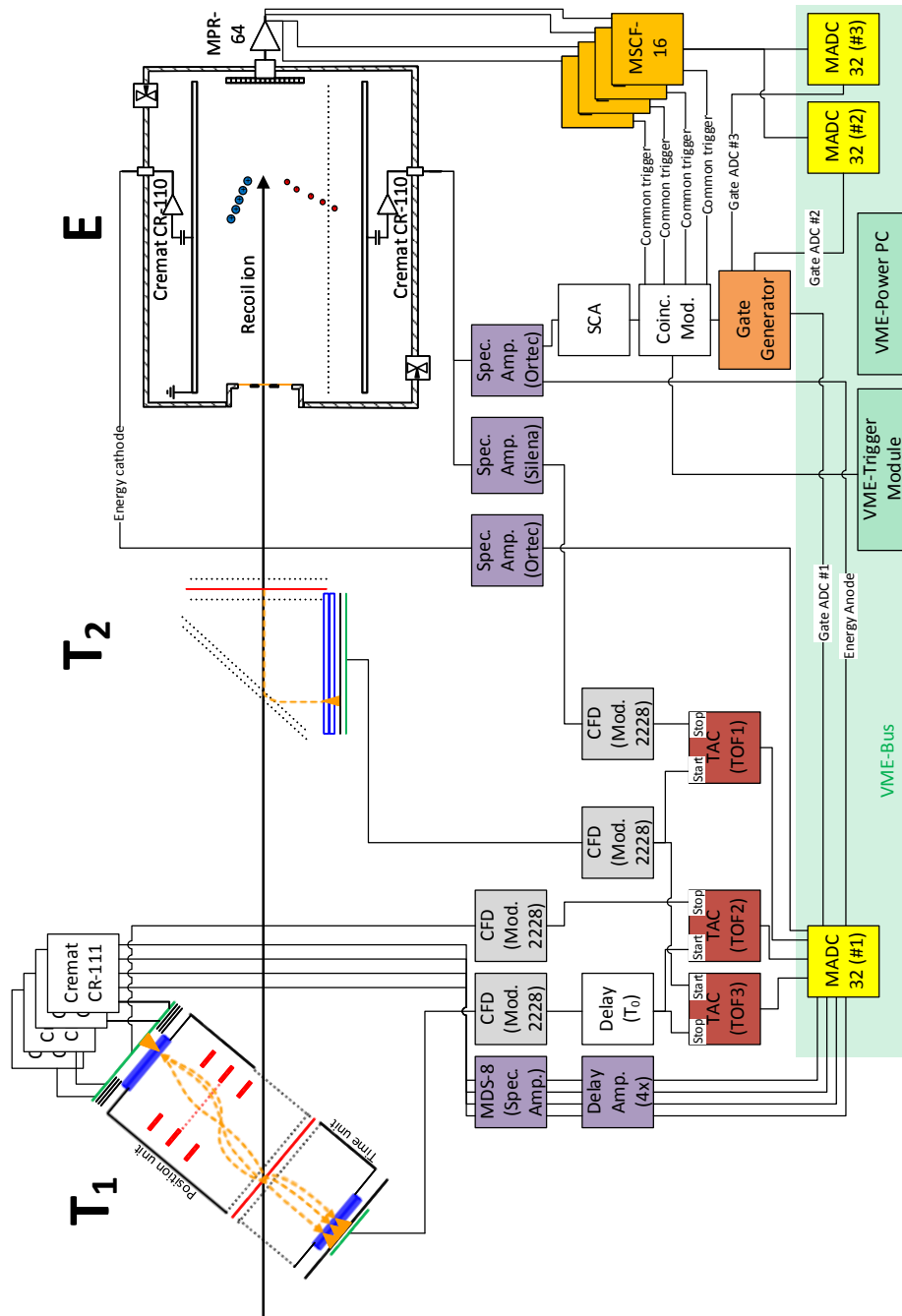
Figure 4.39: *Readout electronics of the TOF-E setup (see text for explanation).*

Chapter 5

Characterization of the TOF-E spectrometer

The previous chapter 4 outlined the development of the time of flight – energy setup, with focus on the position sensitivity of the start timing- and the energy detector. In section 5.1 of the present chapter, first the application of kinematic corrections granted by the various options of position determination is demonstrated. In section 5.2, the energy- and thereby depth resolution of the setup is determined by TOF-E measurements on an appropriate sample. The obtained results in terms of limiting factors are also discussed in section 5.2. For unambiguous recoil ion identification a sufficient mass resolution of the TOF-E spectrometer is required, thus, in section 5.3 first a procedure is described which allows to determine the mass resolution directly from the TOF-E histograms. The mass resolution is then obtained from the measurement of an appropriate sample. The following section 5.4 discusses the TOF detection efficiency of the setup achieved for the 40 MeV ^{197}Au- and the 170 MeV ^{127}I projectile beam. The improvement of mass separation capability and sensitivity due to unique filter conditions created by a combination of the ΔE-E- and the TOF-E method in a TOF-ΔE-E measurement at high recoil ion energies is demonstrated and discussed in the final section 5.5 of this chapter.

5.1   The application of kinematic corrections

In this section a qualitative demonstration of the application of kinematic corrections to ERD measurements carried out with the new developed TOF-E setup is presented. A quantitative discussion of the improvements and final results in terms of energy/depth resolution is given in section 5.2 of this work.

5.1.1   Kinematic correction by a singular position determination

A thin foil sample is analyzed in transmission geometry utilizing the 40 MeV ^{197}Au projectile beam. In this geometry, the effective beam spot size is limited to the beam width of 0.8 mm. The analyzed sample consists of lithium fluoride (LiF) deposited with a thickness of 4 μg/cm^2 on a 4 μg/cm^2 thick carbon (DLC) foil. The histogram on the right side in Fig. 5.1(a) shows the energies of the recoil ions recorded by the energy detector (GIC) versus their position within the scattering plane, also determined by the energy detector. The energy branches of the elements ^6Li, ^7Li, ^{12}C, ^{13}C, O and F are clearly separated. Peaks in the position measurement are caused by the segments of the detector entrance window (see Fig. 4.35). Since the window is centered within the scattering plane, the scattering angle $\varphi = 40°$ is resembled by the position value "0 mm" (see also Fig. 4.1). As seen by the inclination in energy, recoil ions detected at position values of < 0 mm experienced less energy transfer within the binary collision due to scattering angles larger than 40° being accepted. However, particles detected at position values > 0 mm show higher energies due to the smaller scattering angles involved in the collisions. Hence, the kinematic effect $(\Delta E_R/E_R)_{kin}$ due to the angular acceptance within the scattering plane is clearly resolved.

     The projection of the inclined energy values onto the energy axis, illustrated in the left of Fig. 5.1(a), demonstrates the broadening of the energy width due to the kinematic effect. Gaussian functions are fitted to the peaks obtained for ^7Li, ^{12}C and F. It has to be pointed out that they do not represent the obtained energy profiles very well, however, they give an indentation of the impact on energy resolution by the kinematic effect. A second order polynomial correction function (green line in Fig. 5.1(a)) is fitted to the ^{12}C energy branch in order to correct for the kinematic effect. Since $(\Delta E_R/E_R)_{kin}$ only depends on the scattering angle φ and on the angular acceptance $\Delta\varphi$, the correction function is valid for all elemental energy branches occurring in the histogram. The corrected energy versus position histogram is illustrated on the right of Fig. 5.1(b). As seen from the Gaussian fits applied to the projection of the energy values, the widths (FWHM) are reduced by a factor of ≈ 2. The kinematic effect due to

the angular acceptance is reduced to an extend at which other contributions dominate the energy resolution (e.g. energy straggling within the detector entrance window and within the carbon foils of the timing detectors).

(a)

(b)
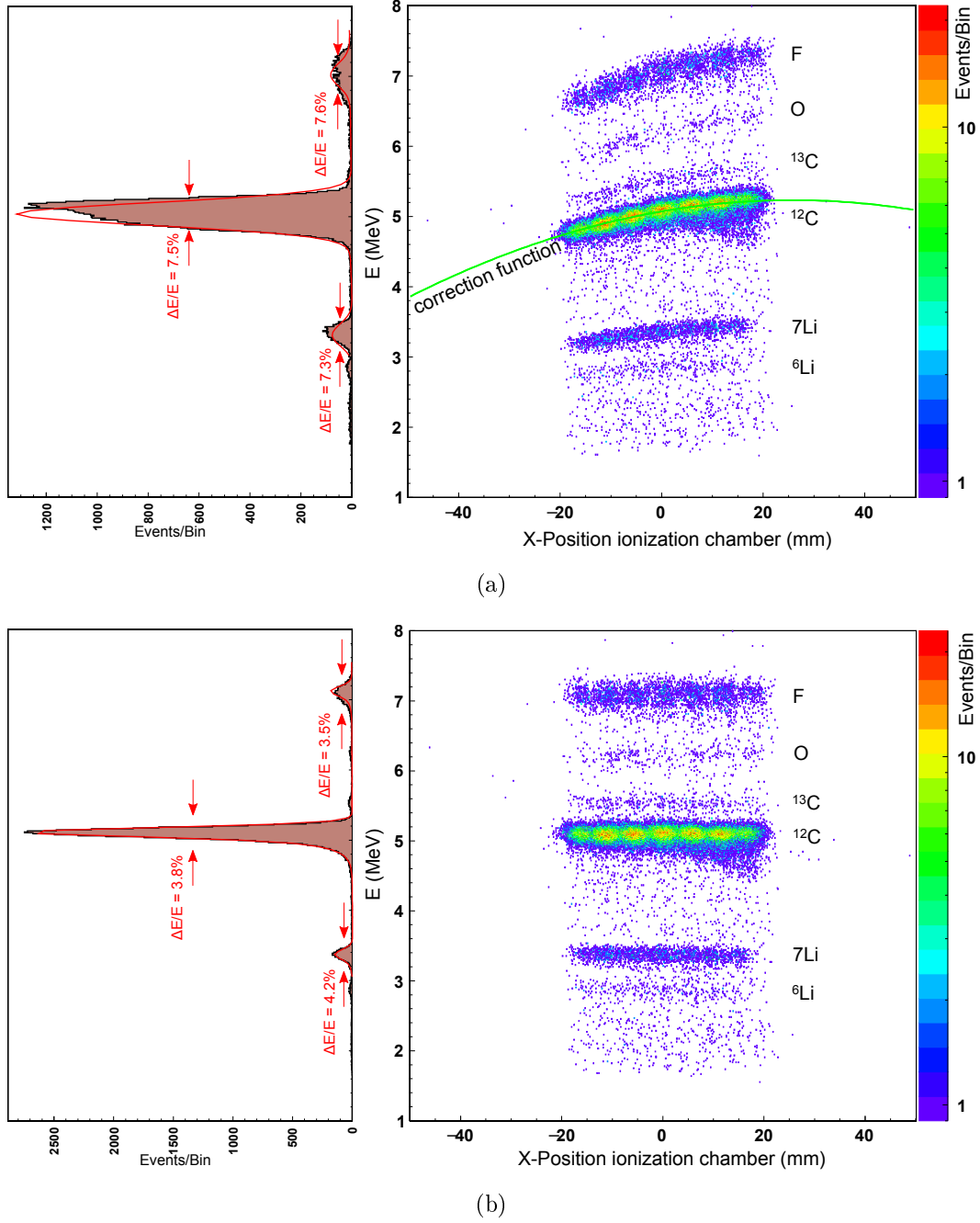
Figure 5.1: *(a): Right histogram: Recoil ion energies determined by the energy detector of the setup versus their position within the scattering plane (sample: $4\,\mu g/cm^2$ LiF on $4\,\mu g/cm^2$ carbon). The kinematic effect due to the angular acceptance within the scattering plane causes an incline in energy. The broadening of each particular "energy branch width" due to the kinematic effect is reflected by the projection onto the energy axis (left histogram). A correction function is fitted through the ^{12}C energy branch (green line). (b): Kinematic correction applied: The width of the energy branches is reduced by a factor of ≈ 2 reducing the impact of the kinematic effect on the energy resolution to an extend at which other contributions dominate the energy resolution (see text for explanation).*

The position information provided by the energy detector can be utilized to apply the same correction procedure also to the time of flight measurement. However, with its position unit, the start timing detector (T_1) allows to determine the position of the recoil ions within the scattering plane as well. Thus, depending on the desired correction method (see section 3.2) the recoil ion energy as well as the time of flight data can also be corrected by the position information provided by T_1. This is demonstrated for the time of flight data in the following:

The right sided histogram of Fig. 5.2(a) shows the time of flight values obtained for the LiF sample. In contrast to the energy measurement, the difference in time of flight between the elemental branches is small. Thus, only the branches of the lithium isotopes ($^6Li + ^7Li$) of both carbon isotopes ($^{12}C + ^{13}C$) and of fluorine (F) are clearly separated. Similar to the energy measurement, the T_0-TOF values (time inversion: see section 4.5) show an incline versus the position (determined by T_1) within the scattering plane. As previously described for the energy values, more energy is transferred within the binary collision for recoil ions occurring at position values > 0 mm (scattering angles $< 40°$). Thus, the higher velocities appear at higher T_0-TOF values and lower velocities for position values < 0 mm, respectively. Hence, the kinematic effect $(\Delta E_R/E_R)_{kin}$ due to the angular acceptance within the scattering plane is also clearly resolved utilizing the position information provided by T_1.

The projection of the inclined T_0-TOF values on the T_0-TOF axis is illustrated on the left side of Fig. 5.1(a), demonstrating the extensive broadening by the kinematic effect. The particular branches overlap significantly. The Gaussian functions fitted to the branches do not describe their shape, however, an indentation of the impact of the kinematic effect on the TOF measurement is given. For correction, a second order polynomial function is fitted through the carbon branch (green line). The corrected T_0-TOF versus position histogram and the corresponding histogram of the T_0-TOF values projected onto the T_0-TOF axis are illustrated in Fig. 5.2(b). The broadening due to the kinematic effect is reduced significantly and the branches do not overlap anymore. From the Gaussian fits of the corrected T_0-TOF peaks, an increase by a factor of ≈ 2 in time resolution can be observed. The kinematic effect is reduced to an extend, at which e.g. straggling effects within the carbon foil of the start timing detector dominate the TOF resolution. Similar to the energy detector, the position information provided by the start timing detector can also be utilized for a kinematic correction of the energy measurement. This depends on the desired method of kinematic correction to be used (see section 3.2).

(a)

(b)
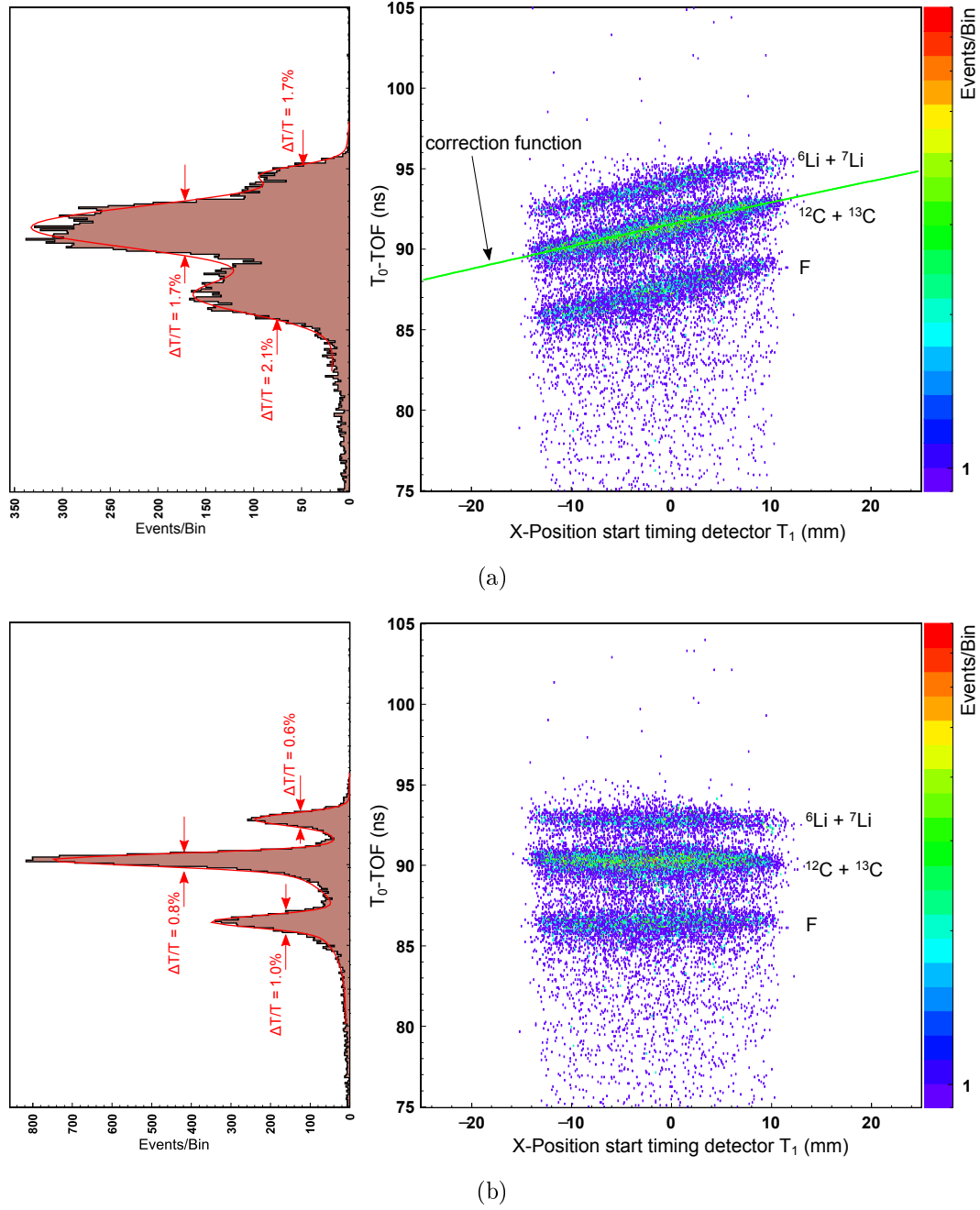
Figure 5.2: *(a): Right histogram: Recoil ion time of flights versus the position within the scattering plane. In this case the position determination is carried out by the position unit of the start timing detector T_1 (sample: $4\,\mu g/cm^2$ LiF on $4\,\mu g/cm^2$ carbon). The kinematic effect due to the angular acceptance within the scattering plane causes the incline in time of flight. A correction function is fitted through the carbon TOF branch (green line). (b): Kinematic correction applied according to the function: In contrast to the uncorrected TOF measurement, the widths of the TOF peaks (left histogram) are reduced by a factor of ≈ 2.*

• The TOF-E histogram and the impact of kinematic correction on it:

Figure 5.1(a) demonstrates the elemental separation by the energy measurement for the thin LiF foil target. However, for thicker samples, the elemental branches can overlap due to the reduction in recoil ion energy with increasing depth of analysis. Thus, elemental separation achieved exclusively be the energy measurement becomes impossible. The same problem accounts even more severely for the time of flight measurement with increasing sample depth. As seen from Fig. 5.2(a) already for the thin foil target, the individual isotopes can not be separated by the TOF measurement, since relative spread in time between the individual elemental branches is reduced in comparison to the energy measurement.

Both quantities, the energy- and the time of flight information being plotted against each other, however, results in the typical "elemental bands" and even isotope separation becomes possible for a large range of energies and thereby sample depths (see Fig. 2.6). The advantage of the TOF-E method to transfer the time information into an energy information which results in a better energy resolution as obtained by the energy dispersive detector (at low recoil ion energies) is clearly observed from the 1-dimensional energy- and TOF histograms illustrated in Fig. 5.1 and 5.2:

The projection of the kinematic corrected ^{12}C energy branch on the energy axis shows an energy resolution of $\Delta E/E = 3.8\,\%$ (FWHM) in case of this particular sample (see Fig. 5.1(b)). In contrast to that, the time of flight information of the carbon branch (see Fig. 5.2(b)) which also includes the ^{13}C isotope (isotope separation not possible in TOF) shows a relative time resolution of $\Delta T/T = 0.8\,\%$ (FWHM). This resolution transforms, according to Eq. 2.18, into an energy resolution of $\Delta E/E = 1.6\,\%$ (FWHM). Hence, an improvement in energy resolution by a factor of 2.4 is observed from the TOF information.
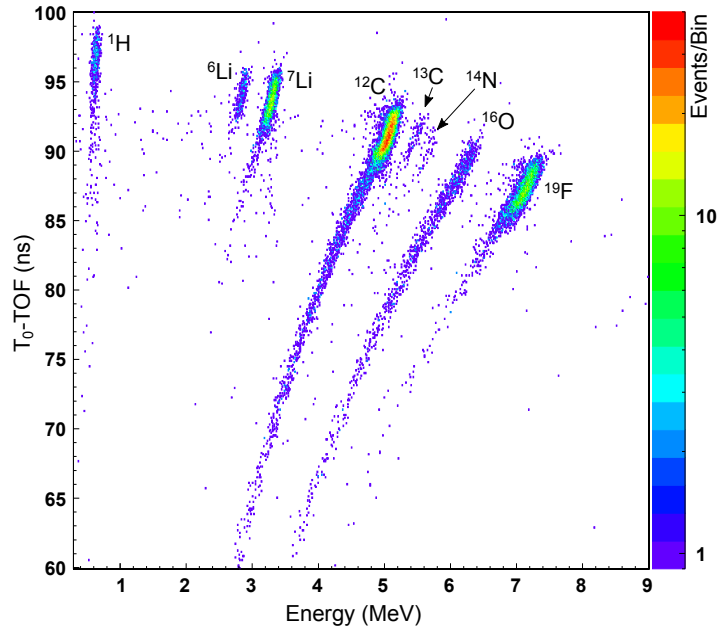
(a)
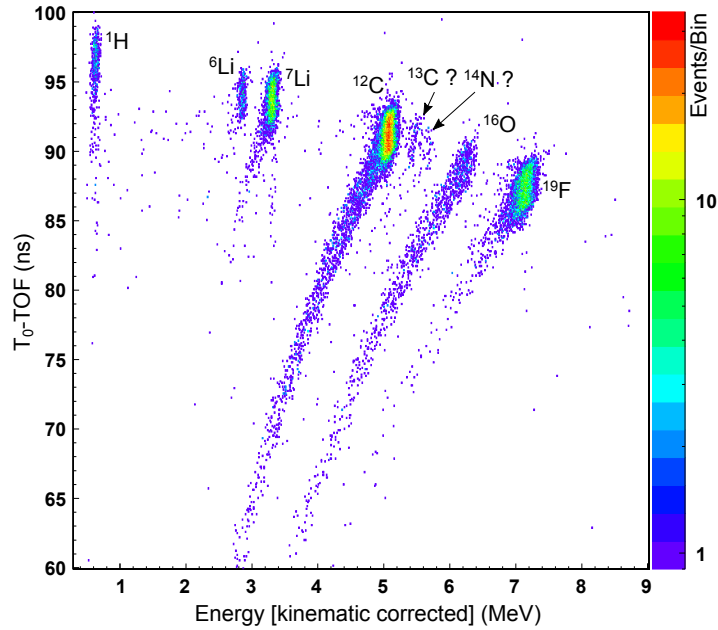
(b)

Figure 5.3: *(a)*: *TOF-E histogram of 4 μg/cm² LiF deposited on a 4 μg/cm² thick carbon foil, measured in transmission geometry utilizing the 40 MeV ¹⁹⁷Au projectile beam. No kinematic corrections are applied to the histogram (raw data). **(b)**: Kinematic correction of the energy measurement only: Mass separation capabilities are reduced or lost (as in case of ¹³C and ¹⁴N in this particular measurement) if only one quantity is kinematic corrected.*
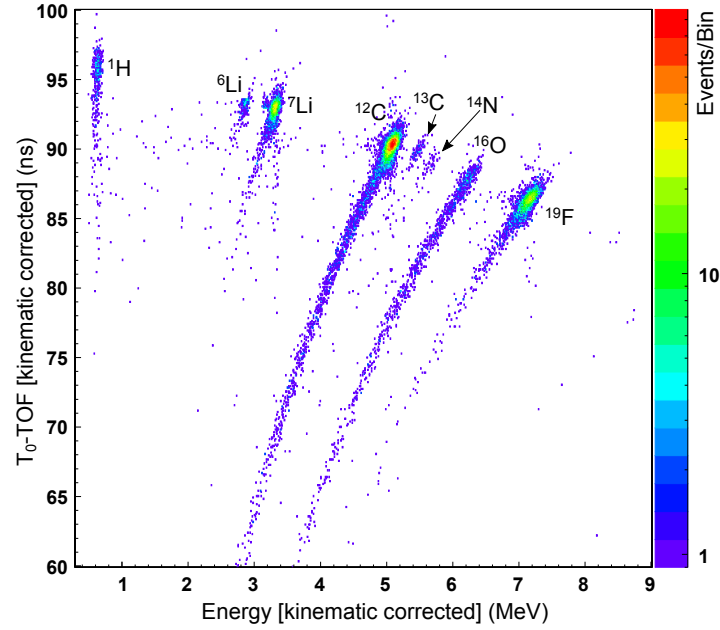
Figure 5.4: *The time of flight- and the energy measurement are kinematically corrected utilizing the position sensitivity of the setup. The width of the elemental branches is reduced for both quantities and the achievable energy-, depth and mass resolution of the setup is increased (see section 5.2).*

The impact of kinematic correction on the TOF-E histograms is demonstrated in Fig. 5.3: The TOF-E histogram, as obtained from the measurement of the LiF foil (raw data) is shown in Fig. 5.3(a). Even with the contributions of the kinematic effect to the energy as well as to the TOF resolution elemental separation is possible, since the kinematic shift is of equal impact to both quantities. However, if the possibility to correct for the kinematic effects is given, both quantities have to be corrected simultaneously. Otherwise mass separation capabilities will be reduced or lost. This is demonstrated in Fig. 5.3(b) which shows the TOF-E histogram of the LiF sample, however, with the energy being the only quantity to be corrected for the kinematic effect: The width in energy is vastly reduced, but as seen for ^{13}C and ^{14}N, the mass separation is reduced. This effect becomes even more severe for heavier recoil ion masses.

In contrast to that, in Fig. 5.4 the fully kinematic corrected TOF-E histogram of the LiF sample is shown: The particular widths in time of flight- and energy measurement are reduced and mass separation capability is not only restored, but enhanced by the corrections applied to the measurement.

5.1.2   Kinematic correction by angular measurement

As described in section 3.1.2 of this work, the kinematic effect caused by the beam spot size on the sample surface has to be considered for small projectile beam incident angles. Due to the given geometry of the setup, it contributes by 0.6% to the energy resolution at an incident angle of $\alpha = 4°$ ($b_{eff} = 6.7\,\text{mm}$). A true angular measurement of every recoil ion trajectory offers the ability to correct for this effect. This is achieved by utilizing the position information provided by both, the start timing detector T_1 and the energy detector, for the calculation of the scattering angle. With the obtained position resolutions (see section 4.2.6 and 4.4.3) the uncertainty in scattering angle $\Delta\varphi$ due to the angular acceptance of the system within the scattering plane is reduced from $\Delta\varphi = 20\,\text{mrad}$ down to $\leq 2.5\,\text{mrad}$. The effect of this correction on the achieved time- and thereby energy resolution is demonstrated in the following:

A 10 nm thick silicon oxide (SiO_2) deposited on a phosphor doped crystalline silicon substrate is analyzed utilizing the 40 MeV ^{197}Au projectile beam at an incident angle of $\alpha = 4°$ (optimum incident angle for high resolution ERD measurements performed with the Q3D magnetic spectrograph). The kinematic shift of the TOF measurement as well as of the energy measurement is corrected utilizing the position information provided by the energy detector (see previous section 5.1.1). The corresponding TOF-E histogram is illustrated in Fig. 5.5. The oxygen of the SiO_2 layer is clearly resolved. Carbon on the surface is found which originates from the atmospheric hydrocarbon content, to which the sample was exposed before analysis. The stable silicon isotopes ^{28}Si, ^{29}Si as well as ^{30}Si are resolved.

The kinematic shift in TOF due to effective beam spot size is revealed in Fig. 5.6(a) which shows the already corrected T_0-TOF values (pos. information energy detector) in the range of $75-95\,\text{ns}$ versus the true scattering angle calculated from the two position determinations provided by the energy detector and T_1:

Even with TOF being corrected by a single position measurement, the histogram clearly illustrates the residual incline in TOF caused by the effective beam spot size. The scattering angle $\varphi = 40°$ is resembled by the value "0 mrad". As expected, scattering angles with deviations $> 0\,\text{mrad}$ show smaller T_0-TOF values due to the reduced energy transfer in the binary collision (scattering angles $> 40°$). Events at measured scattering angles $< 0\,\text{mrad}$ show higher T_0-TOF due to the higher velocities observed at higher energies. Figure 5.6(b) shows the TOF- versus scattering angle histogram with the angular kinematic correction being applied.
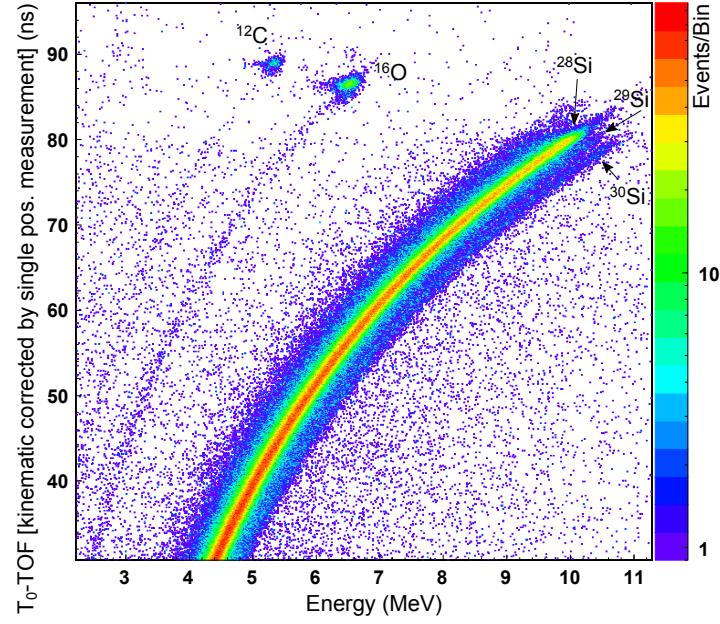
Figure 5.5: *TOF-E histogram of 10 nm silicon oxide deposited on crystalline silicon, analyzed with the 40 MeV ^{197}Au projectile beam at an incident angle of $\alpha = 4°$. The kinematic shift of the TOF is corrected by the position information provided by the energy detector. The oxygen of the silicon oxide (SiO_2) layer is clearly resolved.*
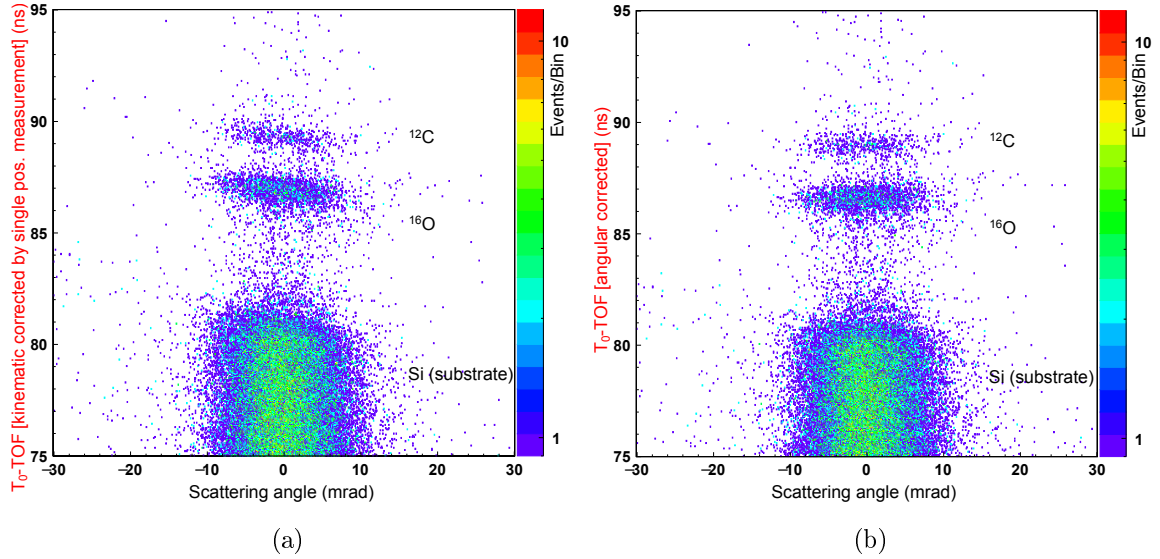
Figure 5.6: *(a): T_0-TOF values of the TOF-E histogram illustrated in Fig. 5.5 versus the true scattering angle: The TOF values have been corrected by the position measurement within the energy detector. However, the true scattering angle which is determined by the position information provided by the energy detector and the start timing detector, reveals the residual kinematic contribution due to the effective beam spot size. (b): The residual kinematic contribution is corrected utilizing the procedure described in section 5.1.1.*

The projection of the T_0-TOF values in Fig. 5.6 onto the T_0-TOF axis, in the range of $83-92$ ns, is illustrated for both cases of kinematic correction in Fig. 5.7. The oxygen profiles are narrowed in the angular corrected histogram shown in Fig. 5.7(b). For comparison purpose, Gaussian functions are fitted to the TOF peaks of oxygen
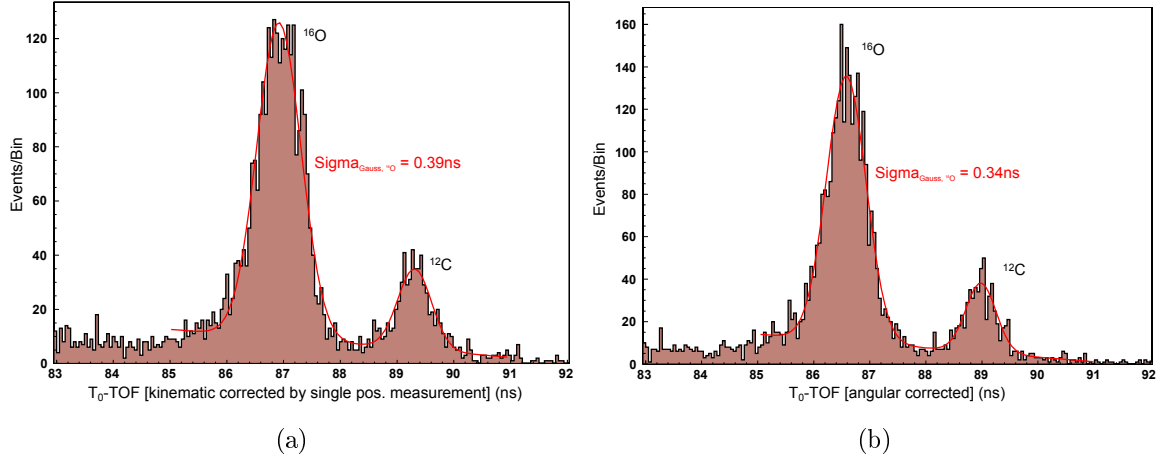
Figure 5.7: *(a): TOF histogram of the silicon oxide sample in range of $83-92$ ns: The kinematic shift in TOF is corrected exclusively utilizing the position information provided by the energy detector. (b): The kinematic shift in TOF is corrected utilizing the angular measurement: The width of the peaks is reduced and the TOF resolution is improved by $\approx 10\%$. Quantitative numbers in terms of the improvement in energy/depth resolution are given in section 5.2.*

in both histograms. It has to be pointed out that they do not correctly represent the obtained TOF profiles, however, an increase in TOF resolution by $\approx 10\%$ can be estimated from the difference in standard deviation Sigma$_{Gauss}$ from 0.39 ns (no angular correction) to 0.34 ns (with angular correction) by the application of the angular based kinematic correction method.

5.2   Energy- and depth resolution

5.2.1   Determination of the energy- and depth resolution

For the determination of the depth resolution a sample consisting of three distinct layers deposited on a crystalline silicon substrate is analyzed utilizing the 40 MeV ^{197}Au projectile beam at an incident angle of $\alpha = 4°$. The first layer is a $0.7\,\mu g/cm^2$ thick ^{13}C layer, on top of a $4.0\,\mu g/cm^2$ thick natural ^{12}C layer, followed by a $8.0\,\mu g/cm^2$ thick Ti layer. The corresponding TOF-E histogram is illustrated in Fig. 5.8:

The isotopes of the carbon layers are clearly separated in the histogram and all
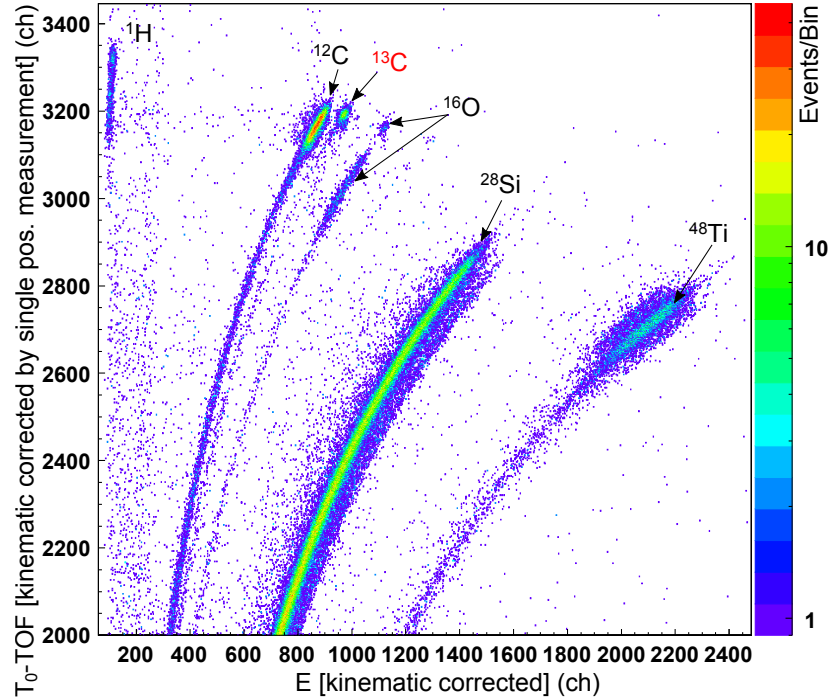
Figure 5.8: *TOF-E histogram of a $0.7\,\mu g/cm^2$ thick ^{13}C layer on a $4.0\,\mu g/cm^2$ thick natural ^{12}C layer on $8.0\,\mu g/cm^2$ Ti, analyzed with the $40\,MeV$ ^{197}Au projectile beam at an incident angle of $\alpha = 4°$. The substrate is crystalline silicon. The depth resolution is determined from the time of flight data of the $0.7\,\mu g/cm^2$ ($\approx 3.5\,nm$) thick ^{13}C layer.*

three layers on top of the silicon substrate are resolved. Oxygen is found on the surface of the ^{13}C layer and a significant amount within the titanium layer. Hydrogen is also detected throughout the entire titanium layer. In the following, only the obtained T_0-TOF values from the events of $0.7\,\mu g/cm^2$ ($\approx 3.5\,nm$) thick ^{13}C top layer are considered for the determination of the depth resolution:

The T_0-TOF values of the ^{13}C recoil events are projected onto the T_0-TOF axis for three particular cases of kinematic correction:

(a): no correction applied (Fig. 5.9(a)), **(b)**: kinematic correction by a single position determination within the energy detector (Fig. 5.9(b)) and **(c)**: kinematic correction by an angular measurement utilizing the position information provided by the energy detector and the start timing detector (Fig. 5.9(c)). A function consisting of a square function and of two error functions is fitted to the data (red line) which allows to determine two standard deviations: σ_L for the slope of the profile at the ^{13}C/^{12}C interface and σ_R to describe the slope of the obtained profile on the surface of the ^{13}C layer. Calibration of the TOF axis was performed utilizing a time calibration module (ORTEC Model 462) providing a conversion factor of $19.02\,$ch/ns.

(a): The uncorrected T_0-TOF profile illustrated in Fig. 5.9(a) could be interpreted as a real plateau of the ^{13}C layer, however, in this case the T_0-TOF profile is broadened due to the impact of the kinematic effect, as previously discussed in section 5.1.1 and exemplarily illustrated in Fig. 5.2. At a ^{13}C recoil ion time of flight of $\mathrm{TOF}_{^{13}C} = 110.26\,$ns, a surface energy resolution of $(\Delta\mathrm{E/E})_{UnCorr} = 1.8 \cdot 10^{-2} \pm 2.4 \cdot 10^{-3}$ (FWHM) which translates into a depth resolution of $\Delta\mathrm{x}_{UnCorr} = 5.6 \pm 0.7\,$nm (FWHM)is achieved according to Eq. 2.9.

(b): By application of the kinematic correction utilizing the position information provided by the energy detector, the T_0-TOF profile of the ^{13}C layer is significantly altered: The fit value σ_R of the surface slope is reduced by a factor of ≥ 2 to $3.8\,$ch and the slope of the interface is broadened ($\sigma_L = 6.5\,$ch) due to the now visible path length effect. A surface energy resolution of $(\Delta\mathrm{E/E})_{PosCorr} = 8.5 \cdot 10^{-3} \pm 8.9 \cdot 10^{-4}$ (FWHM) translating into a depth resolution of $\Delta\mathrm{x}_{PosCorr} = 2.6 \pm 0.3\,$nm (FWHM) is achieved.

(c): The sample is analyzed at an incident angle of $\alpha = 4°$. Hence, the kinematic effect by the beam spot size on the sample surface also contributes to the achievable depth resolution, as discussed in section 3.2 and 4.1. The angular corrected T_0-TOF histogram of the ^{13}C layer is illustrated in Fig. 5.9(c): The width of the surface slope is once more reduced by $\approx 10\,\%$ to $\sigma_R = 3.4\,$ch, resulting in an achieved surface energy resolution of $(\Delta\mathrm{E/E})_{Angcorr} = 7.6 \cdot 10^{-3} \pm 6.7 \cdot 10^{-4}$ (FWHM) and thereby a depth resolution of $\Delta\mathrm{x}_{Angcorr} = 2.3 \pm 0.2\,$nm (FWHM).
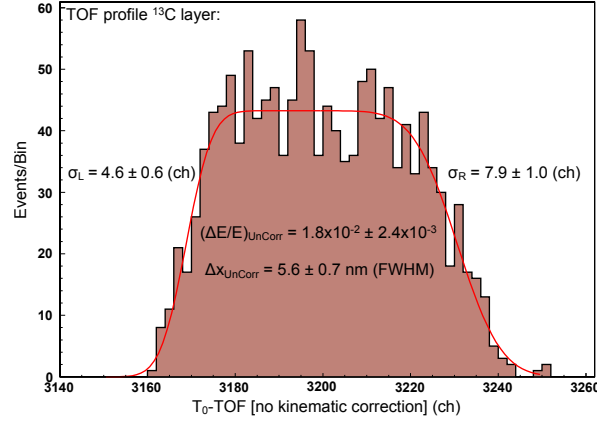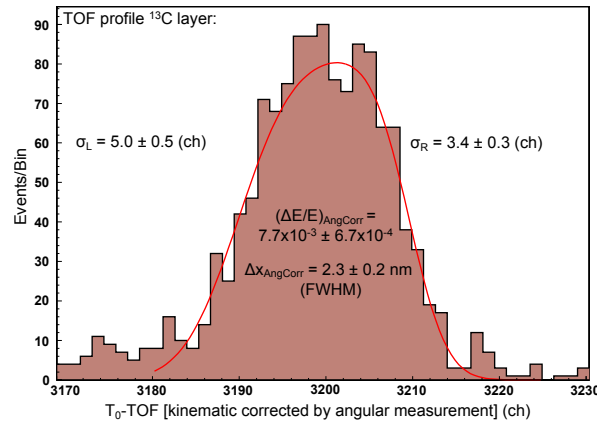
(a)
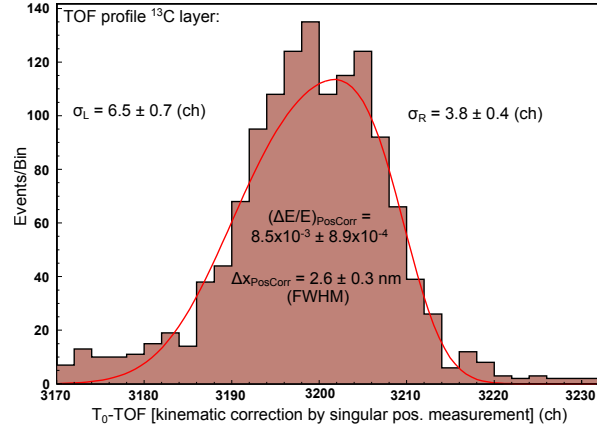
(b)

(c)

Figure 5.9: *TOF profiles of the $0.7\,\mu g/cm^2$ ($\approx 3.5\,nm$) thick ^{13}C layer. A function consisting of a square function and two error functions is fitted to the data (red line). **(a)**: No kinematic correction applied: The virtual width of the profile is given by the kinematic effect. A surface depth resolution of $\Delta x_{UnCorr} = 5.6 \pm 0.7\,nm$ (FWHM) is obtained. **(b)**: Kinematic correction by single position determination: The surface depth resolution is improved by a factor of ≥ 2 to $\Delta x_{PosCorr} = 2.6 \pm 0.3\,nm$. **(c)**: Kinematic correction by measurement of the true scattering angle: The surface depth resolution is further improved by $\approx 10\,\%$ to $\Delta x_{Angcorr} = 2.3 \pm 0.2\,nm$.*

• **Depth profiling:**

The elemental depth profiles are calculated utilizing the KONZERD code [30] on basis of the energy information given by the T_0-TOF data of the previously discussed sample (see TOF-E histogram in Fig. 5.8). They are illustrated in Fig. 5.10. The total TOF detection efficiency of the setup, as presented in section 5.4.1 is considered for the calculations. One can clearly observe that the individual layers of the sample are well reproduced according to their nominal thickness values (see text of Fig.5.10).
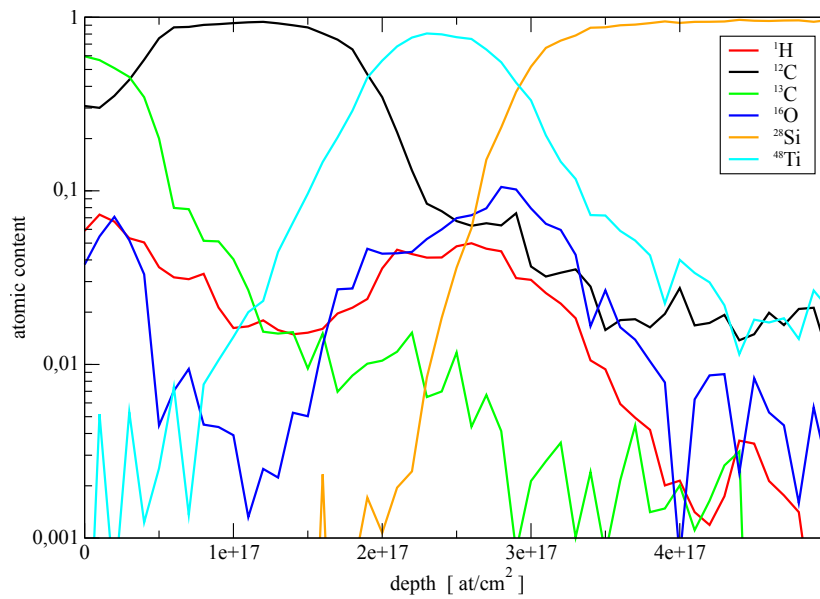
Figure 5.10: *Elemental depth profiles obtained from a sample consisting of a $0.7\,\mu g/cm^2$ (3.2×10^{16} at/cm^2) thick ^{13}C layer on a $4.0\,\mu g/cm^2$ (2.0×10^{17} at/cm^2) thick ^{12}C layer on top of a $8.0\,\mu g/cm^2$ (1.0×10^{17} at/cm^2) thick Ti layer. The substrate is crystalline silicon (see text for further discussion).*

Hydrogen is detected on the surface of the ^{13}C layer which mainly originates from the atmospheric hydrocarbon content to which the sample was exposed before analysis. The hydrogen content decreases throughout the carbon layers, until a significant increase within the titanium layer and at the Ti/Si interface is observed. Virtually no hydrogen is found within the silicon substrate itself.

Oxygen is also observed on the surface, however, basically no oxygen is found within both carbon layers. The oxygen content then increases again within the titanium layer and is clearly present at the interface to the silicon substrate. The observed maximum of the oxygen content on the Ti/Si interface can e.g. be accredited to a natural oxide layer (SiO$_2$) of the used silicon wafer which was not removed before

the deposition of the titanium layer.

As e.g. seen from the ^{13}C depth profile (but also from the profiles of all other top layers) low energy tails occur, due to multiple and plural scattering of the recoil ion and the projectile within the sample at the small utilized incident angle and the low energies of the projectiles and recoil ions, respectively (see also Fig. 2.2 in section 2.1.2).

A further discussion of the results in terms of limitations to the depth resolution is presented in the following section 5.2.2.

5.2.2   Discussion of the results

The contributions to the achievable energy- and therefore surface depth resolution are given by the stability in energy of the projectile beam, the present beam divergency, the kinematic contribution (angular acceptance and beam spot size on the sample surface at low incident angles), the Doppler effect, the time resolution and by the contribution accredited to energy straggling of the recoil ions within the carbon foil of the first timing detector. The individual contributions, except the time resolution and energy straggling within the carbon foils, are discussed in detail in [10, 11, 51]. Quadratic summation of all contributions gives the overall energy-/depth resolution of the TOF-E setup. The values of each particular contribution as found in case of the analysis of the ^{13}C sample as well as the resulting overall energy-/depth resolution are listed in Tab 5.1.

Contributions to the energy resolution	$\Delta E/E$
Energy stability of the projectile beam:	2.0×10^{-4}
Beam divergency (0.8 mrad):	4.5×10^{-4}
Doppler effect ^{13}C:	1.0×10^{-4}
Residual kinematic contribution (after angular correction $\Delta\varphi = 2.5$ mrad):	4.2×10^{-3}
Resolution of the time measurement (280 ps FWHM):[6]	5.0×10^{-3}
Energy straggling within T_1 carbon foil (effective thickness due to tilt angle $= 6\,\mu$g/cm^2, (CORTEO)):	1.2×10^{-3}
Overall energy resolution: Surface depth resolution "^{13}C layer example" (40 MeV ^{197}Au projectile beam):	6.7×10^{-3} 2.1 nm

Table 5.1: *Individual contributions to the overall energy resolution and thereby surface depth resolution, as in case of the TOF-E analysis of the 0.7 μg/cm^2 thick ^{13}C layer presented section 5.2.1. The value of $\Delta E/E = 6.7 \times 10^{-3}$ in surface energy resolution an thereby depth resolution of 2.1 nm is in good agreement with the measurement results of 7.6×10^{-3} and 2.3 nm (FWHM) (see text for further discussion).*

The expected surface depth resolution of 2.1 nm (FWHM) is in good agreement with the measurement result of 2.3 nm (FWHM) presented in section 5.2.1. However, the 0.7 μg/cm^2 (≈ 3.5 nm) thick ^{13}C sample does not represent an optimal choice of

---

[6] This value represented the overall time resolution observed from measurements utilizing the 170 MeV ^{127}I projectile beam (see section 5.5.1)

experimental system to determine the true energy-/depth resolution. Furthermore certain ambiguities exist with respect to the identification of the true limiting contribution. These aspects are discussed in the following with the help of a Monte Carlo based simulation with the CORTEO code [94]:

An ideal layer to determine the response function of the detection system would be one of infinite small thickness. Here, virtually no contribution to the energy resolution would be accredited to the layer itself, thus, the measured response resembled by e.g. a Gaussian distribution would directly represent the achievable energy resolution of the system by its value of the full width at half maximum (FWHM). However, this is not an easy task to execute in reality, since it would demand to acquire sufficient statics from a very thin layer, without altering it in the measurement by e.g. the smallest amount of irradiation damage.

In the measurement of a real layer of finite thickness, the energy shift due to the
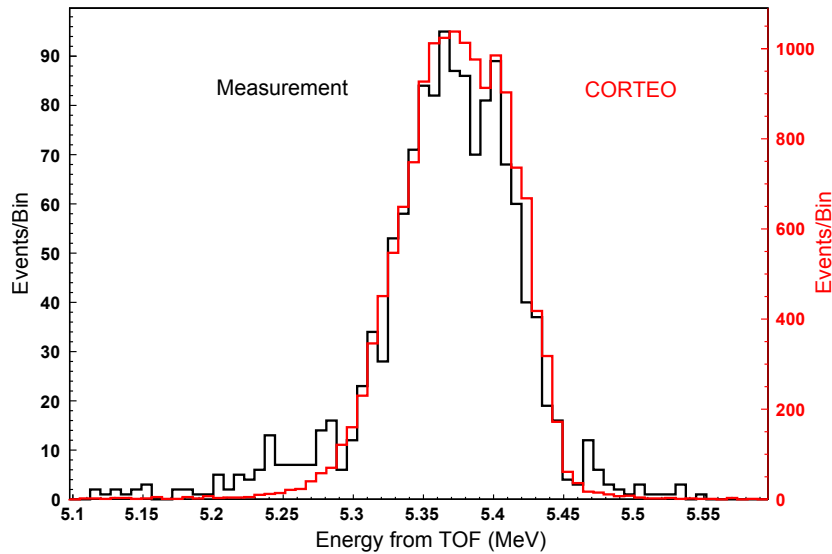
Figure 5.11: *The measured energy profile of a $0.7\,\mu g/cm^2$ ($\approx 3.5\,nm$) thick ^{13}C layer (black lines) can not be reproduced by a single CORTEO simulation considering the nominal layer thickness and a fixed carbon foil thickness within the first start timing detector. However, it is well represented by the summation of individual CORTEO simulation results incorporating carbon foil thicknesses of 2, 4, 6, 10 and $12\,\mu g/cm^2$ (at fixed nominal target thickness). This indicates that the energy resolution is mainly limited by the inhomogeneity of the carbon foil within T_1.*

thickness itself, however, causes a broadening of the Gaussian distribution obtained for the ideal case which produces a certain plateau in the obtained profile, interfering

with the response function of the detection system. This would not result in any ambiguity if all contributions to the energy resolution would have been been corrected or minimized to an absolute minimum, since then the slope of the obtained depth profile would directly represent the response function of the detection system, but this is never the case in reality.

However, in the framework of the TOF-E setup, a plateau of this kind can, besides a residual kinematic contribution (in this case the resulting thickness of the virtual layer of course would not represent a real layer thickness), also be created by different energy losses of the recoil ions within the carbon foil of the first timing detector due to inhomogeneities. The slopes of the individual Gaussian distributions, each per "interval of inhomogeneity", would be overplayed by each other, creating a plateau and thereby an artificial thickness in the measurement. It is supposed that, this actually is the case for the presented results, since the obtained T_0-TOF profile of the ^{13}C layer illustrated in Fig. 5.9(c) could not be reproduced with CORTEO by the use of a constant layer thickness in combination with a constant carbon foil thickness. However, a summation of the results of individual CORTEO simulations incorporating foil thicknesses of 2, 4, 6, 10 and $12\,\mu g/cm^2$ at a constant ^{13}C layer thickness (nominal value of $0.7\,\mu g/cm^2$ is used) allowed to reproduce the measured T_0-TOF profile with good agreement. This is demonstrated in Fig. 5.11 which shows the T_0-TOF profile of Fig. 5.9(c) transformed into the energy information which is overlayed by the summed up CORTEO results

This agreement indicates that the overall energy-/depth resolution can in fact be obtained from the fit results presented in the previous section 5.2.1, because also in case of a significant difference in inhomogeneity, the total slope would be represented by the most broadened individual Gaussian function which is described by the error function fitted to it. The measured depth information, however, remains to be affected by the carbon foil.

5.3 Mass resolution

5.3.1 General aspects

For unambiguous recoil identification a sufficient mass resolution of the TOF-E setup is required. As discussed in section 2.2.3, the absolute mass resolution ΔM_R depends on the resolution of the energy detector $\Delta E_R/E_R$ as well as on the time resolution $\Delta T_R/T_R$ according to

$$\Delta M_R = \sqrt{\left(\frac{\Delta E_R}{E_R}\right)^2 + \left(2 \cdot \frac{\Delta T_R}{T_R}\right)^2} \cdot M_R \ . \tag{5.1}$$

Due to energy loss straggling and small angle scattering of the projectile and the recoil ion within the sample, the obtainable mass resolution is also associated with the utilized type of projectile beam, its energy, the depth of analysis and the sample composition.

Due to the fact that in contrast to the time resolution the energy resolution of the energy dispersive detector degrades for low recoil ion energies, the major contribution to the mass resolution is given by its particular performance. The absolute energy resolution ΔE_{GIC} of the gas ionization chamber, utilized as energy detector of the setup, depends on a variety of individual contributions (excluding kinematic effects). They are discussed in detail in [95] and listed as follows:

- $\Delta E_{stragg,entrance}$: Energy straggling within the entrance window of the detector.
- $\Delta E_{stragg,T_{1+2}}$: Energy straggling within the carbon foils of the timing detectors.
- $\Delta E_{Tandem,T_{1+2}}$: Tandem effect due to the potentials within the timing detectors.
- $\Delta E_{intrinsic}$: Intrinsic energy resolution of the energy detector.

Quadratic summation of all contributions leads to the absolute energy resolution:

$$\begin{aligned}(\Delta E_{GIC})^2 =& (\Delta E_{stragg,entrance})^2 + (\Delta E_{stragg,T_{1+2}})^2 + (\Delta E_{Tandem,T_{1+2}})^2 + \\ & (\Delta E_{intrinsic})^2 \ .\end{aligned} \tag{5.2}$$

Energy straggling within the entrance window $\Delta E_{stragg,entrance}$ is minimized as much as possible by the use of the homogenous, 100 nm thick silicon nitride membranes. However, for a carbon recoil ion with an energy of 5.08 MeV, it still contributes by 23 keV, according to a Monte Carlo based simulation carried out with the program code CORTEO [94]. Total energy straggling $\Delta E_{stragg,T_{1+2}}$ within both carbon foils is estimated utilizing CORTEO (total foil thickness of $10\mu g/cm^2$) to contribute

by 13 keV for the 5.08 MeV carbon recoil ion. The contribution of the tandem effect $\Delta E_{Tandem, T_{1+2}}$ depends on the charge state of the recoil ion before and after passing through the carbon foils of the timing detectors as well as on the traversed potential difference: The charge state of the recoil ion can be altered by stripping of electrons within the carbon foil. Thus, if e.g. the charge state is altered from $^+4$ to $^+7$ and a potential difference of 3 kV is traversed within the timing detectors, the contribution given by the tandem effect is 12 keV which is already in the order of the energy straggling within the carbon foils of the timing detectors. The intrinsic energy resolution $\Delta E_{intrinsic}$ can, in principle, be determined by e.g. utilizing an alpha particle calibration source, which is placed directly into the gas volume.

However, in terms of mass resolution only the achieved energy resolution including all contributions listed previously is of importance, since in the TOF-E measurement they are inevitable. Figure 5.12, shows the obtained energy resolution of the energy detector for a variety of elements, which were deposited with a layer thickness of $4 \, \mu g/cm^2$ onto $4 \, \mu g/cm^2$ thick DLC foils. Analysis is carried out in transmission geometry, utilizing the 40 MeV ^{197}Au projectile beam. Kinematic effects were corrected utilizing the position information provided by the energy detector. As expected, the energy resolution degrades towards lower recoil ion energies. However, even with the observed increase in energy resolution towards higher recoil ion energies, in general the mass separation becomes more difficult towards heavier masses, due to smaller relative mass spread.

5.3.2   Determination of the mass resolution

In the following, the procedure to obtain from every event within the TOF-E histograms the mass information and thereby to create a mass spectrum is described. The approach is similar to the one described by Kottler et al. in [49]:

The time of flight versus energy relation is given by
$$E_R = \frac{1}{2} \cdot M_R \cdot \frac{L^2}{TOF^2} \, , \tag{5.3}$$
with E_R representing the recoil ion energy, M_R its mass, and TOF the required time for the recoil ion to traverse the distance L.

By solving for TOF, the following expression can be utilized to parametrize the elemental 'mass bands' in the TOF-E histograms [96]:
$$TOF = f(t_0, c, d, E_0) = t_0 + c \cdot \sqrt{M_R + d} \cdot \frac{1}{\sqrt{E - E_0}} \, . \tag{5.4}$$
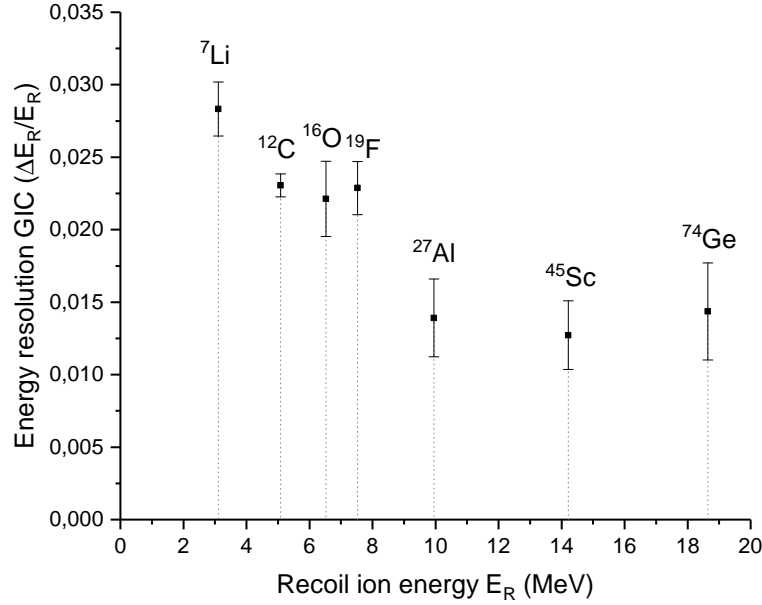
Figure 5.12: *Relative energy resolution $\Delta E_R/E_R$ of the energy detector versus the recoil ion energy obtained under TOF-E measurement conditions, which involves the contributions given by energy straggling within both carbon foils of the timing detectors and within the SiN entrance window. The tandem effect contributes as well (see text for explanation). The particular recoil ion species are scattered from layers with a thickness of $4\,\mu g/cm^2$ deposited on a $4\,\mu g/cm^2$ thick DLC foil. As expected, the energy resolution degrades for the lower recoil ion energies.*

The fit parameters t_0, c, d and E_0 are given by the experimental setup. Therefore, they should be equal for all occurring masses within the histograms and be fitted simultaneously for all 'mass bands' of the TOF-E histograms to determine the 4 constants as well as the associated masses. However, the problem is simplified by fitting each elemental 'mass band' separately with the function

$$f(Tof) = [a] - \frac{[m]}{\sqrt{Tof - [c]}} \,, \tag{5.5}$$

which reflects the shape of the bands and incorporates the three fit parameters $[a]$, $[m]$ and $[c]$. The parameters $[a]$ and $[c]$ (both depending on the experimental setup) can be taken from the fit of one most prominent 'mass band' and kept fixed for all other bands, leaving $[m]$ free, which is associated with the corresponding recoil ion masses. The fitted curves $f(Tof)$, which now correspond to a fixed mass, are used as input for a interpolation procedure to extract the masses for all events in the TOF-E histogram. A mass spectrum is created from the data, which is either filled for the entire data, or only for selected region of interest in the TOF-E histogram. The mass spectrum allows to determine the mass resolution for each specific recoil ion species. However,

it has to be pointed out that this method is not qualified for quantification purposes, as long as the region of interests is chosen arbitrarily.

● **Example of use:**

As mentioned in the beginning of this section, at a given projectile beam type and energy, the mass resolution strongly depends on the depth of analysis. In principal, it has to be determined for each particular analyzed sample and range of depth. Thus, the mass resolution of the TOF-E setup is determined exemplarily for a chosen sample in the following by application of the described procedure:

Fig. 5.13 illustrates the TOF-E histogram obtained from a sample consisting of a 10.6 μg/cm^2 thick MgF$_2$ layer on top of a 23 μg/cm^2 thick Al layer deposited on a borosilicate glass substrate. The fit functions $f(Tof)$ for the known masses M $= 11$ (B), 16 (O), 23 (Na), 28 (Si), 39 (K) and 48 (Ti) are plotted into the histogram. The mass information for every TOF-E event in the histogram is retrieved by the interpolation process, which uses the shown fit functions. The events within the highlighted area (red dotted line) are illustrated in Fig. 5.14(a) and used for the determination of the mass resolution:
A mass spectrum is created exclusively for the MgF$_2$ top layer of the sample according to the selected region in Fig. 5.14(a) (black dotted line). The spectrum is shown in Fig. 5.14(b). Both carbon isotopes ^{12}C (99 %) and ^{13}C (1 %) as well as nitrogen (^{14}N) is found on top of the MgF$_2$ layer, the three masses are clearly separated. Furthermore, the three stable magnesium isotopes ^{24}Mg (79 %), ^{25}Mg (10 %) and ^{26}Mg (11 %) are also well separated. All individual mass peaks are fitted with Gaussian functions and their full width at half maximums (FWHMs), representing the absolute mass resolution ΔM, is determined.

The same procedure is executed to determine the mass resolution obtained for the Al layer including a variety elements of the substrate, all originating from the same depth range. The corresponding area within the TOF-E histogram is marked in Fig. 5.14(a) (red line). The resulting mass spectrum of this area is illustrated in Fig. 5.15(a):
The stable boron isotopes ^{10}B (20 %) and ^{11}B (80 %) within the borosilicate glass substrate are well separated in the mass spectrum. Carbon ^{12}C at the interface between the glass substrate an the Al layer is also resolved. The sensitivity of the TOF-E setup to detect trace elements is demonstrated by the clear mass peak of the stable oxygen isotope ^{18}O (^{18}O/^{16}O $= 2.0 \times 10^{-3}$) within the spectrum. The mass

peaks of aluminium ^{27}Al and silicon ^{28}Si do partially overlap, but they are still clearly resolved. The stable isotopes of potassium ^{39}K (93 %) and ^{41}K (6.7 %) within the substrate are clearly visible. For titanium, however, the mass resolution is reduced and the stable isotope ^{46}Ti (8 %) is hardly be separated from ^{48}Ti (74 %) in terms of the obtained background of ≈ 7 entries per mass bin.

   The absolute mass resolutions ΔM obtained from both mass spectra versus the atomic mass number are illustrated in Fig. 5.15(b). As mass resolution of ΔM ≤ 1 is observed for elements in the mass range of 10 (boron) up to 31 (phosphor) within the total sample depth range being considered for this example of mass resolution determination.

   It has to be emphasized that this procedure to determine the mass resolu-
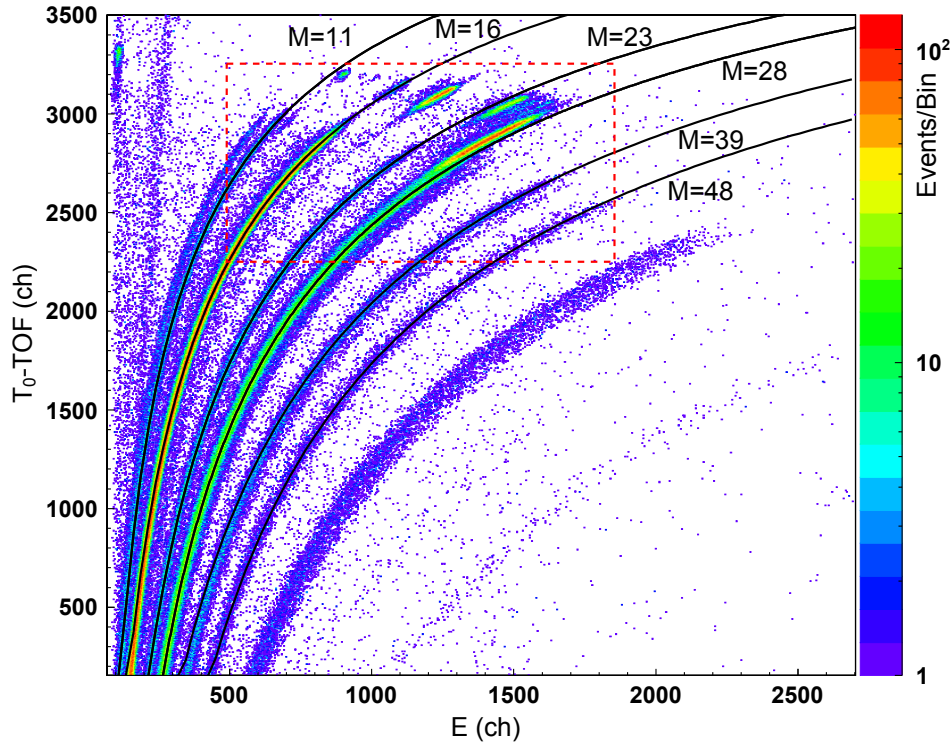
Figure 5.13: *TOF-E histogram of a sample consisting of a 10.6 μg/cm^2 thick MgF$_2$ layer on top of a 23 μg/cm^2 thick Al layer deposited onto a borosilicate glass substrate: Fit functions according to Eq. 5.5 are plotted for the known masses M = 11 (B), 16 (O), 23 (Na), 28 (Si), 39 (K) and 48 (Ti) into the histogram. An interpolation procedure uses the functions to create the mass information for every TOF-E event in the histogram. Mass spectra can be created to determine the mass resolution. The red highlighted area is shown in Fig. 5.14(a) for further discussion.*

tion strongly depends on the quality of the fit functions $f(Tof)$ originating from the TOF-E histogram and on the depth of analysis (for a given sample). The yield obtained in the mass spectra is only usable for quantification purposes, if it is assured that the considered TOF-E events are within the same range of sample depth, or e.g. correspond to one entire layer thickness. In addition to that, the obtained yield has to be weighted according to the scattering cross sections involved.
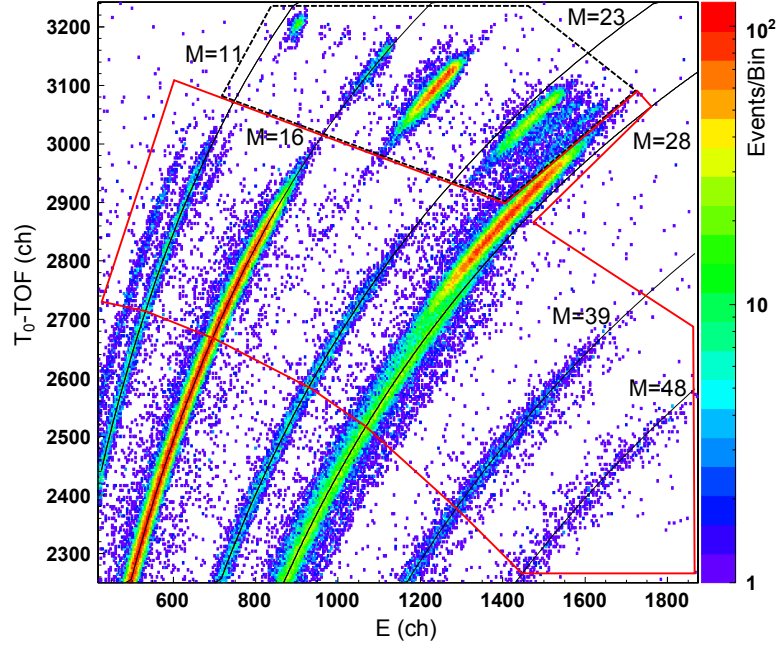
(a)
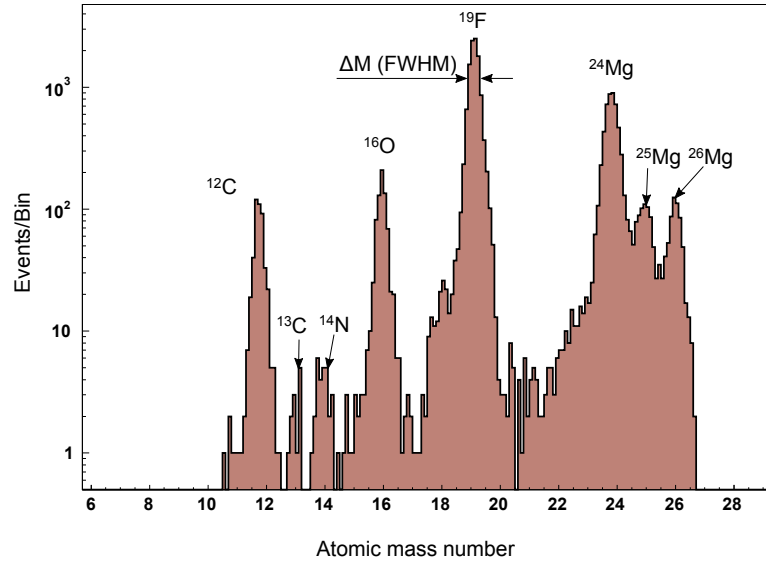
(b)

Figure 5.14: *(a): Highlighted area of Fig. 5.13: Besides the fit functions $f(Tof)$ (thin black lines) two areas within the TOF-E histogram are marked. TOF-E events inside the area marked with the black dotted line correspond to the $10.6\,\mu g/cm^2$ thick MgF_2 top layer and are used to determine the mass resolution obtained within it. The TOF-E events within the area marked with the red line are used to evaluate the mass resolution obtained within the $23\,\mu g/cm^2$ thick Al layer as well as in a certain substrate depth range (equal for all elements of the substrate). (b): Mass spectrum obtained for the MgF_2 layer (black dotted line in Fig. 5.14(a)): The full width at half maximum (FWHM) of each particular peak determines the absolute mass resolution ΔM (see text for discussion of the mass spectrum).*
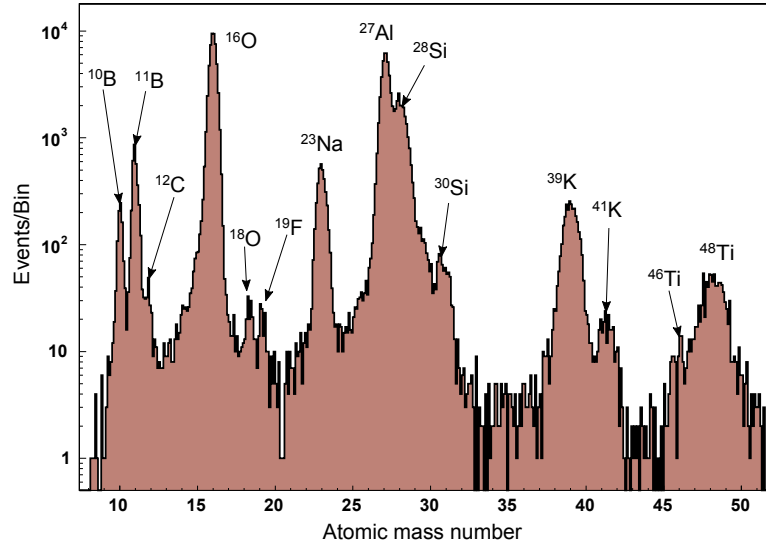
(a)
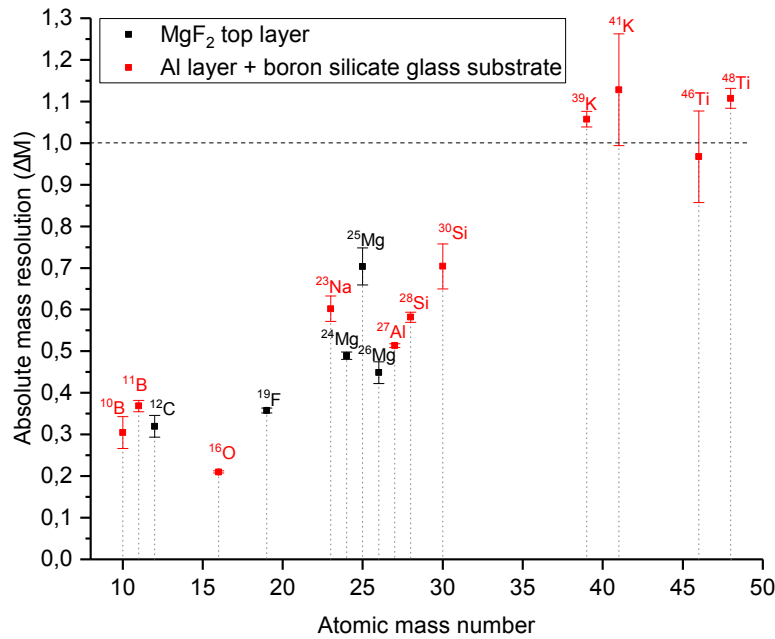
(b)

Figure 5.15: *(a): Mass spectrum obtained for TOF-E events within the Al layer including events originating from the same depth range within the borosilicate glass substrate (area highlighted with red line in Fig. 5.14(a)). The sensitivity of the TOF-E setup for trace elements is demonstrated by the clear mass peak of the stable oxygen isotope ^{18}O ($^{18}O/^{16}O$ = 2.0×10^{-3}, see text for further discussion of the mass spectrum). (b): Mass resolution obtained for both ares highligted in Fig. 5.14(a). For this particular example, a mass resolution of $\Delta M \leq 1$ is observed for elements from 10 (boron) up to 31 (phosphor).*

5.4   TOF detection efficiency

Knowledge of the overall TOF-E detection efficiency is required for accurate determination of elemental concentrations. The efficiency of the energy detector, which in this setup represented by a gas ionization chamber, can be expected to be 100 % over the entire range of recoil masses and energies [49]. The detection efficiency of the timing detectors, however, is governed by the requirement that enough secondary electrons are produced to ensure a CFD threshold crossing. This efficiency is considerably less than 100 %. It mainly depends on

(1) the secondary electron (SE) detection efficiency of the micro channel plates,

(2) the geometrical SE transparency of the grids located within the timing detectors,

(3) And on the secondary electron yield [97].

(1): On impact on the MCP surface, the secondary electrons have an energy of $\approx 2\,$keV in both timing detectors. Thus, the detection efficiency given by the MCP for a single electron can be expected to be $\geq 80\,$% according to [98–100].

(2): The grids used for secondary electron guidance towards the MCP stack within the timing detectors define a geometrical SE transparency: In case of the stop timing detector (T_2) the acceleration grid (wire diameter 35μm, pitch $1\,$mm) as well as the inner mirror grid (wire diameter 35μm, pitch $1\,$mm) have to be taken into consideration (see Fig. 4.33). Disregarding any actual grid to grid alignment effects or electron wire deflections, a geometrical transmission of $\approx 89\,$% is observed.

Due to the design layout of the timing detector (T_1) which features separate timing- and position measurement (see Fig. 4.5) two independent SE transmission values have to be considered: For the dedicated timing measurement a single grid (wire diameter 35μm, pitch $1\,$mm) accelerates the secondary electrons in backward emission direction towards the MCP stack of the timing unit. A geometrical transmission of 97 % is reached. Secondary electron injection into the lens volume in SE forward emission direction is executed by a grid with a wire pitch of $0.5\,$mm at a wire diameter of $35\,\mu$m to assure optimal injection conditions with respect to the optical properties of the electrostatic grid lens (see section 4.2.5). The lens grid consists of wires with a diameter of $25\,\mu$m at a wire pitch of $0.25\,$mm. Both grids limit the geometrical transparency of the position unit to be $\approx 84\,$% for a single electron. The 2-dimensional simulations presented in section 4.2.5, however, state a total electron transparency of the position unit of 88 % taking the grid to grid alignment and wire deflections into account.

(3): Detection efficiencies beyond the limitations given by the MCP detection efficiency and the geometrical transparencies, are observed due to the fact that in most cases more than one secondary electron is produced on penetration of the carbon foil by the recoil ion. The number of secondary electrons strongly depends on the energy and the recoil ion species [59]. According to Sternglass et al. , a proportionality to the electronic stopping forces exists [101], which is confirmed in [97, 102, 103]. Thus, a significant difference of the TOF detection efficiency for recoil ions created by the 40 MeV ^{197}Au projectile beam and by the 170 MeV ^{127}I projectile beam can be expected. Especially for light recoiling elements the detection efficiency can be expected to decrease and grid transmissions as well as MCP detection efficiencies become more dominant again.

● **Measurements:**

For all efficiency determinations presented in the following sections, thin foil samples are measured in transmission geometry ($\alpha = 90°$). The elements Li+F, Al, Sc and ^{74}Ge are deposited with a layer thickness of 50 μg/cm^2 onto 20 μg/cm^2 thick carbon foils. Boron (^{10}B) is deposited with a thickness of 20 μg/cm^2 on a 6 μg/cm^2 thick carbon foil. Silicon and oxygen are scattered from a SiO$_x$ layer with a thickness of 90 μg/cm^2 deposited on a 17 μg/cm^2 thick carbon foil. For each particular efficiency the corresponding surface energies of the recoil ions are considered, since especially for light elements the detection efficiency strongly scales with their energy [97]. Exceptions with respect to sample preparation are given for hydrogen (0.9 μm thick Mylar foil), deuterium (deuterated plastics bulk material) and helium (americium alpha source$^{(7)}$). Timing detector potentials are set according to the values given in section 4.2 and 4.3, representing standard measurement conditions. As shown in section 4.39, the timing signals are directly fed into the constant fraction discriminators without any preamplification. The CFD thresholds are set for both timing detectors to -25 mV (including the time readout of the 2-dimensional Backgammon anode).

Comparative stopping forces are calculated for the surface scattering energies of each particular element utilizing the SRIM code. In case of the stop timing detector, the recoil ions are assumed to penetrate the 4 μg/cm^2 thick DLC foil at an incident angle of 90°. However, the carbon foil of the start timing detector is tilted by 40°. Thus, the effective thickness is increased from 4 μg/cm^2 to 6 μg/cm^2 and the energy loss values have to be scaled accordingly. For the DLC foils a density of 3 g/cm^3

$^{(7)}$The scattering energy of helium, utilizing the 40 MeV ^{197}Au projectile beam at $\varphi = 40°$, is 1.83 MeV. The source, however emits alpha particles with an energy of 5.486 MeV.

is used for the calculations. Since the TOF detection efficiencies are also relevant for the combined TOF-ΔE-E measurements presented in section 5.5, the efficiencies are determined in the following for both projectile beams, the 170 MeV ^{127}I- and the 40 MeV ^{197}Au projectile beam.

5.4.1 Total TOF detection efficiency

The total TOF detection efficiency ϵ_{tot} is defined as the ratio of recoil ions successfully registered by both timing detectors $\eta_{T(1,2)}$ to the number of recoil ions detected by the energy detector η_E:

$$\epsilon_{tot} = \frac{\eta_{T(1,2)}}{\eta_E} = \frac{Number\ of\ recoils\ registered\ by\ both\ timing\ detectors}{Number\ of\ recoils\ detected\ by\ the\ energy\ detector}\ . \tag{5.6}$$

Utilizing the 40 MeV ^{197}Au projectile beam, the values $\eta_{T(1,2)}$ and η_E are directly extracted from the TOF-E histograms. In case of the 170 MeV ^{127}I projectile beam a filter condition is set on the corresponding events within the ΔE-E$_{tot}$ histogram, recorded simultaneously to the TOF acquisition (see section 5.5). This filter condition isolates the corresponding events in the TOF-E$_{tot}$ histograms. Similar to the low energy TOF detection efficiency determinations, the comparison of the number of recoil ions with a correctly assigned time value to the total number of recoil ions being detected defines the total TOF detection efficiency. Error values are given by the counting statistics for each element.

Figure 5.16 illustrates the total TOF detection efficiencies versus the recoil ion masses for both projectile beams. The stopping force dE/dx in carbon for each particular recoil ion mass is also given in Fig. 5.16:

In case of the 40 MeV ^{197}Au projectile beam, a total TOF detection efficiency of $> 90\,\%$ is already reached for ^{7}Li. From ^{10}B up to ^{74}Ge, the efficiency ϵ_{tot} stays above 95 % and reaches a constant value of 100 % within the statistical error. For hydrogen a TOF detection efficiency of 30 % is reached. Helium is detected in the time measurement with an efficiency of 63 %.

The total TOF detection efficiencies utilizing the 170 MeV ^{127}I projectile beam are considerably lower for the light masses from hydrogen (7 %) up to ^{7}Li (72 %), following the trend of the lower stopping forces. A total TOF detection efficiency of $> 95\,\%$ is reached for carbon, continuing by 100 % within the statistical error towards heavier masses.
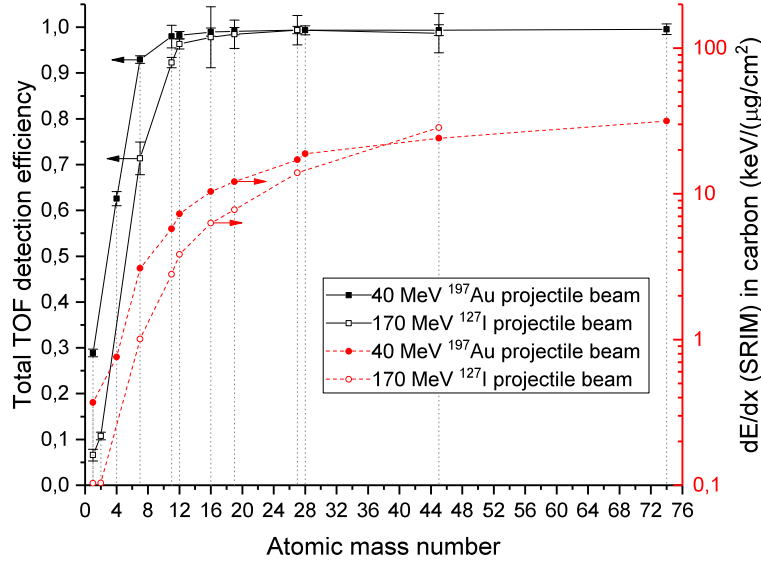
Figure 5.16: *Total TOF detection efficiency and stopping forces within carbon (right, red highlighted axis) for recoil ions created by the 40 MeV ^{197}Au- and the 170 MeV ^{127}I projectile beam versus the recoil ion mass: The TOF detection efficiencies follow the trend of the stopping forces. A TOF detection efficiency of $> 95\%$ is reached for both projectile beams from carbon up to 100 % within the statistical error for heavier recoil masses.*

● **Discussion of the results:**

The total TOF detection efficiency of the setup is $\approx 100\%$ within the statistical error for carbon recoil ions up to heavier masses, for both projectile beams. For the 40 MeV ^{197}Au projectile beam, the results for all recoil ion masses are almost similar to the ones given for two other TOF-E setups presented in [97] (Tandem Accelerator Laboratory of Uppsala University and the Accelerator Laboratory of the University of Helsinki).

For recoil ion masses from hydrogen up to boron, the detection efficiency differs significantly between both projectile beams, due to the increased difference in stopping force and thereby energy deposition within the carbon foils. Thus, in order to be able to measure accurate ERD depth profiles for these elements, additional measurements have to be carried out in order to carefully determine the efficiency of each recoil element in dependence of its scattering energy.

One approach to obtain higher detection efficiencies for light recoil masses is to, either increase the thickness of the carbon foils until secondary electron emission saturation occurs [59], or to coat the foil surface with e.g. a thin LiF- [47] or AlO layer [46]. However, both options degrade the obtainable energy/depth resolution due to an increased energy- and angular scattering within both carbon foils.

An empirical formula to calculate the detection efficiencies in dependence of the stopping forces is given in [97].

5.4.2 Position unit detection efficiency

The detection efficiency of the position unit $\epsilon_{PosUnit}$ is of concern, if the acquired position information provided by T_1 is utilized either for kinematic corrections, or in order to acquire certain filter conditions. Its efficiency can be determined by an internal T_1-time readout (TOF2, see Fig. 4.39) in which the timing unit provides a start signal and the position unit a stop signal taken from the 2-dimensional Backgammon anode. A correct position information is obtained if the time signal from the 2-dimensional Backgammon anode crosses the set CFD threshold of -25 mV. Thus, if a proper TOF2 value is obtained, secondary electron emission occurred in forward- and backward emission direction simultaneously for the corresponding event[8]. With the additional requirement that a successful time of flight value of the actual recoil ion (TOF3, see Fig. 4.39) has to be recorded (T_1-timing unit vs. stop timing detector T_2) the efficiency of the position unit is obtained. Both time readouts are triggered by the energy detector signal of the setup.

The numbers of TOF2-events η_{TOF2} and the number of TOF3-events η_{TOF3} define the detection efficiency of the position unit to be:

$$\epsilon_{PosUnit} = \frac{\eta_{TOF2}}{\eta_{TOF3}} = \frac{Number\ of\ TOF2\text{-}events}{Number\ of\ TOF3\text{-}events}\ . \tag{5.7}$$

The position unit detection efficiencies as well as the stopping forces in carbon, are illustrated in Fig. 5.17 versus the recoil ion masses.

• **Discussion of the results:**

The detection efficiency of the position unit follows the total TOF detection efficiencies closely for both projectile beams (see Fig. 5.16). In case of the 40 MeV ^{197}Au projectile beam, $\epsilon_{PosUnit}$ already reaches values of $> 92\,\%$ for ^{7}Li. Heavier masses are detected by $100\,\%$ within the statistical error. Utilizing the 170 MeV ^{127}I projectile beam, detection efficiencies of $> 92\,\%$ are reached for ^{12}C. Towards heavier recoil ion masses, values of $100\,\%$ are reached within the statistical error, similar to the 40 MeV ^{197}Au projectile

---

[8] The creation of secondary electrons (SE) is independent of the emission direction. Therefore, especially for hydrogen (low SE yield) this represents a substantial requirement for a kinematic correction by an angular measurement.
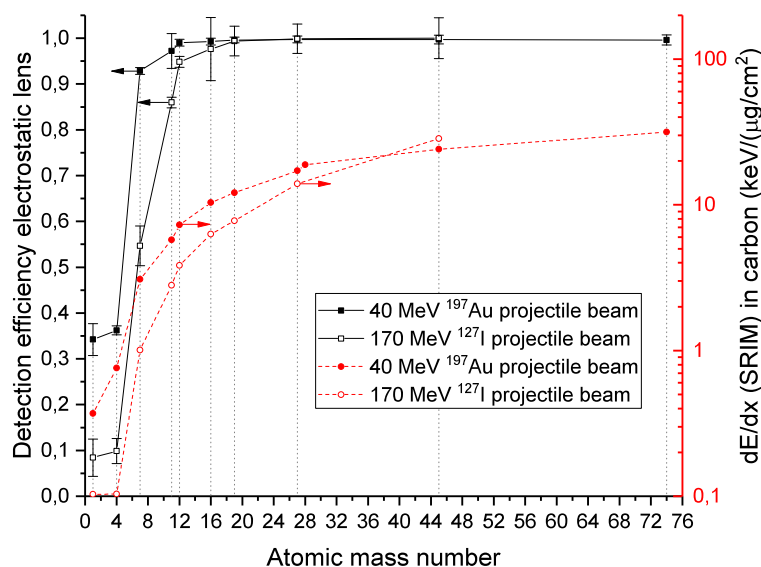
Figure 5.17: *Position unit detection efficiencies and stopping forces within carbon (right, red highlighted axis) for recoil ions created by the 40 MeV ^{197}Au- and the 170 MeV ^{127}I projectile beam, drawn versus the recoil ion mass.*

beam.

The detection efficiency of the position unit is expected to be lower for light recoil ion masses (4 % for H, 20 %^{7}Li) than the one of the timing unit. This mainly contributes to the reduced optical transparency of the position in contrast to the timing unit (84 % vs. 97 %) due to the finer meshed acceleration- and lens grid in combination with the reduced secondary electron yield for light recoil ion masses.

5.5 Combined TOF-ΔE-E method

As previously discussed in section 2.2, the TOF-E method offers a high mass sensitivity and the ΔE-E method a high sensitivity for the nuclear charge of the recoil ion. The combination of both methods into one single setup and thereby to benefit from each particular technique's advantage simultaneously, is demonstrated in this section first in general by an exemplary measurement. In the following sections 5.5.2 and 5.5.3, two further examples are presented, which demonstrate the improvement in mass separation capability and sensitivity achieved by the application of unique filter conditions, exclusively obtained by the combination of both methods.

5.5.1 General aspects and introduction to the method

For TOF-ΔE-E measurements the 170 MeV ^{127}I projectile beam is used. The high recoil ion energies obtained with this beam are on the one hand required to perform the ΔE-E analysis and allow on the other hand to obtain a better depth resolution within greater sample depths compared to the 40 MeV ^{197}Au projectile beam. This contributes to the reduced energy loss straggling and small angle scattering of both, the projectile and the recoil ion within the sample matrix, as discussed in section 2.1.2 of this work (see also Fig. 2.2). To introduce the TOF-ΔE-E method, a measurement on a ^{12}C/^{13}C multilayer structure is presented in the following:

First, a calibration of the ΔE-E histograms is performed by a best fit method of the weighted sum of ΔE- and E_{Res} values, which are obtained for the scattered elements Li, C, N, O, F, Al, and Sc. Each element was deposited with a thickness of $4-5\,\mu g/cm^2$ on thin carbon foils $(3-4\,\mu g/cm^2)$ which were analyzed with the setup in transmission geometry.

Layer	Thickness ($\mu g/cm^2$)
^{13}C	0.2
^{nat}C	2.2
^{13}C	0.2
^{nat}C	2.0
^{13}C	0.3
^{nat}C	1.5
^{13}C	0.3
^{nat}C	1.9
^{13}C	0.3
^{nat}C	4.0
Si substr.	"∞"

**Table 5.2:** *Structure of the $^{12}C/^{13}C$ multilayer sample.*

The multilayer sample structure, consisting of alternating layers of ^{13}C- and natural carbon of different thicknesses (detailed composition shown in Tab. 5.2) is then analyzed at an incident angle of $\alpha = 4°$. The ΔE-E_{Tot} histogram of the sample as well as the corresponding TOF-E_{Tot} histogram acquired simultaneously to the ΔE-E_{Tot} measurement are illustrated in Fig. 5.18. The entire carbon structure on top of the silicon substrate is clearly resolved in both cases (red highlight). As seen by the inset in Fig. 5.18(a), a distinct hydrogen profile is observed in the ΔE-E_{Tot} histogram, whereas due to the low total TOF detection efficiency of 7 % (see section 5.4.1) almost no hydrogen is found in the TOF-E_{Tot} histogram. The different kinds of background occurring in both histograms are object of the following sections 5.5.2 and 5.5.3. However, as expected, the mass separation is better in the TOF-E_{Tot} histogram. This is clearly shown by the magnified views of the read marked areas within both histograms, which are illustrated in Fig. 5.19:

In the ΔE-E_{Tot} histogram both carbon isotope layers can not be separated by the ΔE measurement as seen from the overlap of the first natural carbon layer with the last ^{13}C layer (with respect to the surface energy). In this case the visible separation of both isotope layers is caused by their difference in masses and thereby energy transfer within the binary collision (difference in E_{Tot}). In the TOF-E_{Tot} domain, however, both isotopes are clearly separated over the entire energy range due to the inherent mass sensitivity of the TOF-E technique.

Figure 5.19(a) also shows the projection of the total energies E_{Tot} of all carbon events (^{12}C and ^{13}C) obtained from the multilayer structure. The individual peaks of the layers are clearly resolved and an energy resolution of $\Delta E/E = 0.9\,\% \pm 0.1\,\%$

(FWHM) is obtained from a Gaussian function fitted to the peak obtained from the first ^{12}C layer (including the contribution given by the last ^{13}C layer).

On the right side of Fig. 5.19(b), the projection of the T_0-TOF values on the time axis is shown: In this case, due to the better mass separation, only the T_0-TOF values of the ^{12}C layers are considered (red line in Fig. 5.19(b)). The individual peaks of the layers can not be resolved in the time domain. An error function is fitted to the first ^{12}C layer and a time resolution of $\Delta T/T = 282\,\text{ps} \pm 30\,\text{ps}$ (FWHM) is observed, which transforms into to an energy resolution of $1.3\,\% \pm 0.1\,\%$ (see Eq. 2.18). This clearly demonstrates that the advantage of the TOF-E method to achieve a better energy resolution from the time of flight measurement at low recoil ion energies is not given in case of the high recoil ion velocities obtained with the 170 MeV ^{127}I projectile beam, but still the high mass resolution remains when performing TOF-ΔE-E measurements.

(a)

(b)
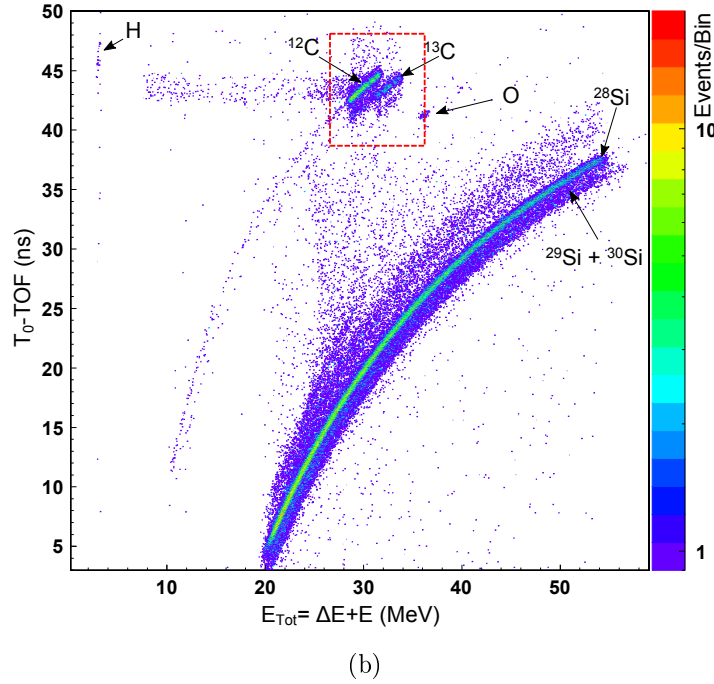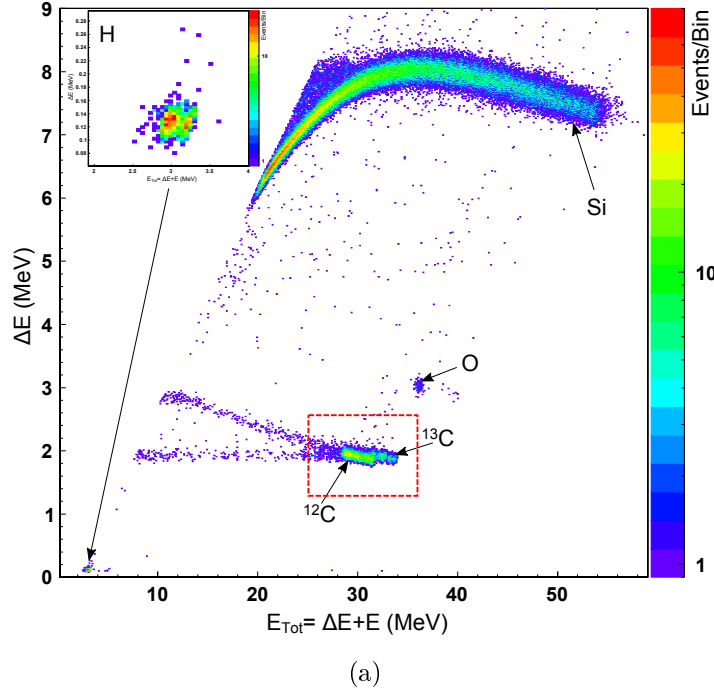
Figure 5.18: *(a): ΔE-E_{Tot} histogram obtained from a $^{12}C/^{13}C$ multilayer sample (see Tab. 5.2): The individual isotope layers are not separated by the ΔE measurement. As seen from the inset, a hydrogen depth profile is obtained. A closer view of the red marked area is illustrated in Fig. 5.19(a) for further discussion. (b): TOF-E_{Tot} histogram acquired simultaneously to the ΔE-E_{Tot} measurement: Due to the inherent mass sensitivity of the TOF-E method, the individual isotope layers are clearly separated. The detection of hydrogen, however, is almost impossible due to the low total TOF detection efficiency given for hydrogen (see section 5.4.1). The read marked area is illustrated in Fig. 5.19(b) for further discussion.*

(a)

(b)
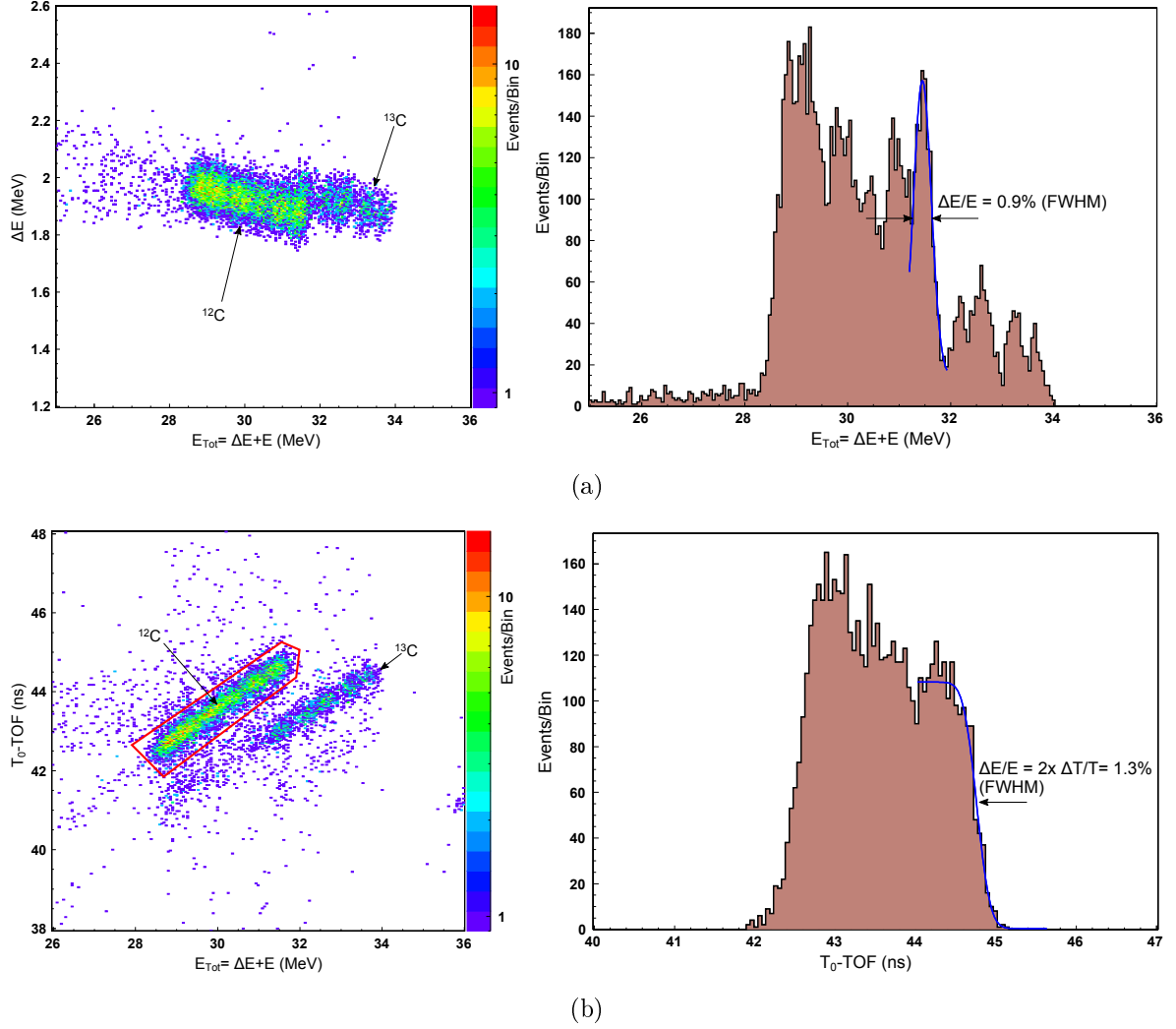
Figure 5.19: *(a)*: ΔE-E_{Tot} *histogram obtained from the* $^{12}C/^{13}C$ *multilayer: The isotopes can not be separated by the* ΔE *measurement as seen by the overlap of carbon events originating from the first* ^{12}C *layer with events of the last* ^{13}C *layer. Right side: The projection of the total energies* E_{Tot} *obtained from all carbon events on the* E_{Tot} *axis is shown. An energy resolution of* $\Delta E/E = 0.9\,\% \pm 0.1\,\%$ *(FWHM) is obtained.* *(b)*: *TOF-*E_{Tot} *histogram of the multilayer structure acquired simultaneously to the* ΔE-E_{Tot} *measurement: The inherent mass sensitivity allows to clearly separate the individual isotope layers. Right side: The* T_0-*TOF values of the* ^{12}C *branch (red line) are projected on the* T_0-*TOF axis. An energy resolution of* $1.3\,\% \pm 0.1\,\%$ *is obtained from the time measurement. Thus, in contrast to the low energy measurements, a worse energy resolution is obtained from the TOF measurement.*

5.5.2   Enhanced isotope separation capability

The isotope separation capabilities are significantly enhanced by the combination of the ΔE-E and the TOF-E method [104]. However, in contrast to the results presented in the previous section, cases exist, in which significant background events caused by other elements within the sample interfere with the events of interest, making an appropriate ERD analysis by only one of both techniques impossible. This problem can be solved by the application of a distinct filter condition obtained by the combined TOF-ΔE-E method, as demonstrated in the following by the analysis of a boron doped carbon layer deposited on a crystalline silicon substrate (results have been published in [56]):

The corresponding ΔE-E_{Tot} histogram of the sample is illustrated in Fig. 5.20. Background in the ΔE-E_{Tot} towards higher ΔE values (larger recoil Z-values, or heavier recoil ion masses) is caused by pile up effects within the ionization chamber due to the high count rates of the dominating elements carbon and silicon within the specimen. Especially recoil ions originating from greater samples depths and thereby with energies low enough to be stopped completely within the ionization gas contribute to this pile up effect: At an effective count rate of 450 Hz obtained from the silicon strip detectors during measurement, the count rate of the ΔE measurement is ≈ 4 kHz. Therefore, even with pile up counteractions being taken, this effect can not be avoided completely.

However, a clear boron signature is obtained, which is not affected by the ΔE pile up. The total content of boron within the carbon layer is determined to be 2.3 at% $\pm$ 0.6 at%. In addition to boron, oxygen is found with a concentration of 1.2 at% $\pm$ 0.4 at% and hydrogen with a concentration of 13.2 at% $\pm$ 0.8 at% within the carbon layer. As seen from the clear boron signature, however, the stable isotopes ^{10}B and ^{11}B can not be separated with the ΔE-E_{Tot} measurement. The corresponding TOF-E_{Tot} histogram, which is acquired simultaneously to the ΔE-E_{Tot} measurement, is illustrated in Fig. 5.21(a):

Due to TOF-ΔE background, neither boron nor its isotopes can be resolved within the TOF-E_{Tot} histogram. The TOF-ΔE background towards lighter masses is created by the fact that the total energy of the recoil ions E_{Tot} is determined by the measurement of their energy loss in the detector gas volume (ΔE) and from their residual energy (E_{Res}) deposited within the silicon strip detectors (see section 4.4.2). Events occur, at which recoil ions create a valuable ΔE signal, but deposit most of their energy within the dead layer of the silicon detector or within its substructures
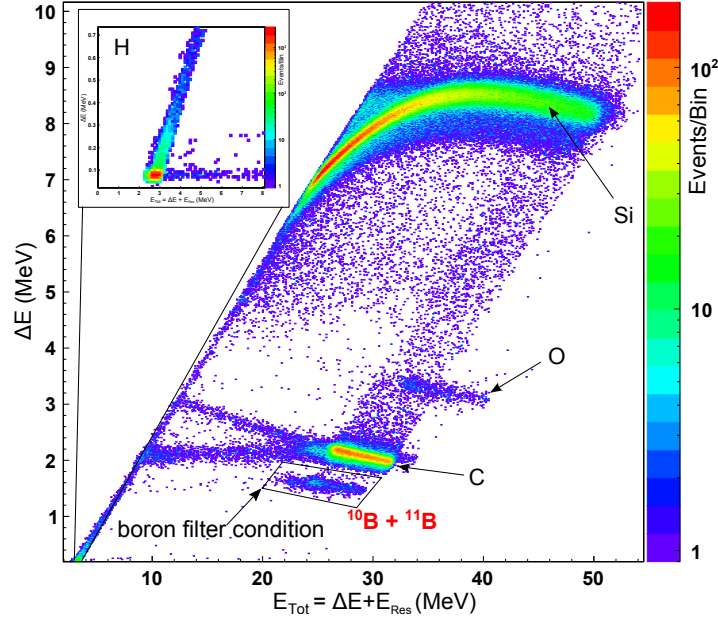
Figure 5.20: *ΔE-E*$_{\mathrm{Tot}}$ *histogram of a boron doped carbon layer on silicon acquired with the 170 MeV* ^{127}*I projectile beam at an incident angle* $\alpha = 7°$. *The stable boron isotopes* ^{10}*B and* ^{11}*B can not be separated with the ΔE-E*$_{Tot}$ *measurement, but the clear boron signature allows to define a filter condition, which can be applied to the TOF-E*$_{Tot}$ *measurement carried out simultaneously to the ΔE-E*$_{Tot}$ *measurement (see Fig. 5.21(a)). The inset shows the detection of hydrogen within the analyzed layer (see text).*

(insufficient charge collection), thereby creating a residual signal pulse height sufficient enough to trigger the data acquisition. Since for these events an appropriate time value is provided, the TOF-ΔE background appears in regions of lighter masses within the TOF-E$_{\mathrm{Tot}}$ histogram. In this specific case, the boron signature overlaps with the TOF-ΔE background originating from the high content carbon layer with the result that boron is not resolved in the histogram.

However, with the combination of both methods by the application of the filter condition obtained for the boron signature from the ΔE-E$_{\mathrm{Tot}}$ histogram to the TOF-E$_{\mathrm{Tot}}$ measurement, boron is isolated from background events and the isotope ^{10}B is well separated from the ^{11}B isotope. Within the statistical accuracy a ^{11}B/^{10}B ratio of 24 %/76 % ± 6.2 % is estimated, which complies with the natural ratio of 19.9 %/80.1 % within the statistical error. In order to extract total elemental concentrations from the TOF-E$_{\mathrm{Tot}}$ measurement, the TOF detection efficiency of the timing detectors has to be taken into account. However, considering a detection efficiency of 100 % for the ΔE-E$_{\mathrm{Tot}}$ system, the acquired TOF-E$_{\mathrm{Tot}}$ data can be scaled accordingly [48].

The TOF-ΔE background towards lighter masses is caused by particles which

deposit most of their energy within the substructures or the dead layer of the silicon strip detectors, but still trigger the data acquisition. One approach to reduce this kind of background would be to additionally perform an energy readout of the entire backside of the silicon strip detectors and filter for events, at which both energies (front and backside) are equal within a certain limit. This method has been successfully applied for double sided silicon strip detectors by Moser et al. [105] in case of proton-proton scattering analysis.

In this example, a single filter condition is created originating from an area within the ΔE-E$_{\text{Tot}}$ histogram, which is not affected by background of any other element present within the analyzed sample. This condition allowed to isolate elements in the TOF-E$_{\text{Tot}}$ histogram from background events and thereby to achieve isotope separation. In case of the detection of nitrogen in carbon, however, the situation changes significantly: Both histograms are affected by background of the carbon matrix and multiple filter conditions have to be established and applied to both histograms. This is demonstrated in the next section of this chapter.
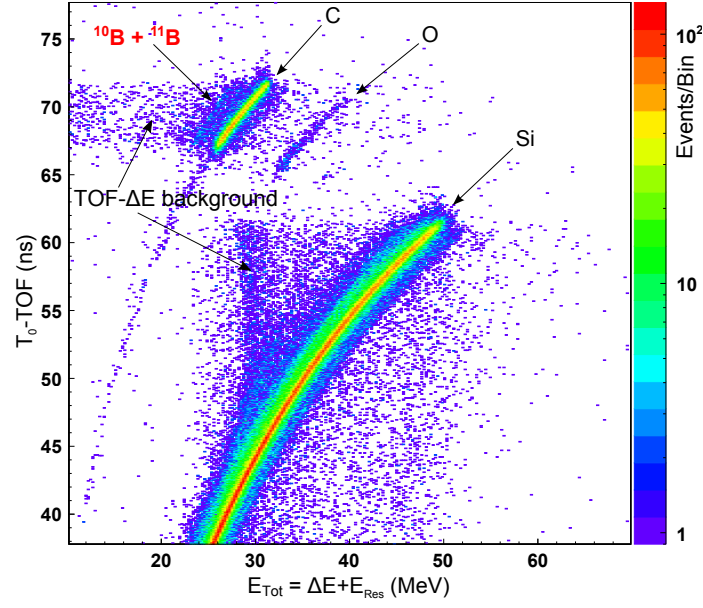
(a)
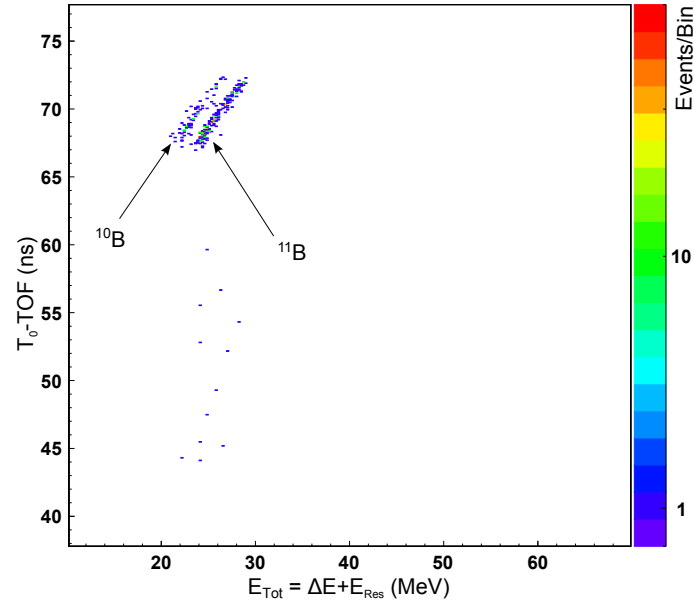
(b)

Figure 5.21: *(a): TOF-E_{Tot} histogram: Due to the TOF-ΔE background (see text for explanation) the boron isotopes can not be separated. (b): The boron filter condition obtained from the clear boron signature within the ΔE-E_{Tot} histogram (see Fig. 5.20) is applied to the TOF-E_{Tot} measurement, which allows to clearly separate the ^{10}B content from the ^{11}B content.*

5.5.3   Detection of nitrogen in diamond

The detection of low nitrogen contents within thin diamond films used as semiconductor materials is of interest since the nitrogen dopant strongly influences the optical and electrical properties of the corresponding layers [106]. Small nitrogen contents within the process gases utilized in the chemical vapour deposition (CVD) processes to create the thin diamond films, either intentionally added or due to contamination, lead by their integration into the diamond to changes in morphology of the produced layers [14, 107]. Thus, exact knowledge of the nitrogen content is besides the scientific aspect also of interest in terms of quality assurance.

The application of the ΔE-E method to detect small amounts of nitrogen in diamond, however, bares difficulties due to pile up signals by the carbon matrix, which create background events within the expected nitrogen region within the ΔE-E histogram.

The detection of nitrogen in diamond with ppm sensitivity was realized in high resolution ERD measurements performed with the Q3D magnetic spectrograph and its focal plane detector, as described in [14]: Multiple redundant particle identification processes and position determinations within the focal plane detector in addition to the magnetic separation by the spectrograph are required to obtain numerous filter conditions, which allow to achieve the high nitrogen sensitivity. However, the disadvantage accompanied with the use of the Q3D magnetic spectrograph for the detection of nitrogen in diamond is the limited, analyzable range of depth of ≈ 100 nm. The ΔE-E detector installed directly within the Q3D scattering chamber running simultaneously to the high resolution Q3D measurements allows to detect nitrogen up to a sample depth of $\approx 1\,\mu$m, but it offers in this case only a sensitivity of $\approx 10^{-3}$ at count rates < 500 Hz to reduce pileup and thereby at long acquisition times.

The combination of the ΔE-E and the TOF-E method, however, offers the opportunity to achieve a better sensitivity for the detection of nitrogen in diamond again up to an analyzable sample depth range of $\approx 1\,\mu$m within a single measurement. This is demonstrated in the following for measurements on a HPHT[9] diamond specimen with a typical nitrogen content of $100 - 1000$ ppm utilizing the 170 MeV ^{127}I projectile beam:

---

[9] $=$ High Pressure High Temperature
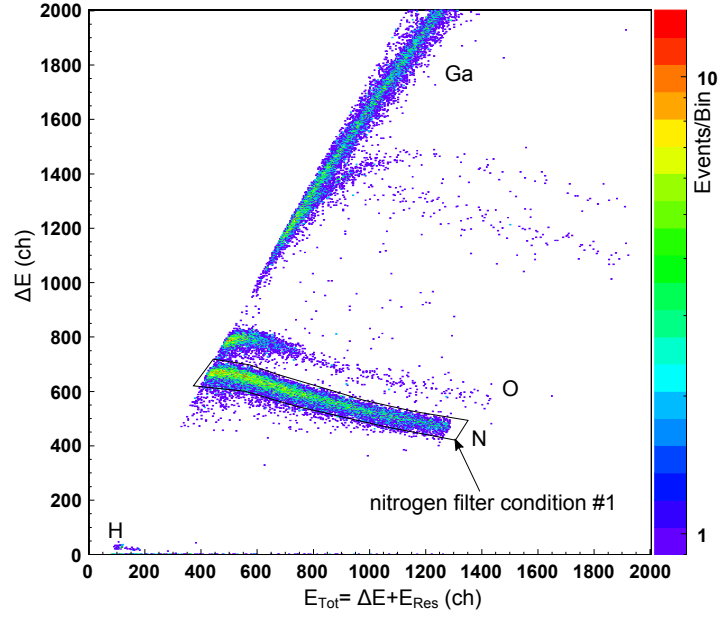
(a)
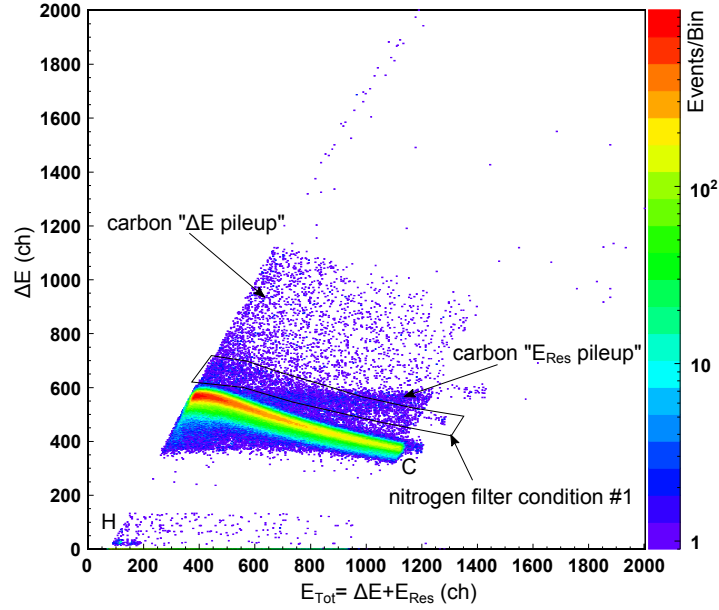
(b)

Figure 5.22: *(a)*: *A gallium nitride sample (GaN) is analyzed in order to establish an exclusive nitrogen filter condition within the ΔE-E_{Tot} histogram. **(b)**: ΔE-E_{Tot} histogram of the diamond sample: Due to the high count rates obtained for carbon, signal pileup is created (ΔE- and E_{Res} pileup) which overlaps with events within the nitrogen filter condition #1. Thus, in this case the determination of the nitrogen concentration is not possible by exclusively carrying out the ΔE-E_{Tot} measurement.*

First, a gallium nitride (GaN) sample is analyzed in order to establish an exclusive nitrogen filter condition (#1) within the ΔE-E$_{Tot}$ histogram, which is valid for the entire analyzable sample depth and all further measurements. The ΔE-E$_{Tot}$ histogram of the GaN sample with the filter condition #1 drawn into it, is illustrated in Fig. 5.22(a). The diamond specimen is subsequently analyzed at the same incident angle. The corresponding ΔE-E$_{Tot}$ is illustrated in Fig. 5.22(b):

Due to the carbon matrix "ΔE pileup" occurs towards larger Z-values within in the histogram. This pileup is caused by the high carbon count rate observed in the gas ionization chamber. Even with pileup rejection actions being taken, this pileup can not be avoided completely. In addition to that, "E$_{Res}$ pileup" is observed, which is created by the high carbon count rates within the silicon strip detectors (E$_{Res}$ measurement). Both kinds of pileup events clearly interfere with the true nitrogen events within the marked nitrogen filter condition obtained from the measurement of the GaN sample. Thus the concentration of nitrogen within the diamond can not be determined exclusively by the ΔE-E$_{Tot}$ measurement. However, the nitrogen filter condition #1 can be applied to the TOF-E$_{Tot}$ histogram, acquired simultaneously to the ΔE-E$_{Tot}$ measurement:

Figure 5.23(a) shows the TOF-E$_{Tot}$ histogram obtained for the ΔE-E$_{Tot}$ events within the nitrogen filter condition. The nitrogen content is clearly visible in the TOF-E$_{Tot}$ histogram. However, besides the nitrogen branch also a carbon branch as well as uncorrelated events are observed. The carbon related branch is caused by real carbon events with energy values altered by "ΔE pileup". Thus they appear in the nitrogen region in the ΔE-E$_{Tot}$, but are in the TOF-E$_{Tot}$ domain close to the a true carbon branch (E$_{Tot}$ = E$_{Res}$+ΔE). The uncorrelated events are caused by e.g. two recoil ions, which are detected by the silicon strip detectors within a time frame short enough to pile up in the energy signal. However, the create false start- and stop triggers of the time measurement, thus the obtained TOF value appears uncorrelated to any real elemental branch within the TOF-E$_{Tot}$ histogram. As illustrated in Fig. 5.23(b), a second filter condition (#2) is defined for the nitrogen in the already filtered TOF-E$_{Tot}$ histogram. This filter condition is then, together with the first nitrogen filter condition #1, applied to the ΔE-E$_{Tot}$ measurement of the diamond sample. The resulting ΔE-E$_{Tot}$ histogram is illustrated in Fig. 5.24:

The carbon background in the ΔE-E$_{Tot}$ measurement is suppressed by both filter conditions and the nitrogen content of the diamond specimen is detected. With 440 nitrogen events and 7.7×10^5 carbon events being detected within an equal depth range as well as by consideration of the different scattering cross sections, the nitrogen content of the diamond sample is determined to be N/C = 5.5×10^{-4}. This value is within

the expected range of this kind of HPHT diamond.

In case of 10 unambiguously detected nitrogen events within the filtered ΔE-E$_{\text{Tot}}$ histogram a sensitivity in the order of 10 ppm can be reached, which is better by two orders of magnitude than achieved with the ΔE-E detector installed directly within the Q3D scattering chamber. Even a sensitivity of 1 ppm can be expected to be reached with the combined TOF-ΔE-E method, which has to be confirmed by future measurements. However, for the determination of concentrations in the range of 1 ppm, the detection is limited by the counting statistics. Thus, in order to detect 1 ppm in diamond by e.g. 5 distinct nitrogen events within the nitrogen filter condition, at least 5×10^6 carbon events have to be detected.
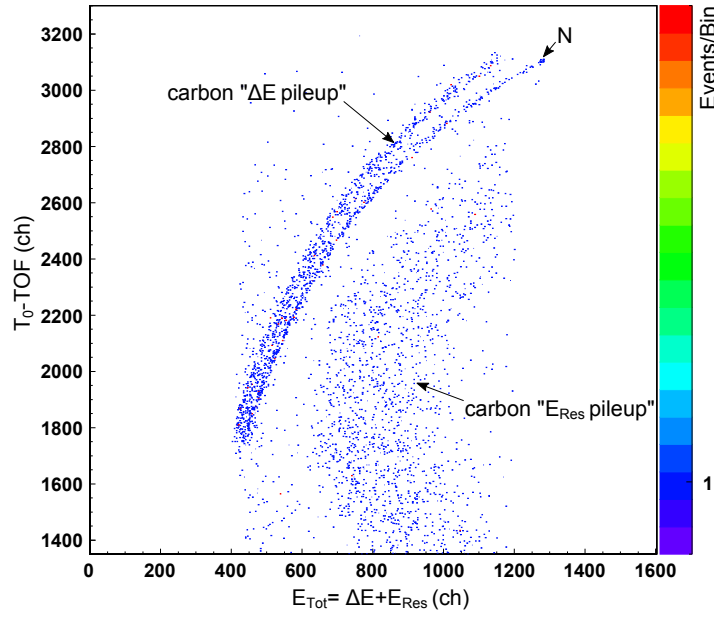
(a)
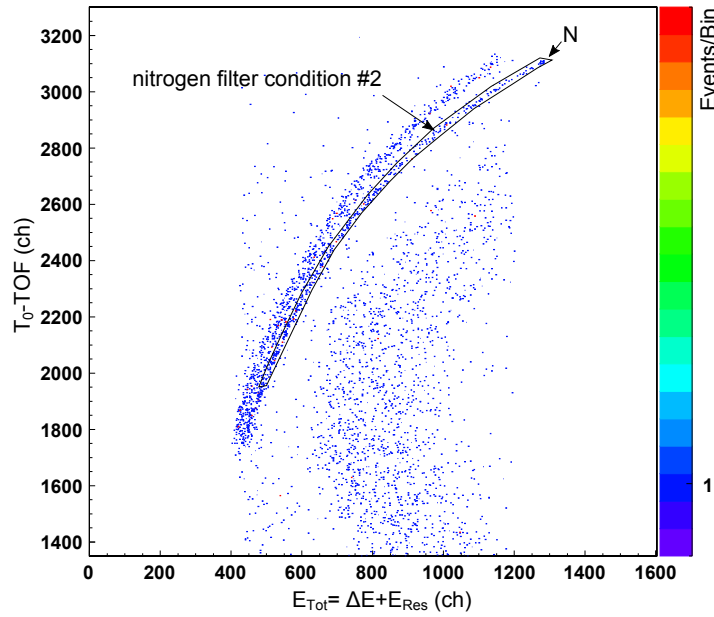
(b)

Figure 5.23: *(a): TOF-E_{Tot} histogram of the events within the nitrogen filter condition #1, acquired simultaneously to the ΔE-E_{Tot} measurement: The events of the ΔE-E_{Tot} histogram within the filter condition (see Fig. 5.22) are clearly separated in carbon pileup- and real nitrogen events. (b): The clear nitrogen separation in the TOF-E_{Tot} domain allows to define a second nitrogen filter condition (#2), which can then be applied together with the filter condition #1 to the ΔE-E_{Tot} measurement of the diamond sample (see Fig. 5.24).*
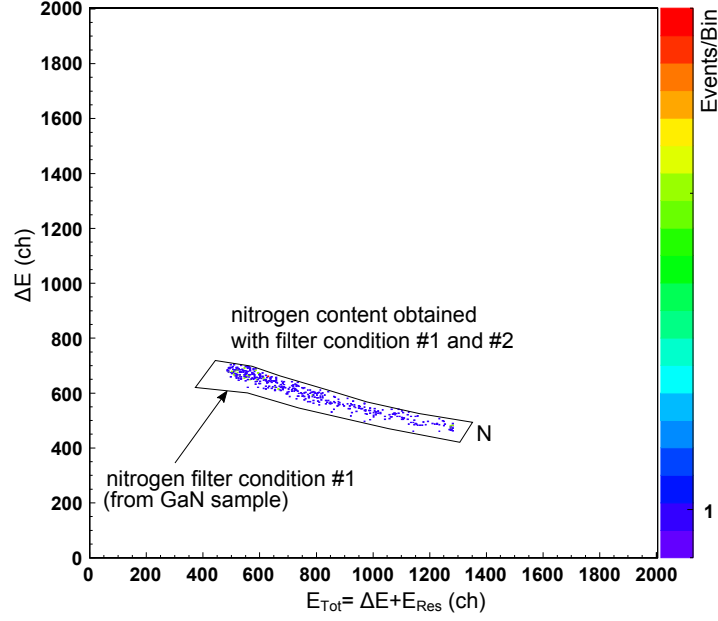
Figure 5.24: *Same ΔE-E$_{Tot}$ histogram as illustrated in Fig. 5.22(b): The application of both filter conditions obtained by the combined TOF-ΔE-E measurement, suppresses the carbon background completely. The nitrogen content of the diamond is clearly resolved and a concentration of N/C = 5.5 × 10^{-4} is found within the particular sample.*

Chapter 6

Conclusion

The aim of this work was to develop a detection system based on the time of flight – energy (TOF-E) method for the quantification of high resolution ERD depth profiles obtained with the Q3D magnetic spectrograph or to work as stand alone detection system for the use with low projectile beam energies (E = 0.2 MeV·A).

Kinematic effects due to the angular acceptance of the TOF spectrometer within the scattering plane as well as due to the beam spot size on the sample worsen the achievable energy resolution and thereby depth resolution of the spectrometer. Thus, main focus of the development was set on the position sensitivity of the start timing detector and the energy detector, which both together allow to carry out a true angular measurement of every recoil ion trajectory within the scattering plane to correct for the kinematic effects.

A novel start time detector was designed, which detects secondary electrons emitted from a thin carbon foil on penetration of the recoil ions in forward- and backward emission direction for separate time- and position measurement in a straight geometry. For signal creation, the secondary electrons are amplified by two identical micro channel plate (MCP) stacks, one for the time readout and one for the position readout. The MCP stack was specifically developed for the integration into the new time detector design layout. An intrinsic time readout resolution of < 100 ps (FWHM) was achieved. For the position readout of the MCP stack a position sensitive 2-dimensional Backgammon anode was designed and a readout resolution of 60 μm (FWHM) was demonstrated.

However, the main contribution to the overall achievable position resolution is accredited to the momentum distribution of the secondary electrons and not to the readout resolution of the MCP stack. Thus, an electrostatic lens was simulated and constructed to focus the secondary electrons from their point of origin on the carbon foil onto the MCP stack, maintaining the position information despite their

momentum distribution. The measured position resolution was in excellent agreement with the simulations and an overall position resolution of $< 0.6\,$mm was determined. This is better by a factor of 2 than ever published in literature and sufficient enough to carry out an angular measurement in combination with the position information provided by the energy detector.

The position sensitive energy detector was developed following a standard gas ionization chamber (GIC) design with two plane electrodes (anode and cathode) and a Frisch grid between them. A multi- segmented $100\,$nm thick silicon nitride (SiN) membrane is used as entrance window of the GIC to reduce energy broadening of the recoil ions and thereby to enhance the detector performance at low energies. The electronics for preamplification of the energy signal are directly mounted onto the readout electrodes within the gas volume to reduce electronic noise.

A position determination of the recoil ion within the energy detector can in principle be obtained from the energy signals induced on the electrodes (anode-cathode ratio), however, the achievable position resolution was greatly improved in this work by a drift time measurement of the ionization electrons within the gas volume of the GIC. The stop timing detector of the TOF-E setup creates the start signal of the drift time measurement, the energy signal of the anode stops it. With this method, the position resolution for the low energetic recoil ions was improved by a factor of ≈ 2, to $2.4\,$mm (FWHM) and the linearity of the position measurement in terms of energy dependency was greatly improved.

With the accuracy given by both position determinations (start timing- and energy detector), the true scattering angle of each recoil ion can be determined with an angular resolution of $2.5\,$mrad (FWHM). This allowed to reduce the contributions of the kinematic effects on the energy- and thereby depth resolution from $3.3\,\%$ to $0.4\,\%$.

The TOF-E setup can also be used at higher recoil ion energies. Therefore silicon strip detectors are added at the end of the ionization volume, which allow to measure the residual energy of the recoil ions after traversing the entire gas volume. This allows to perform a classical ΔE-E$_{Res}$ analysis with the energy detector. Together with the time of flight information a combined TOF-ΔE-E$_{Res}$ measurement can be executed as presented in this work.

The performance of the developed TOF-E setup was characterized by ERD measurements on a variety of well-known samples using a $40\,$MeV ^{197}Au projectile beam (low energetic recoil ions) as well as a $170\,$MeV ^{127}I projectile beam for the combined TOF-ΔE-E$_{Res}$ measurements (high recoil ion energies). With the help of the position information provided by the individual detectors, the contribution of

the kinematic effect to the resolution of the energy measurement as well as to the resolution of the time measurement was reduced to a level at which other contributions dominate.

TOF-E ERD measurements on a $0.7\,\mu\mathrm{g/cm^2}$ thick ^{13}C layer utilizing $40\,\mathrm{MeV}$ ^{197}Au projectile beam demonstrated a surface depth resolution of $\Delta\mathrm{x} = 2.3\,\mathrm{nm} \pm 0.2\,\mathrm{nm}$ (FWHM), which was achieved with the energy information obtained from the time measurement. Simulations carried out with the Monte Carlo code CORTEO indicated that one contribution to the depth resolution is given by inhomogeneities of the carbon foil within the first timing detector.

The achievable mass resolution of the TOF-E setup depends besides the TOF resolution mainly on the resolution of the energy detector, the depth of analysis and on the particular sample composition. Thus, it was characterized by an exemplarily measurement on a sample consisting of a MgF_2 layer on top of a Al layer deposited on a borosilicate glass substrate. A mass resolution $\Delta\mathrm{M}$ of < 1 within a mass range of $1-39$ is achieved with the setup.

The combined TOF-ΔE-E$_{\mathrm{Res}}$ measurements performed at high recoil ion energies utilizing the $170\,\mathrm{MeV}$ ^{127}I projectile beam demonstrate the advantage of this technique to benefit simultaneously from the high sensitivity of the ΔE-E$_{\mathrm{Res}}$ method on the nuclear charge and of the high mass sensitivity of TOF-E method. Unique filter conditions can be established and applied to either one or both spectra acquired within one single measurement to reduce background and increase the sensitivity of the measurement. This was demonstrated for the difficult case of the detection of nitrogen in diamond, in which severe pileup caused by the carbon matrix was suppressed with the help of two individual filter conditions, one in the TOF-E$_{\mathrm{Res}}$ domain and the other in the ΔE-E$_{\mathrm{Res}}$ domain. Hence, the sensitivity for the detection of nitrogen in diamond could be enhanced to $10\,\mathrm{ppm}$ with this technique, which is better by two orders of magnitude compared to standard ΔE-E analysis.

However, there is still room for improvement: The main contribution to the achievable energy resolution of the TOF-E setup is given by the inhomogeneity of the carbon foil within the start timing detector, which causes differences in energy loss of the recoil ions. The carbon foils used in the setup are produced by a laser plasma ablation process (LPA) of pure carbon onto a water soluble Lensodel substrate. This procedure produces a smooth foil surface, but does not account for the inhomogeneities. One potential way to achieve an almost perfect homogeneity as well as a surface roughness in the atomic range would be to use one or a few graphene layers as detector foil. However, this demands that the graphene layers are stable

enough to cover a supporting structure with a high optical transparency.

The results presented in this work showed that the contribution by the kinematic effect due to both the angular acceptance in the scattering plane and due to the beam spot size can be corrected to a level at which other contributions dominate the energy resolution (see Tab. 5.1). This means that a further increase in solid angle of detection would not affect the performance in terms of energy-/depth resolution by any means, but would lead to a better sensitivity with respect to irradiation damage. At the moment, the main limitation in solid angle is given by the close presence of the Q3D magnetic spectrograph, which restricts the possible locations of the individual detectors of the TOF-E setup. This leads to the large distance between the target and start timing detector of 776 mm. With the intention to use the setup or a copy of it as stand alone detection system for low- and high energy measurements at another beam line, the solid angle of detection could be increased by a factor of ≈ 3 by simply decreasing the distance from T_1 to the target to 150 mm.
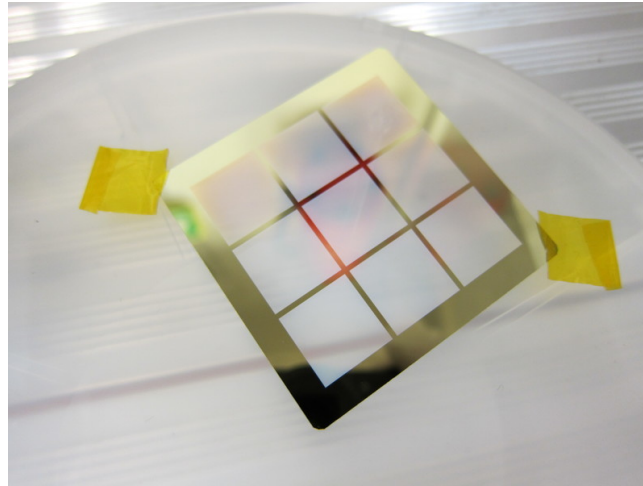
Figure 6.1: *New segmented silicon nitride membrane as entrance window for the energy detector of the TOF-E setup (Amptek, Inc.). The individual membranes are 100 nm in thickness at a size of $13 \times 13\,mm^2$. The future integration into the setup allows to increase the solid angle of detection by $\approx 30\,\%$.*

Due to the segmented structure of the silicon nitride entrance window with its large areas of non transparent material between the individual segments (see Fig. 4.35), the solid angle of detection of the TOF-E setup is limited to 0.25 msr at the moment. However, recently larger silicon nitride membranes became available. Thus, a window with the same overall dimensions, but consisting of 9 segments, each of a size of $13 \times 13\,mm^2$ and a membrane thickness of 100 nm, was acquired (Amptek, Inc.). A photograph of

the window is illustrated in Fig.6.1. This window allows to increase the solid angle of detection by $\approx 30\,\%$ to $0.36\,\mathrm{msr}$ and has to be integrated into the setup in the future.

The unique filter conditions obtained by the combined TOF-ΔE-E$_{\mathrm{Res}}$ technique demonstrated their effectiveness in terms of sensitivity enhancement for e.g. the detection of nitrogen in diamond. However, a further option for background suppression can be achieved by a TOF based pile up rejection, which will be integrated into the setup in the future.

Bibliography

[1] P. Williams, Secondary Ion Mass Spectrometry, Annu. Rev. Mater. Sci. 15 (1985) 517–548.

[2] C. Hubschmid, D. Landolt, H. J. Mathieu, XPS and AES analysis of passive films on Fe-25Cr-X (X = Mo, V, Si and Nb) model alloys, Fresen. J. Anal. Chem. 353 (1995) 234–239.

[3] C. Wagner, G. Muilenberg, Handbook of x-ray photoelectron spectroscopy: a reference book of standard data for use in x-ray photoelectron spectroscopy, Perkin-Elmer Corp., Physical Electronics Division, 1979.

[4] J. Tesmer, M. Nastasi, Handbook of Modern Ion Beam Materials analysis, Materials Research Society, 1995.

[5] J. L'Ecuyer, C. Brassard, C. Cardinal, J. Chabbal, L. Deschénes, J. P. Labrie, B. Terreault, J. G. Martel, R. St.-Jacques, An accurate and sensitive method for the determination of the depth distribution of light elements in heavy materials, Journal of Applied Physics 47 (1976) 381–382.

[6] W. M. A. Bik, F. H. P. M. Habraken, Elastic recoil detection, Reports on Progress in Physics 56 (1993) 859.

[7] W. Assmann, J. Davies, G. Dollinger, J. Forster, H. Huber, T. Reichelt, R. Siegele, ERDA with very heavy ion beams, Nuclear Instruments and Methods in Physics Research Section B: Beam Interactions with Materials and Atoms 118 (1996) 242 – 250.

[8] J. Stoquert, G. Guillaume, M. Hage-Ali, J. Grob, C. Ganter, P. Siffert, Determination of concentration profiles by elastic recoil detection with a ΔE-E gas telescope and high energy incident heavy ions, Nuclear Instruments and Methods in Physics Research Section B: Beam Interactions with Materials and Atoms 44 (1989) 184 – 194.

[9] G. Dollinger, A. Bergmaier, L. Goergens, P. Neumaier, W. Vandervorst, S. Jakschik, High resolution elastic recoil detection, Nuclear Instruments and Methods in Physics Research Section B: Beam Interactions with Materials and Atoms 219 - 220 (2004) 333 – 343.

[10] G. Dollinger, M. Boulouednine, A. Bergmaier, T. Faestermann, C. Frey, Limits in elastic recoil detection analysis with heavy ions, Nuclear Instruments and Methods in Physics Research Section B: Beam Interactions with Materials and Atoms 118 (1996) 291 – 300.

[11] G. Dollinger, C. Frey, A. Bergmaier, T. Faestermann, Elastic recoil detection with single atomic layer depth resolution, Nuclear Instruments and Methods in Physics Research Section B: Beam Interactions with Materials and Atoms 136 - 138 (1998) 603 – 610.

[12] A. Bergmaier, G. Dollinger, C. Frey, A compact ΔE-E$_{res}$ detector for elastic recoil detection with high sensitivity, Nuclear Instruments and Methods in Physics Research Section B: Beam Interactions with Materials and Atoms 136 - 138 (1998) 638 – 643.

[13] G. Dollinger, A. Bergmaier, C. Frey, M. Roesler, H. Verhoeven, Impurities of light elements in CVD diamond, Diamond and Related Materials 4 (1995) 591 – 595.

[14] A. Bergmaier, G. Dollinger, T. Faestermann, C. Frey, M. Ferguson, H. GÃijttler, G. Schulz, H. Willerscheid, Detection of nitrogen in CVD diamond, Diamond and Related Materials 5 (1996) 995 – 997.

[15] A. Flöter, H. Güttler, G. Schulz, D. Steinbach, C. Lutz-Elsner, R. Zachai, A. Bergmaier, G. Dollinger, The nucleation and growth of large area, highly oriented diamond films on silicon substrates, Diamond & Related Materials 7 (1998) 283–288.

[16] J. Stiegler, A. Bergmaier, J. Michler, Y. von Kaenel, G. Dollinger, E. Blank, Impurity and defect incorporation in diamond films deposited at low substrate temperatures, Diamond and Related Materials 7 (1998) 193 – 199.

[17] A. Bergmaier, G. Dollinger, T. Faestermann, C. Frey, W. Dworschak, H. Ehrhardt, Elemental composition of thin c-BN layers, Diamond and Related Materials 4 (1995) 478 – 481.

[18] M. Kuhr, R. Freudenstein, S. Reinke, W. Kulisch, G. Dollinger, A. Bergmaier, Hydrogen incorporation during nucleation and growth of c-BN films, Diamond and Related Materials 5 (1996) 984 – 989.

[19] S. Ulrich, H. Ehrhardt, T. Theel, J. Schwan, S. Westermeyr, M. Scheib, P. Becker, H. Oechsner, G. Dollinger, A. Bergmaier, Phase separation in magnetron sputtered superhard BCN thin films, Diamond and Related Materials 7 (1998) 839 – 844.

[20] H. Angerer, D. Brunner, F. Freudenberg, O. Ambacher, M. Stutzmann, R. Höpler, T. Metzger, E. Born, G. Dollinger, A. Bergmaier, S. Karsch, H.-J. Körner, Determination of the Al mole fraction and the band gap bowing of epitaxial AlxGa1-xN films, Applied Physics Letters 71 (1997) 1504–1506.

[21] O. Ambacher, M. S. Brandt, R. Dimitrov, T. Metzger, M. Stutzmann, R. A. Fischer, A. Miehr, A. Bergmaier, G. Dollinger, Thermal stability and desorption of Group III nitrides prepared by metal organic chemical vapor deposition, Journal of Vacuum Science & Technology B: Microelectronics and Nanometer Structures Processing, Measurement, and Phenomena 14 (1996) 3532–3542.

[22] O. Ambacher, H. Angerer, R. Dimitrov, W. Rieger, M. Stutzmann, G. Dollinger, A. Bergmaier, Hydrogen in Gallium Nitride grown by MOCVD, physica status solidi (a) 159 (1997) 105–119.

[23] G. Dollinger, T. Faestermann, C. Frey, A. Bergmaier, E. Schwabedissen, T. Fischer, R. Schwarz, Depth microscopy at interfaces, Nuclear Instruments and Methods in Physics Research Section B: Beam Interactions with Materials and Atoms 85 (1994) 786 – 789.

[24] G. Dollinger, M. Boulouednine, T. Faestermann, P. Maier-Komor, Depth microscopy for thin film analysis, Nuclear Instruments and Methods in Physics Research Section A: Accelerators, Spectrometers, Detectors and Associated Equipment 334 (1993) 187 – 190.

[25] G. Dollinger, T. Faestermann, C. Frey, P. Maier-Komor, Calcium targets with low hydrogen content, Nuclear Instruments and Methods in Physics Research Section A: Accelerators, Spectrometers, Detectors and Associated Equipment 362 (1995) 60 – 63.

[26] M. Mayer, R. Behrisch, H. Plank, J. Roth, G. Dollinger, C. Frey, Codeposition of hydrogen with beryllium, carbon and tungsten, Journal of Nuclear Materials 230 (1996) 67 – 73.

[27] G. Dollinger, C. M. Frey, A. Bergmaier, T. Faestermann, Depth profile analysis with monolayer resolution using elastic recoil detection (ERD), EPL (Europhysics Letters) 42 (1998) 25.

[28] Y. Wang, M. Nastasi, Handbook of Modern Ion Beam Materials Analysis 2 Volume Set, Materials Research Society, 2010.

[29] H. H. Andersen, F. Besenbacher, P. Loftager, W. Möller, Large-angle scattering of light ions in the weakly screened Rutherford region, Phys. Rev. A 21 (1980) 1891–1901.

[30] A. Bergmaier, G. Dollinger, C. M. Frey, Quantitative elastic recoil detection, Nucl. Instrum. Methods B: Beam Interactions with Materials and Atoms 99 (1995) 488 − 490.

[31] J. F. Ziegler, J. P. Biersack, U. Littmark, The Stopping and Range of Ions in Solids, Pergamon Press, New York, 1985.

[32] L. C. Northcliffe, R. F. Schilling, Range and stopping-power tables for heavy ions, Atomic Data and Nuclear Data Tables 7 (1970) 233–463.

[33] C. Frey, G. Dollinger, A. Bergmaier, T. Faestermann, P. Maier-Komor, Charge state dependence of the stopping power of 1 meV/A 58Ni ions, Nuclear Instruments and Methods in Physics Research Section B: Beam Interactions with Materials and Atoms 107 (1996) 31 − 35.

[34] C. Frey, G. Dollinger, A. Bergmaier, T. Faestermann, P. Maier-Komor, Charge state dependence of the stopping power of 1 meV/A 58Ni-ions in thin carbon foils, Nuclear Instruments and Methods in Physics Research Section B: Beam Interactions with Materials and Atoms 99 (1995) 205 − 209.

[35] A. Bergmaier, Quantitative Elementanalytik an Diamantschichten Mittels elastischer Vorwärtsstreuung (ERD) hochenergetischer schwerer Ionen, Doktorarbeit, Technische Universität München, (1999).

[36] N. H. D. Bohr, The penetration of atomic particles through matter, Munksgaard, 1960.

[37] J. Lindhard, M. Scharff, Energy loss in matter by fast particles of low charge, Matematisk-Fysiske Meddelelser Kongelige Danske Videnskabernes Selskab 27 (1953) 1–31.

[38] W. K. Chu, Calculation of energy straggling for protons and helium ions, Phys. Rev. A 13 (1976) 2057–2060.

[39] Q. Yang, D. O'Connor, Z. Wang, Empirical formulae for energy loss straggling of ions in matter, Nuclear Instruments and Methods in Physics Research Section B: Beam Interactions with Materials and Atoms 61 (1991) 149 – 155.

[40] P. Sigmund, K. Winterbon, Small-angle multiple scattering of ions in the screened Coulomb region: I. Angular distributions, Nuclear Instruments and Methods 119 (1974) 541 – 557.

[41] F. Pászti, E. Szilágyi, E. Kótai, Optimization of the depth resolution in elastic recoil detection, Nuclear Instruments and Methods in Physics Research Section B: Beam Interactions with Materials and Atoms 54 (1991) 507 – 512.

[42] E. Szilágyi, F. Pászti, G. Amsel, Theoretical approximations for depth resolution calculations in IBA methods, Nuclear Instruments and Methods in Physics Research Section B: Beam Interactions with Materials and Atoms 100 (1995) 103 – 121.

[43] E. Szilágyi, Energy and depth resolution in elastic recoil coincidence spectrometry, Nuclear Instruments and Methods in Physics Research Section B: Beam Interactions with Materials and Atoms 268 (2010) 1731 – 1735.

[44] G. Dollinger, A. Bergmaier, T. Faestermann, C. M. Frey, High resolution depth profile analysis by elastic recoil detection with heavy ions, Fresenius' Journal of Analytical Chemistry 353 (1995) 311–315.

[45] W. Bohne, J. Röhrich, G. Röschert, The new time-of-flight ERDA setup at the HMI-berlin, Nuclear Instruments and Methods in Physics Research Section B: Beam Interactions with Materials and Atoms 139 (1998) 219 – 224.

[46] M. Laitinen, M. Rossi, J. Julin, T. Sajavaara, Time-of-flight - Energy spectrometer for elemental depth profiling - Jyväskylä design, Nuclear Instruments and Methods in Physics Research Section B: Beam Interactions with Materials and Atoms 337 (2014) 55 – 61.

[47] Z. Siketić, I. B. Radović, M. Jakšić, Development of a time-of-flight spectrometer at the Ruđer Bošković Institute in Zagreb, Nuclear Instruments and Methods in Physics Research Section B: Beam Interactions with Materials and Atoms 266 (2008) 1328 – 1332.

[48] S. Giangrandi, T. Sajavaara, B. Brijs, K. Arstila, A. Vantomme, W. Vandervorst, Low-energy heavy-ion TOF-ERDA setup for quantitative depth profiling of thin films, Nuclear Instruments and Methods in Physics Research Section B: Beam Interactions with Materials and Atoms 266 (2008) 5144 – 5150.

[49] C. Kottler, M. Döbeli, F. Glaus, M. Suter, A spectrometer for low energy heavy ion ERDA, Nuclear Instruments and Methods in Physics Research Section B: Beam Interactions with Materials and Atoms 248 (2006) 155 – 162.

[50] M. Döbeli, C. Kottler, M. Stocker, S. Weinmann, H.-A. Synal, M. Grajcar, M. Suter, Gas ionization chambers with silicon nitride windows for the detection and identification of low energy ions, Nuclear Instruments and Methods in Physics Research Section B: Beam Interactions with Materials and Atoms 219 - 220 (2004) 415 – 419.

[51] C. Frey, Atomar auflösende Tiefenmikroskopie mit hochenergetischen, schweren Ionen, Doktorarbeit, Technische Universität München, (1997).

[52] A. Kern, Neukonstruktion des Stopdetektors für die Time-of-Flight Methode der Elastic Recoil Detection (ERD), Diploma Thesis, Universität der Bundeswehr München, (2008).

[53] F. Busch, W. Pfeffer, B. Kohlmeyer, D. Schüll, F. Pühlhoffer, A position-sensitive transmission time detector, Nuclear Instruments and Methods 171 (1980) 71 – 74.

[54] M. Laitinen, M. Rossi, J. Julin, T. Sajavaara, Secondary electron flight times and tracks in the carbon foil time pick-up detector, Nuclear Instruments and Methods in Physics Research Section B: Beam Interactions with Materials and Atoms 336 (2014) 55 – 62.

[55] H. Ernst, ENELOSS (routine to calculate the differential energyloss of ionising radiation in matter), 1981, modifiziert von k (1984).

[56] S. Eschbaumer, A. Bergmaier, D. Seiler, G. Dollinger, Time of flight assisted ΔE-E method for enhanced isotope separation capabilities in heavy ion elastic recoil detection analysis, Nuclear Instruments and Methods in Physics Research Section B: Beam Interactions with Materials and Atoms (in press).

[57] Z. Siketić, I. B. Radović, M. Jakśić, N. Skukan, Time of flight elastic recoil detection analysis with a position sensitive detector, Review of Scientific Instruments 81.

[58] C. G. Drexler, R. D. DuBois, Energy- and angle-differential yields of electron emission from thin carbon foils after fast proton impact, Phys. Rev. A 53 (1996) 1630–1637.

[59] P. Koschar, K. Kroneberger, A. Clouvas, M. Burkhard, W. Meckbach, O. Heil, J. Kemmler, H. Rothard, K. O. Groeneveld, R. Schramm, H.-D. Betz, Secondary-electron yield as a probe of preequilibrium stopping power of heavy ions colliding with solids, Phys. Rev. A 40 (1989) 3632–3636.

[60] J. L. Wiza, Microchannel plate detectors, Nuclear Instruments and Methods 162 (1979) 587 − 601.

[61] M. Maier, P. Sperr, On the construction of a fast constant fraction trigger with integrated circuits and application to various photomultipliertubes, Nuclear Instruments and Methods 87 (1970) 13 − 18.

[62] E. Pollacco, J. Jacmart, Y. Blumenfeld, P. Chomaz, N. Frascaria, J. Garron, J. Roynette, A compact gridless channel plate detector for time-of-flight measurements, Nuclear Instruments and Methods in Physics Research 225 (1984) 51 − 56.

[63] M. Lampton, C. W. Carlson, Low-distortion resistive anodes for two-dimensional position-sensitive MCP systems, Review of Scientific Instruments 50 (1979) 1093–1097.

[64] O. Jagutzki, A. Cerezo, A. Czasch, R. Dorner, M. Hattas, M. Huang, V. Mergel, U. Spillmann, K. Ullmann-Pfleger, T. Weber, H. Schmidt-Bocking, G. Smith, Multiple hit readout of a microchannel plate detector with a three-layer delay-line anode, Nuclear Science, IEEE Transactions on 49 (2002) 2477–2483.

[65] O. Jagutzki, J. Lapington, L. Worth, U. Spillman, V. Mergel, H. Schmidt-Böcking, Position sensitive anodes for MCP read-out using induced charge measurement, Nuclear Instruments and Methods in Physics Research Section A: Accelerators, Spectrometers, Detectors and Associated Equipment 477 (2002) 256 − 261.

[66] J. Lapington, A. Breeveld, M. Edgar, M. Trow, A novel imaging readout with improved speed and resolution, Nuclear Instruments and Methods in Physics Research Section A: Accelerators, Spectrometers, Detectors and Associated Equipment 310 (1991) 299 − 304.

[67] J. Lapington, B. Sanderson, L. Worth, J. Tandy, Imaging achievements with the vernier readout, Nuclear Instruments and Methods in Physics Research Section A: Accelerators, Spectrometers, Detectors and Associated Equipment 477 (2002) 250 – 255.

[68] T. Mizogawa, H. Shiromaru, M. Sato, Y. Ito, A two-dimensional position-sensitive ion detector based on modified backgammon method with weighted-coupling capacitors, International Journal of Mass Spectrometry 215 (2002) 141 – 149.

[69] T. Mizogawa, M. Sato, M. Yoshino, Y. Itoh, Y. Awaya, A two-dimensional position-sensitive anode for microchannel plates based on the MBWC technique, Nuclear Instruments and Methods in Physics Research Section A: Accelerators, Spectrometers, Detectors and Associated Equipment 387 (1997) 395 – 400.

[70] T. Mizogawa, Y. Awaya, Y. Isozumi, R. Katano, S. Ito, N. Maeda, New readout technique for two-dimensional position-sensitive detectors, Nuclear Instruments and Methods in Physics Research Section A: Accelerators, Spectrometers, Detectors and Associated Equipment 312 (1992) 547 – 552.

[71] T. Mizogawa, M. Sato, Y. Awaya, Application of the "MBWC" two-dimensional position readout technique to a multiwire proportional counter, Nuclear Instruments and Methods in Physics Research Section A: Accelerators, Spectrometers, Detectors and Associated Equipment 366 (1995) 129 – 136.

[72] M. Burkhard, H. Rothard, C. Biedermann, J. Kemmler, K. Kroneberger, P. Koschar, O. Heil, K. O. Groeneveld, Heavy-ion – induced shock electrons from sputter-cleaned solid surfaces, Phys. Rev. Lett. 58 (1987) 1773–1775.

[73] T. Schäfer, Ein ortsabbildender Sekundärelektronendetektor mit hoher Zeitauflösung für Elastic-Recoil-Detection Analysen, Diploma Thesis, Technische Universität München, (2004).

[74] P. Grivet, P. W. Hawkes, A. Septier, Electron optics, Elsevier, 2013.

[75] A. Adams, F. H. Read, Electrostatic cylinder lenses II: Three element Einzel lenses, Journal of Physics E: Scientific Instruments 5 (1972) 150.

[76] R. Veenhof, Garfield, recent developments, Nuclear Instruments and Methods in Physics Research Section A: Accelerators, Spectrometers, Detectors and Associated Equipment 419 (1998) 726 – 730.

[77] Comsol Multiphysics®, www.comsol.com.

[78] G. Pozzi, P. W. Hawkes, Particles and waves in electron optics and microscopy, Academic Press, 2016.

[79] E. Brüche, W. Henneberg, Geometrische Elektronenoptik, Springer Berlin Heidelberg, 1936.

[80] Y. Efendiev, T. Y. Hou, Multiscale finite element methods: theory and applications, Springer Science & Business Media, 2009.

[81] G. Erskine, Electrostatic problems in multiwire proportional chambers, Nuclear Instruments and Methods 105 (1972) 565 – 572.

[82] P. Bhattacharya, S. Mukhopadhayay, N. Majumdar, S. Bhattacharya, Realistic three dimensional simulation on the performance of micromegas, Nuclear Instruments and Methods in Physics Research Section A: Accelerators, Spectrometers, Detectors and Associated Equipment 628 (2011) 465 – 469.

[83] R. Lutter, O. Schaile, K. Schoffel, K. Steinberger, P. Thirolf, C. Broude, MARaBOOU – A MBS and ROOT based online/offline utility, in: Real Time Conference, 1999. Santa Fe 1999. 11th IEEE NPSS, 1999, pp. 363–366.

[84] O. Scherzer, Über einige Fehler von Elektronenlinsen, Zeitschrift für Physik 101 (1936) 593–603.

[85] W. Blum, W. Riegler, L. Rolandi, Particle Detection with Drift Chambers, Particle Acceleration and Detection, Springer, 2010.

[86] W. Assmann, Ionization chambers for materials analysis with heavy ion beams, Nuclear Instruments and Methods in Physics Research Section B: Beam Interactions with Materials and Atoms 64 (1992) 267 – 271.

[87] H. Fulbright, Ionization chambers, Nuclear Instruments and Methods 162 (1979) 21 – 28.

[88] J. Julin, M. Laitinen, T. Sajavaara, Time-of-flight ERD with a 200 mm2 Si3N4 window gas ionization chamber energy detector, Nuclear Instruments and Methods in Physics Research Section B: Beam Interactions with Materials and Atoms 332 (2014) 271 – 274.

[89] E. Grimsehl, W. Schallreuter, Grimsehl Lehrbuch der Physik, no. Bd. 3, Teubner Verlagsgesellschaft, 1959.

[90] O.Frisch, Unpublished Report BR-49, British Energy Report (1944).

[91] O. Bunemann, T. E. Cranshaw, J. A. Harvey, Design of grid ionization chambers, Canadian Journal of Research 27a (5) (1949) 191–206.

[92] F. Sauli, Principles of operation of multiwire proportional and drift chambers, CERN, 1977, p. 92 p.

[93] A. Chevarier, N. Chevarier, S. Chiodelli, A high resolution spectrometer used in MeV heavy ion backscattering analysis, Nuclear Instruments and Methods in Physics Research 189 (1981) 525 – 531.

[94] F. Schiettekatte, Fast Monte Carlo for ion beam analysis simulations, Nuclear Instruments and Methods in Physics Research Section B: Beam Interactions with Materials and Atoms 266 (2008) 1880 – 1885.

[95] S. Lüke, Ein ortsauflösender Gasionisationsdetektor für die Elastic-Recoil-Detection, Master's thesis, Hochschule für angewandte Wissenschaften-FH München (2011).

[96] C. Kottler, Dünnschichtanalyse mittels Vorwärtsstreuung bei tiefer Energie, Ph.D. thesis, ETH Zürich (2005).

[97] Y. Zhang, H. J. Whitlow, T. Winzell, I. F. Bubb, T. Sajavaara, K. Arstila, J. Keinonen, Detection efficiency of time-of-flight energy elastic recoil detection analysis systems, Nuclear Instruments and Methods in Physics Research Section B: Beam Interactions with Materials and Atoms 149 (1999) 477 – 489.

[98] Hamamatsu, Technical information - MCP assembly, HAMAMATSU PHOTONICS K.K. (September, 2006).

[99] G. Fraser, The electron detection efficiency of microchannel plates, Nuclear Instruments and Methods in Physics Research 206 (1983) 445 – 449.

[100] R. R. Goruganthu, W. G. Wilson, Relative electron detection efficiency of microchannel plates from 0-3 keV, Review of Scientific Instruments 55 (1984) 2030–2033.

[101] E. Sternglass, Theory of secondary electron emission by high-speed ions, Physical Review 108 (1957) 1–12.

[102] H.-G. Clerc, H. Gehrhardt, L. Richter, K. Schmidt, Heavy-ion induced secondary electron emission - A possible method for Z-identification, Nuclear Instruments and Methods 113 (1973) 325–331.

[103] H. Rothard, K. Kroneberger, A. Clouvas, E. Veje, P. Lorenzen, N. Keller, J. Kemmler, W. Meckbach, K.-O. Groeneveld, Secondary-electron yields from thin foils: A possible probe for the electronic stopping power of heavy ions, Physical Review A 41 (1990) 2521–2535.

[104] P. Ström, P. Petersson, M. Rubel, G. Possnert, A combined segmented anode gas ionization chamber and time-of-flight detector for heavy ion elastic recoil detection analysis, Review of Scientific Instruments 87 (2016) 103303.

[105] M. Moser, 3D – Hydrogen Microscopy at the Munich proton microprobe SNAKE, Ph.D. thesis, Universität der Bundeswehr München (2017).

[106] J. Mort, M. A. Machonkin, K. Okumura, Compensation effects in nitrogen-doped diamond thin films, Applied Physics Letters 59 (1991) 3148–3150.

[107] R. Locher, C. Wild, N. Herres, D. Behr, P. Koidl, Nitrogen stabilized <100> texture in chemical vapor deposited diamond films, Applied Physics Letters 65 (1994) 34–36.

[108] S. Biagi, Monte Carlo simulation of electron drift and diffusion in counting gases under the influence of electric and magnetic fields, Nuclear Instruments and Methods in Physics Research Section A: Accelerators, Spectrometers, Detectors and Associated Equipment 421 (1999) 234 – 240.

Appendix

„The problem with the world is that
the intelligent people are full of doubts,
while the stupid ones are full of confidence."   *- Charles Bukowski*

Appendix A

Position determination via drift time measurement

The position sensitivity of the gas ionization chamber, utilized as energy detector of the TOF-E setup, is greatly improved at low recoil ion energies by a drift time measurement of the ionization electrons within the gas volume (see section 4.4.3). The choice of detection gas and thereby the corresponding electron drift characteristics play an important role with respect to the achievable position resolution. This is demonstrated in the following by a drift time simulation utilizing the Garfield code. The simulation compares the position position measurement via drift time for the detection gas isobutane (C_4H_{10}) and tetrafluoromethane (CF_4), the latter being used for the energy detector developed in this work. The simulation result is put in contrast to the measurement presented in section 4.4.3.

The drift chamber simulation program code Garfield features the integrated program code Magboltz [76]. Magboltz allows to compute the drift velocities, longitudinal and transversal diffusion coefficients, as well as other properties of electrons within detection gases by numerical integration of the Boltzmann transport equations under the influence of electrical and magnetic fields [108]. A Monte Carlo method based routine of Garfield utilizes the results provided by Magboltz for the electron drift calculation within the detection gas. Figure A.1 shows the drift velocities obtained with Magboltz for tetrafluoromethane (A.1(a)) and isobutane (A.1(b)) versus the electric field strength at a gas pressure of 20 mbar. The drift velocity in CF_4 is increased by a factor of ≈ 2.5 in contrast to isobutane for the occurring field strengths within the gas ionization chamber. As seen from Fig. A.2, the longitudinal diffusion coefficients (primary relevant for the drift time measurement) are reduced by

(a)   (b)
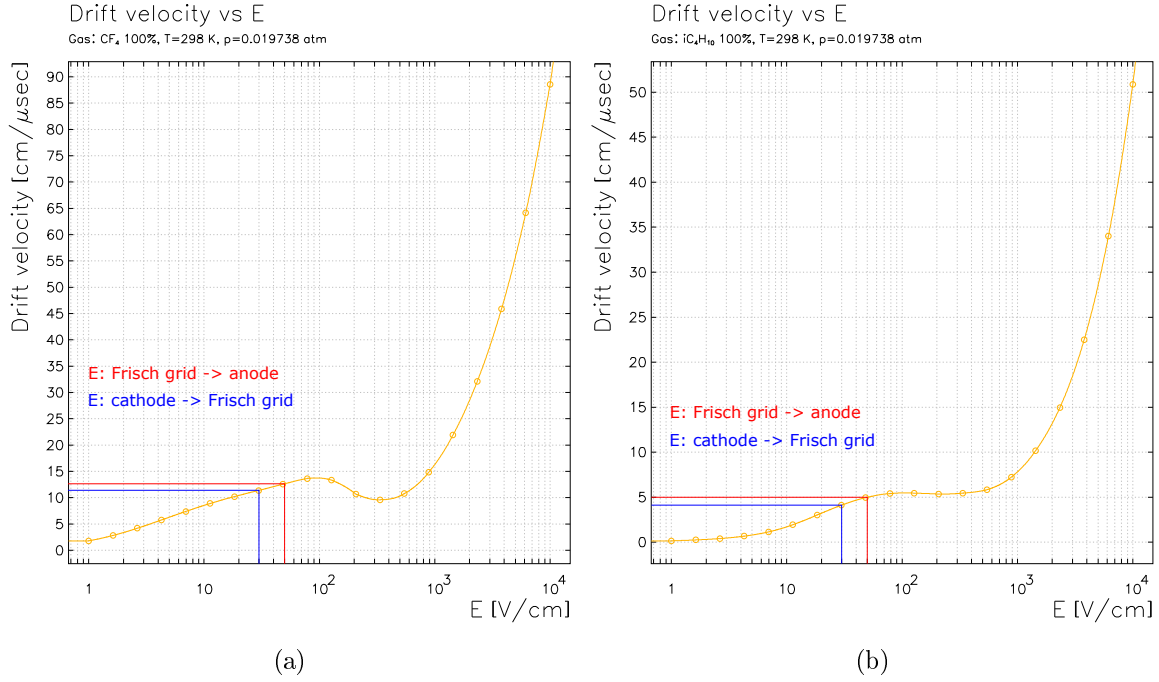
Figure A.1: *(a): Electron drift velocity calculated by Magboltz for the detection gas tetrafluoromethane (CF₄) versus the field strength at a gas pressure of 20 mbar. The for the energy detector relevant values are marked accordingly. (b): Electron drift velocity calculated by Magboltz for the detection gas isobutane (C₄H₁₀) versus the field strength at a gas pressure of 20 mbar. The electron drift velocity in CF₄ is higher by a factor of ≈ 2.5 than in C_4H_{10} for the same field strengths and pressure values.*

a factor of ≈ 2 according to the Magboltz calculations.

The results of the Monte Carlo based drift time simulation, taking the differences in electron drift velocity and diffusion into account, are illustrated in Fig. A.3. The starting points of the ionization electrons in the simulation (zero momentum at start, 500 electrons per starting point, 50 starting points per 5 mm) are set appropriately to resemble the structure of the segmented silicon nitride entrance window shown in Fig. 4.35. The drift time till anode arrival within the electric field is calculated. As seen from Fig A.3(a), the single entrance windows with a width of 5 mm are clearly separated in drift time. However, for isobutane, the simulation only shows a marginal separation in drift time of the individual window segments.

The histogram crated by Garfield illustrated in Fig. A.3(a) is imported into ROOT for subsequent data analysis. A function consisting of a convolution of a Gaussian- and a square function is fitted to the peak position data, as illustrated in Fig. A.4(a).
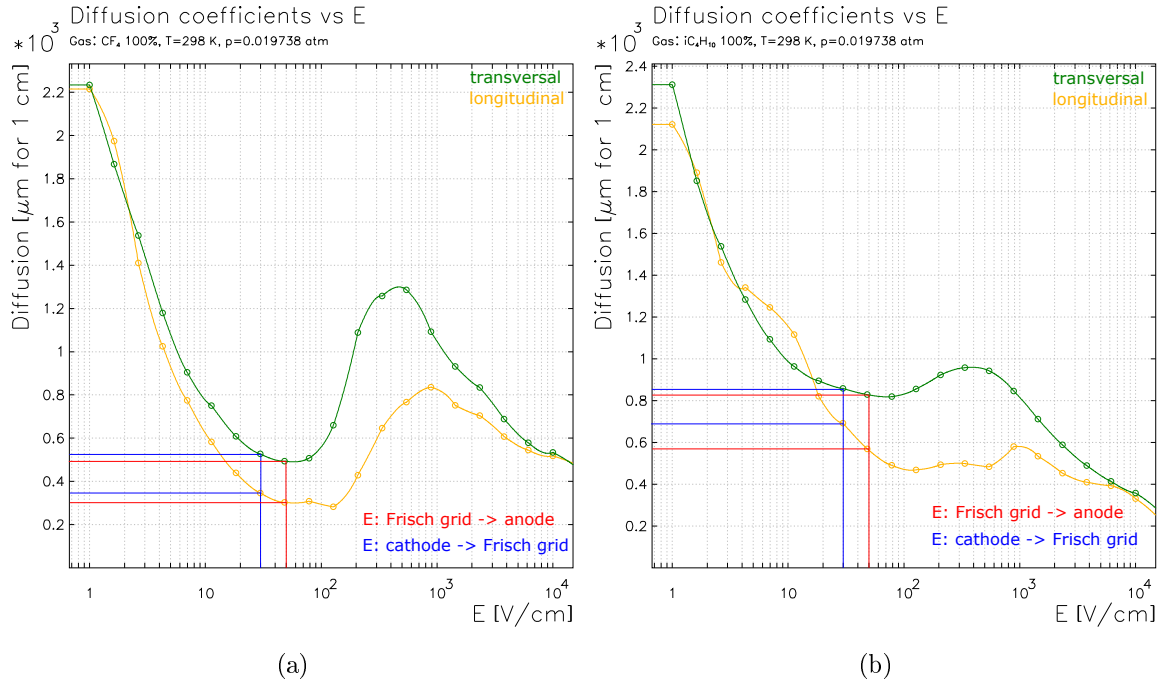
Figure A.2: *(a): Longitudinal and lateral electron diffusion coefficients calculated by Magboltz for the detection gas tetrafluoromethane (CF_4) versus the field strength at a gas pressure of 20 mbar. The for the energy detector relevant values are marked accordingly. (b): Longitudinal and lateral electron diffusion coefficients calculated by Magboltz for the detection gas isobutane (C_4H_{10}) versus the field strength at a gas pressure of 20 mbar. The longitudinal electron diffusion coefficient in CF_4 is lower by a factor of ≈ 2 than in C_4H_{10} for the same field strengths and pressure values.*

Since the drift time data intrinsically resembles the position data and by consideration of the particular widths of the single segments, the simulation shows an average position resolution of $2.6\,\text{mm} \pm 0.1\,\text{mm}$ (FWHM) for all 7 window segments according to the fit. The simulation result is in excellent agreement with the measured drift time data (see section 4.4.3), which is illustrated in Fig. A.4(b). The data shows a position resolution of $2.4\,\text{mm} \pm 0.1\,\text{mm}$ (FWHM). The most outer peaks in Fig. A.4(b) are disregarded, since they are affected by the illumination of the detector in the measurement.

The difference of $0.2\,\text{mm}$ in position resolution between the simulated and the measured value can be attributed to the fact, that the simulation uses the drift time till arrival of the electrons on the anode as stop criteria. The real drift time measurement, however, uses a certain threshold crossing of the energy signal obtained
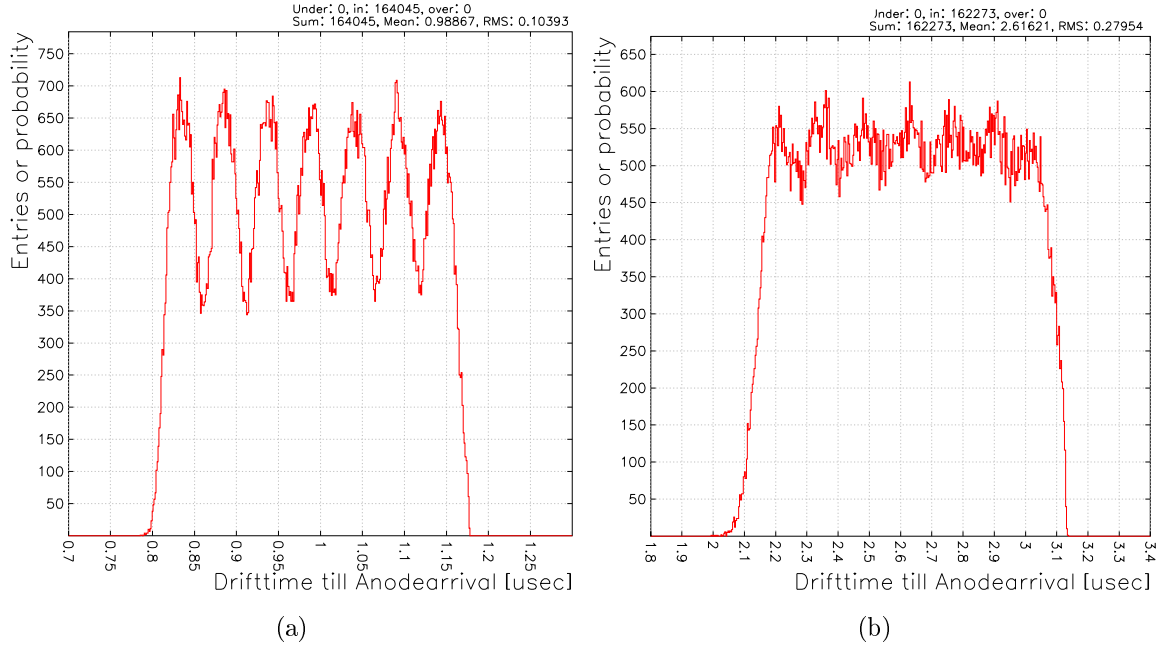
Figure A.3: *(a): Garfield drift time simulation taking the electron drift velocities and diffusion coefficients within the particular detection gases into account. The drift times of the electrons within the electric field of the gas ionization chamber are calculated starting from each segment of the entrance window till anode arrival in case of the detection gas CF_4. Each segment of the silicon nitride window (see Fig. 4.35) is clearly resolved. (b): The same simulation is executed for the detection gas C_4H_{10}. The individual segments are poorly separated in drift time.*

from the anode to stop the drift time measurement (the energy signal at the time of arrival of the electrons on the anode would be zero). Thus, the real drift time measurement is stopped in between the distance of the anode to the Frisch grid by the signal rise, which effectively shortens the drift length and thereby mitigates the influence of diffusion and drift velocity on the drift time.

(a)

(b)
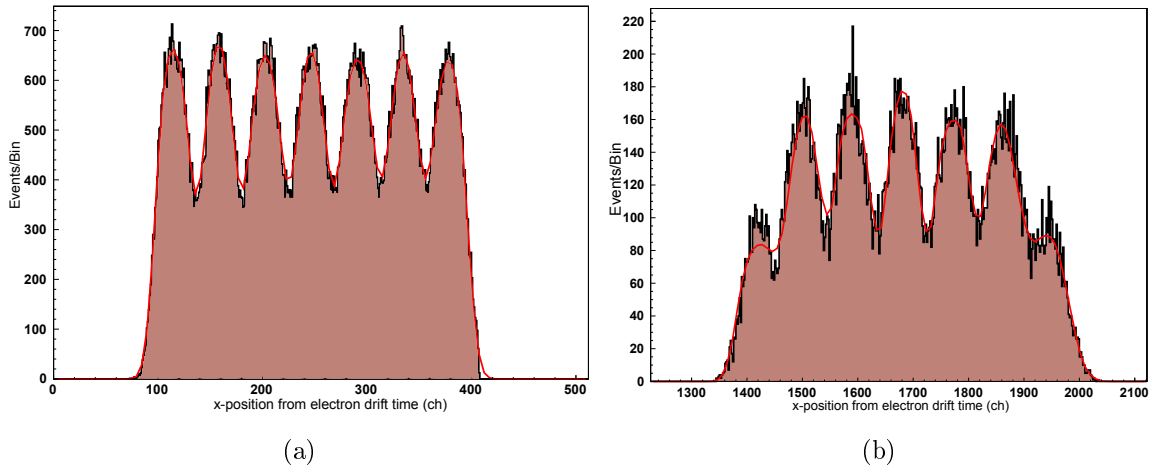
Figure A.4: *(a):* *The simulated drift time spectrum shown in Fig. A.3(a) is imported into ROOT and the peaks of the drift time data are fitted by a function consisting of a convolution of a Gaussian- and a square function. An average position resolution of all peaks of 2.6 mm ± 0.1 mm (FWHM) is obtained.* *(b):* *Drift time spectrum measured for 5.08 MeV carbon recoil ions: The measurement is in excellent agreement with the simulation and shows a position resolution of 2.4 mm ± 0.1 mm (FWHM). See text for further explanation.*

Appendix B

List of publications

Time of flight assisted ΔE-E method for enhanced isotope separation capabilities in heavy ion elastic recoil detection analysis. S. Eschbaumer, A. Bergmaier, D. Seiler,G. Dollinger; 2017. *Nuclear Instruments and Methods in Physics Research Section B: Beam Interactions with Materials and Atoms. (in press).*

A position sensitive time of flight detector for heavy ion ERD. S. Eschbaumer, A. Bergmaier, G. Dollinger; 2016. *Nuclear Instruments and Methods in Physics Research Section B: Beam Interactions with Materials and Atoms. 371 125-131.*

Position and time resolution measurements with a microchannel plate image intensifier: A comparison of monolithic and pixelated $CeBr_3$ scintillators. U. Ackermann, S. Eschbaumer, A. Bergmaier, W. Egger, P. Sperr, C. Greubel, B. Löwe, P. Schotanus, G. Dollinger; 2016. *Nuclear Instruments and Methods in Physics Research Section A: Accelerators, Spectrometers, Detectors and Associated Equipment. 823 56-64.*

A microbeam slit system for high beam currents. T. Vallentin, M. Moser, S. Eschbaumer, C. Greubel, T. Haase, P. Reichart and T. Rösch, G. Dollinger; 2015. *Nuclear Instruments and Methods in Physics Research Section B: Beam Interactions with Materials and Atoms. 348 43-47.*

Conference proceedings

07/2016 Invited Talk: An angular sensitive time of flight setup for heavy ion ERD *ECCART12*, Jyväskylä, Finland.

06/2015 Best PhD Student Poster Award for: An angular sensitive time of flight setup for heavy ion ERD *IBA 2015*, Opatija, Croatia.

04/2013 Talk: A new angular sensitive TOF detector for ERD analysis: Actual state of development *SPIRIT JRA meeting*, Bled, Slovenia.

Appendix C

Danksagung